Evaluation of Synthetic Ligands as Staphylococcal Nuclease Inhibitors for Potential Anti-MRSA Therapy

A Thesis

Submitted in Partial Fulfillment of the
Requirements for the Degree of

DOCTOR OF PHILOSOPHY

by

BARLINA KONWAR

Department of Biosciences and Bioengineering
Indian Institute of Technology Guwahati
Guwahati-781039, Assam, India

August 2023


भारतीय प्रौद्योगिकी संस्थान गुवाहाटी
Indian Institute of Technology Guwahati

Evaluation of Synthetic Ligands as Staphylococcal Nuclease Inhibitors for Potential Anti-MRSA Therapy

A Thesis

Submitted in Partial Fulfillment of the
Requirements for the Degree of

DOCTOR OF PHILOSOPHY

by

BARLINA KONWAR

Department of Biosciences and Bioengineering
Indian Institute of Technology Guwahati
Guwahati-781039, Assam, India

August 2023

Dedicated to My Parents

STATEMENT

I do hereby declare that the research findings of this thesis is the result of research work carried out by me in the Department of Biosciences and Bioengineering, Indian Institute of Technology Guwahati, Guwahati, India, under the supervision of Professor Aiyagari Ramesh.

As per the general norms of reporting research findings, due acknowledgments have been made, wherever the research findings of other researchers have been cited in this thesis.

Barlina Konwar

Date: 4-8-2023

Barlina Konwar

INDIAN INSTITUTE OF TECHNOLOGY GUWAHATI

DEPARTMENT OF BIOSCIENCES AND BIOENGINEERING

CERTIFICATE

It is certified that the work described in this thesis entitled " ***Evaluation of Synthetic Ligands as Staphylococcal Nuclease Inhibitors for Potential Anti-MRSA Therapy*** " by Ms. Barlina Konwar for the award of degree of Doctor of Philosophy is an authentic record of the results obtained from the research work carried out under my supervision in the Department of Biosciences and Bioengineering, Indian Institute of Technology Guwahati, India, and this work has not been submitted elsewhere for the award of any other degree.

CERTIFIED

Aiyagari Ramesh

Aiyagari Ramesh, Ph.D.

(Thesis Supervisor)

Date: 04/08/2023

Barlina Konwar

Barlina Konwar

(Candidate)

Roll No: 176106008

ACKNOWLEDGEMENT

I want to extend my immense gratitude toward all the people who have been part of this journey and who guided and kept their faith in me. I want to acknowledge their presence and support throughout this endeavour. At the very beginning, I would like to express my deep sense of gratitude to my PhD supervisor, **Prof. Aiyagari Ramesh**, for giving me the opportunity to work under him and providing me with all the facilities to carry out my research in a smooth manner. I sincerely thank him for all his help, encouragement, patience, constructive criticism, and scholarly contributions throughout my entire PhD tenure. I will always be appreciative of his encouraging words in all facets of my life.

I want to thank my doctoral committee members, Prof. Gurvinder Kaur Saini, Prof. S. Senthilkumar and Prof. Bhubaneswar Mandal, for their support, perceptive observations and helpful suggestions throughout this tenure, which enabled me to improve my work.

I would also like to express my deepest gratitude to Prof. Gopal Das, Department of Chemistry for providing me with the synthesized compounds in order to proceed with my research work. I would further like to thank him for helping me in data analysis, giving his priceless advice and showing enormous support.

I am highly indebted to the Department of Biosciences and Bioengineering, Centre for Nanotechnology, Centre for the Environment, Central Instrumentation Facility, IIT Guwahati and DBT Program Support Facility for providing the support and assistance required to carry out my thesis work. I am also thankful to the faculty, staff and other members of the Department of Biosciences and Bioengineering, IIT Guwahati.

I would like to thank Prof. Benu Dhawan, AIIMS, New Delhi and Prof. Kasturi Mukhopadhyay, JNU, New Delhi for providing the MRSA strains. I would like to extend my sincere gratitude towards Prof. Siddhartha Sankar Ghosh, Prof. Pranab Goswami, Prof. Lingaraj Sahoo and Dr. Biplab Bose for giving the opportunity to work with the DBT program support team. I sincerely appreciate all my seniors for their love, support and valuable advice. I am thankful to them for providing an amicable work environment. I would like to thank all the members under the DBT program support facility.

I would like to thank Sagnik De, Department of Chemistry, IIT Guwahati for the scientific collaboration and for his help regardingvarious instrument handling.

This journey is incomplete without my friends. I would like to thank my friends Mriyangku Pratim and Rashmi Rekha for their constant support, care and love. I would like to thank Muktashree, Arup, Pratik and Arupam for their support and making my IIT Guwahati campus life more fun-filled.

I would like to specially thank my parents Mrs. Ranju Konwar and Mr. Durgeswar Konwar, for their unending support, love, prayers, and believing in me to realize my own potential. I am deeply indebted to my parents for the sacrifices they have borne to ensure the fulfillment of my dreams. Nothing can be fun and fulfilling without siblings, I want to thank my sisters Kanika, Gargi, and Darshna Drisha for being my biggest support system and my stress buster.

Last but not the least, I thank GOD for giving me the patience and strength to follow my dream.

Barlina Konwar

CONTENTS

Contents i

Abbreviations vii

List of Tables xi

List of Schemes and Figures xv

CHAPTER 1: Introduction and Literature Review

Introduction 3

Literature Review on the Research Topic 4

1.1. Antibiotic-Resistant Pathogenic Bacteria 4

1.2. Methicillin-Resistant *Staphylococcus aureus* (MRSA) 5

1.3. MRSA Infections 7

1.4. Mechanism of Antibiotic Resistance in MRSA 8

1.5. Virulence Factors in *S. aureus* 9

1.6. Staphylococcal Nuclease 10

1.7 Nuclease Inhibitors: Potential Therapeutics for Mitigation of MRSA Infection 12

Motivation and Objective of the Present Investigation 17

CHAPTER 2: Assessment of Anthraquinone-based Ligands as Staphylococcal Nuclease (MNase) Inhibitor

Abstract 21

2.1. Introduction 22

2.2. Materials and Methods 23

- 2.2.1. Growth Media and Chemicals 23
- 2.2.2. Bacterial strain and growth conditions 23
- 2.2.3. Synthetic ligands 24
- 2.2.4. Screening of ligands as MNase inhibitors 24
- 2.2.5. Assessment of C1-MNase interaction 26
- 2.2.6. Evaluation of C1-DNA interaction 27

2.2.7. Nuclease inhibition assay 27
2.2.8. Toluidine blue-DNA (TB-DNA) agar plate assay 28
2.2.9. Plasmid DNA cleavage assay 28
2.2.10. Bactericidal activity and cytotoxic potential of C1 28
2.3. Results and Discussion 29
2.3.1. Design rational of synthetic ligands 29
2.3.2. Design rational of synthetic ligands 30
2.3.3. Interaction of C1 with MNase and CT-DNA 31
2.3.4. Kinetics of MNase activity and inhibition by C1 35
2.3.5. Inhibition of MRSA secreted nuclease and plasmid DNA cleavage by C1 37
2.3.6. Bactericidal activity and cytotoxic potential of C1 38
2.4. Significant Findings 39

CHAPTER 3: Generation of C1-loaded HSA Nanocarrier for Targeting MNase

Abstract 43
3.1. Introduction 44
3.2. Materials and Methods 45
3.2.1. Materials 45
3.2.2. C1-loaded HSA nanocarrier (C1-HNC) 45
3.2.3. Characterization of HNP and C1-HNC 47
3.2.4. In vitro release kinetics 47
3.2.5. MNase inhibition by C1-HNC eluate 48
3.2.6. Cytotoxic potential of C1-HNC 49
3.3. Results and Discussion 49
3.3.1. C1-loaded HSA nanocarrier (C1-HNC) 49
3.3.2. Release studies 50

3.3.3 MNase inhibition by C1-loaded nanocarrier 52
3.3.4 Cytotoxic potential of C1-HNC 55
3.4. Significant Findings 55

CHAPTER 4: Benzimidazole-based Ligand for Targeting MNase and Enhancing MRSA Uptake by Macrophage-like Cells

Abstract 59
4.1. Introduction 60
4.2. Materials and Methods 61
4.2.1. Materials 61
4.2.2. Bacterial Strain and Growth Conditions 62
4.2.3. Synthetic Ligands 62
4.2.4. Screening of ligands as MNase inhibitors 62
4.2.5. Nuclease inhibition assay based on enzyme kinetics 63
4.2.6. Inhibition of secreted Nuclease of MRSA by C2 64
4.2.7. Bactericidal activity of C2 64
4.2.8. Interaction of C2 with MNase 64
4.2.9. Interaction of C2 with CT-DNA 65
4.2.10. Entrapment of MRSA cells in CT-DNA 66
4.2.11. Propagation and activation of THP-1 cells 67
4.2.12. Uptake of MRSA cells by PMA-activated THP-1 cells 69
4.2.13 Confocal microscope analysis to ascertain uptake of MRSA cells by PMA-activated THP-1 cells 70
4.2.14 Estimation of the uptake of viable MRSA cells by PMA-activated THP-1 cells by plating 72
4.2.15 Cytotoxic Potential of C2 72

4.3. Results and Discussion 73

4.3.1. Design of synthetic ligands 73

4.3.2. Evaluation of ligands as MNase inhibitor 73

4.3.3. Effect of C2 on kinetics of MNase activity and inhibition of nuclease secreted by MRSA 75

4.3.4. Solution-based Interaction of C2 with MNase and CT-DNA 77

4.3.5. Effect of C2 on entrapment of MRSA by DNA 80

4.3.6. Effect of C2 on the uptake of MRSA by activated THP-1 cells 83

4.3.7. Cytotoxic potential of C2 90

4.4. Significant Findings 90

CHAPTER 5: Evaluation of Napthalimide-based Ligand as MNase Inhibitor for Targeting MRSA

Abstract 95

5.1. Introduction 96

5.2. Materials and Methods 97

5.2.1. Growth media and chemicals 97

5.2.2. Bacterial strain and growth conditions 97

5.2.3. Synthetic ligands 97

5.2.4. Potential of ligands as MNase inhibitor 97

5.2.5. Effect of C1 on MNase kinetics 98

5.2.6. Interaction of C1 with MNase and DNA 100

5.2.7. Toluidine blue-DNA (TB-DNA) agar plate assay 101

5.2.8. Bactericidal activity of C1 101

5.2.9. Cytotoxic potential of C1 101

5.3. Results and Discussion 102

5.3.1. Design rational of napthalimide-based ligands 102

5.3.2. Appraisal of MNase inhibition by ligands 103

5.3.3. Mechanistic studies on MNase inhibition by C1 104

5.3.4. Inhibition of MRSA nuclease and bactericidal activity of C1 106

5.3.5. Solution-based studies on interaction of C1 with MNase and CT-DNA 107

5.3.6. Cytotoxic potential of C1 110

5.4. Significant Findings 111

CHAPTER 6: Therapeutic Potential of Napthalimide-based MNase Inhibitor for Mitigation of MRSA

Abstract 115

6.1. Introduction 116

6.2. Materials and Methods 117

6.2.1. Growth media and chemicals 117

6.2.2. Bacterial strain and growth conditions 117

6.2.3. Synthetic ligands 117

6.2.4. Assessment of MRSA entrapment in CT-DNA 117

6.2.5. Estimation of the uptake of MRSA by PMA-activated THP-1 cells 118

6.2.6. C1 loaded PF-127 Micellar Carrier (C1-PMC) 118

6.2.7. Characterization of PMC and C1-PMC 119

6.2.8. In vitro release kinetics of C1 from C1-PMC 120

6.2.9. MNase inhibition by C1-PMC eluate 120

6.2.10. Effect of C1-PMC on adhesion of MRSA onto collagen 121

6.2.11. Bactericidal activity of C1-PMC 122

6.2.12 Effect of C1-PMC on adhesion of MRSA onto collagen-coated titanium wire 123

6.2.13 Cytotoxicity studies with C1-PMC and C1-PMC eluate 123

6.3. Results and Discussion 124

6.3.1. Effect of C1 on MRSA entrapment in DNA 124

6.3.2. Uptake of DNA-entrapped MRSA by activated THP-1 cells 126

6.3.3. C1-loaded Pluronic F-127 Micellar Nanocarrier (C1-PMC) 131

6.3.4. Mitigation of MRSA adhesion onto collagen by C1-PMC 134

6.3.5. Inhibition of MRSA adhesion onto orthopaedic implant by C1-PMC 135

6.4. Significant Findings 139

Summary and Future Scope Perspective 143

Bibliography

Appendix

List of Publications

ABBREVIATIONS

µg	Microgram
µL	Microliter
µM	Micromolar
AFM	Atomic Force Microscope
ALA	Alanine
ASN	Asparagine
ASP	Aspartic acid
ARG	Arginine
BHI	Brain-heart infusion broth
CD	Circular dichroism
cFDA-SE	5(and 6)-carboxyfluorescein diacetate succinimidyl ester
CFU	Colony forming unit
CFS	Cell-free Supernatant
clogP	Partition coefficient
cps	Counts per second
CT-DNA	Calf thymus Deoxyribonucleic Acid
C1	Compound 1
C1-HNC	C1-loaded human serum albumin nanocarrier
C1-PMC	C1 loaded Pluronic F127 micellar carrier
C2	Compound 2
C3	Compound 3
C4	Compound 4
C5	Compound 5
C6	Compound 6
CMC	Critical Micellar Concentration
DAPI	4′,6-Diamidine-2′-phenylindole
DLS	Dynamic light scattering
DMEM	Dulbecco's modified eagles medium
DMSO	Dimethyl sulfoxide
DNA	Deoxyribonucleic Acid
EDTA	Ethylenediaminetetraacetic acid
EDX	energy-dispersive X-ray
ESI-MS	Electrospray Ionisation Mass Spectrometry
FBS	Fetal bovine serum

Abbreviations

FESEM	Field emission scanning electron microscope
FETEM	Field-Emission Transmission Electron Microscope
FSC	Forward-angle light scatter
FTIR	Fourier-transform infrared spectroscopy
GLU	Glutamic acid
HEK	Human embryonic Kidney
HEPES	N-2-Hydroxyethyl Piperazine N-2 Ethane Sulphonic acid
HNP	Human serum albumin nanoparticle
HSA	Human serum albumin
$\mathbf{IC_{50}}$	half maximal inhibitory concentration
ITC	Isothermal Titration Calorimetry
$\mathbf{K_a}$	Association constant
K_{cat}	Turnover number
Kcal	Kilocalorie
K_i	Inhibitor constant
Kq	Quenching constant
K_{bin}	Binding Constant
Kg	Kilogram
K_m	Michaelis constant
LEU	Leucine
LYS	Lysine
mdeg	Millidegree
mg	Milli grams
mL	Milliliter
mM	Millimolar
MNase	Micrococcal nuclease
MRSA	Methicillin-resistant *Staphylococcus aureus*
MTT	3-(4,5-Dimethylthylthiazol-2-yl)-2,5-diphenyltetrazolium bromide
MW	Molecular weight
MWCO	Molecular weight cut-off
NC	Nicked circular DNA
NET	Neutrophil extracellular traps
nm	Nanometer
nM	Nanomolar
NMR	Nuclear magnetic resonance
PBS	Phosphate buffered saline
PF-127	Pluronic F127

Abbreviations

pg	Picogram
PMA	Phorbol 12-myristate-13-acetate
PMC	Pluronic F-127 micellar carrier
PRO	Proline
rpm	Revolutions per minute
RPMI	Roswell Park Memorial Institute
RT	Room Temperature
S.aureus	*Staphylococcus aureus*
SBF	Simulated body fluid
SC	Supercoiled DNA
SSC	Side scatter
TAMRA-SE	5-carboxy-tetramethylrhodamine N-succinimidyl ester
TB	Toluidine blue
Tris	Tris(hydroxymethyl)aminomethane
TYR	Tyrosine
U	Unit
UV	Ultraviolet
V_{max}	Maximum velocity
λ_{Em}	Emission wavelength
λ_{Ex}	Excitation wavelength

LIST OF TABLES

CHAPTER 1 **Page No.**

Table 1.1. Classification of antibiotic-resistant pathogenic microbes on the basis of the threat levels as proposed by CDC (CDC Report, 2019). 6

Table 1.2. An overview of infections caused by *Staphylococcus aureus*. 8

Table 1.3. Overview of representative virulence factors of *S. aureus* and their implications in the host. 10

Table 1.4. Inhibitory concentrations of known MNase and DNase inhibitors. 13

CHAPTER 2

Table 2.1. Secondary structure analysis of MNase following interaction with C1. 33

Table 2.2. Kinetics parameters for MNase determined in presence of C1. 36

Table A2.1. Statistical analysis for MNase inhibition rendered by ligands C1-C5. 174

Table A2.2 Secondary structure analysis of HSA following interaction with C1. 174

Table A2.3 Binding interactions and binding energy for C1 with the amino acid residues of MNase determined in molecular docking studies. 176

Table A2.4 Binding interactions and binding energy for C1 with the amino acid residues of DNase I determined in molecular docking studies. 177

Table A2.5 Rate constant for CT-DNA Hoechst dye-C1 preformed complex samples digested with MNase. 178

CHAPTER 3

Table 3.1. Amount of C1 encapsulated in HSA nanoparticle and determination of encapsulation efficiency of C1. 50

Table 3.2. Rate constant for decrease in fluorescence emission intensity of CT-DNA bound Hoechst dye in presence of varying concentrations of C1 eluate obtained from C1-HNC. 54

CHAPTER 4

Table 4.1. Kinetic Parameters for MNase ascertained in presence of C2. 76

Table 4.2. Secondary structure analysis of MNase following interaction with C2. 79

Table A4.1 Statistical analysis for MNase inhibition rendered by ligands C1 - C2. 182

Table A4.2 Rate constant for CT-DNA Hoechst dye-C1 preformed complex samples digested with MNase. 182

Table A4.3 Secondary structure analysis of HSA following interaction with C2. 184

Table A4.4 Binding interactions and binding energy of ligand C2 with the amino acid residues of MNase. 186

Table A4.5 Binding interactions and binding energy for C2 with the amino acid residues of DNase I determined in molecular docking studies. 187

CHAPTER 5

Table 5.1. Kinetic parameters for MNase assessed in presence of C1. 105

Table 5.2. Secondary structure analysis of MNase following interactionwith C1. 108

Table A5.1 Salient attributes of napthalimide-based ligands determined by using Molinspiration tool (www.molinspiration.com). 189

Table A5.2 Rate constant for decrease in fluorescence emission intensity of CT-DNA-bound-picogreen dye in presence of varying concentrations of C1, C2 and C3. 190

Table A5.3 Statistical analysis for MNase inhibition rendered by ligands C1 – C3. 191

Table A5.4 Rate constant for decrease in fluorescence emission intensity of CT-DNA picogreen dye complex with varying concentration of C1 in presence of MNase. 192

Table A5.5 Secondary structure analysis of human serum albumin (HSA) following interaction with C1. 193

Table A5.6 Binding interactions and binding energy for C1 with the amino acid residues of MNase were determined by molecular docking studies. 195

Table A5.7 Binding interactions and binding energy for C1 with the amino acid residues of DNase I determined in molecular docking studies. 196

CHAPTER 6

Table 6.1	Estimation of the amount of encapsulated C1 in C1-PMC and encapsulation efficiency of C1.	133
Table A6.1	Rate constant for decrease in fluorescence emission intensity of CT-DNA-bound picogreen dye in presence of varying concentrations of C1 eluates obtained from C1-PMC.	200
Table A6.2	Statistical analysis for ascertaining the effect of various treatment regimens on adhesion of *S. aureus* MRSA 100 strain onto collagen.	203

LIST OF FIGURES

CHAPTER 1

		Page No.
Figure 1.1.	Classification of antibiotic-resistant pathogenic bacteria belonging to various priority list proposed by WHO (WHO Report, 2014).	4
Figure 1.2.	(A) Structure of staphylococcal nuclease enzyme available from protein data base (PDB ID:1EY0) and visualized using PYMOL. The active site residues of the enzyme is indicated. (B) Amino acid sequence of staphylococcal nuclease enzyme. The amino acids present in the active site of the enzyme are indicated in dark blue letters.	11
Figure 1.3.	Cartoon illustrating the role of staphylococcal nuclease (MNase) in degradation of the DNA scaffold of NETs resulting in dispersion of the pathogen from the DNA trap.	13

CHAPTER 2

Figure 2.1.	General structure of the synthetic ligands used in the current study. (A) C1, (B) C2, (C) C3, (D) C4, (E) C5 and (F) C6.	33
Figure 2.2.	Schematic representation of the fluorescence-based assay used for screening of ligands as MNase inhibitor.	49
Figure 2.3.	Change in fluorescence emission intensity of CT-DNA Hoechst dye complex in presence of MNase and ligands C1-C6 in separate sets. The concentration of the ligands used in the experiments were (A) 100 nM, (B) 600 nM and (C) 5.0 µM. (D) Dose-dependent MNase inhibition rendered by C1, C2, C3, C4 and C5 based on the measurement of end-point fluorescence emission intensity at 450 nm.	49
Figure 2.4.	(A) ITC analysis to determine the binding isotherm of C1 and MNase. (B) UV-visible absorbance spectra of C1 in presence of CT-DNA. (C) Binding isotherm of C1 in presence of an increasing concentration of CT-DNA.	50
Figure 2.5.	(A) Tryptophan fluorescence emission spectra of MNase in presence of an increasing concentration of C1. (B) Stern-Volmer plot for C1 based on the emission spectra obtained in (A). (C) Scatchard plot for C1 based on emission spectra obtained in (A). (D) CD spectra of MNase measured in presence of an increasing concentration of C1.	52

Figure 2.6. (A) Michaelis-Menten plot for MNase in presence of varying concentrations of substrate and C1 (0.1-5.0 µM). (B) Lineweaver-Burk plot to assess MNase inhibition by C1. 52

Figure 2.7. Dixon plot for MNase in the presence of varying concentrations of C1. CT-DNA concentration was varied from 1.05 µM to 2.10 µM in separate sets. 53

Figure 2.8. (A) Toluidine blue DNA agar plate assay to assess inhibition of MNase present in the cell-free supernatant (CFS) of *S. aureus* MRSA 100. The samples in the wells are : (1) CFS only, (2) CFS and 2.0 µM C1, (3) CFS and 40 µM C1, (4) CFS and 300 µM C1, (5) CFS and 1.0 mM C1 and (6) 1.0 mM C1 only. (B) (i) Agarose gel electrophoresis of (1) Undigested pUC18 plasmid DNA, (2-4) pUC18 plasmid DNA digested with MNase, MNase and 0.5 µM C1, MNase and 1.0 µM C1, respectively. (ii) Histogram profile of the pUC18 plasmid DNA band intensity in (i) analyzed by ImageJ software. NC : nicked circular DNA ; SC :supercoiled DNA. 54

Figure 2.9. (A) Antibacterial activity of C1 against *S. aureus* MRSA 100 and *S. aureus* 4s strains. (B) MTT assay-based assessment of the cytotoxic effect of C1 against HEK 293 cells. The data points were acquired from six independent experimental samples and considered to determine mean ± standard deviation. 56

Figure A2.1 (A) Change in fluorescence emission intensity of CT-DNA Hoechst dye complex in presence of (A) MNase and (B-D) MNase in presence of C6. The concentration of C6 in the experiments were (B) 100 nM, (C) 600 nM and (D) 5.0 µM. 173

Figure A2.2 CD spectra of human serum albumin (HSA) measured in presence of an increasing concentration of C1. 173

Figure A2.3 Change in fluorescence emission intensity of CT-DNA Hoechst dye complex in presence of MNase and dialyzed sample of Mnase-C1 complex. 175

Figure A2.4 Docked structure of C1 with MNase. 176

Figure A.2.5 Docked structure of C1 with DNase I. 177

Figure A2.6 Change in fluorescence emission intensity for CT-DNA Hoechst dye-C1 preformed complex samples digested with MNase. The concentration of C1 in the preformed complex was 0.5 µM and 1.0 µM. The concentration of CT-DNA used in the experiments were (A) 1.75 µM and (B) 3.5 µM. 178

Figure A2.7 Agarose gel electrophoresis of (1) Undigested pUC18 plasmid DNA, (2-3) pUC18 plasmid DNA treated with 1.0 μM C1 and 30 mM EDTA, respectively. NC: Nicked circular DNA; SC: Supercoiled DNA. 179

CHAPTER 3

Figure 3.1. Schematic representation of the key steps followed for preparation of human serum albumin (HSA)-based nanoparticle (HNP). 46

Figure 3.2. Schematic representation of the steps followed for generation of C1-loaded HAS nanocarrier (C1-HNC). 46

Figure 3.3. (A) FESEM image of HSA nanoparticle (HNP). Inset indicates particle size distribution of HNP determined by ImageJ software. (B) FETEM image of HNP. The scale bar for the images in (A) and (B) is 200 nm. (C) AFM-based analysis of the height profile for HNP. Inset indicates 3D topography AFM image of HNP. (D) DLS-based size distribution plot of HNP. 50

Figure 3.4. (A) FESEM image of HSA nanoparticle (HNP). Inset indicates particle size distribution of HNP determined by ImageJ software. (B) FETEM image of HNP. The scale bar for the images in (A) and (B) is 200 nm. (C) AFM-based analysis of the height profile for HNP. Inset indicates 3D topography AFM image of HNP. (D) DLS-based size distribution plot of HNP. 51

Figure 3.5. (A) Detection of proteolytic activity of (i) proteinase K (5.0 Unit) and (ii) cell-free supernatant (CFS) of *S. aureus* MRSA 100 strain on milk agar plate. (B) Cumulative release of C1 from C1-HNC incubated in simulated body fluid (SBF), citrate buffer, HEPES buffer and cell-free supernatant (CFS) obtained from *S. aureus* MRSA 100 strain. 52

Figure 3.6. (A) Cartoon indicating inhibition of MNase by eluate from C1-HNC. (B) Change in the fluorescence emission intensity of CT-DNA-Hoechst dye complex in presence of MNase (lowest trace) and eluates from C1-HNC in separate sets. The concentration of C1 in eluates was 0.1, 0.4, 1.0 and 5.0 μM. (C) Fluorescence microscopic images of (i) DAPI stained CT-DNA. (ii) DAPI stained CT-DNA in presence of MNase. (iii) DAPI stained CT-DNA in presence of MNase and C1 (5.0 μM).; (iv) DAPI stained CT-DNA in presence of MNase and eluate from C1-HNC (loaded with 45 μM C1). (D) Relative mean pixel intensity of CT-DNA-DAPI dye complex (%) for the images shown in (C). I-IV correspond to panels i-iv in (C). (E) MTT assay-based assessment of the cytotoxic effect of C1-HNC against HEK 293 cells. Data points acquired from six independent experimental samples were considered to determine mean ± standard deviation. 53

CHAPTER 4

Figure 4.1. Structure of the benzimidazole-based ligands used in the present investigation. (A) C1 and (B) C2. 63

Figure 4.2. Schematic representation of the protocol used for estimation of entrapment of viable MRSA cells in CT-DNA. 66

Figure 4.3. Schematic representation of the fluorescence microscopy-based protocol used for estimation of entrapment of MRSA cells in CT-DNA. 68

Figure 4.4. A schematic representation of the flow cytometry-based protocol to ascertain activation of THP-1 cells by PMA. 69

Figure 4.5. A schematic representation of the flow cytometry-based protocol to ascertain uptake of TAMRA-labelled MRSA cells by activated THP-1 cells. 71

Figure 4.6. (A) Change in fluorescence emission intensity of CT-DNA Hoechst dye complex in presence of MNase and ligands C1 and C2 (10 µM each) in separate sets. (B) Effect of varying concentrations of C1 and C2 on MNase inhibition. (C) Michaelis-Menten plot for MNase inhibition in presence of varying concentrations of C2. (D) Lineweaver-Burk plot to ascertain MNase inhibition by C2. 74

Figure 4.7. Dixon plot for MNase in the presence of varying concentrations of C1. The concentration of CT-DNA was varied from 1050 nM to 2450 nM in separate sets. 76

Figure 4.8. (A) Toluidine-blue DNA agar plate assay to ascertain inhibition of MNase present in the cell-free supernatant (CFS) of *S. aureus* MRSA 100 strain. (1) CFS and 2.0 µM C2. (2) CFS and 30 µM C2. (3) CFS and 100 µM C2. (4) 100 µM C2. (5) CFS of *S. aureus* MRSA 100. (B) Bactericidal activity of C2 against *S. aureus* MRSA 100 strain. 77

Figure 4.9. (A) Change in tryptophan fluorescence emission spectra of MNase in presence of an increasing concentration of C2. (B) Stern-Volmer plot for C2 based on the fluorescence emission spectra obtained in (A). (C) Scatchard plot for C2 based on fluorescence emission spectra obtained for MNase in presence of an increasing concentration of C2. (D) CD spectra of MNase measured in presence of C2. 78

Figure 4.10. (A) Relative fluorescence emission intensity of CT-DNA-picogreen complex in presence of various treatment regimens. (1) Control (CT-DNA alone). CT-DNA incubated with (2) MNase, (3) MNase and C2 (5.0 µM), (4) MRSA, (5) MNase and MRSA, (6) MNase, C2 (5.0 µM) and MRSA. (B) Relative level of MRSA entrapped in CT-DNA 81

in presence of various treatment regimens estimated by plating. (1) CT-DNA incubated with MRSA. (2) CT-DNA incubated with MNase and MRSA. (3) CT-DNA incubated with MNase, C2 (5.0 µM) and MRSA. (C) Fluorescence microscope-based imaging of MRSA entrapped in CT-DNA in presence of various treatment regimens. MRSA cells and CT-DNA were labelled with cFDA-SE and DAPI, respectively. Inset in panels iii, vi, and ix indicate the mean relative green/blue (G/B) emission pixel intensity expressed as a percentage. Scale bar for the images is 50 µm.

Figure 4.11. Flow cytometry-based assessment of the activation of THP-1 cells to macrophage-like cells upon treatment with PMA. (A) Untreated THP-1 cells (control). (B-D) THP-1 cells treated for 48 hours with 25 nM, 50 nM and 100 nM PMA, respectively. The cell population in the upper right quadrant indicate the proportion of activated THP-1 cells. Brightfield microscope imaging of (E) Untreated THP-1 cells and (F) THP-1 cells treated with 100 nM PMA for 48 hours. Scale bar for the images is 50 µm. 84

Figure 4.12. Flow cytometry-based quadrant plots for assessment of the uptake of MRSA cells by PMA-activated THP-1 cells in presence of various treatment regimens. (A) Activated THP-1 cells incubated with CT-DNA and TAMRA-labelled MRSA (10^8 CFU). (B) Activated THP-1 cells incubated with CT-DNA, MNase (5.0 units) and TAMRA-labelled MRSA (10^8 CFU). (C) Activated THP-1 cells incubated with CT-DNA, MNase (5.0 units), TAMRA-labelled MRSA (10^8 CFU) and C2 (5.0 µM). (D) Activated THP-1 cells incubated with CT-DNA, MNase (5.0 units), TAMRA-labelled MRSA (10^8 CFU) and C2 (15 µM). 85

Figure 4.13. Flow cytometry-based assessment of relative uptake of TAMRA-labelled MRSA cells by activated THP-1 cells in presence of various treatment regimens as indicated in the accompanying cartoon. RMFI denotes the relative median fluorescence intensity. 87

Figure 4.14. (A) Confocal microscope-based imaging to assess the uptake of TAMRA-labelled MRSA cells by activated THP-1 cells in presence of various treatment regiments. Activated THP-1 cells were incubated with (i) CT-DNA and TAMRA-labelled MRSA, (ii) CT-DNA, MNase and TAMRA-labelled MRSA, (iii) CT-DNA, MNase, TAMRA-labelled MRSA and C2 (15 µM). Panels (iv-vi) represent the magnified region of the images shown in white dashed boxes in panels (i-iii), respectively. The white arrow in panels (iv-vi) indicate TAMRA-labelled MRSA cells associated with CMAC-labelled THP-1 cells. Relative uptake of MRSA cells by activated THP-1 cells in presence of various treatment regimens ascertained by (B) normalized fluorescence intensity measurement (ratio of TAMRA-labelled MRSA and CMAC-labelled THP-1 cells) and (C) estimation of viable cells by plating method. 88

Figure 4.15. MTT assay to ascertain the cytotoxic effect of C2 against (A) HEK 293 cells and (B) THP-1 cells. Each data point represents mean ± standard deviation obtained from six independent experimental samples, each having three replicas. 89

Figure A4.1 Schematic representation of the reaction for synthesis of C2. 179

Figure A4.2 ^{1}H NMR of C2 in DMSO-d_6 at room temperature. 180

Figure A4.3 ^{13}C NMR of C4 in DMSO-d_6 at room temperature. 180

Figure A4.4 MALDI-MS spectra of C2 in dichloromethane in positive ionization mode. 181

Figure A4.5 Change in fluorescence emission of CT-DNA Hoechst dye complex in presence of MNase and varying concentrations of ligands C1 and C2. 181

Figure A4.6 Change in fluorescence emission intensity for CT-DNA Hoechst dye-C2 preformed complex samples digested with MNase. The concentration of C2 in the preformed complex was 0.5 µM and 1.0 µM. The concentration of CT-DNA used in the experiments were (A) 1.75 µM and (B) 3.5 µM. 182

Figure A4.7 ITC analysis to ascertain the binding isotherm of C2 and MNase. 183

Figure A4.8 (A) UV-visible absorbance spectra of C2 in presence of CT-DNA. (B) Binding isotherm of C2 in presence of an increasing concentration of CT-DNA. 183

Figure A4.9 CD spectra of MNase measured in presence of varying concentrations of C2. 184

Figure A4.10 CD spectra of human serum albumin (HSA) measured in presence of an increasing concentration of C2. 184

Figure A4.11 Change in fluorescence emission intensity of CT-DNA Hoechst dye complex in presence of MNase and dialyzed sample of MNase-C2 complex. 185

Figure A4.12 Docked structure of C2 with MNase. 186

Figure A4.13 Docked structure of C2 with DNase I. 187

Figure A4.14 Flow cytometry-based quadrant plot for activated THP-1 cells incubated with CT-DNA and TAMRA-labelled MRSA cells (10^8 CFU) and C2 (15 µM). 187

Figure A4.15 Confocal microscope-based imaging for ascertaining the uptake of TAMRA- labelled MRSA cells by activated THP-1 cells in presence of various treatment regimens. 188

CHAPTER 5

Figure 5.1. General structure of napthalimide-based synthetic ligands used in the current study. (A) C1, (B) C2, and (C) C3. 98

Figure 5.2. Schematic representation of the key steps in the picogreen-based fluorescence assay for estimating MNase activity. 99

Figure 5.3. (A) Change in fluorescence emission intensity of CT-DNA-picogreen dye complex in presence of MNase and the ligands (C1-C3). (B) Dose-dependent MNase inhibition rendered by C1, C2 and C3. 104

Figure 5.4. (A) Michaelis-Menten plot for MNase in presence of varying concentrations of C1. (B) Lineweaver-Burk plot to assess MNase inhibition by C1. (C) Effect of varying concentrations of C1on the magnitude of kinetic parameters of MNase. (D) Dixon plot for MNase in the presence of varying concentrations of C1. The concentration of CT-DNA was varied from 0.35 μM to 2.10 μM in separate sets. 105

Figure 5.5. (A) Toluidine-blue DNA agar plate assay to detect inhibition of MNase present in the cell-free supernatant (CFS) of *S. aureus* MRSA 100 strain. (1) CFS alone. (2) CFS and 3.0 μM C1. (3) CFS and 30 μM C1. (4) CFS and 100 μM C1. (5) 100 μM C1. (B) Evaluation of the bactericidal activity of C1. 107

Figure 5.6. (A) Effect of C1 on tryptophan fluorescence emission spectra of MNase. (B) Stern-Volmer plot based on the fluorescence emission spectra obtained in (A). (C) Scatchard plot based on fluorescence emission spectra obtained in (A). (D) CD spectra of MNase measured in presence of 5.0 μM C1. 108

Figure 5.7. MTT assay-based evaluation of the cytotoxic effect of C1 against (A) HEK 293 cells, (B) THP-1 and (C) MG-63 cells. The data points were acquired from six independent experimental samples and considered to determine mean ± standard deviation. 110

Figure A5.1 Change in fluorescence emission of CT-DNA-picogreen dye complex in presence of MNase and ligands C1-C3. The concentration of the ligands used in the experiment were (A) 0.25 μM, (B) 0.50 μM, (C) 1.0 μM and (D) 5.0 μM. 189

Figure A5.2 Dose-dependent reduction of MNase activity rendered by ligands C1-C3. 190

Figure A5.3 Change in fluorescence emission intensity of CT-DNA picogreen dye complex with varying concentration of C1 in presence of 191

MNase. The concentration of CT-DNA used in the experiments were (A) 0.5 µM and (B) 1.0 µM.

Figure A5.4 (A) UV-visible absorbance spectra of C1 in presence of CT-DNA. (B) Binding isotherm of C1 in presence of an increasing concentration of CT-DNA. 191

Figure A5.5 CD spectra of MNase measured in presence of an increasing concentration of C1. 192

Figure A5.6 CD spectra of human serum albumin (HSA) measured in presence of an increasing concentration of C1. 192

Figure A5.7 Change in fluorescence emission intensity of CT-DNA picogreen dye complex in presence of MNase and dialyzed sample of MNase-C1 complex. 193

Figure A5.8 Docked structure of C1 with MNase. 194

Figure A5.9 Docked structure of C1 with DNase I. 195

CHAPTER 6

Figure 6.1. Schematic representation of the protocol used for preparation of C1-loaded Pluronic F-127 micellar carrier (C1-PMC). 119

Figure 6.2. Schematic representation of the assay to estimate the release of C1 from C1-PMC incubated in simulated body fluid (SBF), HEPES buffer and citrate buffer. 121

Figure 6.3. Schematic representation of the assay to evaluate MRSA adhesion onto collagen. 122

Figure 6.4. (A) Cartoon illustrating entrapment of MRSA into CT-DNA in the presence of various treatment regimens. (B) Fluorescence microscope-based detection of MRSA entrapped in CT-DNA in presence of various treatment regimens. MRSA cells and CT-DNA were labelled with cFDA-SE and DAPI, respectively. Scale bar for the images is 50 µm. 126

Figure 6.5. Flow cytometry-based analysis of quadrant plots for assessment of the uptake of MRSA cells by PMA-activated THP-1 cells. Activated THP-1 cells were incubated with (A) CT-DNA and TAMRA-labelled MRSA. (B) CT-DNA, MNase and TAMRA-labelled MRSA. (C) CT-DNA, MNase, TAMRA-labelled MRSA and C1 (5.0 µM). (D) CT-DNA, MNase, TAMRA-labelled MRSA and C2 (10 µM). (E) CT-DNA, TAMRA-labelled MRSA cells and C1 (10 µM). 128

Figure 6.6. (A) Flow cytometry-based estimation of relative uptake of TAMRA-labelled MRSA cells by activated THP-1 cells in presence of various treatment regimens. (B) Relative median fluorescence intensity (RMFI) of TAMRA for samples analyzed in (A). (C) Confocal microscope analysis for uptake of TAMRA-labelled MRSA cells by activated THP-1 cells incubated with (i-ii) CT-DNA and TAMRA-labelled MRSA, (iii-iv) CT-DNA, MNase and TAMRA-labelled MRSA, (v-vi) CT-DNA, MNase, TAMRA-labelled MRSA and C1 (10 µM). Panels ii, iv and vi represent the magnified region of the images shown in white dashed boxes in panels i, iii and v, respectively. White arrow in panels ii, iv and vi indicate TAMRA-labelled MRSA cells associated with CMAC-labelled THP-1 cells. 129

Figure 6.7. Relative uptake of MRSA cells by activated THP-1 cells in presence of various treatment regimens estimated by (A) Normalized fluorescence intensity measurement (ratio of TAMRA-labelled MRSA and CMAC-labelled THP-1 cells) and (B) Enumeration of viable cells by plating method. 130

Figure 6.8. (A) FESEM image of C1-loaded PF-127 micellar carrier (C1-PMC). Inset indicates particle size distribution of C1-PMC determined by using ImageJ software. (B) FETEM image of C1-PMC. Scale bar for the images in (A) and (B) is 200 nm and 100 nm, respectively. (C) UV-visible spectra of C1, PMC and C1-PMC. (D) FTIR spectra of C1, PMC and C1-PMC. Arrows indicate the characteristic stretching frequency for the samples. Inset represents the amplified region of the spectra for C1-PMC shown in red dashed box. Arrow in inset indicates the characteristic stretching frequency for Amide-I in C1-PMC. (E) Cumulative release of C1 from C1-PMC incubated in simulated body fluid (SBF), HEPES buffer and citrate buffer. (F) Inhibition of MNase by C1 eluates (corresponding to 5.0, 10 and 20 µM C1) obtained from C1-PMC. 132

Figure 6.9. (A) Adhesion of *S. aureus* MRSA 100 cells onto collagen in presence of various treatment regimen. (B) Fluorescence microscope analysis to visualize adhesion of MRSA cells onto collagen in presence of various treatment regimen. (i) Control. (ii) PMC, (iii) C1 (20 µM) and (iv) C1-PMC (loaded with 100 µM C1). Scale bar for the images is 50 µm. 135

Figure 6.10. FESEM image of titanium wire (Ti wire) coated with different samples. (A) Bare Ti wire, (B) Ti wire coated with collagen, (C) Ti wire coated with collagen and C1 (20 µM), (D) Ti wire coated with collagen and PMC, (E) Ti wire coated with collagen and C1-PMC (loaded with 100 µM of C1). Scale bar for the images is 250 µm. 136

Figure 6.11. (A) Energy Dispersive X-ray (EDX) analysis of collagen and C1-PMC-coated titanium wire (C1-PMC-Ti wire). (B) FTIR spectra of C1-PMC, bare titanium wire (Ti wire) and collagen and C1-PMC-coated titanium wire (C1-PMC-Ti wire). (C) FESEM image analysis to visualize adhesion of MRSA cells onto Ti-wire coated with 137

various samples. (i) Control (Ti wire coated with collagen), (ii) Ti wire coated with collagen and PMC, (iii) Ti wire coated with collagen and C1 (20 µM) and (iv) Ti wire coated with collagen and C1-PMC (loaded with 100 µM of C1). Scale bar for the images is 2.0 µm.

Figure 6.12. MTT assay-based evaluation of the cytotoxic effect of C1 against (A) HEK 293 cells, (B) THP-1 and (C) MG-63 cells. Cytotoxic effect of C1 loaded PF-127 micellar carrier (C1-PMC) against (D) HEK 293 cells, (E) THP-1 and (F) MG-63 cells. Data points acquired from six independent experimental samples were considered to determine mean ± standard deviation. 138

Figure 6.13. MTT assay-based determination of the cytotoxic effect of eluate from Ti-wire coated with various treatment regiments against HEK 293 cells, MG-63 and THP-1 cells. Data points acquired from six independent experimental samples were considered to determine mean ± standard deviation. 138

Figure A6.1 (A) Fluorescence emission of CT-DNA-picogreen complex in presence of different treatment regimens. (S1) CT-DNA. CT-DNA incubated with (S2) MNase, (S3) MNase and C1 (5.0 µM), (S4) MRSA cells, (S5) MNase and MRSA cells, (S6) MNase and C1 (5.0 µM) and MRSA cells. (B) Relative proportion of MRSA cells trapped in CT-DNA in presence of various treatment regimens ascertained by plating. (C) Fluorescence microscope-based detection of MRSA entrapped in CT-DNA in presence of various treatment regimens. MRSA cells and CT-DNA were labelled with cFDA-SE and DAPI, respectively. Scale bar for the images is 50 µm. 196

Figure A6.2 Estimation of the entrapment of MRSA cells in CT-DNA (expressed as percentage) by measuring mean relative green/blue (G/B) emission pixel intensity in fluorescence microscope-based imaging studies. 197

Figure A6.3 Confocal microscope-based imaging to ascertain the uptake of TAMRA-labelled MRSA cells by activated THP-1 cells in presence of various treatment regimens. 198

Figure A6.4 (A) FESEM image of PF-127 nanocarrier (PMC). Inset indicates particle size distribution of PMC determined by using ImageJ software. (B) FETEM image of PMC. The scale bar for the images in (A) and (B) is 200 nm and 100 nm, respectively. 199

Figure A6.5 DLS-based size distribution plot for (A) PMC and (B) C1-PMC. 199

Figure A6.6 (A) Absorbance spectra of varying concentration of C1. (B) Calibration plot for C1 generated from the absorbance spectra shown in (A). 200

Figure A6.7	Change in fluorescence emission intensity of CT-DNA-picogreen dye complex in presence of (A) MNase and varying concentrations of C1 eluates obtained from C1-PMC and (B) MNase and PMC.	200
Figure A6.8	Bactericidal activity of C1-PMC (loaded with 100 μM C1) against *S. aureus* MRSA 100 strain.	201
Figure A6.9	Energy dispersive X-ray (EDX) analysis of (A) Bare titanium wire, (B) Collagen-coated titanium wire, (C) Collagen and C1-coated titanium wire and (D) Collagen and PMC- coated titanium wire.	201
Scheme 1	Schematic representation of the significant findings of the present investigation.	145

Chapter 1

Introduction and Literature Review

Introduction

The prevalence of antibiotic-resistant pathogenic bacteria is an impending global healthcare crisis, which demands a radical approach for discovery of potent therapeutic agents that can act upon vital cellular targets and are counterproductive to resistance development. Amongst the antibiotic-resistance pathogenic bacteria, methicillin-resistant *Staphylococcus aureus* (MRSA) is of serious concern as it is associated on a large-scale with hospital as well as community-acquired infections. Based on the risk factor, the World Health Organization (WHO) has classified MRSA under serious threat under priority level 2: High. MRSA is implicated in a plethora of serious ailments ranging from wound infection, toxic shock syndrome, endocarditis, osteomyelitis, bacteremia and prosthetic device and medical implant-associated infection. Alleviation of MRSA infection is particularly challenging as the number of therapeutic antibiotics effective against the pathogen are limited. Hence, there is an urgent need for effective therapeutic approaches to mitigate MRSA infections.

Infections by pathogenic bacteria are normally curbed by sentinels of the innate immune system, such as the neutrophil extracellular trap (NET), which eventually facilitates pathogen elimination by macrophage-mediated phagocytosis. *S. aureus* secretes a nuclease enzyme, also known as micrococcal nuclease (MNase), which degrades NET by cleaving the DNA and thereby promotes pathogen escape. MNase is also implicated in facilitating MRSA biofilm formation in implants. The staphylococcal nuclease enzyme is thus considered as a virulence factor based on its ability to promote immune evasion and advance pathogenesis. Given the high resistance of MRSA strains to therapeutic antibiotics and the key role of MNase in establishing staphylococcal infection, development of a potent MNase inhibitor can bear significant therapeutic implications to combat the pathogen.

Based on the aforementioned premise, the present investigation is an endeavour towards the selection of rationally designed synthetic small molecules and exploring their prospect as staphylococcal nuclease inhibitors. The investigation is focused towards a critical evaluation of the ligands as MNase inhibitors based on studies that reflect structure-function relationship, unravel their effect on enzyme kinetics, indicate their mode of inhibition and evaluate their therapeutic potential. The study also aims to develop biocompatible nanocarriers that render favourable delivery of the synthetic MNase inhibitor and can be leveraged for potential anti-MRSA therapy.

Literature Review on the Research Topic

1.1. Antibiotic-Resistant Pathogenic Bacteria

The current investigation is an endeavor to address the global healthcare concern regarding the development of effective antibacterials to curb the menace of antibiotic-resistant pathogenic bacteria. In order to acquire a fundamental understanding on the subject matter, the following section presents an overview on antibiotic-resistant pathogenic bacteria.

In recent years there has been an alarming rise in the emergence of pathogenic bacteria in the clinic that display an innate resistance toward several therapeutic antibiotics. Given the serious healthcare burden linked with antibiotic-resistance, several review articles have highlighted the nuances with regard to antibiotic-resistant pathogenic bacteria (Varela *et al*., 2021; Tacconelli *et al.*, 2018; Huemer *et al.*, 2020; Peterson and Kaur, 2018; Petchiappan and Chatterjee, 2017; Fair and Tor, 2014). Considering the overall mortality, availability of effective therapy, healthcare burden, and the increase in drug resistance, World Health Organization (WHO) has proposed a priority list that categories all the drug-resistant pathogenic bacteria into three categories as (a) Critical (b) High and (c) Medium (Tacconelli *et al*., 2018; WHO Report 2014). A schematic representation of the various pathogens belonging to these categories is indicated in Figure 1.1. The Centers for Disease Control and Prevention (CDC) in the USA has placed antibiotic-resistant microbes under four categories based on their threat levels (CDC Report, 2019). A representation of the various categories and the pathogens belonging to each classification is illustrated in Table 1.1. The implications of antibiotic-resistant microbe is articulated in the CDC report of 2019. To this end, it was stated that antibiotic-resistant infections recorded in the United States are in excess of 2.8 million each year, and more than 35,000 people die as a consequence of these infections. There are several literature reports that discuss the mechanisms of antibiotic-resistance in pathogenic bacteria. Based on these studies, following modes of resistance can be proposed: (a) presence of a permeability barrier, (b) presence of an efflux pump, (c) modification of drug targets, (d) presence of a metabolic bypass, (e) presence of antibiotic-altering or degrading enzymes (Nikaido, 2009; Wright, 2011; Chambers and DeLeo, 2009). Further, an indiscriminate use of antibiotics in the clinics can also trigger the development of resistance traits on a large scale (Fair and Tor 2014, Toprak *et al*., 2012).

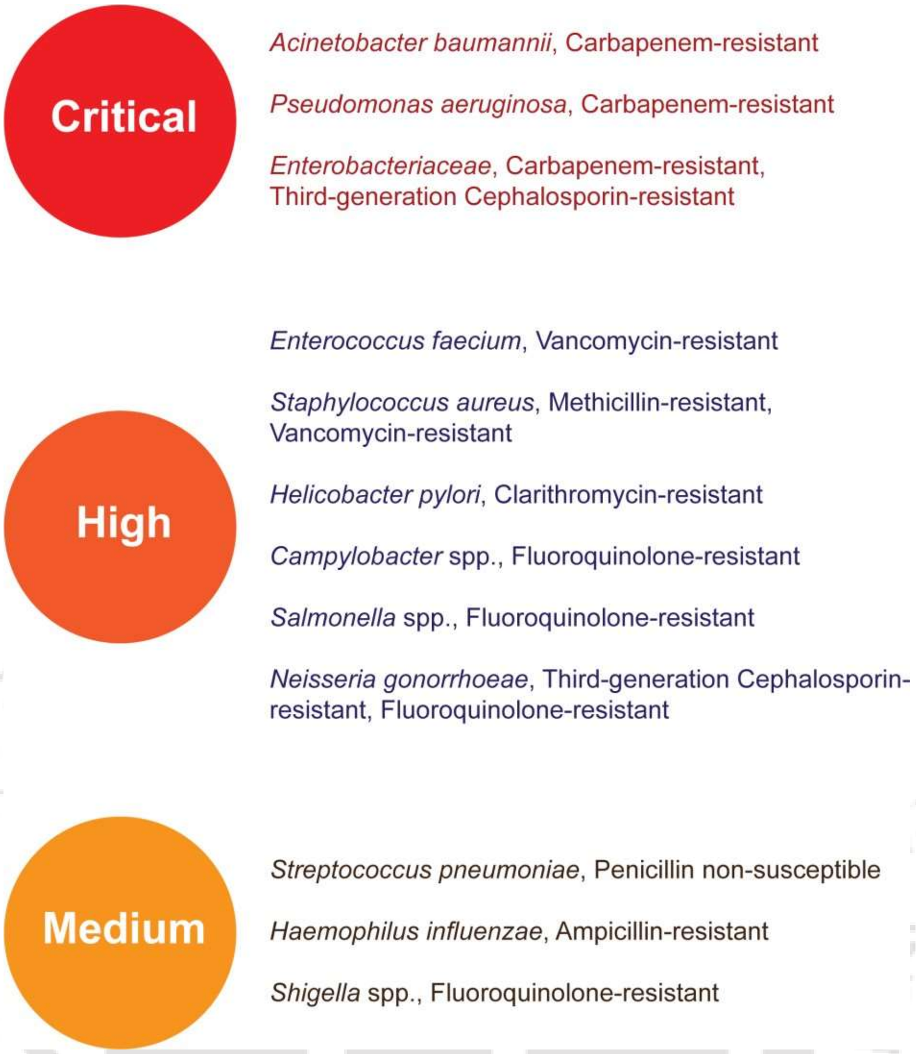

Critical:

Acinetobacter baumannii, Carbapenem-resistant

Pseudomonas aeruginosa, Carbapenem-resistant

Enterobacteriaceae, Carbapenem-resistant, Third-generation Cephalosporin-resistant

High:

Enterococcus faecium, Vancomycin-resistant

Staphylococcus aureus, Methicillin-resistant, Vancomycin-resistant

Helicobacter pylori, Clarithromycin-resistant

Campylobacter spp., Fluoroquinolone-resistant

Salmonella spp., Fluoroquinolone-resistant

Neisseria gonorrhoeae, Third-generation Cephalosporin-resistant, Fluoroquinolone-resistant

Medium:

Streptococcus pneumoniae, Penicillin non-susceptible

Haemophilus influenzae, Ampicillin-resistant

Shigella spp., Fluoroquinolone-resistant

Figure 1.1. Classification of antibiotic-resistant pathogenic bacteria belonging to various priority list proposed by WHO (WHO Report, 2014).

1.2. Methicillin-Resistant Staphylococcus aureus (MRSA)

Amongst the clinical strains of staphylococci, the prevalence of MRSA is of deep concern. In the present investigation, synthetic ligands were designed and evaluated as potential inhibitors of the staphylococcal nuclease enzyme and their application potential for anti-MRSA therapy was assessed. In the following section, a brief overview on the pathogen is presented.

MRSA is a human pathogen, it is highly dominant in healthcare as well as in the community domain. The pathogen is largely implicated in a number of ailments such as bacteremia, endocarditis, skin and soft tissue infections, bone and joint infections and other hospital-associated infections (Lee *et al*., 2018; Turner *et al*., 2019; Tong *et al*., 2015; Craft *et al*., 2019). Owing to less treatability and a high mortality rate, MRSA is

Table 1.1. Classification of antibiotic-resistant pathogenic microbes on the basis of the threat levels as proposed by CDC (CDC Report, 2019).

Threat Level	**Examples**
Urgent	Carbapenem-resistant *Acinetobacter* *Candida auris* *Clostridioides difficile* Carbapenem-resistant Enterobacteriaceae (CRE) Drug-resistant *Neisseria gonorrhoeae*
Serious	Drug-resistant *Campylobacter* Drug-resistant *Candida* Extended-spectrum beta-lactamase (ESBL)-producing Enterobacteriaceae Vancomycin-resistant *Enterococci* (VRE) Multidrug-resistant *Pseudomonas aeruginosa* Drug-resistant nontyphoidal *Salmonella* Drug-resistant *Salmonella* serotype Typhi Drug-resistant *Shigella* Methicillin-resistant *Staphylococcus aureus* (MRSA) Drug-resistant *Streptococcus pneumoniae* Drug-resistant Tuberculosis (TB)
Concerning	Erythromycin-resistant group A *Streptococcus* Clindamycin-resistant group B *Streptococcus*
Watch List	Azole-resistant *Aspergillus fumigatus* Drug-resistant *Mycoplasma genitalium* Drug-resistant *Bordetella pertussis*

associated with an increased healthcare burden (Tacconelli *et al*., 2018). Moreover, MRSA infections lead to protracted stay in hospitals, escalate hospital costs and necessitate excess use of antibiotics (Danesh *et al*., 2019; Boussion *et al*., 2021; Adams and Dancer, 2020). From its advent in the clinics in 1960, MRSA has evolved as a robust pathogen and its growing spread in the community has drawn lots of attention. The healthcare burden of MRSA is a global phenomenon ranging from a relatively scanty occurrence in Scandinavia to its very high prevalence in North America and Asia (Lee *et al*., 2018). In the United States, 323,700 cases of MRSA infection were recorded in hospitalized patients in 2017, of which around 10,600 deaths were recorded

(CDC Report, 2019). The overwhelming resistance of MRSA to several therapeutic β- lactam antibiotics is a major bottleneck for mitigation of MRSA infection in the clinic (Lee *et al.*, 2018; Craft *et al.*, 2019). Besides, MRSA expresses a gamut of virulence factors such as adhesins, toxins, tissue-destroying enzymes and other factors that assist in host immune-evasion and establish invasive infections in the host (Lee *et al.*, 2018; Turner *et al.*, 2019; Thammavongsa *et al.*, 2013).

1.3. MRSA Infections

S. aureus is an opportunistic pathogen capable of causing a wide spectrum of acute and chronic infections. Two broad categories of MRSA infections are prevalent, namely community-acquired infections (CA) and hospital-acquired infections (HA) (Balasubramanian *et al.*, 2017; Turner *et al.*, 2019). The ecological niche of *S. aureus* in humans is the anterior nares. Approximately 20%–25% of healthy human population harbor persistently colonized *S. aureus* while 75%–80% are intermittently or never colonized. Literature studies have shown that there is a strong association between *S. aureus* nasal carriage and increased risk of nosocomial infection (Archer *et al.*, 2011; Gordon and Lowy, 2008). MRSA is a common cause for implant-related infection, wherein the pathogen is known to readily form biofilm. The biofilm matrix can shield the encased cells from the host immune system and can also act as a strong permeability barrier against therapeutic agents and antibiotics (Craft *et al.*, 2019; Arciola *et al.*, 2018; Stoodley, *et al.*, 2011; Oliveira *et al.*, 2018; Hall and Mah, 2017). Hence, biofilm infections are particularly recalcitrant to treatment as the antibacterial agent needs to breach the matrix and inhibit the growth of the underlying cells (Tuon *et al.*, 2023; Oliveira *et al.*, 2018; Arciola *et al.*, 2018). During invasion of implant by MRSA biofilm, host extracellular matrix proteins such as collagen can be deposited on the surface of the implant and render adhesion of MRSA cells, which can subsequently elicit robust biofilm formation on the implant (Lee *et al.*, 2018; Foster *et al.*, 2014).

S. aureus is responsible for nosocomial infection and bloodstream infections (Thomar *et al.*, 2016, Mo *et al.*, 2019). The pathogen is also acknowledged as a major causative agent for skin and soft tissue infections such as abscesses (boils), furuncles, and cellulitis and other infections include osteomyelitis, arthritis, infective endocarditis, empyemas, urinary tract infections, pneumonia, and meningitis (Tuon *et al.*, 2023; Balasubramanian *et al.*, 2017; Rizzetto *et al.*, 2022; Krauss *et al.*, 2019; Lu *et al.*, 2022;

Table 1.2. An overview of infections caused by *Staphylococcus aureus*.

Serial No.	**Category of Infection**	**Examples**
1.	Acute Infection	Skin infections such as abscesses, folliculitis, carbuncles, respiratory infections such as sinusitis, food poisoning
2.	Chronic Infection	Pneumonia, meningitis, osteomyelitis, endocarditis, toxic shock syndrome, bacteremia, sepsis
3.	Device – related Infection	Contact lens, central venous catheter, endotracheal tube, intrauterine device, pacemaker, prosthetic joint

Masters *et al.*, 2022). Surgical site infection, implant and medical device-related infections caused by MRSA are considered as a major concern in the healthcare system, as it increases the mortality rate and healthcare burden (Arciola *et al.*, 2018; Oliveira *et al.*, 2018; Pongbangli *et al.*, 2021; Wu *et al.*, 2023; Tong *et al.*, 2015, Lee *et al.*, 2018). An overview of infections caused by *S. aureus* is presented in Table 1.2.

1.4. Mechanism of Antibiotic Resistance in MRSA

The presence of mobile genetic elements (MGEs) carrying antibiotic-resistance genes in MRSA is well documented. MRSA harbors a 20-65 kb *SCCmec* element, which contains the *mecA* gene complex coding for the methicillin-resistance trait (Turner *et al.*, 2019). In MRSA, the MGEs encode for resistance against several therapeutic antibiotics including aminoglycoside, penicillin, chloramphenicol, trimethoprim, macrolide, mupirocin, methicillin, tetracycline and others (Turner *et al.*, 2019). MRSA expresses an accessory penicillin-binding protein (PBP), known as PBP2a, having very low affinity towards β-lactams. Owing to this protein, the pathogen displays high resistance against several β-lactams and antibiotics such as penicillin, cephalosporin and carbapenem are futile against MRSA (Craft *et al.*, 2019). Since β-lactam resistance is prevalent in MRSA, vancomycin has emerged as a critical therapeutic antibiotic for alleviation of MRSA infections. However, literature reports have described the emergence of vancomycin-resistant staphylococci (Weigel *et al.*, 2003; Rossi *et al.*, 2014). It has been reported that *S. aureus* can develop resistance against aminoglycosides by decreasing its membrane permeability (Guo *et al*., 2020). Staphylococci is also known to harbor efflux pump proteins, which are implicated in development of resistance against several therapeutic agents (Li and Nikaido, 2009; Costa *et al*., 2015; Jang, 2016). A significant number of efflux pumps present in *S. aureus* belong to the major facilitator superfamily (MFS), wherein the activity of prominent antibiotics such as ciprofloxacin, norfloxacin, linezolid, erythromycin, cetrimide and chlorhexidine are affected (Kaatz *et al*., 2005; Truong-Bolduc and Hooper, 2010; Floyd *et al*., 2010; Brown and Skurray, 2001).

1.5. Virulence Factors in S. aureus

Virulence factors present in pathogenic bacteria are attractive therapeutic targets as they play a significant role in pathogenesis, tissue injury and in acquisition of resistance against therapeutic interventions (Ford *et al*., 2021; Dickey *et al*., 2017; El-Aleam *et al*., 2021). MRSA is known to produce a host of virulence factors that assist the pathogen in colonization, dissemination, and host cell infection. These virulence factors include capsular polysaccharides, staphylococcal protein A, fibronectin binding protein, collagen binding protein, extracellular toxins and enzymes, superantigens and others (Algammal *et al*., 2020; Wojcik-Bojek *et al*., 2022; Soe *et al*., 2021; Cheung *et al*., 2021). Capsular polysaccharides can encase the MRSA cell surface and protect it from the host immune system (Whitfield *et al*., 2020; Visansirikul *et al*., 2020; Algammal *et al*., 2020). Protein A is known to sequester IgG molecules and prevents phagocytosis of bacterial cells (Algammal *et al*., 2020; Kong *et al*., 2016). Fibronectin- and collagen-binding proteins are critical for cell adhesion and in initial stages of biofilm formation (Speziale *et al*., 2019; Josse *et al*., 2017; Speziale and Pietrocola, 2020). *S. aureus* can produce a plethora of toxins such as hemolysins, enterotoxins, Panton-Valentine leukocidin, toxic shock syndrome toxins, exfoliative toxins that can damage epithelial cells, endothelial cells, erythrocytes, monocytes, cause food poisoning, skin and soft tissue infection, pneumonia, musculoskeletal diseases and bacteremia (Yoshikawa *et al*., 2019; Zhang *et al*., 2017; Bennett and Thomsen, 2020; Ahmad-Mansour *et al*., 2021; Tam and Torres, 2018; Oliveira *et al*., 2018; Otto, 2014; Friesen *et al*., 2020). In addition, *S. aureus* can produce a number of extracellular enzymes such as coagulase, staphylokinase and nuclease that are implicated in clotting of plasma or blood, inflammasome activation, circumventing phagocytosis by degrading neutrophil

Table 1.3. Overview of representative virulence factors of *S. aureus* and their implications in the host.

Virulence Factor	Implications in Host
Staphylococcal protein A	Binds Fc region of IgG and inhibits opsonization and phagocytosis
Fibronectin-binding protein	Facilitates enable adhesion to host tissues and biomaterials
Capsular polysaccharide	Hinders phagocytosis
Hemolysins	Lysis of red blood cells, platelets, leukocytes
Panton-Valentine leukocidin (PVL)	Lysis of neutrophils, monocytes, macrophages
Coagulase	Clot formation
Staphylokinase	Degradation of extracellular matrix
Nucleases	Destruction of NETs

extracellular traps (NETs) of the host immune system (Cheung *et al.*, 2021; Algammal *et al.*, 2020; Liesenborghs *et al.*, 2020; Wang *et al.*, 2022; Speziale and Pietrocola, 2021; Herzog *et al.*, 2019; Papayannopoulos, 2017). An overview of the representative virulence factors present in *S. aureus* is depicted in Table 1.3.

1.6. Staphylococcal Nuclease

The present investigation essentially focusses on developing synthetic ligands targeting the staphylococcal nuclease (Nuc) also referred to as micrococcal nuclease (MNase), which is a key virulence factor present in MRSA. Hence, a brief outline of the staphylococcal nuclease enzyme is presented in the following section.

It is well known that *S. aureus* secretes a thermostable nuclease enzyme. Manifestation of nuclease activity is highly conserved amongst clinical isolates of *S. aureus* and is thus considered as a marker for detection of the pathogen (Gonzalez and Hernandez, 2022; Sharma *et al.*, 2019). Nuc is a secreted enzyme that consists of a 63 residue long secretory signal sequence. The secreted form of Nuc consists of 168 residues, which is further processed by most *S. aureus* strains to a shorter form having

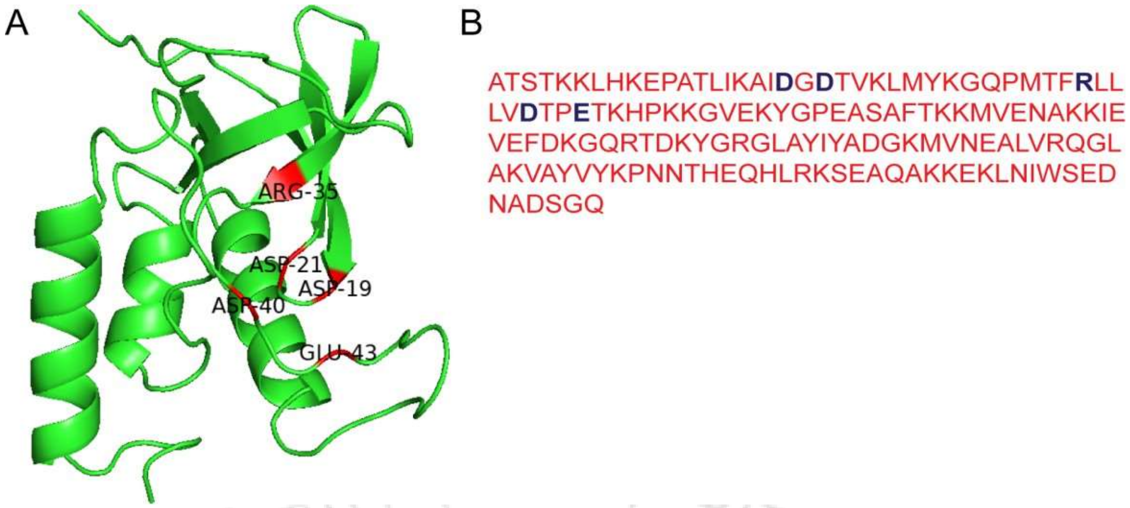

Figure 1.2. (A) Structure of staphylococcal nuclease enzyme available from protein data bank (PDB ID:1EY0) and visualized using PYMOL. The active site residues of the enzyme is indicated. (B) Amino acid sequence of staphylococcal nuclease enzyme. The amino acids present in the active site of the enzyme are indicated in dark blue letters.

149 residues (Heins *et al*., 1967; Taniuchi *et al*., 1967; Davis *et al*., 1977). MNase is a Ca^{2+}-dependent enzyme with a single polypeptide chain of 149 residues and is known to catalyze the hydrolysis of DNA and RNA to yield a free 5'-hydroxyl group and a 3'-phosphate monoester (Cotton *et al*., 1979). The active-site residues of MNase have been identified as Asp-19, Asp-21, Arg-35, Asp-40, and Glu-43 (Cotton *et al*., 1979; Chaiken and Anfinsen, 1971; Sanchez *et al*., 1973). A schematic representation of the structure of staphylococcal nuclease enzyme (PDB ID-1EY0) and the active site residues of the enzyme is indicated in Figure 1.2.

NETs are integral to the host innate immune system machinery, which render physical entrapment and elimination of an invading pathogen (Brinkmann *et al*., 2004; Papayannopoulos, 2018). There are literature reports that support the notion that neutrophils can trigger NET formation and engulf *S. aureus* cells by phagocytosis (Gunther *et al*., 2009; Bhattacharya *et al*., 2018). However, by virtue of the nuclease enzyme or MNase, *S. aureus* destroys the DNA scaffold of NETs and thereby foils pathogen entrapment and subsequent killing by NETs and neutrophils (Guerra *et al*., 2017; de Vor *et al*., 2020; Berends *et al*., 2010; Thammavongsa *et al*., 2013; Herzog *et al*., 2019; Bhattacharya *et al*., 2020). A schematic figure illustrating the essential role of MNase in degradation of the DNA scaffold of NETs is shown in Figure 1.3. In addition, studies have also shown that MNase plays a germane role in staphylococcal infections, regulation of biofilm formation, enhancing biofilm growth on implants and

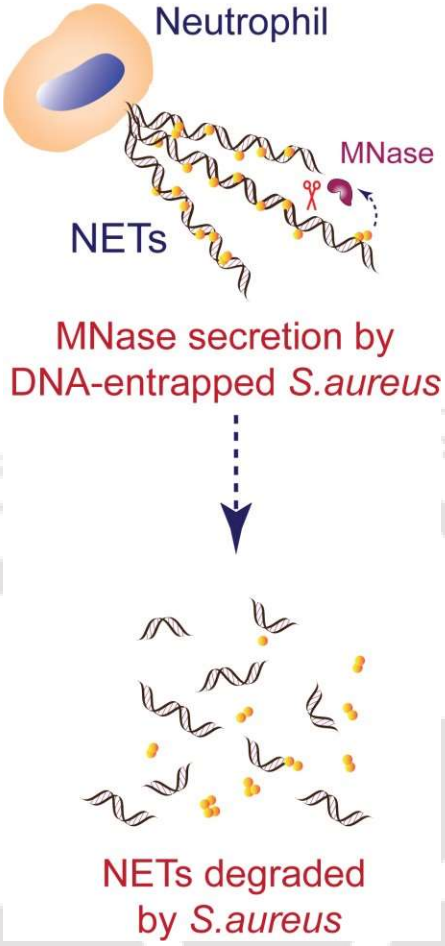

Figure 1.3. Cartoon illustrating the role of staphylococcal nuclease (MNase) in degradation of the DNA scaffold of NETs resulting in dispersion of the pathogen from the DNA trap.

generating nucleotides from DNA, which may elicit apoptosis and eliminate macrophages (Thammavongsa *et al*., 2013; Herzog *et al*., 2019; Kiedrowski *et al*., 2011; Moormeier *et al*., 2014; Forson *et al*., 2022). Based on its relevant role in immune evasion and in establishing infection, MNase can thus be considered as a key virulence factor and a viable therapeutic target.

1.7. Nuclease Inhibitors: Potential Therapeutics for Mitigation of MRSA Infection

Alleviation of MRSA infection in the clinics by antibiotic-mediated therapy is challenging, since the pathogen is known to be resistant to several therapeutic antibiotics. Hence, deployment of a complementary anti-virulence therapeutic intervention by targeting the nuclease enzyme is considered as an attractive option to curb the virulence of the pathogen and render its elimination by the host innate immune

Table 1.4. Inhibitory concentrations of known MNase and DNase inhibitors.

Compound / Source	**Target Enzyme**	**Inhibitory Concentration**	**Reference**
Thymidine Oligonucleotide Analog	MNase	0.03 mM	Rammler *et al.*, 1972
Pyridine-based Synthetic Amphiphiles	MNase	500 nM	Sahareen *et al.*, 2018
Clindamycin	MNase	0.03 µg/ml	Schilcher *et al.*, 2014
Immunoglobulin	MNase	2.5 -25 mg/ml	Schilcher *et al.*, 2014
Phage Peptide Library	DNase I	0.8 – 8.0 µM	Choi *et al.*, 2005
(3-Methyl-1,4-dioxothiazolidin-2-ylidene)-N-(2-phenylethyl)ethanamide	DNase I	115.96 µM	Kolarevic *et al.*, 2019
Ascorbic Acid	DNase I	330.74 µM	Ilic *et al.*, 2018
4-(4-Chlorophenyl)-2-(4-hydroxyphenylamino)thiazole-5-carboxamide	DNase I	79.79 µM	Smelcerovic *et al.*, 2020
2-substituted-1, 3-thiazolo[3,2-a]benzimidazolones	DNase I	79.46 µM	Kolarevic *et al.*, 2018

system. Several studies have reported the design and application of synthetic inhibitors for the nuclease enzyme DNase I (Smelcerovic *et al.*, 2020; Kolarevic *et al.*, 2018; Kolarevic *et al.*, 2014; Kolarevic *et al.*, 2019; Gajic *et al.*, 2022). In the context of the design rational of nuclease inhibitors, lipophilicity and the presence of H-donor/acceptor groups seem to be critical (Kolarevic *et al.*, 2014). In comparison to several literature reports on synthetic inhibitors of DNase I, studies reporting the characterization of staphylococcal nuclease inhibitors is limited (Schlicher *et al.*, 2014; Sahareen *et al.*, 2018). Hence, there is a distinct prospect to design and critically evaluate synthetic nuclease inhibitors as potential therapeutics to alleviate MRSA infections. Based on literature reports, the inhibitory concentrations of representative MNase and DNase I inhibitors is indicated in Table 1.4.

MOTIVATION AND OBJECTIVES OF THE PRESENT INVESTIGATION

MOTIVATION AND OBJECTIVES OF THE PRESENT INVESTIGATION

The origin of the present research investigation and the principal motivating factors emerge from the following considerations:

1. The high incidence of serious MRSA infections in the clinics in conjunction with the limited number of antibiotics that are effective against MRSA underpins the need for a radical therapeutic strategy in order to curb the pathogen. In this regard, targeting a key virulence factor of the pathogen can be considered as a viable option.
2. Given the germane role of nuclease in staphylococcal pathogenesis and virulence, it is envisaged that development of rationally designed synthetic ligands as inhibitors of staphylococcal nuclease also referred to as MNase is likely to yield therapeutic dividends and minimize the chances of resistance development.
3. The ability to secrete a nuclease enzyme empowers MRSA to degrade NETs and evade the host immune response. Hence, deployment of small synthetic molecules as MNase inhibitor is an exciting prospect in the realm of anti-MRSA therapy since they are likely to reinstate entrapment of the pathogen in NETs and eventually facilitate pathogen elimination by macrophage-mediated phagocytosis.
4. In order to explore synthetic nuclease inhibitors as emerging chemotherapeutics against MRSA, it is pertinent to select rationally designed ligands, evaluate their potency based on a structure-function study and acquire a nuanced understanding of the mode of inhibition rendered by the ligands. The outcome of the study is likely to provide a foundation and a guiding design principle for the development of potentially therapeutic synthetic molecules for combating MRSA infections.
5. In order to leverage the potential of synthetic nuclease inhibitors for anti-MRSA therapy, it is critical that a suitable delivery system is developed that supports sustained release of the payload and also curbs the cytotoxic effect of the synthetic inhibitors. In this context, development of biocompatible nanocarriers

can bear significant implications in leveraging staphylococcal nuclease inhibitor-based therapeutics in order to counter MRSA infections.

6. It is critical that the potential of a synthetic staphylococcal nuclease inhibitor is validated through models, which can mimic clinical problems such as NET degradation by MNase and orthopaedic implant-associated MRSA infection and also ascertain the toxic potential of the candidate molecules.

Objectives:

Based on the prospect of synthetic staphylococcal nuclease inhibitors in anti-MRSA therapy, the essential objectives of the Ph.D. thesis are as follows:

1. Evaluation of anthraquinone-based ligands as MNase inhibitor based on enzyme kinetics and binding studies.
2. Development of an anthraquinone ligand-loaded therapeutic nanocomposite for potential anti-MRSA therapy.
3. Assessment of benzimidazole-based ligands as MNase inhibitor and their potential in facilitating MRSA uptake by macrophage-like cells.
4. Appraisal of napthalimide-based ligands as MNase inhibitor based on enzyme kinetics and binding studies.
5. Development of a napthalimide ligand-loaded therapeutic nanocomposite for anti-MRSA therapy and mitigation of MRSA adhesion onto an orthopaedic implant.

Chapter 2

Assessment of Anthraquinone-based Ligands as Staphylococcal Nuclease Inhibitor

This chapter illustrates a comparative appraisal of anthraquinone-based synthetic ligands (C1-C4) as an inhibitor of staphylococcal nuclease also referred to as micrococcal nuclease (MNase). The mechanism of inhibition rendered by the most potent ligand C1 on MNase is also discussed.

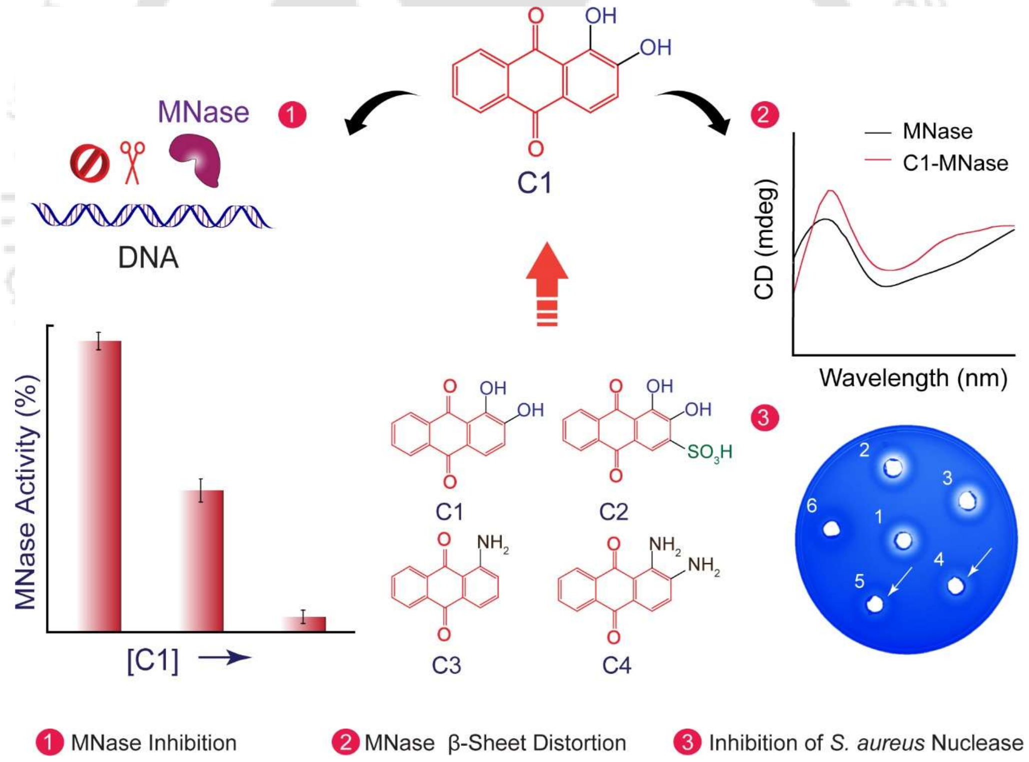

ABSTRACT

This chapter presents the potential of anthraquinone-based synthetic ligands (C1-C4) as MNase inhibitor. A fluorescence-based nuclease assay was performed to assess the potential of the ligands as MNase inhibitor. The assay indicated that amongst the tested ligands, C6 failed to render any inhibition of the activity of MNase enzyme. Based on end-point fluorescence, it was noted that ligand C1 could render the highest degree of MNase inhibition followed by C2 and C4. Although a dose-dependent increase in MNase inhibition was clearly evident for the ligands C1-C5, the magnitude of MNase inhibition rendered by C1, C2 and C4 was distinctly higher as compared to the inhibition caused by equivalent levels of C3 and C5. In solution-based studies, ITC could validate the favorable binding of C1 with MNase ($K_a = 9.5 \times 10^4$ M^{-1}), while fluorescence spectroscopy with MNase and varying concentration of C1 indicated that the Stern-Volmer constant and binding constant for C1 was 2.3 x 10^{13} $M^{-1}s^{-1}$ and 320 nM^{-1}, respectively. In CD spectroscopy, a notable change in the peak of MNase at 209 nm and 221 nm was observed, indicating a distortion in the structural conformation of β-sheet present in MNase, which is also known to harbor the enzyme's active site. Molecular docking studies suggested that ligand C1 was involved in hydrophobic interaction with the active site residue Asp 19 and H-bond formation with Asp 21 and Arg 35 of MNase. Estimation of the kinetic parameters from a Lineweaver-Burk plot (L-B plot) revealed that C1 rendered non-competitive inhibition of MNase as K_m for MNase was constant, while V_{max} of MNase-catalyzed reaction was decreased in presence of an increasing concentration of C1. There was a systematic decrease in the turnover number (K_{cat}) as well as the catalytic efficiency (K_{cat}/K_m) of MNase in presence of an increasing concentration of C1. The IC_{50} value of C1 for MNase was 323 nM. Interestingly, C1 could also render a dose-dependent inhibition of nuclease secreted by a clinical isolate of MRSA. Solution-based inhibition of MNase and MRSA-secreted nuclease rendered by C1 was also validated by agarose gel electrophoresis, which indicated inhibition of the cleavage of pUC18 plasmid DNA by MNase in presence of C1. An MTT assay suggested that C1 was non-toxic to cultured HEK 293 cells till a concentration of 12.5 µM, which was many folds higher than the concentration required to inhibit MNase.

2.1. Introduction

S. aureus is considered as a serious human pathogen, which is implicated in a range of clinical infections (Alder *et al.*, 2020; Tong *et al.*, 2015; Lee *et al.,* 2018; Turner *et al.*, 2019; Thomer *et al*, 2016; Kwiecinski and Horswill, 2020). The pathogen has an inherent ability to subvert the host-mediated immune response and poses a significant clinical challenge as it is resistant to several therapeutic antibiotics (Tong *et al.*, 2015; Lee *et al.,* 2018; Turner *et al.*, 2019; Tacconelli *et al.*, 2018). The rise of methicillin-resistant *Staphylococcus aureus* (MRSA), has resulted in a tremendous increase in the overall burden of infection, in both healthcare as well as the community domain. (Turner *et al.*, 2019) A large proportion of staphylococcal infections are caused by planktonic cells of *S. aureus*, which demonstrate the ability to secrete toxins and exo- enzymes (Tong *et al.*, 2015; Lee *et a.l,* 2018). However, *S. aureus* is versatile and can also adopt to environmental signals and display a biofilm mode of growth, which enables the pathogen to initiate invasion and persistence in host tissues (Otto *et al.*, 2008; Archer *et al.*, 2011). Biofilm cells are characterized by a protective matrix, which can assume the role of a penetration barrier for antibiotics and can also bear significance in evasion of the host immune response (Hall and Mah, 2017; De la Fuente-Nunez *et al.*, 2013; Scherr *et al.*, 2014). Besides, the pathogen is also known to invade and form biofilm on the surface of medical devices and implants (Oliveira *et* al, 2018; Arciola *et* al, 2012; Arciola *et* al., 2018, Craft *et al.*, 2019).

S. aureus is known to secrete a thermostable nuclease (Nuc) also referred to as micrococcal nuclease (MNase). Considering the large-scale presence of MNase in clinical isolates of *S. aureus*, the enzyme can be considered as a marker for detection and identification of staphylococcal infections (Gonzalez and Hernandez, 2022; Sharma *et al.*, 2019). MNase is a Ca^{2+}-dependent enzyme that can catalyze the hydrolysis of DNA as well as RNA, while its active-site residues have been identified as Asp-19, Asp-21, Arg-35, Asp-40, and Glu-43 (Cotton *et al.*, 1979; Chaiken and Anfinsen, 1971; Sanchez *et al.*, 1973). Literature reports reveal that staphylococcal nuclease bears significant implications in modulation of biofilm and persistence of biomaterial-associated biofilm infection in a murine model (Yu *et al.*, 2021; Forson *et al.*, 2022). Staphylococcal nuclease also plays a critical role in eluding the host-mediated innate immunity by destroying the neutrophil extracellular traps (NETs), which in turn helps in dissemination of the pathogen and in progression of systemic infection (Bhattacharya *et al*., 2020; Herzog *et al*., 2019; Thammangsova *et al*., 2013; Papayannopoulos, 2018).

Based on the significant relevance of nuclease in staphylococcal pathogenesis and virulence, it is foreseen that the enzyme is a potential drug target. Besides, it is anticipated that targeting a virulence factor such as the nuclease enzyme may not impede pathogen growth. Hence, this approach is likely to decrease the probability of resistance development against nuclease inhibitors. There are several literature reports on synthetic inhibitors against a nuclease enzyme such as DNase I (Kolarevic *et al*., 2014; Kolarevic *et al*., 2018; Kolarevic *et al*., 2019; Smelcerovic *et al*., 2020, Gajic *et al*., 2022). However, studies that have characterized inhibitors against staphylococcal nuclease are relatively limited (Schilcher *et al*., 2014; Sahareen *et al*., 2018).

Based on the manifestation of resistance against many therapeutic antibiotics in *S. aureus* strains given the relevant role of MNase in staphylococcal infection, selection of synthetic MNase inhibitors can be considered as an alternate and viable approach to curb the menace of the pathogen. To this end, in the present study, anthraquinone-based ligands (C1-C4) have been evaluated for their potential to inhibit MNase activity. The mechanism of MNase inhibition by the most potent ligand C1 is also described in the present study.

2.2. Materials and Methods

2.2.1. Growth media and chemicals

Calf thymus DNA (CT-DNA), pUC18 plasmid DNA were procured from Sisco Research Laboratories Pvt. Ltd., India. Micrococcal nuclease (MNase), ethidium bromide (EtBr), Hoechst 33258 dye, DAPI dye was procured from Sigma-Aldrich (USA). Brain Heart Infusion (BHI) broth and Toluidine Blue-DNA Agar was procured from HiMedia, Mumbai, India. Dimethyl sulfoxide (DMSO) was obtained from Merck. The synthetic ligands C1-C6 used in the current investigation were commercially available and procured from Sigma-Aldrich (USA).

2.2.2. Bacterial strain and growth conditions

In the present investigation, the clinical MRSA strains namely *S. aureus* MRSA 100 and *S. aureus* 4s were used. The strains were propagated in BHI broth at 37 ºC and 180 rpm for 12 h as described previously (Dey *et al*., 2018; Thiyagarajan *et al*., 2017).

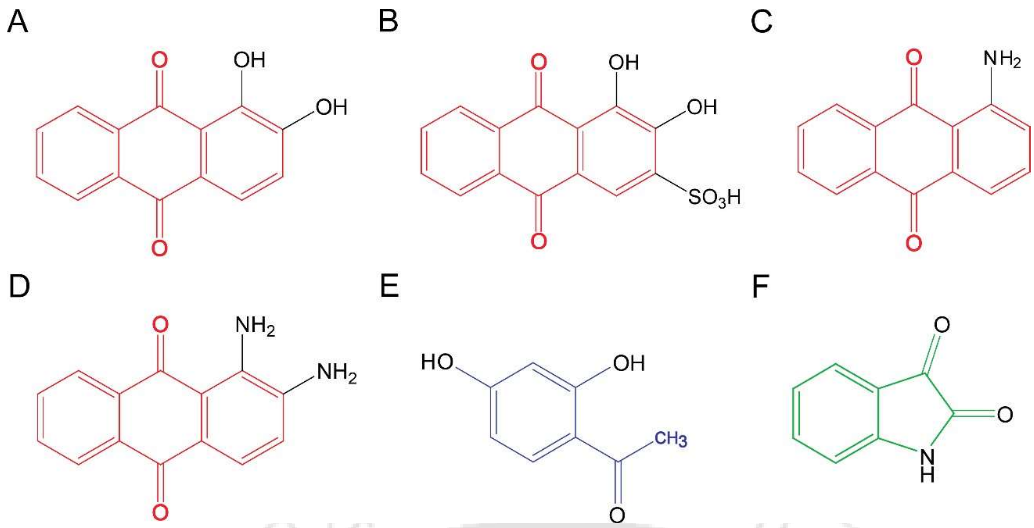

Figure 2.1. General structure of the synthetic ligands used in the current study. (A) C1, (B) C2, (C) C3, (D) C4, (E) C5 and (F) C6.

2.2.3. Synthetic ligands

The structure of the ligands used in the current study is shown in Figure 2.1. A 10 mM stock solution of the ligands (C1-C6) was prepared in DMSO. Prior to the experiments, appropriate dilutions of the stock solutions were made.

2.2.4. Screening of ligands as MNase inhibitors

A solution-based nuclease assay was performed to ascertain the efficacy of the synthetic ligands as MNase inhibitors. The nuclease assays were performed in multiple sets in Tris-$CaCl_2$ buffer by essentially following a previously described method (Sahareen *et al.*, 2018). In these experiments, 1.0 µg of CT-DNA was initially incubated in separate sets with Hoechst dye (1.0 µg mL^{-1}) for 30 min in the dark. In another set, the enzyme solution (2.0 units of MNase) was incubated separately with varying concentrations of the ligands C1-C6 for 30 min at 37 ºC and 180 rpm. The ligands were used at a concentration of 0.1 µM, 0.6 µM, and 5.0 µM. Following incubation, the enzyme-ligand complex was added to CT-DNA-Hoechst dye complex and the samples were incubated for another 30 min. Subsequently, the fluorescence spectra of the samples were recorded at an excitation wavelength of 350 nm at 30 sec time intervals till 600 sec. In a separate set of experiments, CT-DNA-Hoechst dye complex samples (having 0.5 µg mL^{-1} and 1.0 µg mL^{-1} CT-DNA) were incubated separately with C1 (0.5 µM and 1.0 µM) for 30 min. Subsequently, MNase solution (2.0 units) was added to these samples and their fluorescence spectra was measured

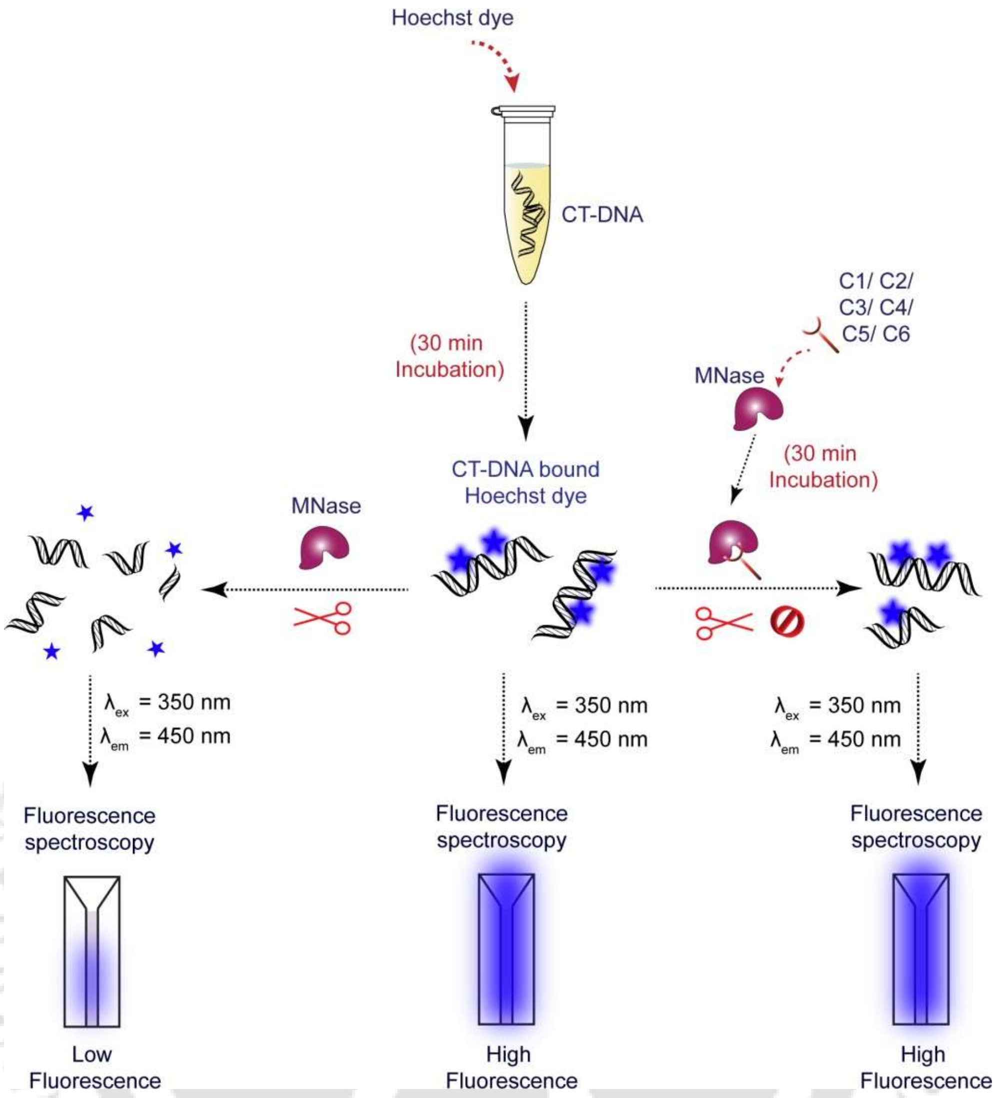

Figure 2.2. Schematic representation of the fluorescence-based assay used for screening of ligands as MNase inhibitor.

over a period of 600 sec as mentioned previously. In parallel sets, the fluorescence emission was also recorded for control samples wherein MNase was added to CT- DNA -Hoechst dye complex in the absence of the ligands. The Hoechst dye emission at 450 nm was considered a measure of MNase activity and considered as 100% activity for samples devoid of the ligands. In another set of experiment, MNase (1.4 μM prepared in Tris-$CaCl_2$ buffer) was incubated with 5.0 μM C1 for 30 min at room temperature. Subsequently, the MNase-C1 complex was subjected to dialysis (12,000 MWCO) against deionized water overnight and MNase activity of the dialyzed sample was also estimated by the fluorescence-based assay described earlier. For all the samples, MNase activity was expressed relative to the control sample (devoid of ligand C1). All the experiments were performed in three independent sets and every set consisted of three replicates. A schematic illustrating the key steps and the principle of the screening assay for the ligands is indicated in Figure 2.2.

2.2.5. Assessment of C1-MNase interaction

Isothermal titration calorimetry (ITC) was conducted to ascertain the binding of C1 to MNase. ITC measurement was performed at 25 ºC (MicroCal ITC200 device, Malvern Panalytical). Prior to the experiments, the samples were degassed under vacuum to prevent the formation of air bubbles. Initially, a 2.0 µM MNase solution was prepared in Tris-$CaCl_2$ buffer and loaded onto the cell and titrated against 80 µM of C1. The resulting data representing the integrated heat effects, after correction for heats of dilution was analyzed by nonlinear regression (MicroCal origin).

The interaction of C1 with MNase was also ascertained by solution-based fluorescence spectroscopy and the binding constant was calculated. Herein, MNase solution (0.272 µM in 50 mM Tris-HCl, pH 7.5 supplemented with 10 mM $CaCl_2$) was titrated with varying concentrations of C1 (0 µM – 1.6 µM) and the fluorescence emission spectra of the samples were recorded in scan mode from 310 nm - 530 nm in a spectrofluorimeter (Fluoromax-4, Horiba) at an excitation wavelength of 295 nm with a slit width of 5 nm at 298 K. All the experiments were performed in multiple independent sets and every set consisted of three replicates.

The effect of C1 on the secondary structure of MNase was determined by circular dichroism spectroscopy. MNase (1.4 µM prepared in Tris-$CaCl_2$ buffer) was titrated with varying concentrations of C1 (0 µM - 5.0 µM) and the CD spectra of the samples was recorded in a spectropolarimeter (Jasco, J-815). The scan range was set from 190 nm to 240 nm. A quartz cuvette of 2 mm path length was used and each spectrum was recorded from an average of six runs at a fixed temperature of 298 K. The spectra were expressed in terms of milli degree (mdeg). In a separate set, the effect of C1 (1.0 µM and 5.0 µM) on HSA protein (40 µg mL^{-1}) was also evaluated by recording the CD spectra by following the conditions outlined before. In another set of experiment, MNase (1.4 µM prepared in Tris-$CaCl_2$ buffer) was incubated with 5.0 µM C1 for 30 min at room temperature. Subsequently, the MNase-C1 complex was subjected to dialysis (12,000 MWCO) against deionized water overnight and the CD spectra of the sample was recorded as mentioned before. Interaction of C1 with MNase was further studied by molecular docking as described in the Appendix section.

2.2.6. Evaluation of C1-DNA interaction

A fixed concentration of C1 was taken in separate sets (20.0 µM each prepared in 5.0 mM Tris, 50 mM NaCl, pH 7.2) and varying concentrations of CT-DNA solution(0 µM - 25 µM, prepared in 5.0 mM Tris, 50 mM NaCl, pH 7.2) was added to each set of C1 solution and incubated for 30 min. The absorption spectra of the samples were recorded in a UV-visible spectrophotometer (Carry 60) in scanning mode ranging from 200 nm - 600 nm and the binding constant of C1 for CT-DNA was ascertained by a previously described method (Ramachandran *et al.*, 2012; Wolfe *et al.*, 1987). All the experiments were performed in three independent sets and every set consisted of three replicates.

2.2.7. Nuclease inhibition assay

The effect of C1 on MNase enzyme kinetics was determined. All the experiments were performed in a Tris-$CaCl_2$ buffer. In separate sets, varying concentrations of CT-DNA (350 nM -3500 nM) was incubated with Hoechst dye (1.0 µg mL^{-1}) for 30 minutes at 37 ºC and 180 rpm. Subsequently, MNase solution (2.0 U mL^{-1}) pre-incubated with varying concentrations of C1 (0.1 µM - 5.0 µM) at 37 ºC and 180 rpm for 30 min was added to the CT-DNA-Hoechst dye complex samples and the fluorescence emission intensity of the samples was recorded at 450 nm at 30 sec time intervals till 600 sec, The excitation wavelength was 350 nm. In parallel sets, the fluorescence emission was also recorded for samples wherein MNase enzyme alone was added to the CT-DNA-Hoechst dye complex in the absence of C1. The decrease (%) in fluorescence emission intensity for CT-DNA-Hoechst dye complex at 450 nm for all the samples was estimated at every time interval and the values were plotted as a function of time (at 30 sec time intervals till 600 sec). The slope estimated from these plots was again plotted as a function of CT-DNA concentration to obtain a velocity versus substrate concentration plot similar to an enzyme-substrate kinetics plot (Michaelis-Menton plot). Thereafter, the double-reciprocal plot (analogous to the Lineweaver-Burk plot) and Dixon plot was constructed to determine the kinetic parameters such as V_{max}, K_m, K_{cat} and K_i (Nelson and Cox, 2018; Segel, 2010). All the experiments were performed in three independent sets and every set consisted of three replicates.

2.2.8. Toluidine blue-DNA (TB-DNA) agar plate assay

S. aureus MRSA 100 strain was grown overnight. The cells were then separated by centrifugation at 8000 rpm for 5.0 min and the cell-free supernatant (CFS) was collected. The CFS was then incubated in boiling water for 10 min to deactivate the thermolabile components. Subsequently, the CFS was incubated in separate sets with varying concentrations of C1 (2.0 µM, 40 µM, 300 µM and 1.0 mM) for 30 min at 37 ºC and 180 rpm. In TB-DNA agar plates, 5.0 mm wells were punctured and 60 µL aliquot of the following samples were added in separate wells: (1) CFS, (2) CFS pre-incubated with 2.0 µM C1, (3) CFS pre-incubated with 40 µM C1, (4) CFS pre-incubated with 300 µM C1, (5) CFS pre-incubated with 1.0 mM C1 and (6) 1.0 mM C1. The samples were allowed to drain and diffuse in the wells and then the plates were incubated overnight at 37 °C in an upright position. Following incubation, images of the zone of clearance around each well were recorded.

2.2.9. Plasmid DNA cleavage assay

In separate sets, MNase solution (2.0 U mL^{-1} prepared in Tris-$CaCl_2$ buffer) was incubated with varying concentrations of C1 (0.5 µM and 1.0 µM) for 30 min at 37 ºC and 180 rpm. Following incubation, MNase-C1 complex was added to a solution of pUC18 plasmid DNA (1.0 µg mL^{-1}) and the samples were incubated for 2.0 min. Subsequently, 30 mM of EDTA (final concentration) was added to the solution to terminate the reaction. The samples were then analyzed by agarose gel (0.8%) electrophoresis. The DNA bands were stained with EtBr solution and observed in a gel documentation system (Gel Doc XR + System, Bio-Rad). The intensity of the bands was quantified by ImageJ analysis (http://rsb.info.nih.gov/ij/).

2.2.10. Bactericidal activity and cytotoxic potential of C1

BHI media containing various concentrations of C1 (12.5 µM – 700 µM) in separate sets was inoculated with 10^6 CFU of *S. aureus* MRSA 100 strain and grown overnight at 37 ºC and 180 rpm. The growth of the MRSA strain (in %) with respect to the untreated control cells was determined by measuring absorbance at 600 nm in a microtitre plate reader (Infinite M200, TECAN, Switzerland). The experiments were performed in three independent sets and every set consisted of three replicates.

In the cytotoxicity studies, HEK 293 cells were grown in a 25 cm^2 tissue culture flask in Dulbecco's Modified Eagle Medium (DMEM) supplemented with 10% (v/v) fetal bovine serum (FBS) at 37 °C under a humidified atmosphere of 5% CO_2 in an incubator till the cells achieved ~80% confluency. The cells were then seeded onto 96-well tissue culture plates at a density of 8×10^3 cells per well and incubated in separate sets. After 24 h of incubation, DMEM media in the plates was aspirated and replaced by varying concentrations of C1 (3.0 μM- 300 μM taken in DMEM) and the plates were again incubated for 24 h. Subsequently, the media from each well was carefully aspirated and fresh DMEM medium containing MTT solution (final concentration of 25 μg mL^{-1}) was added to the wells and the plates were incubated for 3 h at 37 °C under 5% CO_2. Subsequently, the supernatant was discarded and the insoluble formazan product was solubilized in DMSO and its absorbance was measuredin a microtiter plate reader (Infinite M200, TECAN, Switzerland) at 570 nm. The absorbance for the untreated cells was considered as 100% cell viability (control) and the absorbance for the treated cells was used to determine % cell viability with respect to the control. All the experiments were performed in three independent sets and every set consisted of three replicates.

2.3 Results and Discussion

2.3.1. Design rational of synthetic ligands

The synthetic compounds used in the current study (Figure 2.1) have been selected on the basis of varying physicochemical properties such as lipophilicity and presence of H-donor/acceptor groups, in accordance with the design rational of known nuclease inhibitors (Kolarevic *et al.*, 2014). The anthraquinone-based ligands C1-C4 possess adequate lipophilic balance as well as H-bond donor/acceptor groups. It may be mentioned here that the structure of the ligands differ due to the presence of phenolic, sulfonic and amine groups. Ligand C5 is an acetophenone bearing two hydroxyl groups, while ligand C6 is an indole derivative. Ligand C5 and C6 are deficient in lipophilic balance as compared to ligands C1-C4. Besides, the anthraquinone and acetophenone derivatives hold special interest due to their therapeutic potential as antibacterial as well as antioxidant agents (Lee *et al.*, 2016; Kemeng *et al.*, 2017; Markovic *et al.*, 2016; Emami *et al.*, 2018, Hasanien *et al.*, 2022).

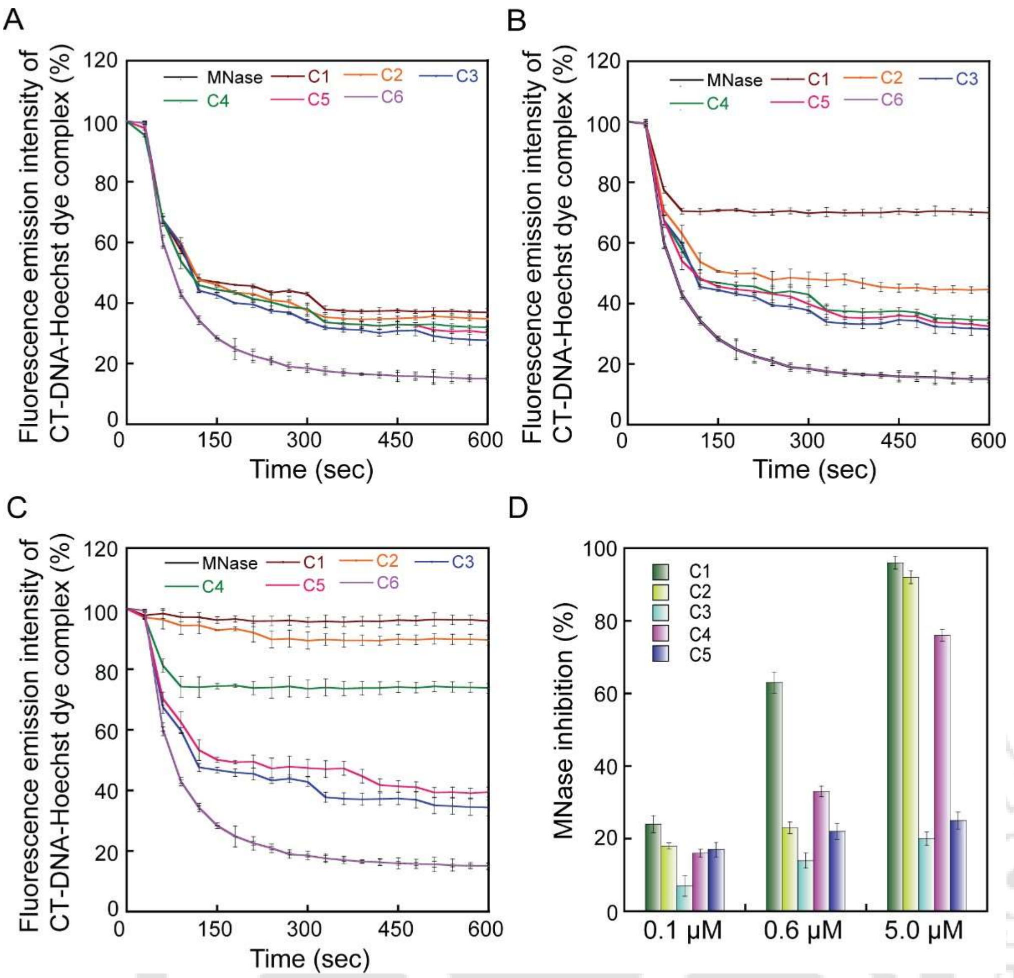

Figure 2.3. Change in fluorescence emission intensity of CT-DNA Hoechst dye complex in presence of MNase and ligands C1-C6 in separate sets. The concentration of the ligands used in the experiments were (A) 100 nM, (B) 600 nM and (C) 5.0 μM. (D) Dose-dependent MNase inhibition rendered by C1, C2, C3, C4 and C5 based on the measurement of end-point fluorescence emission intensity at 450 nm.

2.3.2. Evaluation of ligands as MNase inhibitor

In presence of MNase, a systematic reduction in the fluorescence emission intensity of CT-DNA-bound Hoechst dye at 450 nm was observed (Figure 2.3A-2.3C), which indicated cleavage of CT-DNA by MNase. Interestingly, in presence of ligands C1-C5, there was a decrease in the emission intensity of DNA-bound Hoechst dye (Figure 2.3A-2.3C), which suggested that ligands C1-C5 can inhibit MNase activity. However, in case of C6, it was observed that the reduction in the emission intensity of DNA-bound Hoechst dye was on par with that observed for MNase alone in presence of varying concentrations of C6 (Appendix, Figure A2.1), which indicated that the ligand failed to inhibit MNase. It may be mentioned here that the fluorescence emission intensity of DNA-bound Hoechst dye was not affected in presence of the ligands per se. On the basis of end-point fluorescence, the highest magnitude of MNase inhibition was rendered by C1, followed by C2 and C4 (Figure 2.3D). Although a dose-dependent increase in MNase inhibition was unambiguously observed for the ligands (C1-C5), the magnitude of MNase inhibition rendered by C1, C2 and C4 was higher as compared to the inhibition rendered by equivalent levels of C3 and C5 (Figure 2.3D). To this end, at the highest tested concentration of 5.0 µM, MNase inhibition rendered by C1, C2 and C4 were observed to be ~96%, ~92% and ~76%, respectively (Figure 2.3D). A comparative analysis indicated that C1 was the most effective MNase inhibitor (Figure 2.3D, Appendix, Table A2.1). Amongst the salient features of known nuclease inhibitors, lipophilicity and presence of H-donor/acceptor groups are considered to be critical (Kolarevic *et al.*, 2014). The anthraquinone-based ligands C1-C4 possess adequate lipophilic balance and H-bond donor/acceptor groups, while the ligands C1 and C2 are acidic. Apparently, the presence of an additional acidic SO_3H group in C2 or a basic NH_2 group in C3 and C4 does not seem to heighten the magnitude of MNase inhibition as compared to ligand C1. MNase is a Ca^{2+}-dependent enzyme and coordination of Ca^{2+} by the ligands may serve as a possible means of decreasing the apparent activity of MNase. In this regard,it may be mentioned that Ca^{2+}-coordinating ability of the ligands C1, C3, C4 and C5 is likely to be on par, while it is anticipated that ligand C2 would possess a higher Ca^{2+}-coordinating ability owing to the presence of a sulphonic acid group. However, in the present study, there were inherent differences observed in the magnitude of MNase- inhibition activity of the ligands, wherein C1 was the most effective MNase inhibitor (Figure 2.3D). This implied that the Ca^{2+}-coordinating activity of the ligands does not seem to have an overriding effect on inhibition of MNase activity rendered by the ligands.

2.3.3. Interaction of C1 with MNase and CT-DNA

It is vital to determine whether the ligand C1 could interact favorably with MNase as a stable interaction of the ligand with the enzyme in solution is critical for effective enzyme inhibition. ITC studies supported this notion as evidenced by the binding of C1 with MNase ($K_a = 9.5 \times 10^4$ M^{-1}) (Figure 2.4A). UV-visible absorption spectroscopic analysis was also performed to ascertain the binding of C1 to the CT-DNA. Herein, a hyperchromic shift in the absorbance band of C1 was noted in presence of an increasing concentration CT-DNA and the intrinsic binding constant of C1 for CT- DNA was estimated to be 44.89 nM^{-1} (Figure 2.4B-2.4C).

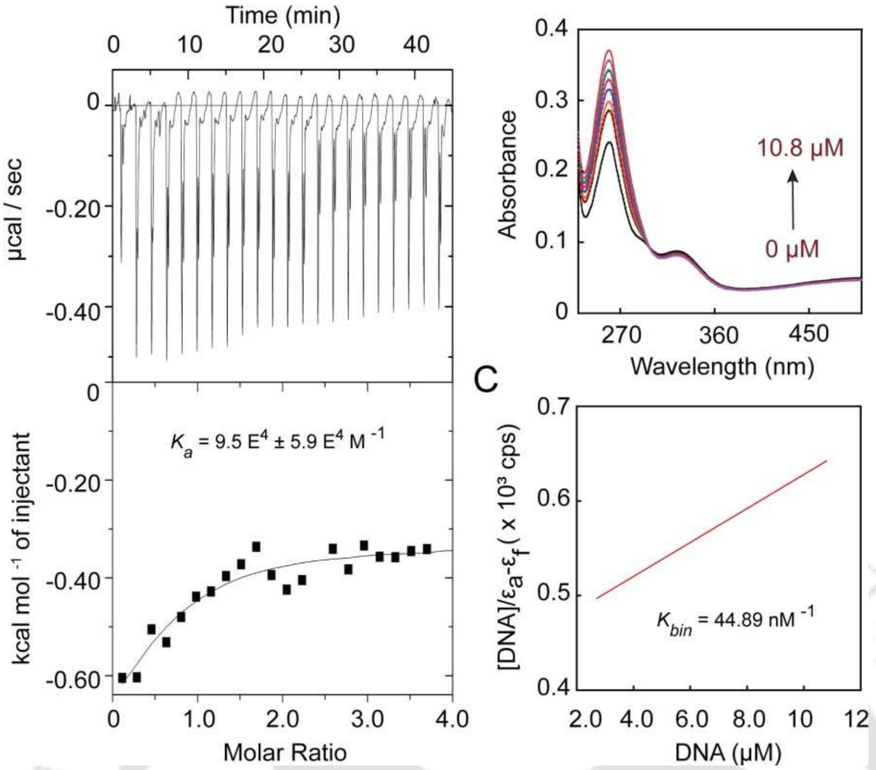

Figure 2.4. (A) ITC analysis to determine the binding isotherm of C1 and MNase. (B) UV-visible absorbance spectra of C1 in presence of CT-DNA. (C) Binding isotherm of C1 in presence of an increasing concentration of CT-DNA.

To further evaluate the solution-based interaction of C1 and MNase, fluorescence spectroscopy and CD spectroscopy was performed with MNase and C1. A titration spectrum of MNase with C1 revealed a systematic decrease in the intensity of tryptophan fluorescence in MNase, wherein the Stern-Volmer constant and binding constant for C1 was 2.3 x 10^{13} $M^{-1}s^{-1}$ and 320 nM^{-1}, respectively (Figure 2.5A-2.5C). To further analyze the interaction, CD spectroscopy was performed with MNase and varying concentration of C1. Upon sequential addition of C1, a notable change in the peak of MNase at 209 nm and 221 nm was evident (Figure 2.5D), along with a change in the positive peak of MNase (Figure 2.5D), which suggested a change in the structural conformation of β-sheet present in MNase. The active site of MNase is located in a β-sheet rich region of the protein (Cotton *et al*., 1979). Hence, from the CD spectra, it can be presumed that C1 perhaps binds in the vicinity of the active site of MNase, which results in a distortion in the β-sheet structure of the enzyme. A perturbation of the secondary structure of MNase was also evident upon increasing the concentration of C1 (Table 2.1).

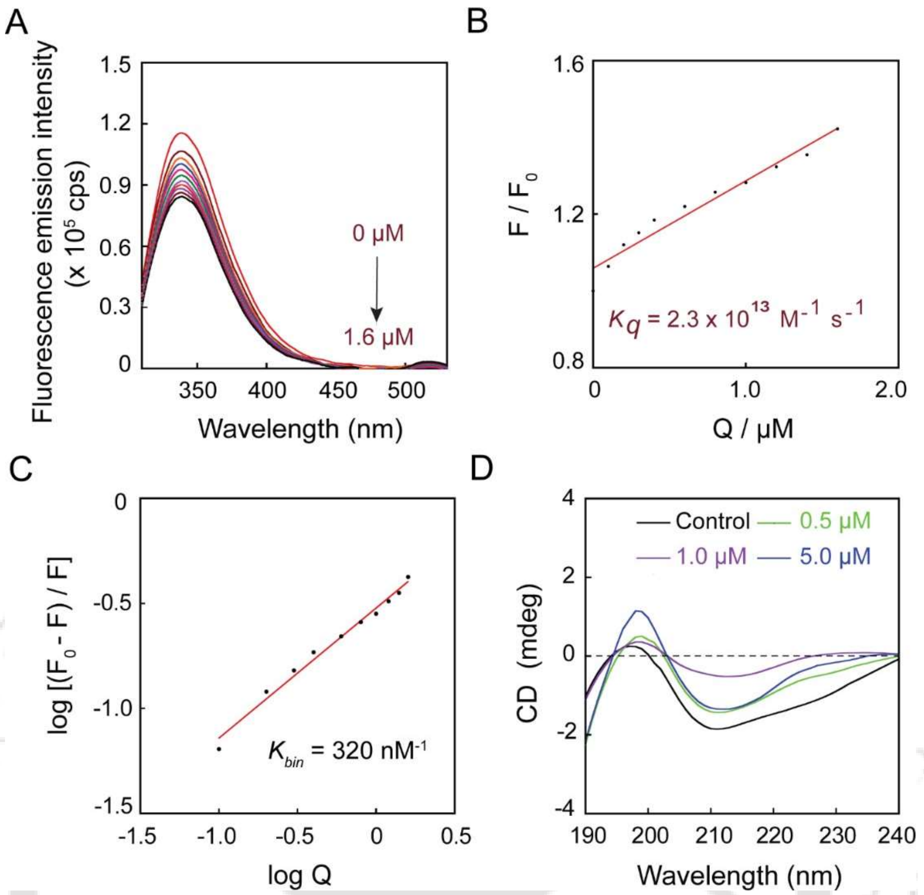

Figure 2.5. (A) Tryptophan fluorescence emission spectra of MNase in presence of an increasing concentration of C1. (B) Stern-Volmer plot for C1 based on the emission spectra obtained in (A). (C) Scatchard plot for C1 based on emission spectra obtained in (A). (D) CD spectra of MNase measured in presence of an increasing concentration of C1.

Table 2.1. Secondary structure analysis of MNase following interaction with C1.

Sample	Secondary Structure Content in MNase			
	α - Helix (%)	β - Sheet (%)	Turn/Loop (%)	Random Coil (%)
MNase	20.9	21.5	26.2	31.4
MNase + C1 (0.5 µM)	16.1	35	24.5	24.4
MNase + C1 (1.0 µM)	5.8	70.2	9.9	14.1
MNase + C1 (5.0 µM)	13.2	50.7	18.7	17.4

However, to ascertain whether C1 was selective, CD spectroscopy of human serum albumin (HSA) was also pursued upon interaction with C1. It is worth mentioning here that the concentration of C1 used in these experiments was 1.0 µM and 5.0 µM, which was sufficient to render significant inhibition of MNase activity as observed in earlier studies (Figure 2.3D). Interestingly, CD spectroscopy revealed that there was no significant change in the characteristic absorbance peaks as well as the secondary structure of HSA upon interaction with C1 (Appendix, Figure A2.2, Table A2.2). This observation seems to suggest that the ligand C1 was perhaps selective in its interaction with MNase and not a promiscuous protein unfolder, which augers well in future therapeutic applications. Further, CD spectroscopy of the dialyzed MNase-C1 preformed complex having a high concentration of C1 (5.0 µM) revealed that the secondary structure content of the enzyme comprised of 37.9 % α-helix, 20% β-sheet, 21.9% turn/loop and 20.2% random coil. This observation suggested that upon removal of the ligand C1 by dialysis, MNase seems to regain a significant proportion of its β- sheet content, which was comparable to the β-sheet content of the native enzyme (~21.5%) (Table 2.1). The active site residues of MNase are known to be located in a β-sheet rich region (Cotton *et al.*, 1979). Given that the β-sheet content of the dialyzed sample of MNase-C1 preformed complex was comparable to the native MNase enzyme, it was thus envisaged that the dialyzed sample of MNase-C1 preformed complex will exhibit considerable MNase activity. Estimation of MNase activity in the dialyzed sample of MNase-C1 preformed complex indeed indicated retention of enzymatic activity as the decrease in fluorescence emission intensity of CT-DNA Hoechst dye complex noted for the sample was equivalent to that observed for MNase (Figure A2.3). Collectively, the CD-based secondary structure analysis and retention of MNase activity in the dialyzed sample of MNase-C1 preformed complex imply that the interaction between the ligand C1 and MNase is quite selective in nature.

In addition, molecular docking studies revealed that ligand C1 exhibited favorable binding energy and exhibited hydrophobic interactions and H-bond formation with certain amino acid residues of MNase (Appendix, Figure A2.4, Table A2.3). For instance, ligand C1 displayed hydrophobic interaction with the active site residue Asp 19 and H-bond formation with Asp 21 and Arg 35 of MNase, while the binding energy was -5.23 kcal/mol (Appendix, Figure A2.4, Table A2.3). Collectively, these findings suggested that ligand C1 could likely inhibit MNase through interactions with

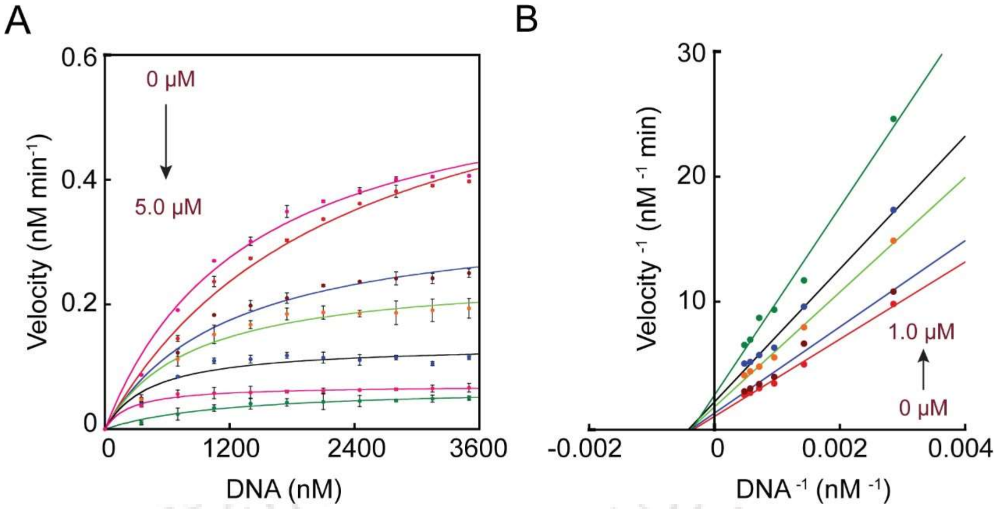

Figure 2.6. (A) Michaelis-Menten plot for MNase in presence of varying concentrations of substrate and C1 (0.1-5.0 µM). (B) Lineweaver-Burk plot to assess MNase inhibition by C1.

active site residues of the enzyme. Molecular docking studies also indicated that ligand C1 could bind with a generic nuclease such as the bovine pancreas DNase I (Appendix, Figure A2.5, Table A2.4). Notably, ligand C1 displayed hydrophobic interaction with tyrosine residue and H-bond formation with other residues of DNase I (Appendix, Figure A2.5, Table A2.4). It may be mentioned here that these residues do not belong to the active site of the enzyme as it has been shown that His 131 is the active center of DNase I (Suck *et al*., 1984). In comparison to DNase I, it does seem apparent from molecular docking studies that ligand C1 has a superior potency against MNase as an inhibitor as it displayed the potential to interact with some of the active site residues of the enzyme (Table A2.3).

2.3.4. Kinetics of MNase activity and inhibition by C1

The effect of the most potent inhibitor C1 on MNase enzyme kinetics was assessed by performing a solution-based nuclease assay. Herein, it was observed that the rate of CT-DNA cleavage was decreased in presence of an increasing concentration of C1 (Figure 2.6A). A significant inhibition of MNase was observed in presence of 5.0 µM C1 (Figure 2.6A). Estimation of the kinetic parameters revealed that the Michaelis-Menten constant (K_m), maximum velocity of enzyme-catalyzed reaction (V_{max}) and the enzyme turnover number (K_{cat}) for MNase was 2644 nM, 0.925 nM min^{-1} and 0.034 min^{-1}, respectively. From the Lineweaver-Burk plot (LB plot), it was observed that

Table 2.2. Kinetics parameters for MNase determined in presence of C1.

C1 (µM)	V_{max} (nM min $^{-1}$)	K_{cat} (min $^{-1}$)	K_{cat} / K_m (min $^{-1}$ nM^{-1})
0	0.925	0.034	1.28×10^{-5}
0.1	0.685	0.025	9.52×10^{-6}
0.2	0.544	0.019	7.56×10^{-6}
0.4	0.385	0.014	5.35×10^{-6}
0.6	0.298	0.011	4.14×10^{-6}
1.0	0.205	0.008	2.85×10^{-6}
5.0	0.049	0.002	6.94×10^{-7}

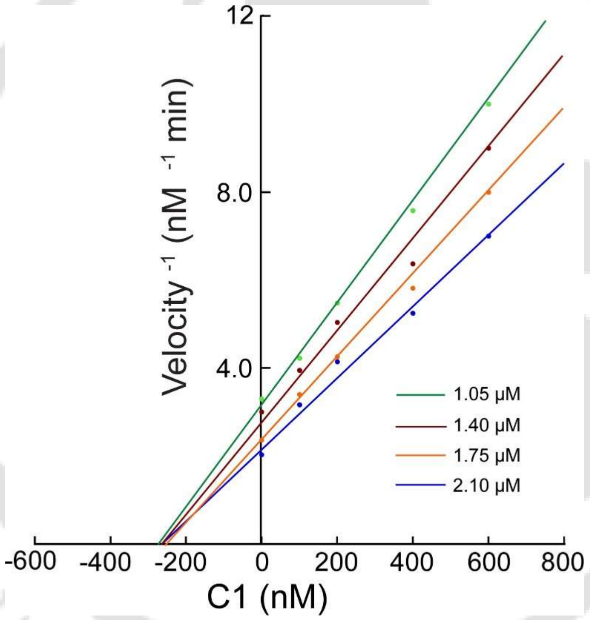

Figure 2.7. Dixon plot for MNase in the presence of varying concentrations of C1. CT-DNA concentration was varied from 1.05 µM to 2.10 µM in separate sets.

C1 rendered a non-competitive inhibition of MNase as K_m for MNase remained constant, but V_{max} of MNase-catalyzed reaction was reduced in presence of an increasing concentration of C1 (Figure 2.6B, Table 2.2). A non-competitive mode of inhibition rendered by C1 is perhaps an indication that the ligand binds to MNase-substrate complex and reduces the rate of enzyme-catalyzed reaction and product formation. This mode of inhibition is desirable as the inhibitory effect rendered by the ligand is likely to prevail even at high substrate concentration. Experiments were also conducted to ascertain whether a part of MNase inhibition rendered by C1 was due to the ligand interacting with DNA and thereby modifying the substrate. To this end, in the fluorescence-based MNase assay, the reduction of fluorescence emission intensity for preformed CT-DNA-C1 complex digested with MNase was observed to be similar to the sample wherein CT-DNA alone was digested with MNase (control) (Appendix, Figure A2.6). Further, the rate constant estimated for digestion of CT-DNA alone or CT-DNA-C1 preformed complexes were also on par (Appendix, Table A2.4). Collectively, these results suggested that in solution the ligand C1 does not seem to modify the substrate DNA, which resulted in effective digestion of the CT-DNA-C1 complex by MNase. Hence, the inhibition of MNase observed in presence of C1 may be attributed to a direct effect of the ligand on the enzyme. A conspicuous decrease in MNase turnover number (K_{cat}) was also recorded in presence of an increasing concentration of C1 (Table 2.2), which suggested that C1 could perhaps affect the number of catalytic cycles rendered by the enzyme. Besides, there was also a reduction in the catalytic efficiency (K_{cat}/K_m) of MNase upon increasing the concentration of C1 (Table 2.2). The catalytic efficiency of an enzyme involves substrate binding as well as the catalytic event. Since K_m for MNase remained virtually unchanged in presence of C1 (Figure 2.6B), it can be construed that the ligand C1 perhaps interfered with the frequency of the association of MNase with its substrate. From the kinetics data, the IC_{50} value of C1 for MNase was estimated to be 323 nM. Further, a Dixon plot indicated that the inhibitor constant (K_i) for C1 was ~285 nM (Figure 2.7). It is noteworthy that the inhibitory concentration of C1 against MNase compares well with other known inhibitors of MNase as well as DNase (Appendix, Table A2.5).

2.3.5. Inhibition of MRSA secreted nuclease and plasmid DNA cleavage by C1

S. aureus secretes a thermostable nuclease enzyme, which bears significance in biofilm dispersion and resistance against NETs (Yu *et al.*, 2021, Forson *et al.*, 2022; Bhattacharya *et al.*, 2020; Herzog *et al.*, 2019; Thammavongsa *et al.*, 2013). Based on the inhibition of MNase rendered by C1 (Figure 2.6), it was worthwhile to determine whether the ligand C1 could also inhibit nuclease secreted by a clinical isolate of MRSA. To this end, a toluidine blue DNA agar assay was performed which could detect a prominent zone of clearance and indicate the presence of nuclease activity in the CFS of the clinical MRSA strain S. aureus MRSA 100 (Figure 2.8A, well no. 1).

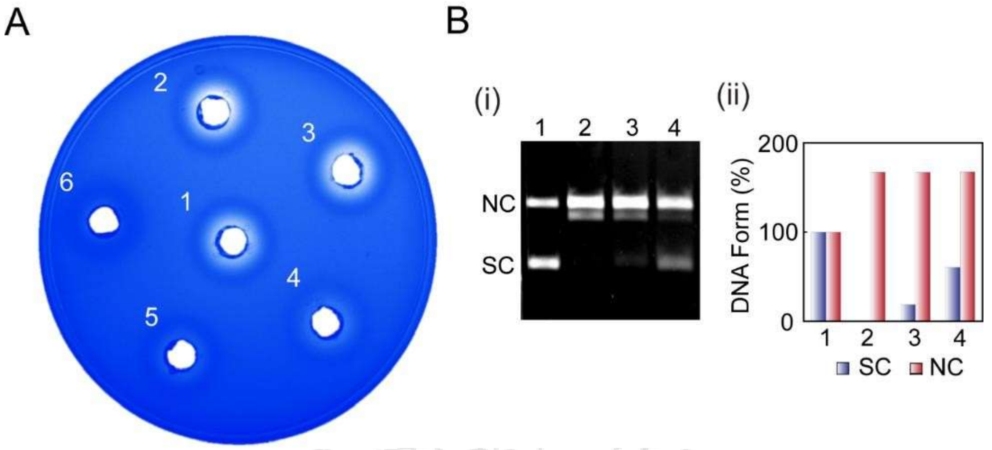

Figure 2.8. (A) Toluidine blue DNA agar plate assay to assess inhibition of MNase present in the cell-free supernatant (CFS) of *S. aureus* MRSA 100. The samples in the wells are : (1) CFS only, (2) CFS and 2.0 µM C1, (3) CFS and 40 µM C1, (4) CFS and 300 µM C1, (5) CFS and 1.0 mM C1 and (6) 1.0 mM C1 only. (B) (i) Agarose gel electrophoresis of (1) Undigested pUC18 plasmid DNA, (2-4) pUC18 plasmid DNA digested with MNase, MNase and 0.5 µM C1, MNase and 1.0 µM C1, respectively. (ii) Histogram profile of the pUC18 plasmid DNA band intensity in (i) analyzed by ImageJ software. NC : nicked circular DNA ; SC : supercoiled DNA.

Interestingly, in presence of C1, a dose-dependent inhibition of nuclease present in the CFS of MRSA was noted (Figure 2.8A), which suggested that C1 can perhaps hold potential as a nuclease inhibitor for therapeutic applications targeting MRSA.

A plasmid DNA cleavage assay was also conducted to validate the inhibition of MNase and MRSA secreted nuclease by C1. To this end, an agarose gel electrophoresis analysis indicated inhibition of the cleavage of pUC18 plasmid DNA by MNase in presence of an increasing concentration of C1 (Figure 2.8B, panel i). Herein, the relative proportion of supercoiled (SC) form of plasmid DNA observed upon cleavage with MNase in presence of 0.5 µM and 1.0 µM C1 was ~26% and ~55%, respectively, as compared ~165% nicked circular (NC) plasmid DNA noted upon cleavage with MNase in the absence of the ligand (Figure 2.8B, panel ii). Control experiments indicated that C1 or EDTA (used to terminate plasmid cleavage assay) failed to cleave pUC18 plasmid DNA (Appendix, Figure A2.7).

2.3.6. Bactericidal activity and cytotoxic potential of C1

The potential of C1 as an MNase inhibitor was evident in multiple experiments. In order to further characterize C1, it was pertinent to evaluate its antibacterial efficacy against MRSA strains. To this end, it was observed that a significant bactericidal

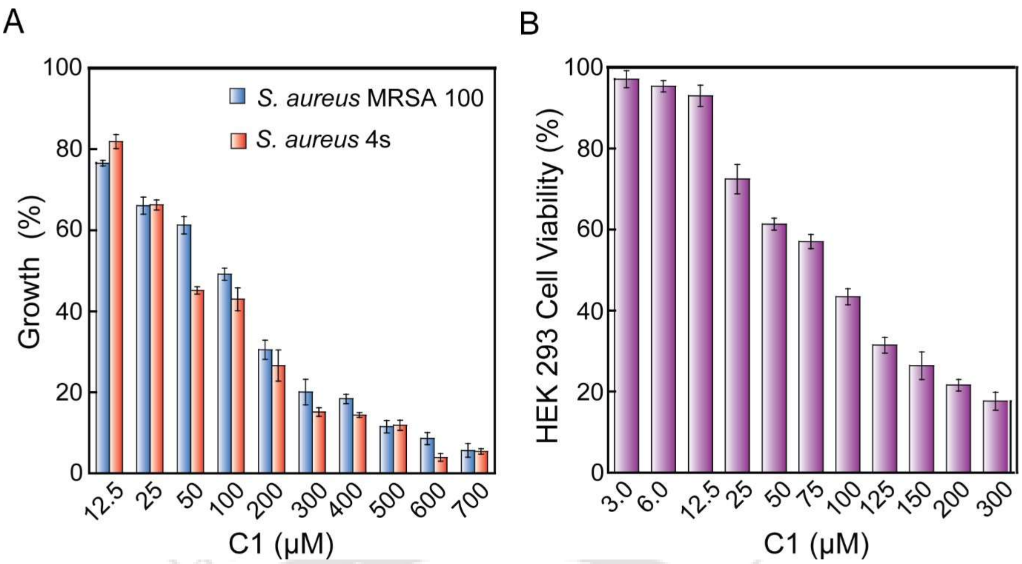

Figure 2.9. (A) Antibacterial activity of C1 against *S. aureus* MRSA 100 and *S. aureus* 4s strains. (B) MTT assay-based assessment of the cytotoxic effect of C1 against HEK 293 cells. The data points were acquired from six independent experimental samples and considered to determine mean ± standard deviation.

activity against the tested MRSA strains was observed only at very high concentrations of C1 (in excess of 12.5 μM) (Figure 2.9A). However, on comparison, inhibition of MNase could be observed in presence of only 5.0 μM C1 (Figure 2.2). Interestingly, C1 was non-toxic to cultured HEK 293 cells (human embryonic kidney cells) till a concentration of 12.5 μM (Figure 2.9B), which was many folds higher than its IC_{50} value for MNase inhibition (~323 nM). This observation has therapeutic implications as it suggested that at concentrations relevant for MNase inhibition, C1 was unlikely to impart any cytotoxic effect on cultured HEK 293 cells. However, it was noted that at very high concentrations, there was a decrease in the viability of HEK 293 cells (Figure 2.9B).

2.4 Significant Findings

The salient findings of the present study are as follows:

1. The anthraquinone-based ligands (C1-C5) could inhibit MNase in solution. Ligand C1 displayed superior inhibition of MNase as compared to the other ligands and the nature of inhibition rendered by C1 was non-competitive.
2. ITC revealed favorable binding of C1 with MNase ($K_a = 9.32 \times 10^4$ M^{-1}), while CD analysis indicated that C1 rendered perturbations in the secondary structure of MNase.

3. C1 could inhibit the activity of the secreted nuclease present in the CFS of MRSA and also inhibited cleavage of plasmid DNA by MNase.
4. C1 exhibited anti-MRSA activity only at extremely high concentrations, while it was non-toxic to HEK 293 cells till a concentration of 12.5 µM, which was significantly higher than the concentration required for MNase inhibition.

Based on the aforementioned results, it was apparent that C1 holds considerable promise as an MNase inhibitor. To leverage the therapeutic potential of C1, it is critical to develop a biocompatible nanocarrier, which will favor the sustained release of C1. To this end, the following chapter describes the generation of C1-loaded HSA nanocarrier for potential application in anti-MRSA therapy.

Chapter 3

Generation of C1-loaded HSA Nanocarrier for Targeting MNase

This chapter illustrates the generation of anthraquinone ligand (C1)-loaded human serum albumin nanocarrier (C1-HNC). The study demonstrates the potential of the nanocarrier for delivery of C1 and illustrates MNase inhibition by C1 eluate emerging from the nanocarrier.

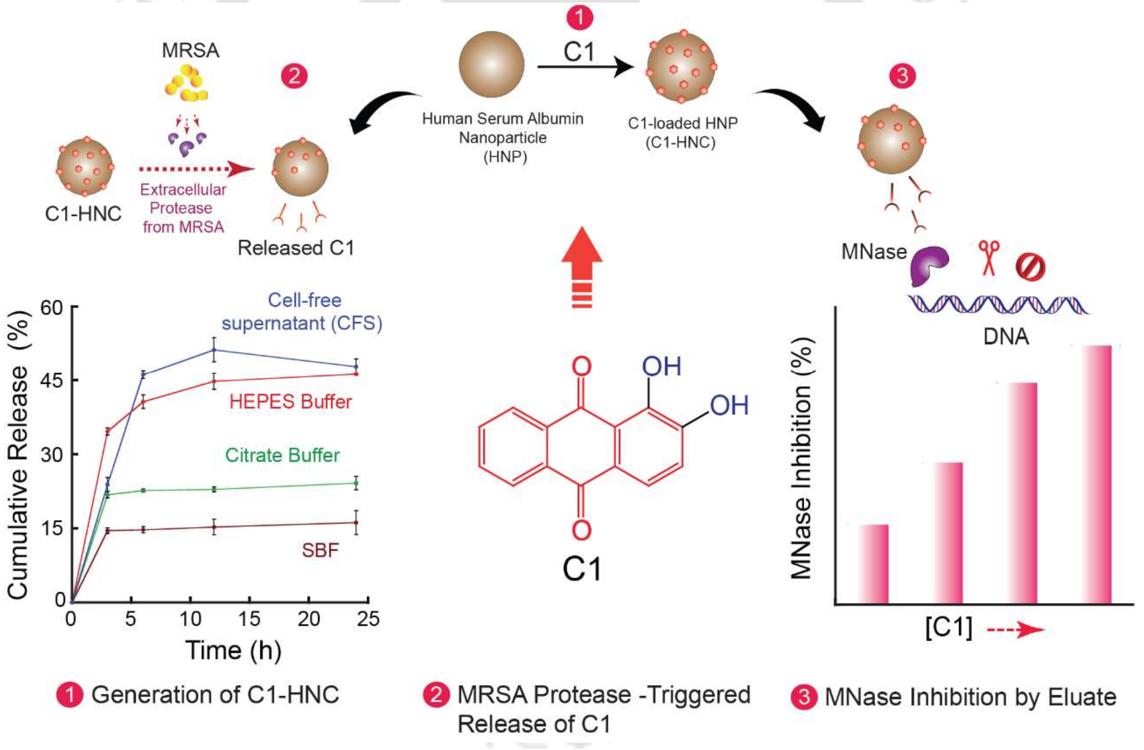

ABSTRACT

This chapter describes the generation of C1-loaded HSA nanocarrier (C1-HNC) for potential anti-MRSA therapy. Initially, HSA nanoparticle (HNP) was synthesized by a desolvation method and C1-HNC was generated by incubating HNPs with varying concentrations of C1. FESEM and FETEM analysis indicated the spherical shape of HNP and C1-HNC. The average particle size of C1-HNC estimated by FESEM was ~220 nm. AFM analysis indicated that the average height profile of C1-HNC was ~ 44 nm, while DLS analysis revealed that the hydrodynamic radius of C1-HNC was ~ 832 nm. Loading of C1 in HNPs was dose-dependent, wherein the highest loading of ~136 µM was achieved at a loading concentration of 180 µM C1, with an encapsulation efficiency of ~75%. Loading of C1 in HNP was validated by UV-visible spectroscopy, which indicated the presence of the characteristic absorbance peak of C1 at 260 nm. FTIR analysis of C1-HNC indicated the presence of the characteristic stretching frequencies of C1 at 1018, 1288, and 1452 cm^{-1}, which further validated the loading of C1 in HSA nanocarrier. C1 release from the nanocarrier was highest in presence of the cell-free supernatant (CFS) of MRSA, which exhibited a proteolytic activity. Following 12 h of incubation, the release of C1 from the nanocarrier in the presence of MRSA CFS was ~51%, and was superior than the release of C1 observed in HEPES buffer (~46%), simulated body fluid (SBF) (~16%) and citrate buffer (~24%). The protease- triggered release profile of C1 from the nanocarrier augers well for potential therapeuticapplications. Inhibition of MNase activity by C1-containing eluates obtained from the payload nanocarrier was also evident and a decrease in the rate of MNase-mediated DNA digestion was observed in presence of an increasing concentration of the eluate. Inhibition of MNase by C1 as well as the eluate obtained from C1-HNC was also verified by fluorescence microscopy. Interestingly, C1-HNC was nontoxic to HEK 293 cells till a concentration of 46 µM of C1. This observation enhances the therapeutic index of the developed nanocarrier since it implied that at concentrations of C1 relevant for MNase inhibition (IC_{50} ~323 nM), the payload nanocarrier was non-toxic.

3.1. Introduction

The prevailing resistance of MRSA against therapeutic antibiotics has created an enormous healthcare burden in the clinics. In order to address this crisis, a viable strategy to counter the peril of MRSA infections is to design and engage small synthetic molecules that can effectively target a virulence factor in the pathogen. In this endeavor, the leads emerging from earlier studies described in Chapter 2 indicated that the anthraquinone ligand C1 could effectively inhibit MNase activity, which is a key virulence factor in staphylococci. Further, the ligand C1 could also inhibit the secreted nuclease present in the CFS of a clinical MRSA strain. In order to advance the leads from the previous study and capitalize the prospect of C1 in anti-MRSA therapy, development of a robust and biocompatible delivery system that can facilitate sustained release of ligand C1 in a physiological milieu is desirable. In this context, generation of nanoscale materials for effective encapsulation and delivery of the MNase inhibitor C1 holds interesting prospects.

Nanomaterials have demonstrated tremendous promise in drug delivery by enhancing the bioavailability of drugs at infection sites and reducing undesirable side-effects (Patra *et al*., 2018; Yeh *et al*., 2020; Roque-Borda *et al*., 2022). A plethora of materials have been used to develop nanocarriers as a cargo for delivery of bioactive and antibacterial agents. These nanomaterials range from metallic nanoparticles, liposomes, lipid-based nanoparticles, mesoporous silica nanoparticles to the FDA approved poly(lactide-co-glycolide) (PLGA)-based nanoparticle (Bajaj *et al*., 2017; Yamakami *et al*., 2013, Lewies *et al*., 2017; Tenland *et al*., 2019; Danhier *et al*., 2012; Swider *et al*., 2018). In order to enhance the selectivity and therapeutic efficacy of a payload bearing nanocarrier, a stimuli-responsive sustained delivery of the bioactive payload is desirable. It is well established that *S. aureus* secretes several proteases and toxins that display protease like activity, some of which are critical in establishing virulence of the pathogen (Pietrocola *et al*., 2017; Tam and Torres, 2018; Cassat *et al*., 2013; Ahmad-Mansour *et al*., 2021; Otto, 2014). Hence, it is conceived that the choice of proteinaceous nanomaterials for delivery of an anti-staphylococcal agent can hold interesting prospects.

In the context of proteinaceous nanomaterials, the choice of nanocarriers developed from human serum albumin (HSA) holds special interest. Albumin is particularly favorable for drug delivery applications owing to its high biocompatibility, biodegradability, non-immunogenicity, amicability for loading of hydrophobic drugs and their protection from in vivo metabolism (Shimanovich *et al*., 2014; Elzoghby *et al*., 2012; Emami *et al*., 2021). The application of HSA-based nanoscale material for delivery of bactericidal agents and for other drug delivery applications is well documented (Goswami, *et al*., 2014; Thiyagarajan *et al*., 2016; Ulbrich *et al*., 2009; Karami *et al*., 2020; Tarhini *et al*., 2020; Yi *et al*., 2015). Based on the aforementioned rationale, the focus of the present study was to develop an HSA-based nanocarrier for encapsulation of the MNase inhibitor C1. The study investigates the loading efficiency and the release kinetics of C1-loaded HSA nanocarrier (C1-HNC) and also ascertains the MNase inhibition rendered by the payload bearing nanocarrier and it cytotoxic potential in an *in vitro* cell culture model.

3.2. Materials and Methods

3.2.1. Materials

Calf thymus DNA (CT-DNA), Micrococcal nuclease (MNase), Hoechst 33258 dye, DAPI dye and human serum albumin (HSA) was procured from Sigma-Aldrich (USA). Dimethyl sulfoxide (DMSO), absolute ethanol and glutaraldehyde were obtained from Merck. The synthetic ligand C1 used in the current investigation was commercially available and procured from Sigma-Aldrich (USA).

3.2.2. C1-loaded HSA nanocarrier (C1-HNC)

HSA nanoparticles (HNPs) were prepared by a following a desolvation process (Langer *et al*., 2008). A schematic cartoon indicating the essential steps in the generation of HNPs is shown in Figure 3.1. For the generation of C1-loaded HSA nanocarrier (C1-HNC), 1.0 mg mL^{-1} HNP was dissolved in sterile MilliQ water and incubated overnight in separate sets with varying concentrations of C1 (15 µM - 180 µM) on a rocker at room temperature. Following incubation, the solution was centrifuged at 12000 rpm for 5 min. The supernatant was collected and the pellet which encompassed C1-HNC was resuspended in sterile MilliQ water. A schematic representation of the salient steps followed for generation of C1-HNC is shown in Figure 3.2. HNP and C1-HNC were characterized by FESEM, FETEM, AFM, DLS, UV-visible spectroscopy and FTIR analysis. The magnitude of loading of the ligand in C1-HNC was also estimated. Initially, a UV-visible absorbance spectrum of varying

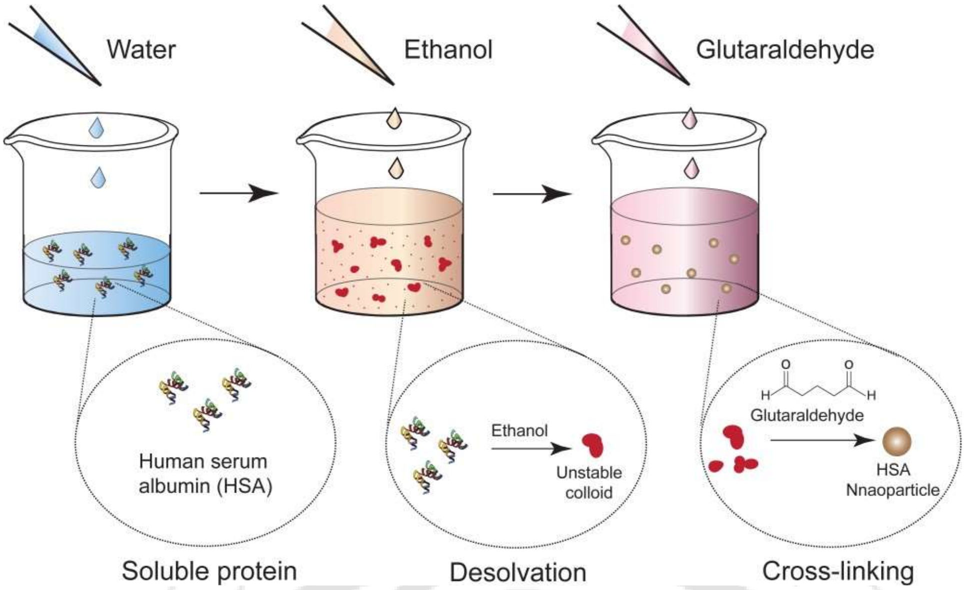

Figure 3.1. Schematic representation of the key steps followed for preparation of human serum albumin (HSA)-based nanoparticle (HNP).

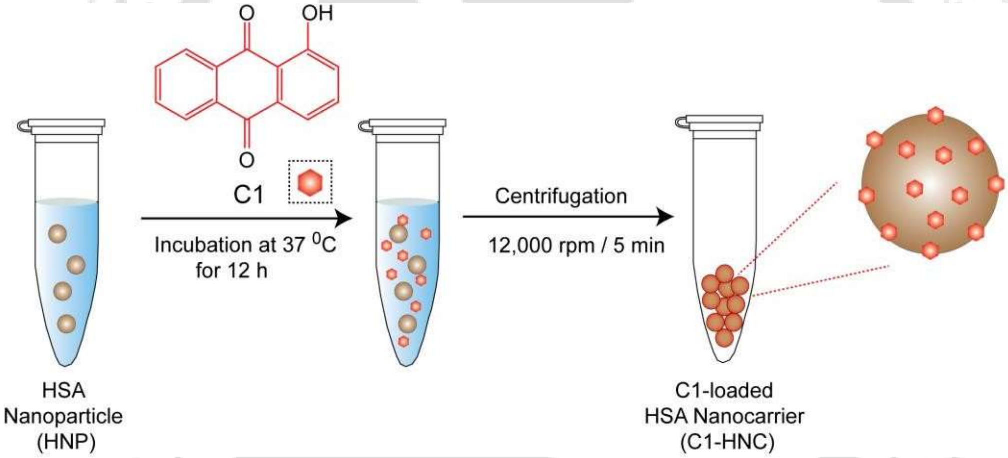

Figure 3.2. Schematic representation of the steps followed for generation of C1-loaded HAS nanocarrier (C1-HNC).

concentrations of C1 (1.0 µM - 180 µM) was recorded at 444 nm (the absorbance maxima of C1) in a spectrophotometer (Lambda 25, Perkin-Elmer). The absorbance values obtained at 444 nm for varying concentrations of C1 was used to construct a calibration plot. For estimation of loading of C1, the concentration of free or residual C1 present in the collected supernatant was determined using the previously generated calibration plot for C1. The magnitude of loading of C1 was then ascertained from the difference between the concentration of C1 used initially for loading and the concentration of C1 present in the supernatant. The magnitude of loading was expressed in percentage.

3.2.3. Characterization of HNP and C1-HNC

A 10 µL aliquot of HNP (1.0 mg mL^{-1} in sterile MilliQ water) and C1-HNC (1.0 mg mL^{-1} HNP having a loading concentration of 45 µM C1) was separately drop-casted onto aluminium foil. The samples were then dried overnight in a laminar hood and visualized in a field emission scanning electron microscope (Zeiss Sigma, USA). Likewise, aliquots of HNP and C1-HNC were separately drop-casted onto a carbon-coated copper grid, dried overnight in a laminar hood and analyzed by FETEM (Model 2100F, JEOL) operating at 200 kV. For AFM analysis, a 10 µL aliquot of HNP(1.0 mg mL^{-1} in sterile MilliQ water) and C1-HNC (1.0 mg mL^{-1} HNP having a loading concentration of 45 µM C1) was separately spotted onto a sterile glass cover slip(18 mm × 18 mm), air dried overnight in a laminar hood and AFM images were acquired in non-contact mode over a 10 µm × 10 µm area at a scan rate of 0.5-1.0 line/s(Oxford Instruments plc, U.K). Cantilevers made up of silicon nitride were used having a resonant frequency of ca. 150 to 200 kHz. Analysis of the amplitude channel and topographic images was accomplished by using the WSxM v5.0 Develop 6.5 image viewer software. For estimation of particle size in solution, HNP (1.0 mg mL^{-1}) and C1-HNC (1.0 mg mL^{-1} HNP having a loading concentration of 69 µM C1) wereresuspended in sterile MilliQ water and 0.2 ml aliquot of the sample was further dilutedin sterile MilliQ water (10 × dilution) and subjected to DLS analysis (Zetasizer, Malvern, UK). The DLS experiments were performed in three independent sets and every set consisted of three replicates. The absorbance spectra of C1 (15 µM), HNP (1.0 mg mL^{-1}) and C1-HNC (1.0 mg mL^{-1} HNP loaded with 45 µM C1) were measured in a spectrophotometer (Lambda 25, Perkin-Elmer) in scanning mode from 200 nm to 800 nm. Absorbance measurements were recorded from three independent experimental samples. FTIR spectra of HNP (1.0 mg mL^{-1}) and C1-HNC (1.0 mg mL^{-1} HNP loaded with 45 µM C1) were recorded in KBr pellets at 4.0 cm^{-1} resolution in an infrared spectrometer (Spectrum One, Perkin-Elmer). Eight scans were performed for each sample in the wavenumber ranging from 4000 cm^{-1} to 500 cm^{-1}. A backgroundspectrum for pure KBr was also recorded.

3.2.4. In vitro release kinetics

C1-HNC (1.0 mg mL^{-1} HNPs loaded with 45 µM of C1) was incubated in separate sets in 1.0 mL each of 10 mM HEPES buffer (pH 7.4), simulated body fluid (SBF, pH 7.4), 10 mM citrate buffer (pH 3.0) and cell-free supernatant (CFS) collected from an overnight grown culture of *S. aureus* MRSA 100. The composition of SBF was as described in an earlier study (Marques *et al*., 2011). The samples were incubated in an orbital shaker at 180 rpm at 37 °C. At specific time intervals (3 h, 6 h, 12 h and 24 h), the samples were withdrawn and centrifuged at 12000 rpm for 5 min. The supernatant from various samples was transferred into a fresh microcentrifuge tube and the UV-visible absorbance of the solutions was measured in a spectrophotometer. The absorbance value of C1 obtained at 444 nm at various time periods was compared with a previously generated calibration plot for C1 and expressed as cumulative release (%) of C1. All the experiments were performed in three independent sets and every set consisted of three replicates.

3.2.5. MNase inhibition by C1-HNC eluate

For MNase inhibition analysis, 1.0 µg of CT-DNA was initially incubated in separate sets with Hoechst dye (1.0 µg mL^{-1}) for 30 min in the dark. In a separate set, C1-HNC having a loading concentration of 92 µM C1 was incubated overnight in Tris-$CaCl_2$ buffer (500 µl) at 37 ºC and 180 rpm for elution of C1 into the buffer solution. The solution was then centrifuged at 12,000 rpm for 5.0 min to separate the HNPs and the supernatant representing the eluate (52 µM C1) was collected. Varying dilutions of the eluate solution (0.1 µM, 0.4 µM, 1.0 µM, 5.0 µM) was made and then added to MNase solution in separate sets (2.0 U each) and incubated for 30 min. MNase-eluate solution was then added to CT-DNA-Hoechst complex and the decrease in fluorescence intensity of CT-DNA-Hoechst dye complex at 450 nm upon excitation at 350 nm was measured periodically over 10 min. The slope of the emission intensity plot was ascertained as a measure of the rate constant of the MNase-catalysed DNA digestion reaction.

The potential of the eluate of C1-HNC to inhibit MNase activity was also accomplished by fluorescence microscopic analysis. In separate sets, CT-DNA (500 µg mL^{-1}) was incubated with DAPI dye (4.0 µM). In another set, MNase solution (2.0 U) was incubated with either C1 (5.0 µM) or the eluate from C1-HNC complex (eluate obtained from C1-HNC loaded with 45 µM C1) for 30 min. Following incubation, C1-MNase and C1 eluate-MNase complex were added in separate sets to DAPI-stained CT-DNA solution and held for 2 min. The reaction was terminated by adding 30 mMof EDTA (final concentration) to the solution.

On a clean glass slide, a 2.0 µL aliquot of the sample was spotted and observed under a fluorescence microscope (Eclipse Ti-U, Nikon) with a filter that allowed UV light excitation and the images were recorded.

3.2.6. Cytotoxic potential of C1-HNC

The cytotoxic potential of C1-HNC loaded with varying concentrations of C1 (1.5 µM - 92 µM C1) taken in DMEM was ascertained against HEK 293 cells. The essential steps of growing HEK 293 cells and the protocol for performing the MTT assay following treatment of HEK 293 cells with C1-HNC were similar to a standard MTT assay protocol described earlier in section 2.2.10.

3.3. Results and Discussion

3.3.1. C1-loaded HSA nanocarrier (C1-HNC)

In order to leverage the therapeutic potential of the anthraquinone-based ligand C1 as an MNase inhibitor, development of a non-toxic delivery system for sustained release of the ligand was pertinent. In order to fulfil this objective, HSA nanoparticle (HNP) was synthesized given its biocompatible and biodegradable attributes, an inherent high loading capacity for payload and its well documented usage in drug delivery (Langer *et al*., 2008; Shimanovich *et al*., 2014; Elzoghby *et al*., 2012; Emami *et al*., 2021). C1-loaded HSA nanocarrier (C1-HNC) was generated by incubating HNPs with varying concentration of C1. FESEM and FETEM analysis revealed that HNP and C1- HNC was spherical in shape (Figure 3.3A-3.3B, Figure 3.4A-3.4B). The average particle size of HNP and C1-HNC determined by FESEM was ~ 213 nm and ~220 nm, respectively. In AFM analysis, the average height profile of HNP and C1-HNC was ~47 nm and ~44 nm, respectively (Figure 3.3C, Figure 3.4C). DLS analysis revealed that the hydrodynamic radius of HNP and C1-HNC in solution was ~804 nm and ~832 nm, respectively (Figure 3.3D, Figure 3.4D). A dose-dependent loading of C1 was observed, wherein a highest loading of ~136 µM was accomplished at a loading concentration of 180 µM C1 and the encapsulation efficiency was ~75% (Table 3.1). The loading of C1 in HSA nanocarrier was also verified by UV-visible spectroscopy, wherein the characteristic absorbance peak of C1 at 260 nm was evident (Figure 3.4E). FTIR analysis validated loading of C1, based the presence of the salient stretching frequencies of C1 at 1018, 1288 and 1452 cm^{-1} in C1-HNC (Figure 3.4F).

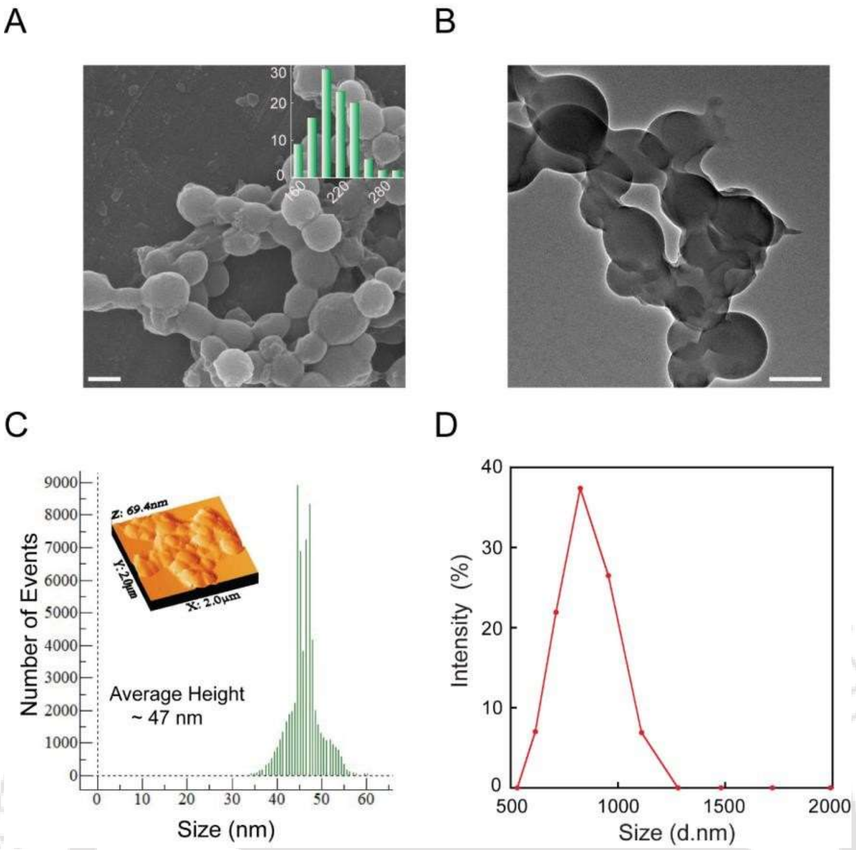

Figure 3.3. (A) FESEM image of HSA nanoparticle (HNP). Inset indicates particle size distribution of HNP determined by ImageJ software. (B) FETEM image of HNP. The scale bar for the images in (A) and (B) is 200 nm. (C) AFM-based analysis of the height profile for HNP. Inset indicates 3D topography AFM image of HNP. (D) DLS-based size distribution plot of HNP.

Table 3.1. Amount of C1 encapsulated in HSA nanoparticle and determination of encapsulation efficiency of C1.

Loading Concentration of C1 (µM)	**Encapsulated C1 in C1-HNC (µM)**	**Encapsulation Efficiency (%)**
15	6.13 ± 0.83	40.86
30	18.04 ± 0.99	60.13
45	28.29 ± 0.20	62.86
60	44.50 ± 0.52	74.16
75	55.68 ± 0.20	74.24
90	69.92 ± 0.81	77.68
120	91.85 ± 0.83	76.54
180	136.37 ± 0.88	75.76

3.3.2. Release studies

It is widely acknowledged that *S. aureus* can secrete a large number of proteases and toxins that display protease like activity, some of which are implicated in the virulence of the pathogen (Pietrocola *et al.*, 2017; Tam and Torres, 2018; Cassat *et al.*, 2013;

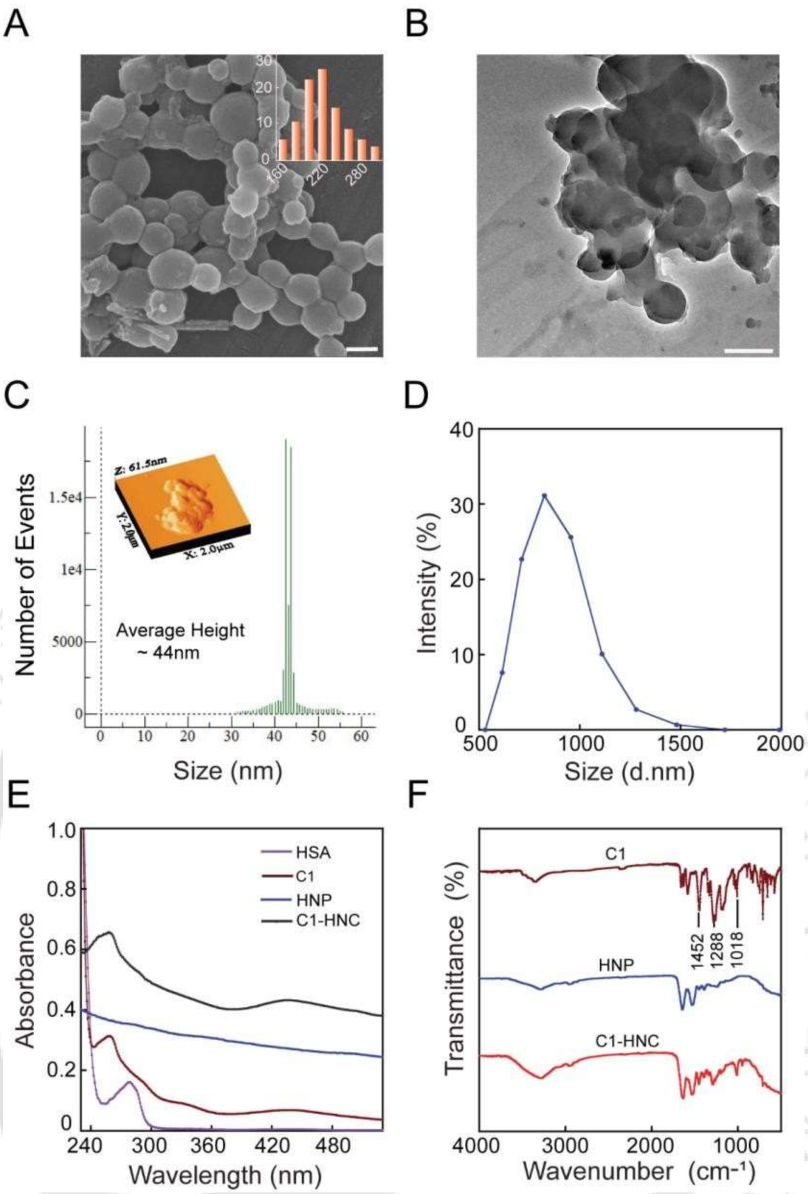

Figure 3.4. (A) FESEM image of C1-loaded HSA nanocarrier (C1-HNC). Inset indicates particle size distribution of C1-HNC estimated by using ImageJ software. (B) FETEM image of C1-HNC. The scale bar for the images in (A) and (B) is 200 nm. (C) AFM-based analysis of the height profile for C1-HNC. Inset indicates 3D topography AFM image of C1-HNC.
(D) DLS-based size distribution plot of C1-HNC. (E) UV-visible spectra of C1, HSA protein, HNP and C1-HNC. (F) FTIR spectra of C1, HNP and C1-HNC.

Ahmad-Mansour *et al.*, 2021; Otto, 2014). The presence of protease in the cell-free supernatant (CFS) of the MRSA strain *S. aureus* MRSA 100 was confirmed based on the presence of a large clearance zone produced on a milk agar plate (Figure 3.5A). It was thus envisioned that the CFS of the tested MRSA strain exhibiting proteolytic activity may facilitate degradation of the proteinaceous nanocarrier C1-HNC, which may result in enhanced release of C1. This premise of a protease- triggered release was corroborated in the release studies, which revealed that the magnitude of C1 release

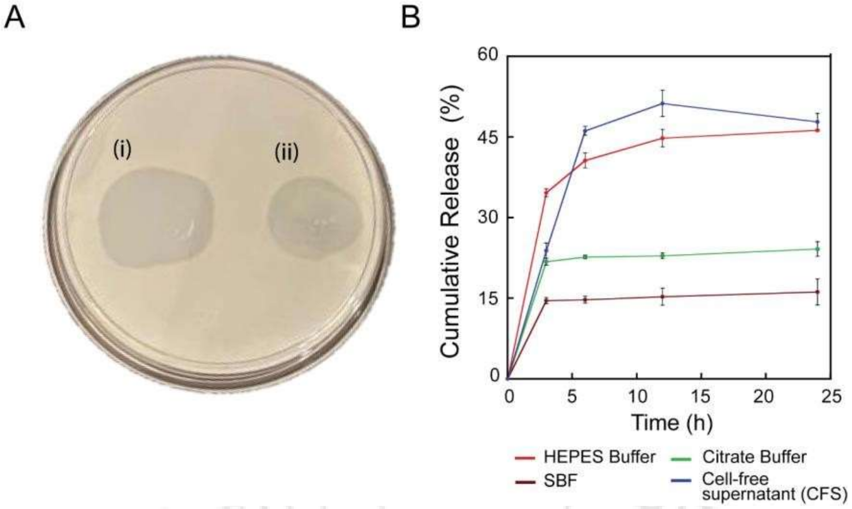

Figure 3.5. (A) Detection of proteolytic activity of (i) proteinase K (5.0 Unit) and (ii) cell-free supernatant (CFS) of *S. aureus* MRSA 100 strain on milk agar plate. (B) Cumulative release of C1 from C1-HNC incubated in simulated body fluid (SBF), citrate buffer, HEPES buffer and cell-free supernatant (CFS) obtained from *S. aureus* MRSA 100 strain.

from the nanocarrier was highest in presence of the CFS of the MRSA strain (Figure 3.5B). Following 12 h of incubation, the release of C1 from the nanocarrier in presence of MRSA CFS was ~51%, which was superior than the corresponding release of C1 in SBF (~16%), citrate buffer (~24%) and HEPES buffer (~46%) (Figure 3.5B). It may also be mentioned here that the developed nanocarrier enabled sustained release of the payload in presence of HEPES buffer and CFS of MRSA, which bears potential therapeutic implications (Figure 3.5B).

3.3.3. MNase inhibition by C1-loaded nanocarrier

Based on the results emerging from the release studies, it was conceived that the ligand C1 released as an eluate from the nanocarrier is likely to inhibit MNase, resulting in the retention of high fluorescence in Hoechst dye-stained CT-DNA as depicted in the schematic of the MNase assay shown in Figure 3.6A. Control experiments conducted in the absence of released C1 revealed a systematic decrease in the fluorescence emission intensity of CT-DNA-bound Hoechst dye at 450 nm (Figure 3.6B), which indicated facile cleavage of CT-DNA by MNase. In presence of the eluate obtained from C1-HNC having varying concentrations of released C1, the reduction in the emission intensity of DNA-bound Hoechst dye could be correlated with the concentration of C1 present in the eluate (Figure 3.6B). This suggested that following release from the nanocarrier, the activity of C1 eluate was still retained, which resulted in inhibition of

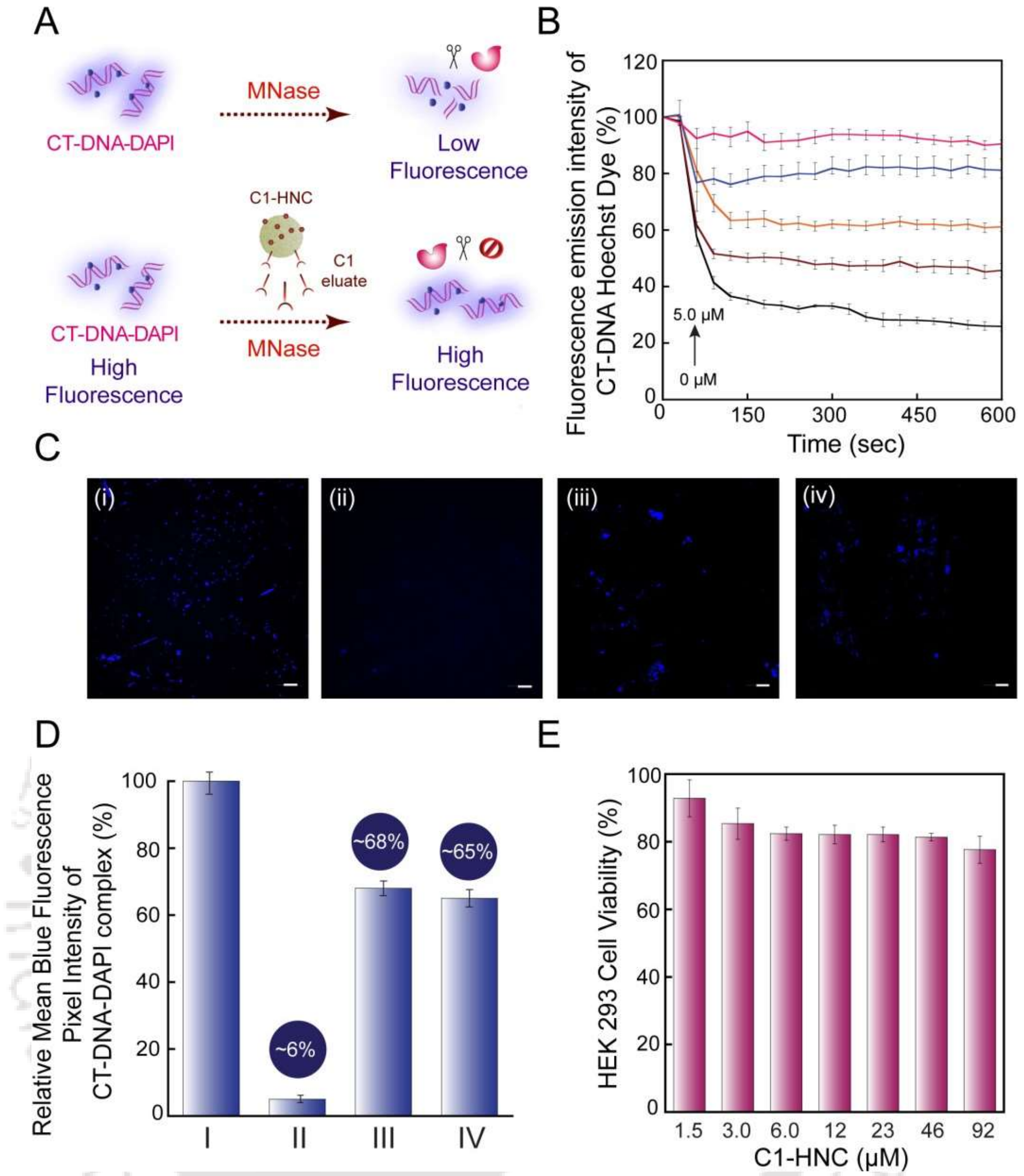

Figure 3.6. (A) Cartoon indicating inhibition of MNase by eluate from C1-HNC. (B) Change in the fluorescence emission intensity of CT-DNA-Hoechst dye complex in presence of MNase (lowest trace) and eluates from C1-HNC in separate sets. The concentration of C1 in eluates was 0.1, 0.4, 1.0 and 5.0 µM. (C) Fluorescence microscopic images of (i) DAPI stained CT-DNA. (ii) DAPI stained CT-DNA in presence of MNase. (iii) DAPI stained CT-DNA in presence of MNase and C1 (5.0 µM).; (iv) DAPI stained CT-DNA in presence of MNase and eluate from C1-HNC (loaded with 45 µM C1). (D) Relative mean pixel intensity of CT-DNA-DAPI dye complex (%) for the images shown in (C). I-IV correspond to panels i-iv in (C). (E) MTT assay-based assessment of the cytotoxic effect of C1-HNC against HEK 293 cells. Data points acquired from six independent experimental samples were considered to determine mean ± standard deviation.

MNase activity in the fluorescence-based assay. The retention of MNase inhibition activity in C1 eluates augers well for its future therapeutic applications. The concentration-dependent inhibition of MNase activity by C1-containing eluates was

Table 3.2. Rate constant for decrease in fluorescence emission intensity of CT-DNA bound Hoechst dye in presence of varying concentrations of C1 eluate obtained from C1-HNC.

Concentration of C1 in eluate (μM)	**Rate Constant (s^{-1})**
0	0.72
0.1	0.60
0.4	0.35
1.0	0.23
5.0	0.06

also evidenced in the decrease in rate constant determined from the slope of the plot representing decrease in the emission intensity of DNA-bound Hoechst dye (Table 3.2).

Inhibition of MNase by C1 as well as the eluate obtained from C1-HNC was also verified by fluorescence microscopy. In the absence of C1, a high fluorescence associated with DAPI-stained CT-DNA was observed (Figure 3.6C, panel i). Upon treatment with MNase, the intensity of fluorescence emanating from DAPI-stained CT- DNA scaffold was quite weak (Figure 3.6C, panel ii), which indicated digestion of the CT-DNA scaffold by MNase. Interestingly, in presence of either C1 or eluate of C1 obtained from C1-HNC, a high fluorescence associated with DAPI-stained CT-DNA was again observed (Figure 3.6C, panel iii-iv), which suggested that MNase was effectively inhibited by C1 alone or C1 eluate and the integrity of the DNA scaffold was conserved. As a measure of DNA digestion by MNase, the relative mean pixel intensity of blue fluorescence (DAPI-labelled CT-DNA) was also estimated for the representative images acquired in fluorescence microscope analysis. In presence of MNase, the relative mean intensity of blue fluorescence emission was only ~6.0 % compared to the control sample (Figure 3.6D), clearly indicating large scale digestion of CT-DNA by MNase. However, in presence of either C1 or C1 eluates, the relative mean intensity of blue fluorescence emission was ~68 % and ~65 %, respectively (Figure 3.6D), which reiterated that the ligand either present alone or as an eluate of the nanocarrier could effectively hinder DNA digestion by MNase. Collectively, the solution-based assays and fluorescence microscope analysis highlighted the ability of the developed payload nanocarrier to inhibit MNase, which augers well for future therapeutic prospect of the nanocarrier.

3.3.4. Cytotoxic potential of C1-HNC

Interestingly, C1-HNC was nontoxic to HEK 293 cells till a concentration of 46 µM of C1 (Figure 3.6E). This observation is significant, since in an earlier experiment it was observed that C1 was non-toxic to cultured HEK 293 cells till a concentration of only 12.5 µM (Figure 2.9B in Chapter 2). Hence, the therapeutic dividend of developing a payload nanocarrier was evident, since the slow release of C1 from the nanocarrier led to a decrease in the high local concentration of the ligand in the vicinity of HEK 293 cells. Moreover, C1-HNC loaded with 46 µM of C1 holds significant therapeutic implications as it can not only ensure effective inhibition of MNase (IC_{50} value of C1 against MNase is ~323 nM) but is also likely to remain biocompatible.

3.4. Significant Findings

The essential findings of the present study are as follows:

1. A potentially therapeutic anthraquinone ligand C1-loaded HSA nanocarrier (C1-HNC) was developed. C1-HNC was spherical in shape with an average particle size 220 nm. Loading of C1 in the nanocarrier was dose-dependent, with a highest loading of ~136 µM achieved at a loading concentration of180 µM C1, wherein the encapsulation efficiency was ~ 75%.
2. C1-HNC nanocarrier supported sustained release of C1 in physiologically relevant buffers.
3. Interestingly, release of C1 from the nanocarrier incubated in the cell-free supernatant of a clinical MRSA strain exhibiting proteolytic activity was highest (~51%) as compared to the release observed in HEPES buffer (~46%), simulated body fluid (SBF) (~16%) and citrate buffer (~24%). This suggested a protease-triggered release of C1 from the nanocarrier.
4. The developed nanocarrier not only supported sustained release of the ligand but could also retain the activity of the payload C1 as evidenced in the effective MNase inhibition rendered by C1 eluates.
5. C1-HNC was nontoxic to HEK 293 cells till a concentration of 46 µM of C1. This indicated the therapeutic merit of the payload nanocarrier since the slow release of C1 from the nanocarrier could effectively reduce the local concentration of the ligand in the vicinity of HEK 293 cells. The therapeutic index of the developed nanocarrier was also high as the payload (46 µM of C1)

can not only render effective inhibition of MNase (IC_{50} value of C1 against MNase is ~323 nM) but was also biocompatible.

The ability of the payload nanocarrier C1-HNC to inhibit MNase in conjunction with the non-competitive nature of MNase inhibition rendered by C1 offers interesting therapeutic prospect. It would be worthwhile to harness the leads of the current study and conduct more rigorous *in vivo* experiments in future to ascertain the potential of the developed payload nanocarrier in alleviation of MRSA infections. In continuation of the endeavor to develop rationally designed synthetic small molecules and exploring their prospect as staphylococcal nuclease inhibitors, the following chapter presents the potential of benzimidazole-based ligands as MNase inhibitors.

Chapter 4

Benzimidazole-based Ligand for Targeting MNase and Enhancing MRSA Uptake by Macrophage-like Cells

This chapter illustrates the potential of benzimidazole-based synthetic ligands as MNase inhibitors. The chapter also demonstrates the ability of the most potent ligand C2 in preventing MNase-mediated CT-DNA digestion, which led to enhanced uptake of CT-DNA entrapped MRSA cells by activated THP-1 cells.

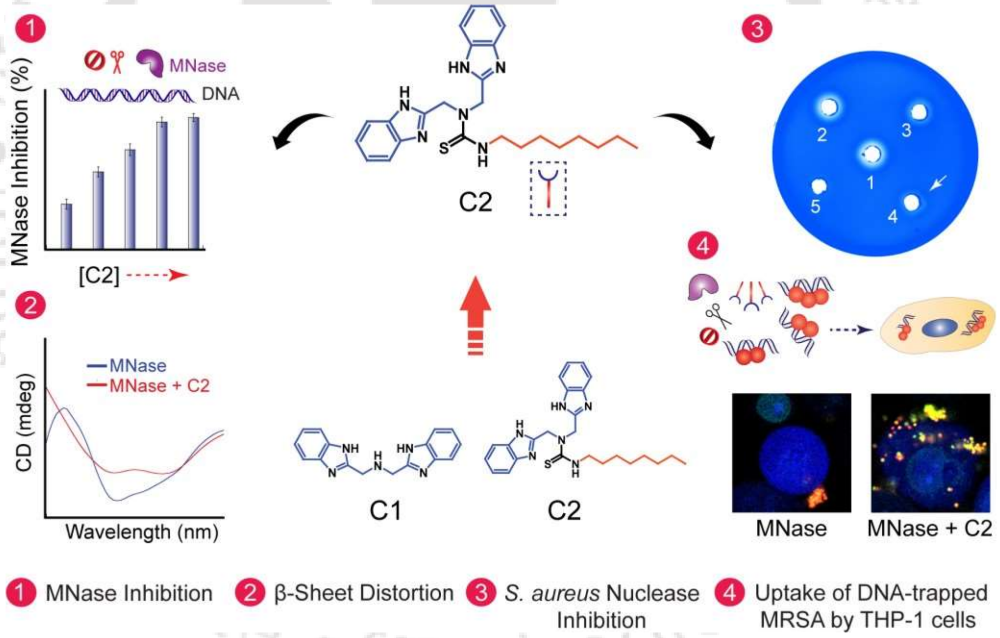

ABSTRACT

This chapter describes the potential of benzimidazole-based synthetic ligands (C1-C2) as MNase inhibitors. A fluorescence-based nuclease assay indicated a dose-dependent increase in MNase inhibition in the presence of the ligands, with ligand C2 rendering a higher degree of inhibition than C1. To this end, MNase inhibition rendered by C1 and C2 was observed to be ~55% and ~72% at the highest ligand concentration of 10 µM. Estimation of the enzyme kinetic parameters from a standard Lineweaver-Burk (L-B) plot revealed that in presence of an increasing concentration of C2, the V_{max} value for MNase-catalyzed reaction was reduced, although the K_m value for MNase was virtually constant. This observation indicated a non-competitive mode of inhibition. There was also a systematic decrease in MNase turnover number (K_{cat}) and catalytic efficiency ($Kcat/Km$) in the presence of an increasing concentration of C2. The kinetics data also revealed that the IC_{50} value of C2 for MNase was 1122 nM, while the inhibitor constant (K_i) for C2 was ~750 nM, based on a Dixon plot. On the basis of solution-based studies, the Stern-Volmer constant and binding constant for C2 calculated from the titration spectrum of MNase was 2.0×10^{13} $M^{-1}s^{-1}$ and 0.34 μM^{-1}, respectively and a favorable binding of C2 with MNase was also evidenced in ITC analysis ($K_a = {\sim}9.7 \times 10^4$ M^{-1}). In CD spectroscopy, a notable perturbation of the peak of MNase at 209 nm and 221 nm and a considerable change in the β-sheet content of MNase was observedin presence of C2. The solution-based studies were further substantiated by molecular docking studies, which indicated that the ligand C2 exhibited hydrophobic interaction with Asp-40, and Glu-43 and H-bond formation with Arg-35, which are known to be the active-site residues of MNase. Inhibition of MNase rendered by ligand C2 was also evident in fluorescence-microscope based analysis, wherein entrapment of MRSA in CT-DNA was restored in presence of C2. The uptake of CT-DNA entrapped MRSA cells by activated THP-1 cells was also studied in presence of MNase and C2. Interestingly, a flow cytometry-based analysis clearly revealed that uptake of MRSA cells by activated THP-1 cells could be reinstated in a dose-dependent manner in presence of C2. Confocal microscope analysis further corroborated these findings,wherein the uptake of MRSA cells by activated THP-1 cells in the presence of MNase and C2 was many folds higher compared to the uptake observed in case of activated THP-1 cells in the presence of MNase alone. Ligand C2 was essentially non-toxic to cultured HEK 293 cells and THP-1 cells and exhibited a high therapeutic index.

4.1. Introduction

The prevalence of methicillin-resistant *Staphylococcus aureus* (MRSA) is an impending global healthcare crisis as the pathogen is known to cause hospital as well as community-acquired infections (Turner *et al.*, 2019). MRSA is implicated in serious chronic as well as acute ailments and alleviation of MRSA infection is particularly challenging as the pathogen is capable of evading the host immune response and is resistant to the action of a number of therapeutic antibiotics (Turner *et al.*, 2019; Tong*et al.*, 2015; Lee *et al.*, 2018; Craft *et al.*, 2019; Mlynarczyk-Bonikowska *et al.*, 2022). In addition, elimination of *S. aureus* infections in the clinic is hampered by an innate ability of the pathogen to form resilient biofilms that can invade host tissues and colonize the surface of medical devices and implants (Otto., 2008; Archer *et al.*, 2011; Oliveira *et al.*, 2018; Arciola *et al.*, 2012; Arciola *et al.*, 2018). Evidently, there is a need of a radical approach in the discovery of effective therapeutics in order to mitigate infections caused by MRSA.

Infections by pathogenic bacteria are normally restricted by the host innate immune system machinery, such as the neutrophil extracellular trap (NET), which facilitates physical entrapment and elimination of the pathogen (Brinkmann *et al.*, 2004; Papayannopoulos, 2018). Studies have also demonstrated that neutrophils stimulate NET formation and engulf *S. aureus* cells by phagocytosis (Gunther *et al.*, 2009; Bhattacharya *et al.*, 2018). However, *S. aureus* has the ability to elude as well as deter neutrophil-mediated immune response (Guerra *et al.*, 2017; de Vor *et al.*, 2020). In particular, *S. aureus* secretes a thermonuclease enzyme, also known as micrococcal nuclease (MNase), which degrades the DNA scaffold of NETs and thereby hampers pathogen entrapment and killing by NETs and neutrophils (Berends *et al.*, 2010; Thammavongsa *et al.*, 2013; Herzog *et al.*, 2019; Bhattacharya *et al.*, 2020). MNase also plays a critical role in staphylococcal infections, regulation of biofilm formation, promoting biofilm growth on implants as well as producing nucleotides from digested DNA, which may initiate apoptosis and eliminate macrophages (Thammavongsa *et al.*, 2013; Herzog *et al.*, 2019; Kiedrowski *et al.*, 2011; Moormeier *et al.*, 2014; Forson *et al.*, 2022). Based on its germane role in promoting immune evasion and establish infection, MNase can thus be considered as a key virulence factor and a viable therapeutic target.

Owing to the limited scope of antibiotic-mediated therapy against MRSA (Turner *et al.*, 2019; Craft *et al.*, 2019; Mlynarczyk-Bonikowska *et al.*, 2022), development of a therapeutic strategy, which targets a virulence factor such as MNase is a viable option to disarm MRSA and facilitate its elimination by the host innate immune system. In this regard it has been demonstrated that the combined use of clindamycin and immunoglobulin can hinder nuclease activity and facilitate staphylococcal clearance by neutrophils (Schilcher *et al.*, 2014). It is widely recognized that entrapment of staphylococci in the DNA scaffold is a critical requirement for subsequent elimination by NETs and the host innate immune system (von Kockritz-Blickwede and Winste, 2022). It is thus envisaged that use of rationally designed synthetic MNase inhibitors would likely ensure entrapment of MRSA in the DNA scaffold and thereby pave the way for higher levels of pathogen uptake by immune cells such as macrophages. In this regard, literature seems to indicate that as compared to reports on synthetic inhibitors of DNase I (Kolarevic *et al.*, 2014; Kolarevic *et al.*, 2019; Smelcerovic *et al.*, 2020; Gajic *et al.*, 2022), studies on the characterization of synthetic staphylococcal nuclease inhibitor is limited (Sahareen *et al.*, 2018). Hence, there is a potential scope to design and explore synthetic nuclease inhibitors as therapeutics to mitigate MRSA infections.

Based on this premise, benzimidazole-based synthetic ligands (C1-C2) were selected in the current study and their ability to inhibit MNase was evaluated. The investigation reports the mode of MNase inhibition rendered by the most effective ligand C2. The study also validates the potential of the synthetic MNase inhibitor C2 in anti-MRSA therapy through the use of an *in vitro* model, which mimics NET-mediated entrapment and uptake of MRSA by macrophage-like cells.

4.2. Materials and Methods

4.2.1. Materials

Calf thymus DNA (CT-DNA) was procured from Sisco Research Laboratories Pvt. Ltd., India. Micrococcal nuclease (MNase), Hoechst 33258 dye, 5 (and 6)- carboxyfluorescein diacetate succinimidyl ester (cFDA-SE), 4′, 6-diamidino-2- phenylindole (DAPI), 5-carboxy-tetramethylrhodamine N-succinimidyl ester (TAMRA-SE), phorbol 12-myristate-13-acetate (PMA), Dulbecco’s Modified Eagle’s Medium (DMEM), Trypsin-EDTA were procured from Sigma-Aldrich (USA).

Brain Heart Infusion (BHI) broth, Toluidine blue-DNA agar and RPMI-1640 were procured from HiMedia, Mumbai, India. Dimethyl sulfoxide (DMSO) was obtained from Merck. CellTracker Blue CMAC Dye and Picogreen were procured from Invitrogen.

4.2.2. Bacterial strain and growth conditions

Staphylococcus aureus MRSA 100 was used in the current study. The target strain was propagated in BHI broth at 37 °C and 180 rpm for 12 h as reported in an earlier study (Dey *et al*., 2018).

4.2.3. Synthetic ligands

The general structure of the benzimidazole-based ligands C1 and C2 is indicated in Figure 4.1. Synthesis and characterization of C1 has been reported in an earlier study (Borah *et al*., 2019). Synthesis and characterization of ligand C2 is described in the Appendix section. Stock solutions for each ligand (10 mM) were prepared in DMSO and the required working concentration of the ligands for each experiment was prepared accordingly from the stocks.

4.2.4 Screening of ligands as MNase inhibitors

To determine the potential of the benzimidazole-based ligands as MNase inhibitors, a solution-based nuclease assay was performed by following a standard method (Sahareen *et al*., 2018). The assays were performed in multiple sets in Tris-$CaCl_2$ buffer. Initially, 1.0 µg of CT-DNA was incubated with Hoechst dye (1.0 µg mL^{-1}) for 30 min in the dark in separate sets. In another set, the enzyme solution (2.0 units of MNase) was incubated separately with varying concentrations of the ligands C1 and C2 (0.25 µM, 0.5 µM, 1.0 µM, 5.0 µM and 10 µM) for 30 min at 37 ºC and 180 rpm. Following incubation, the enzyme-ligand complex was added to the CT-DNA-Hoechst dye complex and the samples were incubated for another 30 min in the dark. Subsequently, the fluorescence emission spectra of the samples were recorded at an excitation wavelength of 350 nm and an emission wavelength of 450 nm at 30 sec time intervals till 600 sec. In a separate set of experiments, CT-DNA-Hoechst dye complex samples (having 0.5 µg mL^{-1} and 1.0 µg mL^{-1} CT-DNA) were incubated separately with C2 (0.5 µM and 1.0 µM) for 30 min. Subsequently, MNase solution (2.0 units) was added to these samples and their fluorescence spectra was measured over a period of

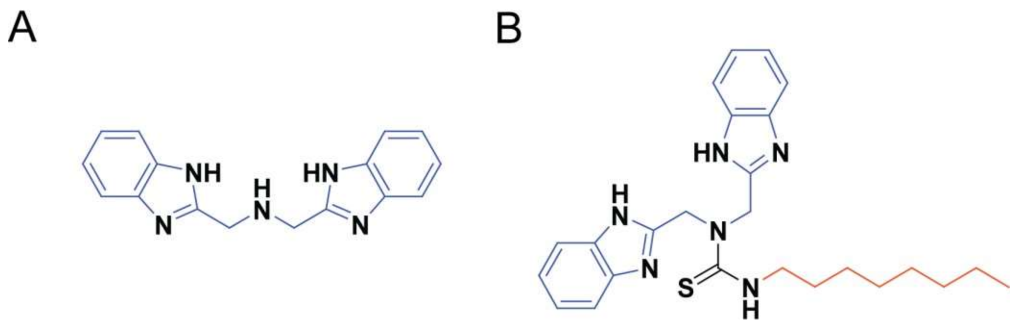

Figure 4.1. Structure of the benzimidazole-based ligands used in the present investigation. (A) C1 and (B) C2.

600 sec as mentioned previously. In parallel sets, the fluorescence emission spectra were also recorded for control samples wherein MNase was added to the CT-DNA-Hoechst dye complex in the absence of the ligands. The emission recorded for the CT- DNA-Hoechst dye complex at 450 nm was considered as a measure of nuclease activity and considered as 100% activity for samples devoid of the ligands. In another set of experiment, MNase (1.4 µM prepared in Tris-$CaCl_2$ buffer) was incubated with 5.0 µM C2 for 30 min at room temperature. Subsequently, the MNase-C2 complex was subjected to dialysis (12,000 MWCO) against deionized water overnight and MNase activity of the dialyzed sample was also estimated by the fluorescence-based assay described earlier. For all the samples, MNase activity was expressed relative to the control sample (devoid of ligand C2). All the experiments were performed in three independent sets and every set consisted of three replicates.

4.2.5. Nuclease inhibition assay based on enzyme kinetics

The effect of C2 on MNase enzyme kinetics was determined by conducting an MNase assay in presence of the ligand. All the experiments were carried out in Tris-$CaCl_2$ buffer. In separate sets, varying concentrations of CT-DNA (350 nM -3500 nM) were incubated with Hoechst dye (1.0 µg mL^{-1}) for 30 minutes at 37 ºC and 180 rpm. Subsequently, MNase solution (2.0 U mL^{-1}) pre-incubated with varying concentrations of C2 (0.25 µM - 5.0 µM) at 37 ºC and 180 rpm for 30 min was added to the CT-DNA-Hoechst dye complex samples and the fluorescence emission intensity of the samples at 450 nm were recorded at 30 sec time intervals till 600 sec at an excitation wavelength of 350 nm. In parallel sets, the fluorescence emission was also recorded for control samples wherein MNase enzyme alone was added to CT-DNA-Hoechst dye complex in the absence of C2. A velocity versus substrate concentration plot similar to

Enzyme-substrate kinetics plot (Michaelis-Menton plot), a double-reciprocal plot (analogous to Lineweaver-Burk plot) and a Dixon plot were constructed and used to estimate the kinetic parameters such as V_{max}, K_m, K_{cat} and K_i (Nelson and Cox, 2013; Segel, 2010). All the experiments were performed in three independent sets and every set consistedof three replicates.

4.2.6. Inhibition of secreted Nuclease of MRSA by C2

Detection of the secreted nuclease in the cell-free supernatant (CFS) of *S. aureus* MRSA 100 strain and its inhibition by C2 was ascertained by a toluidine blue (TB)- DNA agar plate assay as described in section 2.2.8. of Chapter 2. In the TB-DNA agar plates, the following samples were added in separate wells: (1) CFS and 2.0 µM C2, (2) CFS and 30 µM C2, (3) CFS and 100 µM C2, (4) 100 µM C2 and (5) CFS of *S. aureus* MRSA 100 strain.

4.2.7. Bactericidal activity of C2

S. aureus MRSA 100 cells were grown overnight at 37 ºC and 180 rpm in BHI media containing various concentrations of C2 (50 µM - 600 µM) in separate sets. Growth of MRSA cells (%) relative to the untreated control cells was assessed by measuring absorbance at 600 nm in a microtitre plate reader (Infinite M200, TECAN, Switzerland). The experiments were performed in three independent sets and every set consisted of three replicates.

4.2.8. Interaction of C2 with MNase

The interaction of C2 with MNase was ascertained by solution-based fluorescence spectroscopy and the binding constant was calculated. To this end, a solution of MNase (0.27 µM in 50 mM Tris-HCl, pH 7.5 supplemented with 10 mM $CaCl_2$) was titrated with varying concentrations of C2 (0 µM - 5.0 µM), and the fluorescence emission spectra of the samples were recorded in scan mode from 310 nm - 530 nm in a spectrofluorimeter (Fluoromax-4, Horiba) at an excitation wavelength of 295 nm with a slit width of 5 nm at 298 K. All the experiments were performed in multiple independent sets and every set consisted of three replicates.

To ascertain the binding of C2 with MNase, isothermal titration calorimetry (ITC) was conducted. The measurement was performed at 25 ºC (MicroCal ITC200 device, Malvern Panalytical). The samples were degassed under vacuum to prevent the formation of air bubbles. For the ITC experiment, a 2.0 µM MNase solution was prepared in Tris-$CaCl_2$ buffer and loaded onto the cell and titrated against 80 µM of C2. The output data encompassing the integrated heat effects, after correction for heats of dilution was analyzed by nonlinear regression (MicroCal origin).

The effect of C2 on the secondary structure of MNase was determined by circular dichroism spectroscopy. MNase (1.4 µM) prepared in Tris-$CaCl_2$ buffer was titrated with varying concentrations of C2 (0 µM - 6.0 µM) in separate sets, and the CD spectra of the samples were recorded in a spectropolarimeter (Jasco, J-815). The scan range was from 190 nm to 240 nm. A standard quartz cuvette of 2 mm path length was used and each spectrum was acquired from an average of six runs at a fixed temperature of 298 K. The spectra were expressed in terms of milli degree (mdeg). In a separate set, the effect of C2 (1.0 µM and 5.0 µM) on HSA protein (40 µg mL^{-1}) was also evaluated by recording the CD spectra by following the conditions outlined before. In another set of experiment, MNase (1.4 µM prepared in Tris-$CaCl_2$ buffer) was incubated with 5.0 µM C2 for 30 min at room temperature. Subsequently, the MNase-C2 complex was subjected to dialysis (12,000 MWCO) against deionized water overnight and the CD spectra of the sample was recorded as mentioned before. Interaction of C2 with MNase was further studied by molecular docking as described in the Appendix section.

4.2.9. Interaction of C2 with CT-DNA

The working solution of CT-DNA and ligands were prepared in Tris-NaCl buffer (5.0 mM Tris, 50 mM NaCl, pH 7.2). A fixed concentration of C2 was taken in separate sets(20.0 µM each) and varying concentrations of CT-DNA solution (0.5 µM - 10 µM) prepared in 5.0 mM Tris, 50 mM NaCl (pH 7.2) was added to each set of C2 solution and incubated for 30 min. The absorption spectra of the samples were recorded in a UV-visible spectrophotometer (Carry 60) in scanning mode ranging from 200 nm - 600 nm and the binding constant of C2 for CT-DNA was estimated (Ramachandran *et al.*, 2012; Wolfe *et al.*, 1987). All the experiments were performed in three independent sets and every set consisted of three replicates.

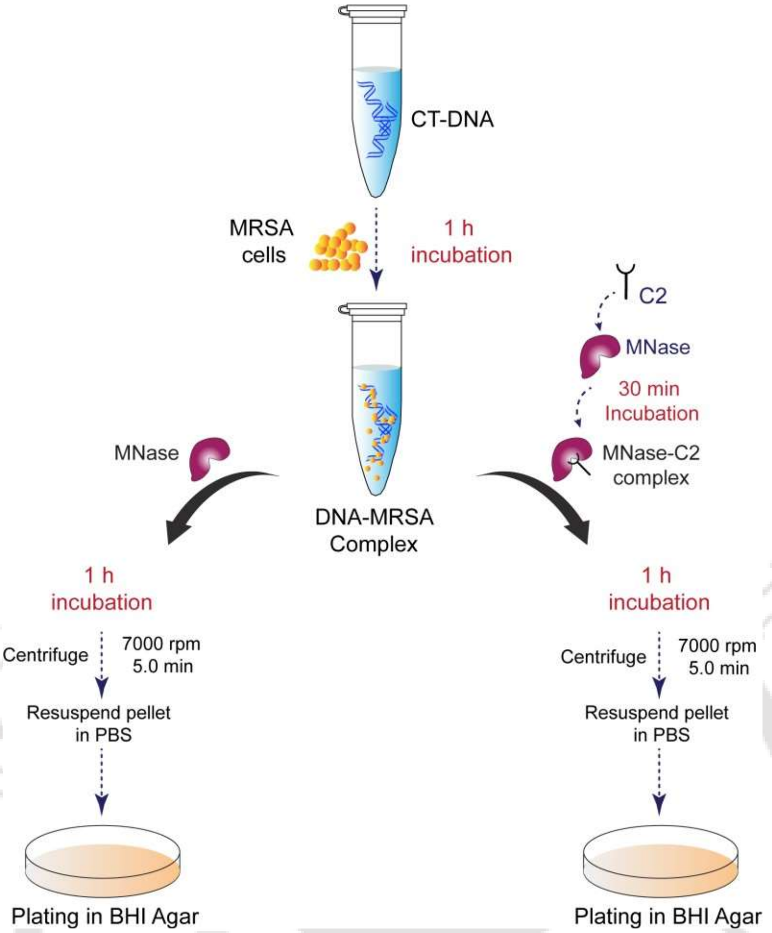

Figure 4.2. Schematic representation of the protocol used for estimation of entrapment of viable MRSA cells in CT-DNA.

4.2.10. Entrapment of MRSA cells in CT-DNA

Prior to the estimation of entrapment of MRSA cells in DNA, the effect of MRSA cells on MNase activity was ascertained. Initially, *S. aureus* MRSA 100 was grown overnight in BHI media at 37 ºC. CT-DNA (10 µg mL^{-1}) was labelled with picogreen (0.1 pg mL^{-1}) by incubating for 30 minutes in dark 37 ºC. In a separate set, MNase solution (2.0 U mL^{-1}) was pre-incubated with C2 (5.0 µM) at 37 ºC and 180 rpm to form an MNase-C2 complex. Picogreen labeled CT-DNA was incubated with MRSA cells (10^{4} CFU mL^{-1}) for 1 h to form a DNA-MRSA complex. This DNA-MRSA complex was incubated with MNase (2.0 U mL^{-1}) and C2-MNase complex for another 1 h in separate sets. Following incubation, fluorescence emission spectra for each sample was recorded at an excitation wavelength of 485 nm. The emission recorded for the CT-DNA-picogreen dye complex at 528 nm was considered as control (100%). Fluorescence intensity for other samples at same excitation and emission was measured relative to the control sample.

For estimation of viable MRSA cells trapped in CT-DNA, DNA-MRSA complex samples were incubated with MNase and MNase-C2 complex for 1 h at 37 ºC in separate sets as mentioned previously. Following incubation, the DNA trapped cells were separated by centrifugation at 7000 rpm for 5 min at 4 °C. The pellet was resuspended in fresh sterile PBS and the viable MRSA cells trapped in CT-DNA were estimated by plating the above samples in BHI-agar plates. A schematic representation of the protocol for estimating the magnitude of viable MRSA cells trapped in CT-DNA is shown in Figure 4.2. Viable MRSA cells trapped in CT-DNA alone were considered as control (100 %) and the relative entrapment of viable MRSA cells in CT-DNA was measured for other samples.

Further validation of the entrapment of MRSA cells in CT-DNA was accomplished by fluorescence microscope analysis. CT-DNA (500 µg mL^{-1}) was stained with DAPI (20 µM) by incubating in dark for 1 h. MNase solution (2.0 U mL^{-1}) was pre-incubated with C2 (5.0 µM) at 37 ºC and 180 rpm to form an MNase-C2 complex. MRSA cells were labelled with cFDA-SE by incubating in dark for 30 min. Following incubation, cFDA-SE-labelled MRSA cells (10^{4} CFU mL^{-1}) were washed with sterile PBS and incubated with DAPI stained CT-DNA for 1 h to generate DNA-MRSA complex. Subsequently, the DNA-MRSA complex was incubated with MNase and MNase-C2 complex in separate sets in dark for another 1 h. Following incubation, the samples were centrifuged at 7000 rpm for 5 min at 4 °C, and the pellet was resuspended in 100 µl of sterile PBS. On a clean glass slide, a 2.0 µL aliquot of the sample was applied and observed under a fluorescence microscope (Eclipse Ti-U, Nikon) with a filter that allowed UV light excitation and blue light excitation and the images were recorded. From representative images, the ratio of green/blue (G/B) mean pixel intensity was estimated by using ImageJ software. G/B mean pixel intensity of the DNA-MRSA complex was considered as control and the relative G/B mean pixel intensity value for the remaining samples were estimated. A schematic representation of the protocol for estimation of the entrapment of MRSA cells in CT-DNA is shown in Figure 4.3.

4.2.11. Propagation and activation of THP-1 cells

THP-1 cells were grown in 75 cm^{2} tissue culture flask in RPMI-1640 medium supplemented with non-heat-treated 10% (v/v) fetal bovine serum (FBS) at 37 °C under

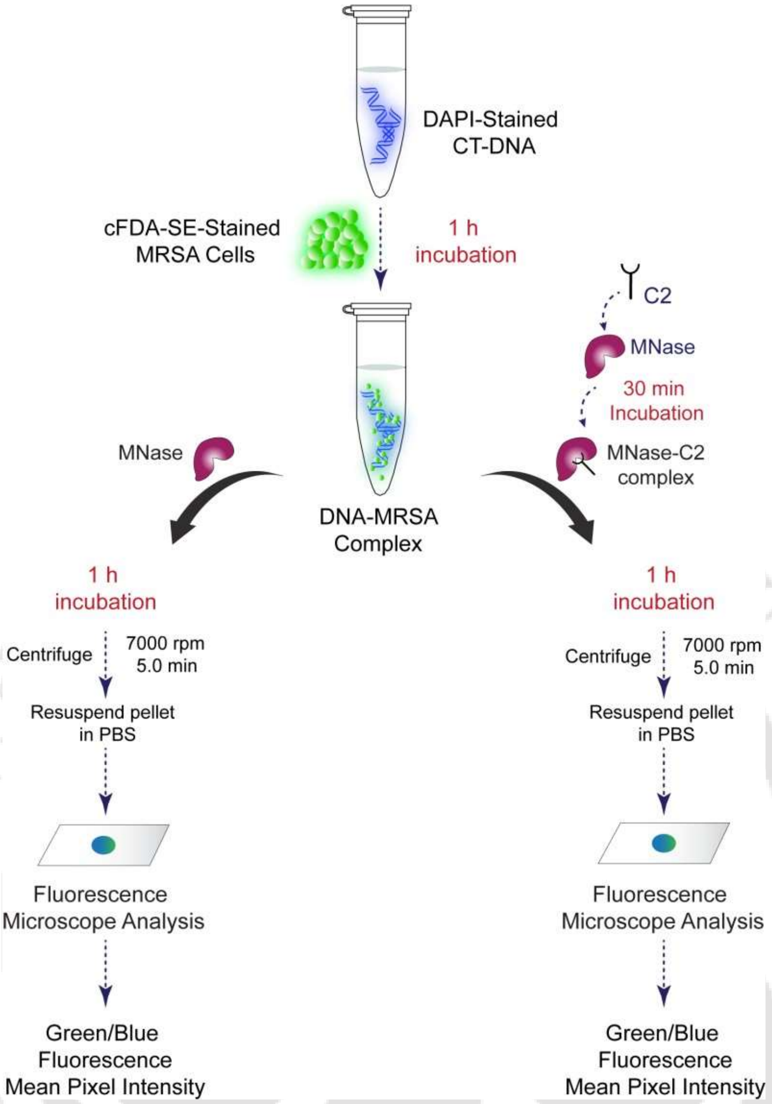

Figure 4.3. Schematic representation of the fluorescence microscopy-based protocol used for estimation of entrapment of MRSA cells in CT-DNA.

a humidified atmosphere of 5% CO_2 in an incubator. For differentiation and activation, THP-1 cells (10^6 cells) were incubated in 90 mm tissue culture plate with varying concentrations of PMA (25 nM – 100 nM) for 48 h in RPMI media at 37 °C under 5% CO_2. Following incubation, the spent media from all the wells was aspirated. The cells were washed with sterile PBS and the washings were collected. Subsequently, by using cell scraper, the cells were detached from the wells and harvested by centrifugation at 1500 rpm for 5 min at 4 °C and resuspended in fresh sterile PBS. The cells present in the washing as well as in the scrapped sample were pooled and then subjected to flow cytometry analysis (Cytoflex, Beckman Coulter Inc., CA, USA) at a low flow rate and the instrument was set to acquire 10,000 events. Forward-angle light scatter (FSC) vs. side scatter (SSC) plots were analyzed to detect PMA-activated

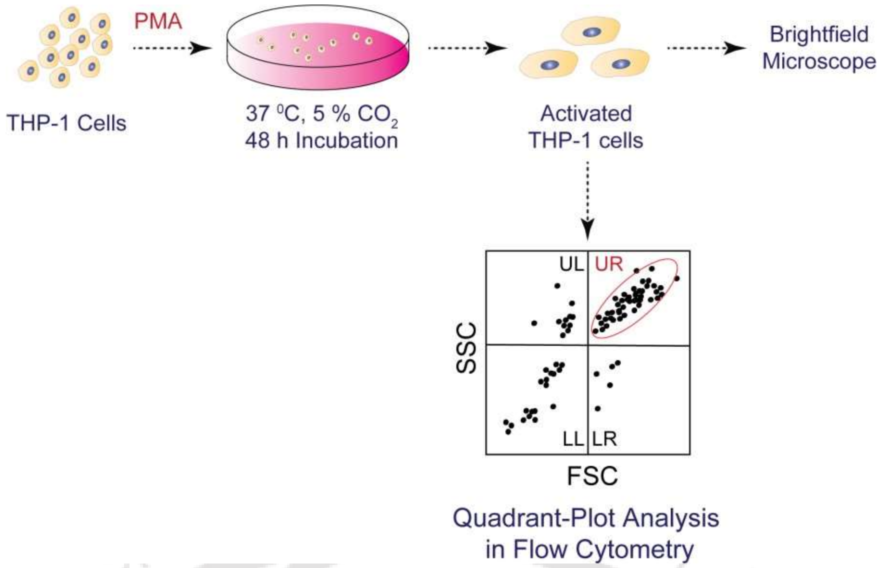

Figure 4.4. A schematic representation of the flow cytometry-based protocol to ascertain activation of THP-1 cells by PMA.

macrophage-like THP-1 cells in the right upper quadrant (Bhattacharyya and Ghosh, 2020). PMA-mediated activation of THP-1 cells were also analyzed by microscopy. Herein, in separate sets THP-1 cells were treated with PMA as mentioned earlier. Subsequently, the media was gently aspirated from the wells and the cells were washed with sterile PBS and observed under brightfield in an inverted microscope (Eclipse Ti-U, Nikon). A schematic representation of the flow cytometry-based protocol to ascertain activation of THP-1 cells by PMA is shown in Figure 4.4.

4.2.12. Uptake of MRSA cells by PMA-activated THP-1 cells

Initially, *S. aureus* MRSA 100 cells (10^8 CFU/ml) were labelled with TAMRA-SE dye (50 µM in PBS solution) by incubating for 30 min in the dark. Subsequently, TAMRA-labelled MRSA cells were washed twice with PBS to remove the residual dye. In another set, MNase solution (5.0 U mL^{-1}) was pre-incubated with varying concentrations of C2 (5.0 µM and 15 µM) in separate sets at 37 ºC and 180 rpm for 1 h to form a CT-DNA-MNase-C2 complex. Subsequently, in separate sets, TAMRA-labelled MRSA cells were incubated with CT-DNA (50 µg mL^{-1}) or MNase (5.0 U mL^{-1}) digested CT-DNA or CT-DNA-MNase-C2 complex for 1 h. Following incubation, these complexes were added to PMA-activated THP-1 cells and incubated for another 1 h at 37 °C under 5% CO_2. Following 1 h incubation, the media was aspirated from all the samples, the cells were washed twice with sterile PBS and the washings were collected. Subsequently, the adhered cells from the wells were gently detached by using a cell scraper, and the cells were separated by centrifugation at 1500 rpm for 5 min at 4 °C and resuspended in fresh sterile PBS. The cells present in the washing as well as in the scrapped sample were pooled and then subjected to flow cytometry analysis (Cytoflex, Beckman Coulter Inc., CA, USA) at a low flow rate and the instrument was set to acquire 30,000 events. FSC vs. SSC plots were analyzed to detect PMA-activated macrophage-like THP-1 cells in the upper right quadrant (Bhattacharyya and Ghosh, 2020). Uptake of TAMRA-labelled MRSA cells by activated THP-1 cells was assessed by measuring the median fluorescence intensity (MFI) in the PE1 channel (band pass filter of 610 nm/20 nm). Data acquisition was accomplished with CytExpert 2.3 and data analysis was performed with FlowJo v10.8.1. Following FlowJo analysis, the MFI observed for TMRA-labelled MRSA cells trapped in CT-DNA complex and incubated with PMA-activated THP-1 cells was considered as control and the relative percentage of MFI was ascertained for the following samples: (a) MRSA cells trapped in MNase-digested CT-DNA and incubated with PMA-activated THP-1 cells, (b) MRSA cells trapped in C2-MNase complex-digested CT-DNA and incubated with PMA-activated THP-1 cells, (c) MRSA cells trapped in C2-CT-DNA complex and incubated with PMA-activated THP-1 cells. All the experiments were performed in triplicates and the mean and standard deviation was calculated. A schematic representation of the flow cytometry-based protocol for estimation of MRSA cell uptake in activated THP-1 cells is shown in Figure 4.5.

4.2.13. Confocal microscope analysis to ascertain uptake of MRSA cells by PMA- activated THP-1 cells

For the confocal microscope analysis, CT-DNA (50 µg mL^{-1}) was labelled with picogreen (0.25 pg mL^{-1}) for 30 min and PMA-activated THP-1 cells were labelled with cell tracker CMAC Blue dye (50 nM) for 30 min. MNase solution (5.0 U mL^{-1}) was incubated with C2 (15 µM) for 1 h to form an MNase-C2 complex. In separate sets, the following samples were prepared: (a) TAMRA-labelled MRSA cells trapped in picogreen-labelled CT-DNA complex and incubated with CMAC blue labelled PMA-activated THP-1 cells for 1 h, (b) TAMRA-labelled MRSA cells trapped in MNase-digested picogreen-labelled CT-DNA complex and incubated with CMAC blue labelled PMA-activated THP-1 cells for 1 h, (c) TAMRA-labelled MRSA cells trapped

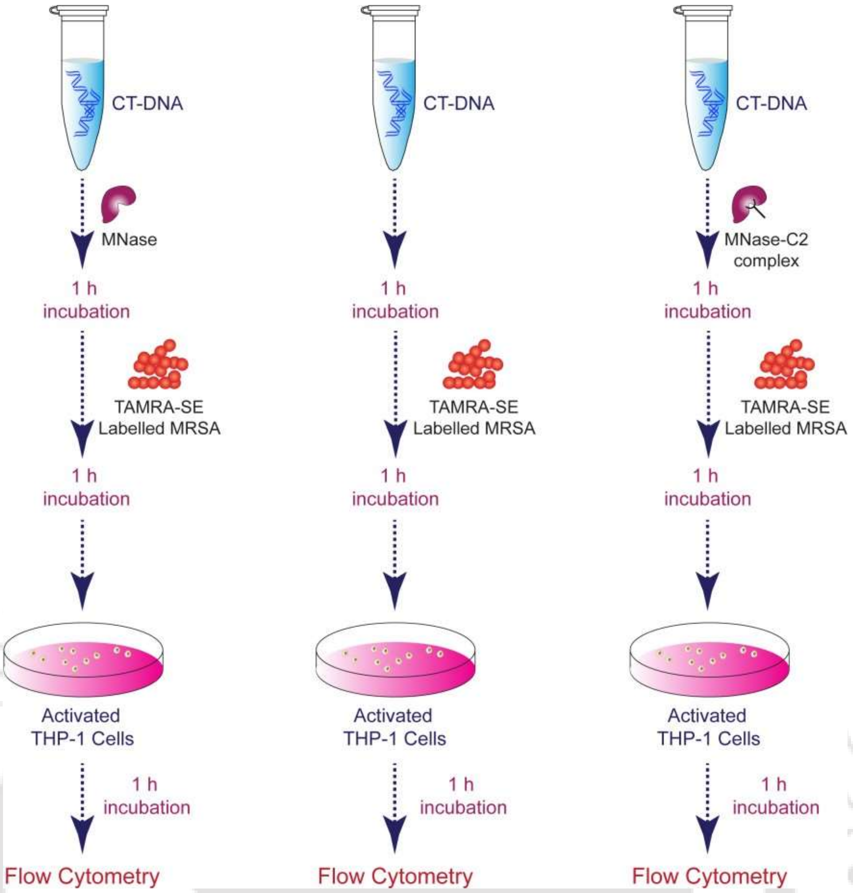

Figure 4.5. A schematic representation of the flow cytometry-based protocol to ascertain uptake of TAMRA-labelled MRSA cells by activated THP-1 cells.

in MNase-C2 complex digested picogreen-labelled CT-DNA complex and incubated with CMAC blue labelled PMA-activated THP-1 cells for 1 h. Following incubation, the media was aspirated from all the samples and the wells were washed with sterile PBS. The cells were then observed under confocal microscope (Zeiss LSM 880). Images of the cells were acquired in red (550 nm), blue (405 nm) and green (485 nm) channels. The relative uptake of MRSA cells by PMA-activated THP-1 cells in the experimental samples was ascertained by measuring the ratio of the pixel intensity observed for red fluorescence (index of MRSA cells) and blue fluorescence (index of PMA-activated THP-1 cells) using ImageJ software. The uptake of MRSA cells by PMA-activated THP-1 cells in presence of CT-DNA was considered as control and the relative uptake of MRSA cells by PMA-activated THP-1 cells in presence of either CT-DNA digested with MNase or CT-DNA digested with MNase-C2 complex was calculated.

4.2.14. Estimation of the uptake of viable MRSA cells by PMA-activated THP-1 cells by plating

Prior to the experiment, MNase solution (5.0 U mL^{-1}) was pre-incubated with C2 (15 µM) at 37 ºC and 180 rpm for 1 h to form MNase-C2 complex. MRSA cells were incubated with CT-DNA (50 µg mL^{-1}) or MNase (5.0 U mL^{-1}) digested CT-DNA or CT-DNA-MNase-C2 complex for 1 h. Following incubation, these samples were added to the PMA-activated THP-1 cells and incubated for another 1 h at 37 °C under 5% CO_2. Following 1 h incubation, the media was aspirated from all the samples, the cells were washed twice with sterile PBS. Subsequently, the adhered cells from the wells were gently detached by using a cell scraper, and the cells were separated by centrifugation at 1500 rpm for 5 min at 4 °C and resuspended in fresh sterile PBS. Uptake of MRSA cells by PMA-activated THP-1 cells was estimated by plating the above samples in BHI-agar plates. Uptake of MRSA trapped in CT-DNA alone was considered as control (100 %) and relative uptake of MRSA was measured for other samples.

4.2.15. Cytotoxic potential of C2

HEK 293 cells were grown in a 25 cm^2 tissue culture flask in Dulbecco's Modified Eagle Medium (DMEM) supplemented with 10% (v/v) fetal bovine serum (FBS) at 37 °C under a humidified atmosphere of 5% CO_2 in an incubator till the cells achieved ~80% confluency. THP-1 cells were grown in RPMI-1640 with 10% (v/v) fetal bovine serum (FBS) at 37 °C under a humidified atmosphere of 5% CO_2 in an incubator till the cells reached 6 x 10^5 cells/ml. The HEK-293 cells were then seeded onto 96-well tissue culture plates at a density of 8 x 10^3 cells per well and incubated in separate sets. After 24 h of incubation, DMEM media in the plates was replaced by varying concentrations of C2 (3.0 µM - 100 µM taken in DMEM) and again incubated for a period of 24 h. In a separate set, THP-1 cells were seeded onto 96-well tissue culture plates at a density of 1 x 10^4 cells per well in presence of 100 nM of PMA and incubated for 48 h. Following incubation, RPMI-1640 media in the plates was aspirated and varying concentrations of C2 was added (1.25 µM - 80 µM taken in RPMI-1640) and incubated for a period of 24 h in separate sets. Subsequently, the media from each well was carefully removed and fresh DMEM medium containing MTT solution was added to the HEK-293 cells in the well, and fresh RPMI-1640 medium containing MTT solution (25 µg mL^{-1} final concentration) was added to THP-1 cells in the well and incubated for 3 h at 37 °C under 5% CO_2. Subsequently, the supernatant was aspirated and the insoluble formazan product was solubilized in DMSO and its absorbance was measured in a microtiter plate reader (Infinite M200, TECAN, Switzerland) at 570 nm. The absorbance for the untreated cells was considered as 100% cell viability and the absorbance for the treated cells was compared to determine % cell viability with respect to the solvent control. All the experiments were performed in six independent sets and every set consisted of three replicates.

4.3. Results and Discussion

4.3.1. Design of synthetic ligands

The design principle of known nuclease inhibitors seems to suggest that lipophilicity and presence of H-bond donor/acceptor groups are prime features that determine the efficiency of their inhibitory activity (Kolarevic *et al*., 2014). Based on this premise, in the current study, benzimidazole-based ligands C1 and C2 were selected (Figure 4.1). Apart from the presence of a reasonable lipophilic balance as well as H-bond donor/acceptor groups in both C1 and C2, it may be mentioned that the ligand C2 bears an aliphatic chain (Figure 4.1B) and is thus more hydrophobic as compared to C1. This inherent difference between the ligands is likely to be reflected in structure-function studies and it was envisaged that an increased hydrophobicity in C2 may enhance its propensity to interact with the buried active site residues of MNase. Moreover, selection of the benzimidazole scaffold is also based on its well documented therapeutic potential as an antibacterial agent (Song and Ma, 2016; Malasala *et al*., 2021; Zha *et al*., 2021).

4.3.2. Evaluation of ligands as MNase inhibitor

In order to ascertain the efficacy of the ligands as an MNase inhibitor, a fluorescence-based nuclease assay was performed (Sahareen *et al*., 2018). In case of MNase-mediated CT-DNA digestion, a rapid decline in the fluorescence emission intensity of CT-DNA-bound Hoechst dye was observed at 450 nm (Figure 4.6A, Appendix Figure A4.5). The systematic reduction in the emission intensity of CT-DNA-Hoechst dye complex indicated that MNase could readily digest CT-DNA in solution. Notably, in presence of varying concentrations of both the ligands C1 and C2, there was only a marginal decrease in the emission intensity of DNA-bound Hoechst dye (Figure 4.6A,

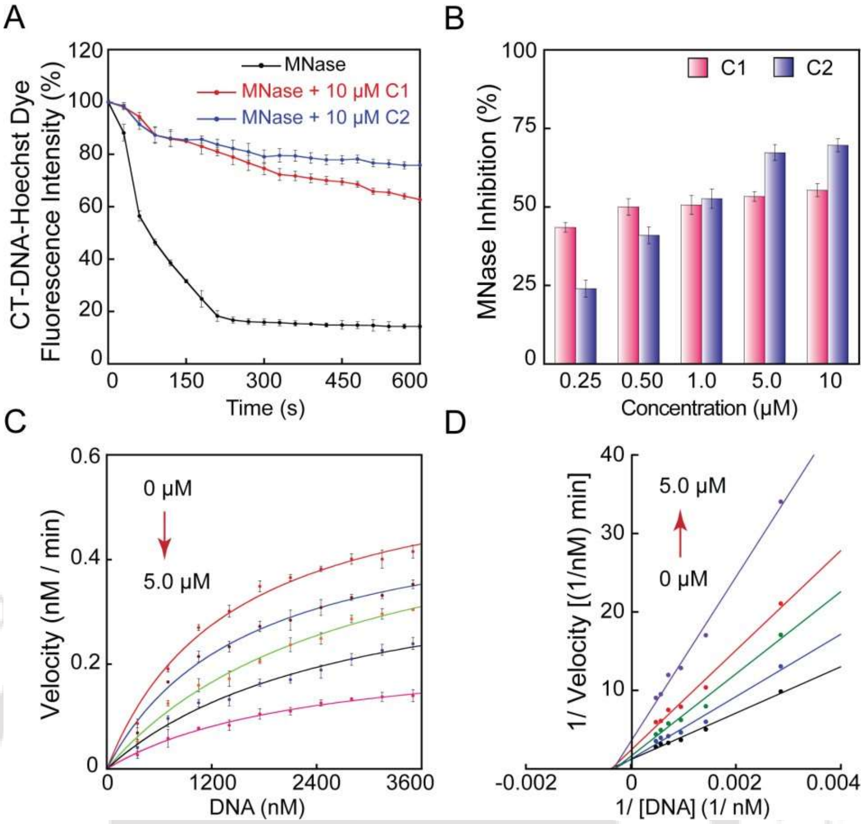

Figure 4.6. (A) Change in fluorescence emission intensity of CT-DNA Hoechst dye complex in presence of MNase and ligands C1 and C2 (10 µM each) in separate sets. (B) Effect of varying concentrations of C1 and C2 on MNase inhibition. (C) Michaelis-Menten plot for MNase inhibition in presence of varying concentrations of C2. (D) Lineweaver-Burk plot to ascertain MNase inhibition by C2.

Appendix Figure A4.5), which suggested that the ligands could inhibit MNase activity. Further, it was apparent that at higher concentrations of the ligands, the magnitude of the decrease in emission intensity of CT-DNA-bound Hoechst dye was comparatively less than that observed at lower concentrations of the ligands (Figure 4.6A, Appendix Figure A4.5). Estimation of the end-point fluorescence emission intensity in the assay clearly indicated that a dose-dependent increase in MNase inhibition was ubiquitous in presence of the ligands, with ligand C2 rendering a higher degree of inhibition as compared to C1 (Figure 4.6B, Appendix Table A4.1). To this end, it may be mentioned that MNase inhibition rendered by C1 and C2 was observed to be ~55% and ~72% at the highest ligand concentration of 10 µM (Figure 4.6B). Both the ligands C1 and C2 possess significant lipophilic balance as well as H-donor/acceptor groups and these attributes have been recognized in nuclease inhibitors (Kolarevic *et al.*, 2014). However, the presence of the aliphatic carbon chain in C2 does seem to enhance its hydrophobicity, which in turn, perhaps leads to better access of the buried active site residues of MNase, resulting in a higher degree of MNase inhibition as compared to that observed in case of ligand C1.

4.3.3. Effect of C2 on kinetics of MNase activity and inhibition of nuclease secreted by MRSA

Based on the efficient inhibition of MNase activity rendered by C2, the subsequent endeavor was to evaluate the effect of C2 on MNase enzyme kinetics. To this end, it was evident from a solution-based MNase assay that the rate of CT-DNA cleavage was systematically decreased in presence of an increasing concentration of C2 (Figure 4.6C). At the highest substrate concentration (3500 nM DNA), the velocity of MNase-mediated CT-DNA digestion was reduced by ~68% in presence of 5.0 µM C2 (Figure 4.6C). Estimation of the kinetic parameters from a standard Lineweaver-Burk (L-B) plot (Figure 4.6D) revealed that the Michaelis-Menten constant (K_m), maximum velocity of enzyme-catalyzed reaction (V_{max}) and the enzyme turnover number (K_{cat}) for MNase was ~2699 nM, ~0.926 nM min^{-1} and ~0.034 min^{-1}, respectively. From the L-B plot, it was also evident that in presence of an increasing concentration of C2, the V_{max} value for MNase-catalyzed reaction was reduced, although the K_m value for MNase was virtually constant (Figure 4.6D). This observation indicated a non-competitive mode of inhibition, wherein the ligand C2 perhaps binds to the MNase-CT-DNA complex and subsequently hampers the rate of enzyme-catalyzed reaction. A positive outcome of the non-competitive mode of inhibition rendered by C2 is that the inhibitory effect is likely to prevail even in the presence of a high concentration of the substrate. Experiments were also performed to determine whether MNase inhibition rendered by C2 was due to the ligand interacting with DNA and thereby causing substrate modification. A fluorescence-based MNase assay indicated that the reduction of fluorescence emission intensity for preformed CT-DNA-C2 complex digested with MNase was similar to the sample wherein CT-DNA alone was digested with MNase (control) (Appendix, Figure A4.6). Further, the rate constant estimated for digestion of CT-DNA alone or CT-DNA-C2 preformed complexes were also on par (Appendix, Table A4.2). Collectively, it wasapparent from these results that in solution the substrate DNA was not modified upon interaction with C2, which resulted in effective digestion of the CT-DNA-C2 complex by MNase. Hence, the inhibition of MNase observed in presence of C2 is likely a direct effect of the ligand on the enzyme.

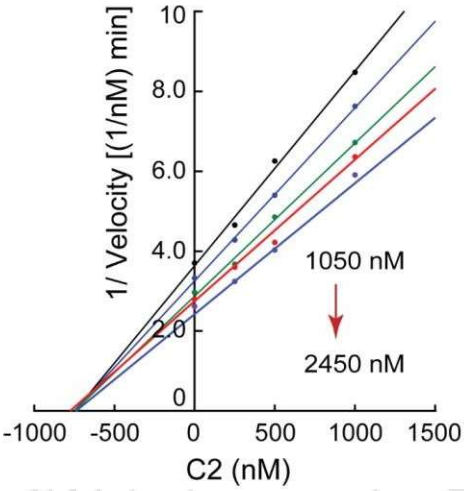

Figure 4.7. Dixon plot for MNase in the presence of varying concentrations of C2. Theconcentration of CT-DNA was varied from 1050 nM to 2450 nM in separate sets.

Table 4.1. Kinetic parameters for MNase ascertained in presence of C2.

C2 (µM)	V_{max} **(nM^{-1} min)**	K_{cat} **(min^{-1})**	K_{cat} / K_m **(min^{-1} nM^{-1})**
0	0.926	0.034	1.26×10^{-5}
0.25	0.647	0.024	9.52×10^{-6}
0.50	0.497	0.018	7.59×10^{-6}
1.0	0.340	0.013	5.43×10^{-6}
5.0	0.096	0.004	1.65×10^{-6}

There was also a systematic decrease in MNase turnover number (K_{cat}) in presence of an increasing concentration of C2 (Table 4.1), which suggested that C2 could hinder the number of catalytic cycles mediated by the enzyme. In addition, the catalytic efficiency (K_{cat}/K_m) of MNase was also decreased in presence of an increasing concentration of C2 (Table 4.1). The catalytic efficiency of an enzyme is influenced by substrate binding as well as the catalytic event. Results emanating from the enzyme kinetics experiments indicated that K_m for MNase was not altered in presence of C2 (Figure 4.6D). This suggested that C2 likely hinders the frequency of association of MNase with its substrate. The kinetics data also revealed that the IC_{50} value of C2 for MNase was 1122 nM, while the inhibitor constant (K_i) for C2 was ~750 nM based on a Dixon plot (Figure 4.7).

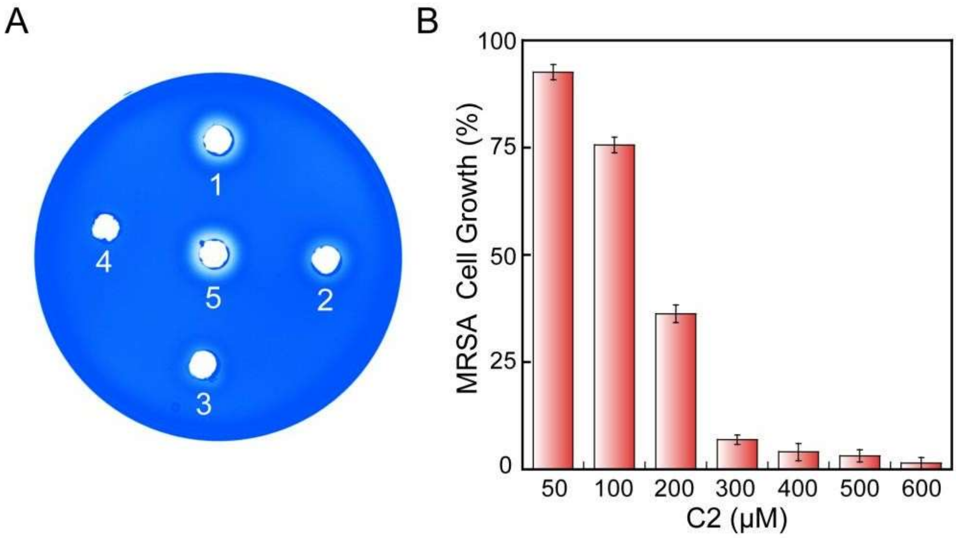

Figure 4.8. (A) Toluidine-blue DNA agar plate assay to ascertain inhibition of MNase present in the cell-free supernatant (CFS) of *S. aureus* MRSA 100 strain. (1) CFS and 2.0 µM C2. (2) CFS and 30 µM C2. (3) CFS and 100 µM C2. (4) 100 µM C2. (5) CFS of *S. aureus* MRSA 100. (B) Bactericidal activity of C2 against *S. aureus* MRSA 100 strain.

S. aureus is known to secrete a thermostable nuclease enzyme, which has a profound role in biofilm dispersal and in combating the bactericidal activity of NETs (Forson *et al*., 2022; Bhattacharya *et al*., 2020; Thammavongsa *et al*., 2013). Given the efficacy of C2 as an MNase inhibitor, it was worthwhile to probe the potential of C2 as an inhibitor of the secreted nuclease of MRSA. In this regard, a dose-dependent inhibition of nuclease present in the cell-free supernatant (CFS) of the clinical MRSA strain *S. aureus* MRSA 100 by C2 was evident in a toluidine-blue DNA agar assay (Figure 4.8A). The bactericidal activity of C2 against MRSA was also ascertained. To this end, it was observed that C2 rendered a detrimental effect on the growth of the tested MRSA strains only at concentrations in excess of 100 µM (Figure 4.8B), although it could effectively inhibit MNase at very low concentrations (IC_{50} =1122 nM).

4.3.4. Solution-based Interaction of C2 with MNase and CT-DNA

Given that the ligand C2 could effectively inhibit MNase activity, it was pertinent to ascertain the solution-based interaction of the ligand with the enzyme. To this end, a notable decrease in the intensity of tryptophan fluorescence originating from MNase was observed on recording a titration spectrum of the enzyme in presence of increasing concentrations of C2 (Figure 4.9A). The Stern-Volmer constant and binding constant for C2 calculated from the titration spectrum of MNase was 2.0×10^{13} $M^{-1}s^{-1}$ and

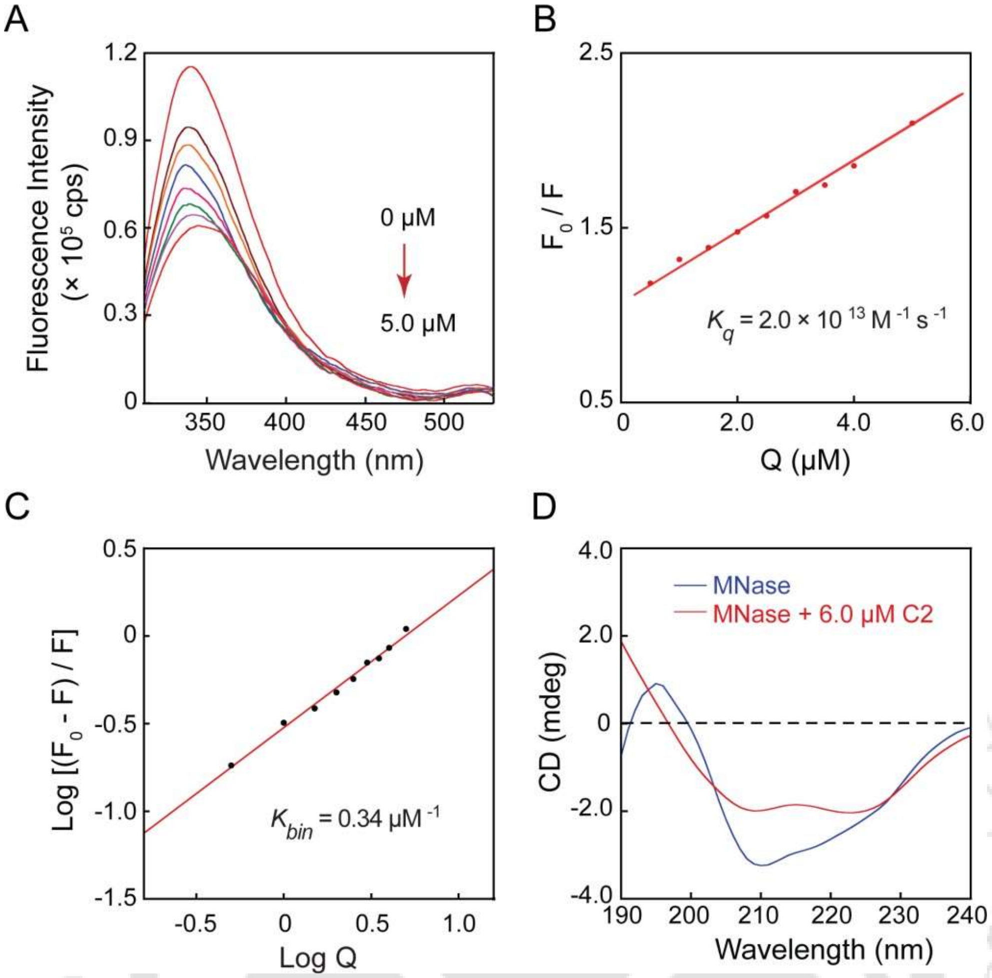

Figure 4.9. (A) Change in tryptophan fluorescence emission spectra of MNase in presence of an increasing concentration of C2. (B) Stern-Volmer plot for C2 based on the fluorescence emission spectra obtained in (A). (C) Scatchard plot for C2 based on fluorescence emission spectra obtained for MNase in presence of an increasing concentration of C2. (D) CD spectra of MNase measured in presence of C2.

0.34 μM^{-1}, respectively (Figure 4.9B-4.9C). A favorable binding of C2 with MNase was also evidenced in ITC analysis (K_a = ~9.7 × 10^4 M^{-1}) (Appendix, Figure A4.7). For comparative analysis, the binding of C2 to CT-DNA was also ascertained by absorptionspectroscopy. To this end, the absorbance band of C2 at 260 nm displayed a hyperchromic shift in the presence of an increasing concentration CT-DNA (Appendix, Figure A4.8A). The intrinsic binding constant of C2 for CT-DNA was ~1.60 nM^{-1} (Appendix, Figure A4.8B). In order to acquire a fundamental understanding on the effect of C2 on MNase, CD spectroscopy was conducted with MNase in presence of varying concentrations of C2. To this end, a notable perturbation of the peak of MNase at 209 nm and 221 nm was noted in presence of C2 (Figure 4.9D, Appendix, Figure A4.9) and a heightened distortion of the secondary structure of MNase was manifested

Table 4.2. Secondary structure analysis of MNase following interaction with C2.

Sample	**Secondary Structure Content in MNase**			
	α – Helix (%)	**β – Sheet (%)**	**Turn/Loop (%)**	**Random Coil (%)**
MNase	19	22.4	24.6	34
MNase + C2 (0.5 µM)	22.1	28.6	20.6	28.7
MNase + C2 (1.0 µM)	28.4	19	18.8	33.7
MNase + C2 (3.0 µM)	25.9	14.8	21	38.3
MNase + C2 (6.0 µM)	28.7	0	25.3	46

in presence of an increasing concentration of C2 (Table 4.2). The notable change in the β-sheet content of MNase observed in presence of C2 (Table 4.2) augers well and bears functional implications, since the active site of MNase is located in a β-sheet rich region of the enzyme (Cotton *et al*., 1979). In order to determine whether C2 was selective in distorting the secondary structure of MNase or a non-selective protein unfolder, CD spectroscopy of human serum albumin (HSA) was also pursued in presence of C2. The concentration of C2 used in these experiments was 1.0 µM and 5.0 µM, which was adequate to render inhibition of MNase activity as observed in earlier studies (Figure 4.6C). CD spectroscopy indicated that there was no significant change in the characteristic absorbance peaks as well as the secondary structure of HSA upon interaction with C2 (Appendix, Figure A4.10, Table A4.3). These results indicated that the ligand C2 was perhaps selective in its interaction with MNase and was not a promiscuous protein unfolder, which augers well in future therapeutic applications. Further, CD spectroscopy of the dialyzed MNase-C2 preformed complex having a high concentration of C2 (5.0 µM) indicated that the secondary structure content of the enzyme consisted of 32.5 % α-helix, 19.6 % β-sheet, 17.5 % turn/loop and 30.4 % random coil. This observation implied that upon removal of the ligand C2 by dialysis, MNase seems to regain a significant proportion of its β-sheet content, which was comparable to the β-sheet content of the native enzyme (~22.4%) (Table 4.2). The active site residues of MNase are known to be located in a β-sheet rich region (Cotton *et al*., 1979). Given that the β-sheet content of the dialyzed sample of MNase-C2 preformed complex was comparable to the native MNase enzyme, it was thus envisaged that the dialyzed sample of MNase-C2 preformed complex will exhibit considerable MNase activity. Estimation of MNase activity in the dialyzed sample of MNase-C2 preformed complex indicated retention of enzymatic activity as the reduction in fluorescence emission intensity of CT-DNA Hoechst dye complex estimated for the sample was on par with that observed for MNase (Appendix, Figure A4.11). Collectively, the CD-based secondary structure analysis and recovery of MNase activity in the dialyzed sample of MNase-C2 preformed complex imply that the interaction between the ligand C2 and MNase was quite selective in nature.

In order to substantiate the interaction of ligand C2 with MNase, molecular docking studies were pursued. To this end, C2 displayed a favorable binding energy, wherein hydrophobic interactions, and H-bond formation with specific amino acid residues of MNase could be captured (Appendix, Figure A4.12, Table A4.4). Notably, ligand C2 exhibited hydrophobic interaction with Asp-40, and Glu-43 and H-bond formation with Arg-35 (Appendix, Table A4.4), which are known to be the active-site residues of MNase (Cotton *et al.*, 1979; Chaiken and Anfinsen., 1971; Sanchez *et al.*, 1973). These observations suggested that ligand C2 can potentially bind with key active-site residues of MNase, resulting in effective inhibition of its activity. Molecular docking studies also indicated that C2 could bind with a non-specific nuclease such as the bovine pancreas DNase I (Appendix, Figure A4.13, Table A4.5). Notably, ligand C2 displayed hydrophobic interaction with Asn-74, Tyr-76 and Ala-136 and H-bond formation with Ser-110 and Arg-111 of DNase I (Appendix, Figure A4.13, Table A4.5). These interacting residues do not belong to the active site of the enzyme as it has been shown that His 131 is the active center of DNase I (Suck *et al.*, 1984). In comparison to DNase I, it is apparent from molecular docking studies that ligand C2 has a superior potency against MNase as an inhibitor as it displayed the potential to interact with some of the active site residues of the enzyme and also displayed a lower binding energy (Appendix, Table A4.4).

4.3.5. Effect of C2 on entrapment of MRSA by DNA

Amongst a plethora of host-directed responses mounted against an invading pathogen, NET constitutes a key machinery that ensures physical entrapment of the pathogen for subsequent uptake and annihilation by the host innate immune system (Brinkmann *et al.*, 2004; Papayannopoulos., 2018). However, degradation of the extracellular trap DNA scaffold by staphylococcal nuclease can lead to rapid disassembly of NETs and

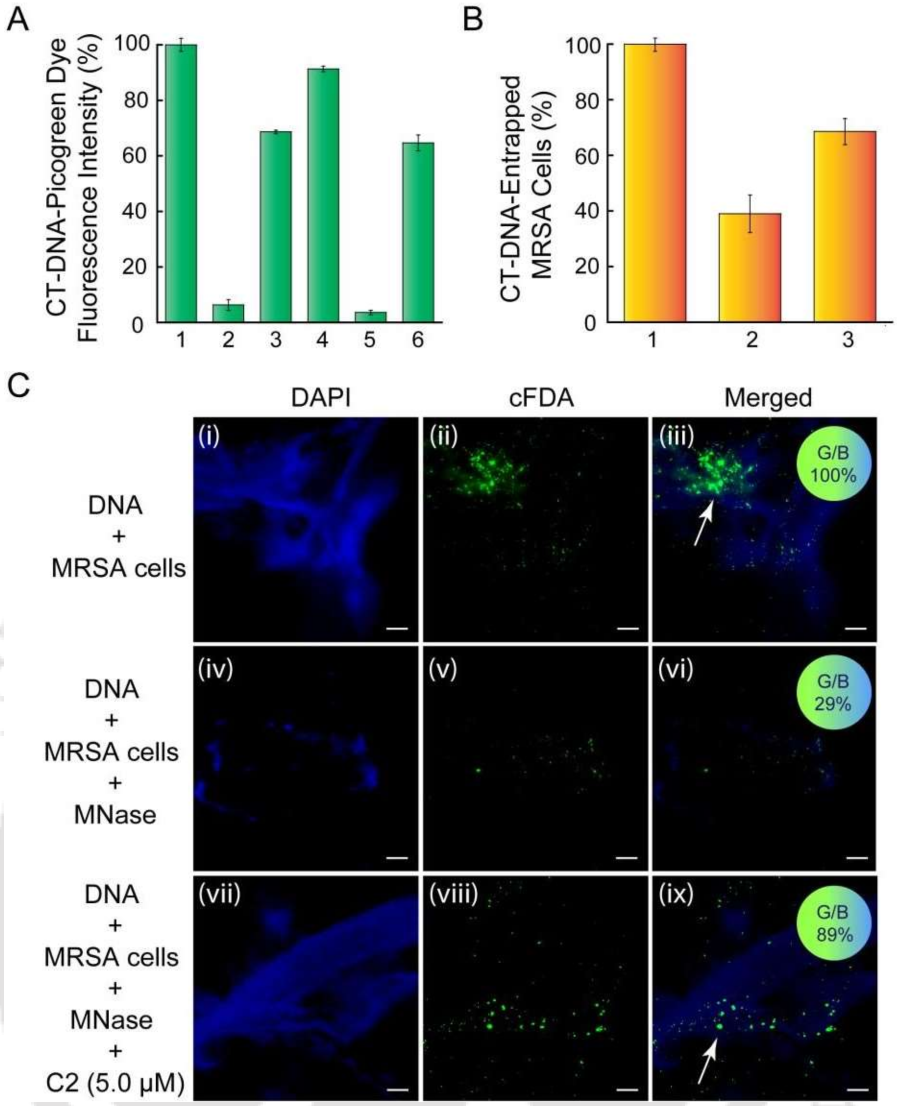

Figure 4.10. (A) Relative fluorescence emission intensity of CT-DNA-picogreen complex in presence of various treatment regimens. (1) Control (CT-DNA alone). CT-DNA incubated with (2) MNase, (3) MNase and C2 (5.0 μM), (4) MRSA, (5) MNase and MRSA, (6) MNase, C2 (5.0 μM) and MRSA. (B) Relative level of MRSA entrapped in CT-DNA in presence of various treatment regimens estimated by plating. (1) CT-DNA incubated with MRSA. (2) CT-DNA incubated with MNase and MRSA. (3) CT-DNA incubated with MNase, C2 (5.0 μM) and MRSA. (C) Fluorescence microscope-based imaging of MRSA entrapped in CT-DNA in presence of various treatment regimens. MRSA cells and CT-DNA were labelled with cFDA-SE and DAPI, respectively. Inset in panels iii, vi, and ix indicate the mean relative green/blue (G/B) emission pixel intensity expressed as a percentage. Scale bar for the images is 50 μm.

assist the pathogen in evading physical entrapment and subsequent killing by NETs and associated neutrophils (Berends *et al*., 2010; Thammavongsa *et al*., 2013; Herzog *et al*., 2019; Bhattacharya *et al*., 2020). In the context of NETs, it was envisaged that the MNase inhibitor C2 is likely to prevent DNA degradation and ensure enhanced entrapment of staphylococci. In order to verify this hypothesis, model experiments were conducted with fluorescently labelled CT-DNA and MRSA in presence of extraneously added MNase and the extent of entrapment of MRSA cells in CT-DNA was determined. Preliminary experiments were conducted to ascertain whether the presence of MRSA cells interfered with nuclease-mediated DNA digestion either in the absence or presence of C2. Based on the remarkable decrease in the relative fluorescence emission intensity of picogreen-labelled CT-DNA, it was evident that MNase could readily digest CT-DNA either in the absence or presence of MRSA cells (Figure 4.10A), which suggested that the presence of MRSA cells did not impede the efficiency of CT-DNA digestion by MNase. Further, the magnitude of the relative fluorescence emission intensity of picogreen-stained CT-DNA in presence of MNase-C2 complex was nearly ~65%, which was comparable to that observed in case of MNase-C2 complex in presence of MRSA cells (~68%) (Figure 4.10A). This again indicated that the presence of MRSA cells did not curtail the efficiency of C2 as an MNase inhibitor. Given the encouraging leads from these experiments, the subsequent goal was to determine the magnitude of viable MRSA cells entrapped in CT-DNA. To this end, plating experiments revealed that the relative level of viable MRSA cells trapped in CT-DNA in presence of MNase-C2 complex was nearly 68% and was many folds higher as compared to treatment with MNase alone (~38%) (Figure 4.10B). This reiterated that the MNase inhibitor C2 could perhaps reduce the extent of DNA degradation by the enzyme and thereby facilitate enhanced entrapment of MRSA cells.

In order to substantiate the aforementioned findings, fluorescence microscopic analysis was also pursued. In case of the control sample (MRSA cells incubated with CT-DNA), a prominent cluster of cFDA-labelled MRSA cells entrapped in DAPI-stained CT-DNA was clearly visible (Figure 4.10C, panels i-iii). Upon treatment with MNase, a scanty level of DAPI-stained CT-DNA and only a few and discrete cFDA-labelled MRSA cells were visible, which clearly suggested that digestion of the CT-DNA scaffold by MNase resulted in disassembly of the DNA trap, leading to dispersion of MRSA cells (Figure 4.10C, panels iv-vi). As a measure of MRSA entrapment in DNA, the ratio of the mean pixel intensity of green fluorescence (cFDA- labelled MRSA) to blue fluorescence (DAPI-stained DNA) was also ascertained for the representative images acquired in fluorescence microscope analysis. To this end, in presence of MNase, the green/blue (G/B) fluorescence emission intensity was only ~29% relative to the control sample, clearly indicating a low level of MRSA entrapment in DNA in presence of the enzyme (Figure 4.10C, panel vi). Interestingly, in presence of MNase-C2 complex, the integrity of the DNA scaffold was largely intact, akin to the control sample and copious number of MRSA cells were observed to be entrapped in CT-DNA (Figure 4.10C, panels vii-ix). Further, the G/B fluorescence emission intensity was ~89% relative to the control sample, which clearly suggested that the ligand C2 hindered DNA digestion by MNase, resulting in high entrapment of MRSA by DNA (Figure 4.10C, panel ix). Collectively, the solution-based assays and fluorescence microscope analysis highlighted the ability of C2 to inhibit MNase and enhance DNA-mediated entrapment of MRSA, which augers well for future therapeutic prospect of the ligand.

4.3.6. Effect of C2 on the uptake of MRSA by activated THP-1 cells

Previous studies have demonstrated that neutrophils can initiate NET formation and engulf *S. aureus* cells by phagocytosis (Gunther *et al.*, 2009; Bhattacharya *et al.*, 2018). However, by virtue of the secreted MNase enzyme, *S. aureus* cells can readily dismantle NETs and thereby evade the defense mechanism of the host immune system (Berends *et al.*, 2010; Thammavongsa *et al.*, 2013; Herzog *et al.*, 2019; Bhattacharya *et al.*, 2020). Based on the results obtained in the DNA entrapment experiments, it was envisaged that the MNase inhibitor C2 can perhaps be leveraged to prevent DNA digestion and enable higher entrapment of MRSA cells, which subsequently may bolster uptake of the pathogen by macrophages. In order to test this premise, model experiments were conducted to evaluate the potential of C2 in facilitating uptake of DNA-entrapped MRSA cells by activated THP-1 cells. The human monocyte cell line THP-1 was chosen for these studies based on the rational that these cells can be induced to differentiate into macrophage-like cells and they have been widely used to study macrophage biology as well as host-pathogen interactions (Chanput *et al.*, 2014; Srisuwan *et al.*, 2014; Starr *et al.*, 2018). In the present study, differentiation of THP-1 cells into macrophage was accomplished by growing the cells in presence of various concentrations (25 nM, 50 nM and 100 nM) of phorbol 12-myristate-13-acetate (PMA) for 48 h. In these experiments, PMA was used since it has been shown that the compound can induce THP-1 cells to differentiate and generate cells with attributes similar to human monocyte-derived macrophages (MDMs) (Chanput *et al.*, 2014; Meijer *et al.*, 2015). Flow cytometry analysis revealed that upon exposure to an

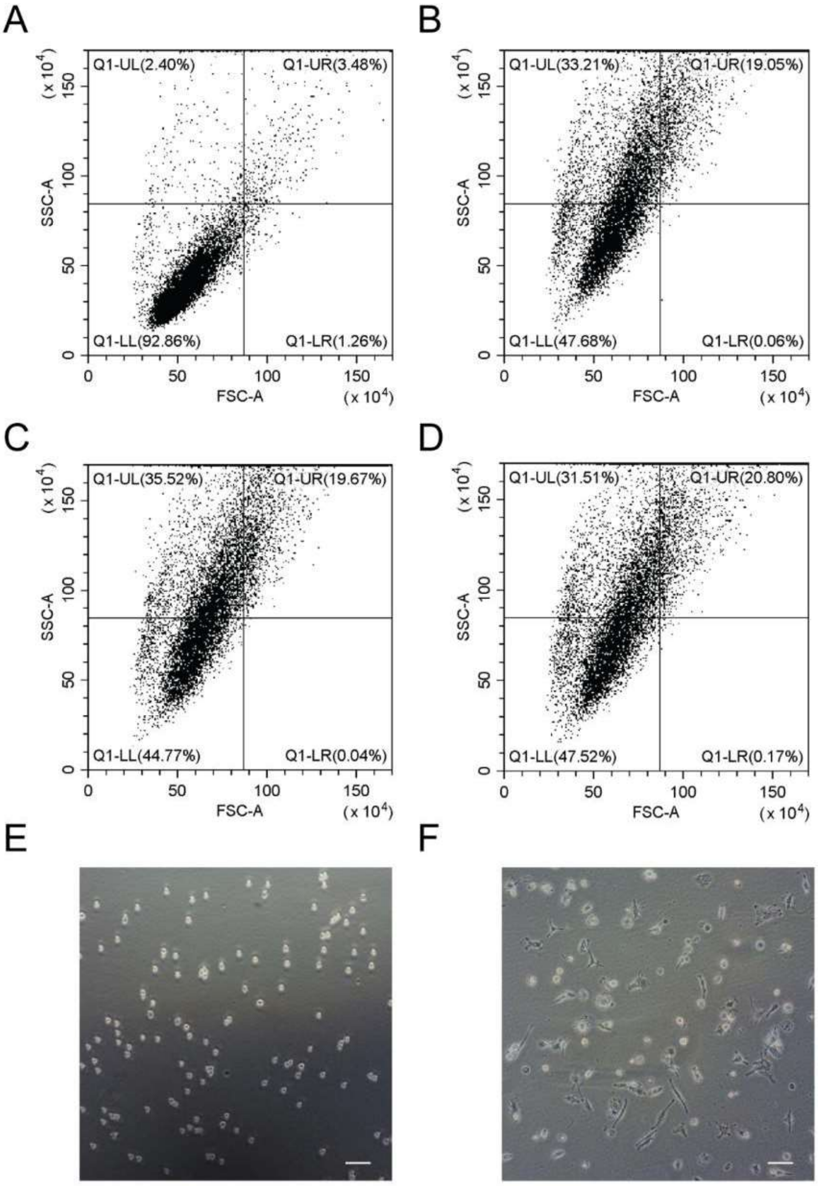

Figure 4.11. Flow cytometry-based assessment of the activation of THP-1 cells to macrophage-like cells upon treatment with PMA. (A) Untreated THP-1 cells (control). (B-D) THP-1 cells treated for 48 hours with 25 nM, 50 nM and 100 nM PMA, respectively. The cell population in the upper right quadrant indicate the proportion of activated THP-1 cells. Brightfield microscope imaging of (E) Untreated THP-1 cells and (F) THP-1 cells treated with 100 nM PMA for 48 hours. Scale bar for the images is 50 µm.

increasing concentration of PMA, a systematic increase in the population of cells exhibiting high forward scattering (FSC) and side scattering (SSC) was evident (Figure 4.11A-4.11D, top right quadrant), which suggested an increase in both cell size and granularity owing to differentiation of THP-1 cells into macrophage-like cells (Bhattacharyya and Ghosh, 2020). The maximum population of differentiated macrophage-like cells (~21%) were observed when THP-1 cells were induced in

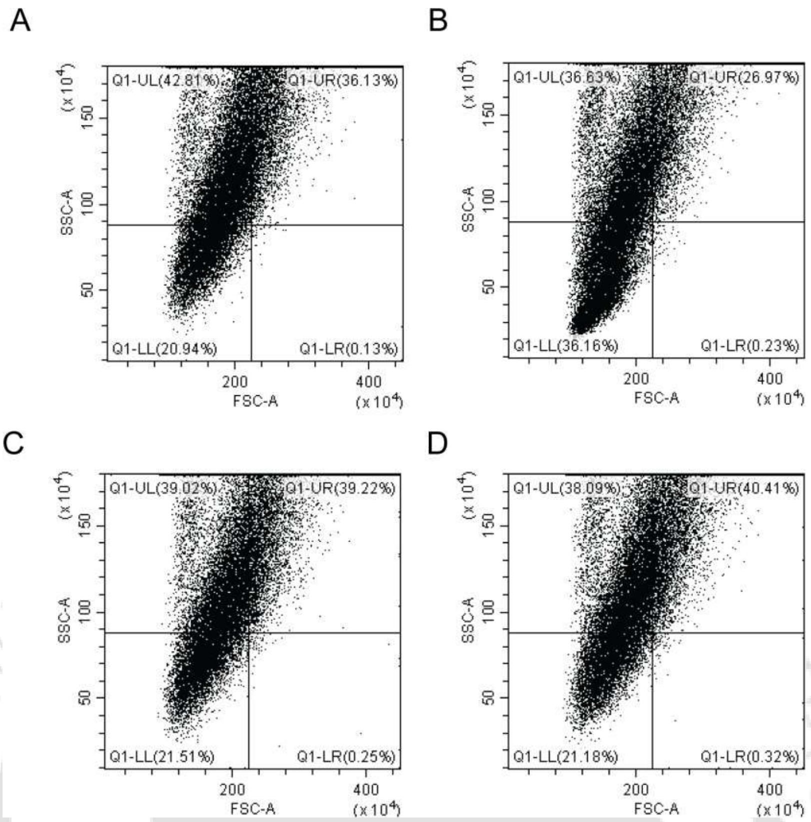

Figure 4.12. Flow cytometry-based quadrant plots for assessment of the uptake of MRSA cells by PMA-activated THP-1 cells in presence of various treatment regimens. (A) Activated THP-1 cells incubated with CT-DNA and TAMRA-labelled MRSA (10^8 CFU). (B) Activated THP-1 cells incubated with CT-DNA, MNase (5.0 units) and TAMRA-labelled MRSA (10^8 CFU). (C) Activated THP-1 cells incubated with CT-DNA, MNase (5.0 units), TAMRA-labelled MRSA (10^8 CFU) and C2 (5.0 µM). (D) Activated THP-1 cells incubated with CT-DNA, MNase (5.0 units), TAMRA-labelled MRSA (10^8 CFU) and C2 (15 µM).

presence of 100 nM PMA for 48 h (Figure 4.11D, top right quadrant). From brightfield microscopic analysis, it was evident that following treatment with 100 nM PMA for 48 h, the THP-1 cells became more adherent, larger in size, granular, and less refractive (Figure 4.11E-4.11F), which again indicated differentiation of these cells to macrophage-like cells.

To determine whether the inhibition of MNase by C2 assisted the PMA-activated THP-1 cells to engulf higher number of DNA-entrapped MRSA cells, flow cytometry and confocal microscopic analysis were pursued. Data acquired from 30,000 events in flow cytometry analysis indicated that the population of activated macrophage-like cells exhibiting high FSC and SSC signal was marginally reduced upon incubation with MRSA entrapped in MNase-digested CT-DNA (~27%) as compared to incubation with MRSA entrapped in CT-DNA (~36%) (Figure 4.12A-

4.12B, top right quadrant). It is known that *S. aureus*-derived products such as N-formyl methionyl peptide and peptidoglycan can prime neutrophils (Guerra *et al*., 2017; van Kessel *et al*., 2014; Askarian *et al*., 2018). Thus, the integrity of CT-DNA as well as the higher levels of MRSA entrapped in intact CT-DNA likely assist in priming and turnover of higher numbers of differentiated macrophage-like THP-1 cells. Interestingly, the population of activated macrophage-like THP-1 cells exhibiting high FSC and SSC signal in case of incubation with MRSA entrapped in CT-DNA-MNase-C2 complex (~39% and 40% in presence of 5.0 µM and 15 µM C2, respectively) were comparable to incubation with MRSA entrapped in CT-DNA (~36%) (Figure 4.12A, 4.12C-4.12D, top right quadrant), which again indicated that when CT-DNA digestion by MNase was inhibited by C2, the higher levels of MRSA entrapped in intact CT-DNA perhaps led to effective priming and turnover of higher numbers of differentiated macrophage-like THP-1 cells. Further, the population of activated THP-1 cells in case of incubation with CT-DNA-C2 complex (~36%) was again comparable to incubation with MRSA entrapped in CT-DNA (~36%) (Figure 4.12A, Appendix Figure A4.14, topright quadrant), which again indicated that the presence of C2 per se did not influence the turnover of higher numbers of differentiated macrophage-like THP-1 cells. The leads obtained from these analyses are interesting and can be verified in future through more rigorous experiments that can unravel the underlying molecular events, whichlead to a higher number of differentiated macrophage-like cells.

Subsequently, in flow cytometry analysis, uptake of TAMRA-labelled MRSA by activated THP-1 cells was quantified by measuring the relative median fluorescence intensity (RMFI) of TAMRA for the cell population gated in the upper right quadrant. Uptake of MRSA cells by activated THP-1 cells was clearly reduced in case of incubation with MRSA entrapped in MNase-digested CT-DNA as the estimated RMFI was only ~60% as compared to incubation with MRSA entrapped in intact CT-DNA (RMFI of 100%) (Figure 4.13A-4.13B). The reduced levels of MRSA entrapped in CT-DNA digested by MNase perhaps resulted in significantly lower levels of uptake of MRSA by activated THP-1 cells. Interestingly, the levels of MRSA uptake by activated THP-1 cells in presence of MRSA cells entrapped in CT-DNA-MNase-C2 complex was again enhanced with an RMFI of ~73% and ~94% in presence of 5.0 µM and 15 µM C2, respectively (Figure 4.13C-4.13D). Herein, at the highest tested concentration of C2 (15 µM), the uptake of DNA-entrapped MRSA by activated THP-1

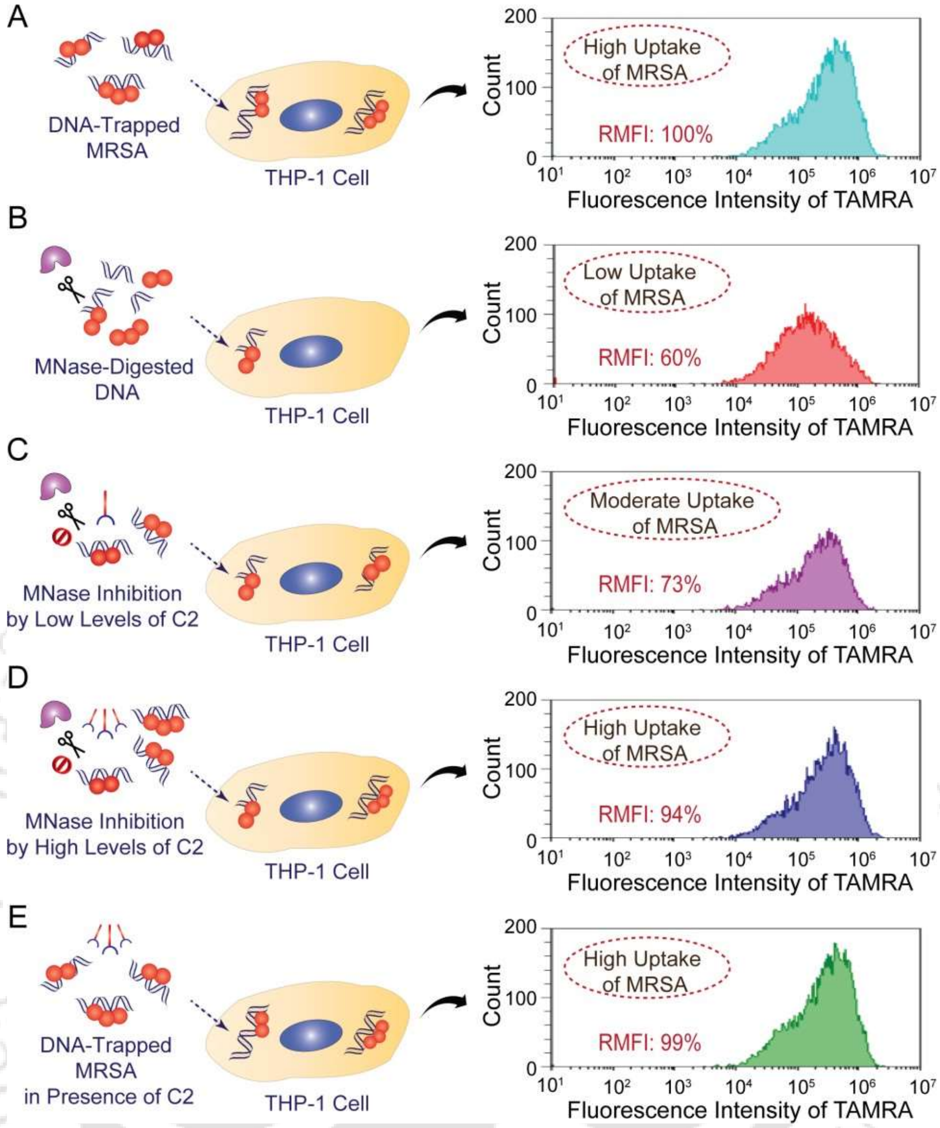

Figure 4.13. Flow cytometry-based assessment of relative uptake of TAMRA-labelled MRSA cells by activated THP-1 cells in presence of various treatment regimens as indicated in the accompanying cartoon. RMFI denotes the relative median fluorescence intensity.

cells (RMFI ~94%) was on par with MRSA entrapped in CT-DNA (RMFI of 100%) (Figure 4.13A, 4.13D), which again indicated that inhibition of MNase by C2 could facilitate higher levels of MRSA entrapment in intact CT-DNA, which in turn resulted in higher magnitude of MRSA uptake by activated THP-1 cells. It was also noteworthy that the uptake of MRSA cells by activated THP-1 cells incubated with CT-DNA-C2 complex (RMFI ~99%) was equivalent to incubation with MRSA entrapped in CT-DNA alone (RMFI of 100%) (Figure 4.13A, Figure 4.13E), which suggested that the presence of C2 did not curtail the efficiency of uptake of MRSA by activated THP-1 cells.

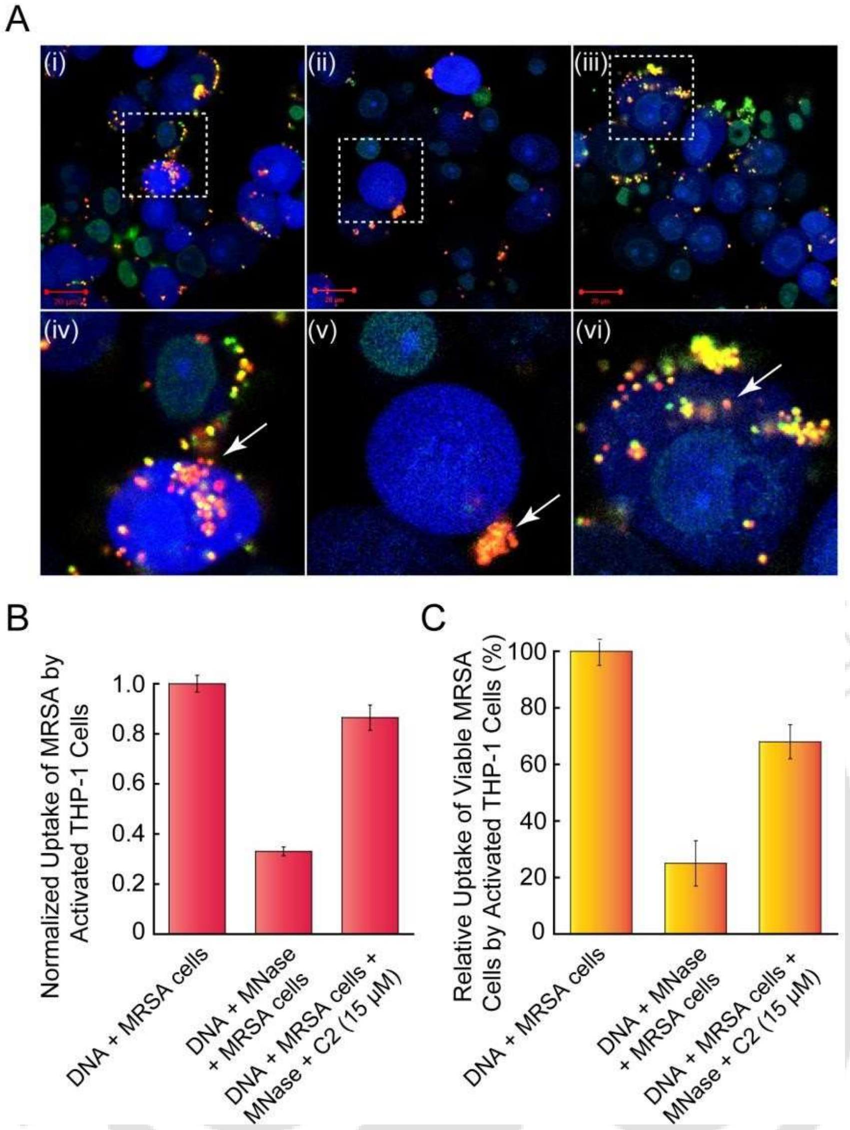

Figure 4.14. (A) Confocal microscope-based imaging to assess the uptake of TAMRA-labelled MRSA cells by activated THP-1 cells in presence of various treatment regiments. Activated THP-1 cells were incubated with (i) CT-DNA and TAMRA-labelled MRSA, (ii) CT-DNA, MNase and TAMRA-labelled MRSA, (iii) CT-DNA, MNase, TAMRA-labelled MRSA and C2 (15 µM). Panels (iv-vi) represent the magnified region of the images shown in white dashed boxes in panels (i-iii), respectively. The white arrow in panels (iv-vi) indicate TAMRA-labelled MRSA cells associated with CMAC-labelled THP-1 cells. Relative uptake of MRSA cells by activated THP-1 cells in presence of various treatment regimens ascertained by (B) normalized fluorescence intensity measurement (ratio of TAMRA-labelled MRSA and CMAC-labelled THP-1 cells) and (C) estimation of viable cells by plating method.

Uptake of MRSA cells by PMA-activated THP-1 cells was also analyzed by multi-channel confocal microscopy, wherein CT-DNA, MRSA cells and activated THP-1 cells were stained with picogreen, TAMRA and CMAC blue, respectively. In these experiments, it was evident that high number of CT-DNA-entrapped MRSA cells were taken up by PMA-activated THP-1 cells (Figure 4.14A, panels i and iv, Appendix

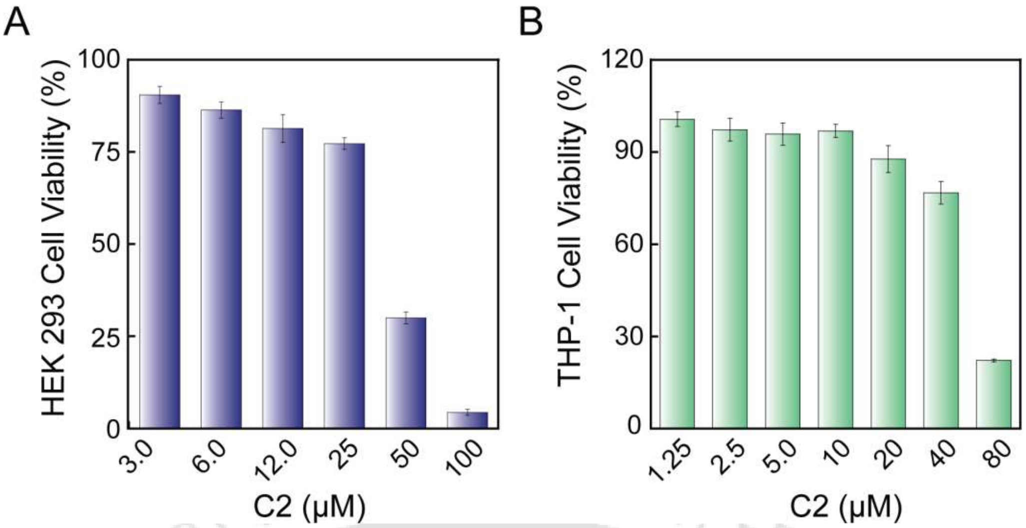

Figure 4.15. MTT assay to ascertain the cytotoxic effect of C2 against (A) HEK 293 cells and (B) THP-1 cells. Each data point represents mean ± standard deviation obtained from six independent experimental samples, each having three replicas.

Figure A4.15, panels i-v). When CT-DNA was digested with MNase, the number of MRSA cells associated with activated THP-1 cells was distinctly less, which clearly suggested that destruction of the CT-DNA integrity by MNase resulted in dismantling of the DNA trap, leading to high dispersion of MRSA cells and low levels of uptake of the pathogen by THP-1 cells (Figure 4.14A, panels ii and v, Appendix Figure A4.15, panels vi-x). Enhanced uptake of MRSA by activated THP-1 cells was again observed when MNase-mediated digestion of CT-DNA was hindered in presence of C2 (Figure 4.14A, panels iii and vi, Appendix Figure A4.15, panels xi-xv). The relative uptake of MRSA cells by PMA-activated THP-1 cells was also measured by ascertaining the ratio of the pixel intensity observed for red fluorescence (index of MRSA cells) and blue fluorescence (index of PMA-activated THP-1 cells) signals in confocal microscopy. Based on this analysis, the magnitude of uptake of CT-DNA-entrapped MRSA cells and for MRSA cells trapped in CT-DNA digested with MNase-C2 complex by activated THP-1 cells was comparable and much higher as compared to the uptake for MRSA cells incubated with MNase-digested CT-DNA (Figure 4.14B). Following uptake, the relative levels of viable MRSA cells estimated by plating THP-1 cell lysates also suggested high uptake of MRSA cells entrapped in either intact CT-DNA or in CT-DNA digested with MNase-C2 complex as compared to MRSA cells incubated with MNase-digested CT-DNA (Figure 4.14C). Collectively, theconfocal microscope analysis in conjunction with the plating results were concurrent with the results obtained in the flow cytometry analysis and they seem to strengthen the notion that C2 has the ability to effectively inhibit MNase activity and bolster higher levels of entrapment of MRSA cells by DNA leading to effective uptake by macrophage-like cells.

4.3.7. Cytotoxic potential of C2

In order to establish the merit of C2 as a therapeutic, it was pertinent to ascertain its cytotoxic potential. Interestingly, C2 was non-toxic to cultured HEK 293 cells (human embryonic kidney cells) till a concentration of 12 µM (~81% cell viability) (Figure 4.15A), with an IC_{50} value of ~31 µM. Further, the MNase inhibitor C2 was also found to be non-toxic to cultured THP-1 cells till a concentration of 20 µM (~87% cell viability) (Figure 4.15B). The IC_{50} value of C2 against THP-1 cells was estimated as ~55 µM. From a therapeutic point of view, these observations are encouraging as it indicated that at concentrations effective for inhibition of MNase (IC_{50} value of ~1.12 µM), the inhibitor C2 was unlikely to impart any detrimental effect on the viability of both HEK 293 cells as well as activated THP-1 cells. This tenet is also captured in the high therapeutic index (IC_{50} value against cultured mammalian cell / IC_{50} value for MNase inhibition) of the MNase inhibitor C2 against HEK 293 cells (~31 µM/~1.12 µM = ~27) and THP-1 cells (~55 µM/~1.12 µM = ~49). Based on its non-toxic attribute and its ability to render effective entrapment of MRSA in DNA and facilitate high uptake of the pathogen by activated macrophage- like cells, it is envisaged that the MNase inhibitor C2 may hold potential in facilitating NET-mediated MRSA entrapment and empower the host innate immune response to combat MRSA infections.

4.4. Significant Findings

The key findings of the present study can be stated as follows:

1. The benzimidazole-based ligands (C1-C2) could inhibit MNase in solution. The ligand C2 displayed superior inhibition of MNase as compared to C1 and the nature of inhibition was observed to be non-competitive.
2. CD analysis suggested distortion of the secondary structure of MNase in presence of C2 and ITC studies suggested favorable binding of C2 with MNase ($K_a = 9.7 \times 10^4$ M^{-1}).

3. C2 could inhibit MNase present in the CFS of MRSA and exhibited anti-MRSA activity only at extremely high concentrations.
4. Fluorescence-based experiments in conjunction with plating indicated that the entrapment of MRSA in CT-DNA could be restored in presence of C2 as compared to treatment with MNase alone.
5. Flow cytometry and confocal microscope analysis indicated uptake of CT-DNA entrapped MRSA cells by activated THP-1 cells could be restored in presence of C2 as compared to the low levels of uptake in case of treatment with MNase alone.
6. C2 was non-toxic to HEK 293 cells and THP-1 cell till a concentration of 12 µM and 20 µM respectively, and exhibited a high therapeutic index.

The leads obtained in the present study suggest an exciting prospect for C2 in the realm of anti-MRSA therapy. The outcome of the present study is likely to provide a guiding design principle for developing synthetic anti-virulence therapeutics that can disarm MRSA, rejuvenate the host innate immune response and facilitate effective mitigation of infections caused by strains of MRSA that are resistant to many therapeutic antibiotics. In future, it would be interesting to further consolidate the leads of the present study by selecting *in vivo* infection models. In order to advance the central objective on evaluating rationally designed synthetic small molecules as staphylococcal nuclease inhibitors, the following chapter presents the potential of napthalimide-based ligands as MNase inhibitors.

Chapter 5

Evaluation of Napthalimide-based Ligand as MNase Inhibitor for Targeting MRSA

This chapter provides a comparative appraisal of napthalimide-based synthetic ligands (C1-C3) as MNase inhibitor. The mechanism of inhibition rendered by the most potent ligand C1 is also discussed.

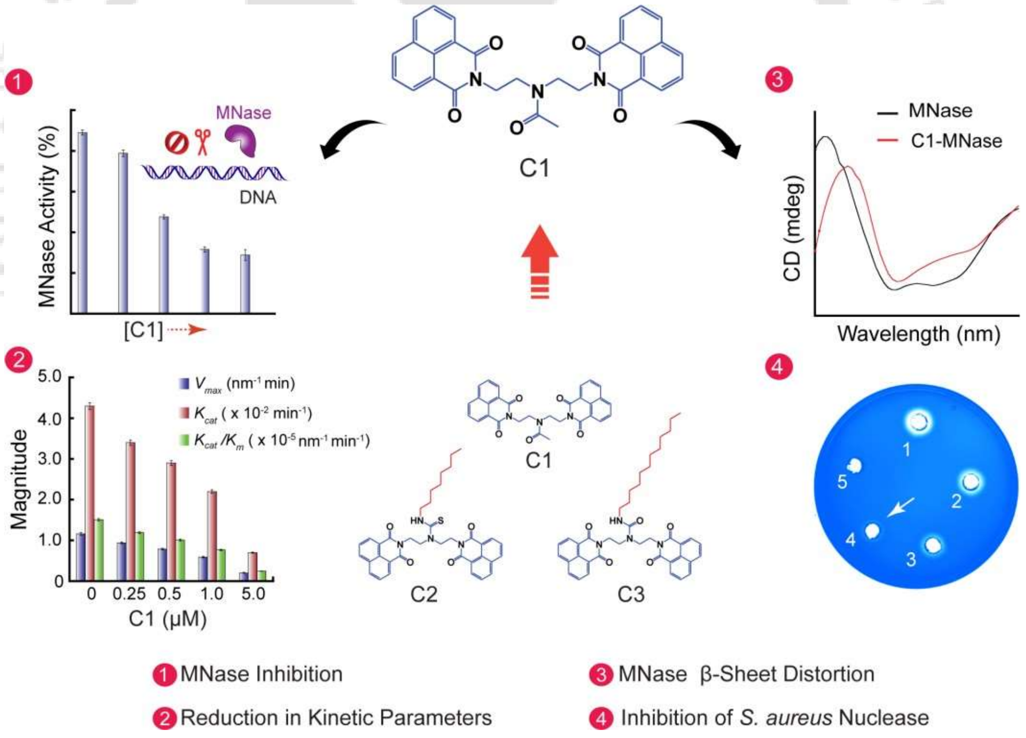

ABSTRACT

This chapter describes the potential of napthalimide-based synthetic ligands (C1-C3) as MNase inhibitor. A solution-based nuclease assay clearly revealed that the activity of MNase was systematically reduced in the presence of an increasing concentration of the ligands, wherein ligand C1 rendered the highest degree of inhibition compared to the other ligands. For instance, at the highest ligand concentration of 10 μM, MNase activity was inhibited by ~71%, ~47% and ~10% in presence of C1, C2 and C3, respectively. Estimation of the enzyme kinetic parameters from a standard Lineweaver-Burk (L-B) plot indicated that in presence of an increasing concentration of C1, the V_{max} value for MNase-catalyzed reaction was reduced, although the K_m value for MNase was virtually constant, which suggested a non-competitive mode of inhibition. There was also a notable decrease in MNase turnover number (K_{cat}) as well as catalytic efficiency (K_{cat}/K_m) in presence of an increasing concentration of C1. Solution-based spectroscopic studies indicated that upon sequential titration of MNase with an increasing concentration of C1, a systematic reduction in the intensity of tryptophan fluorescence originating from the enzyme was noted. The Stern-Volmer constant and binding constant for C1 estimated from the titration spectrum of MNase was 5.3×10^{13} $M^{-1}s^{-1}$ and 0.53 μM^{-1}, respectively. CD spectroscopy revealed a prominent perturbation of the peak of MNase at 209 nm and 221 nm and a significant change in the β-sheet content of MNase in presence of C1. Interestingly, C1 could also render a dose-dependent inhibition of nuclease enzyme secreted by a clinical isolate of MRSA. An MTT assay suggested that C1 was non-toxic to cultured HEK 293 cells, THP-1 cells and MG-63 cells till a concentration of 25 μM. This indicated that at concentrations relevant for MNase inhibition, the ligand C1 was essentially non-toxic and hence holds potential in anti-MRSA therapy.

5.1, Introduction

MRSA is a serious human pathogen, which is a major causative agent of a number of ailments and is widespread in both healthcare as well as the community-associated infections (Lee *et al.*, 2018; Turner *et al.*, 2019; Craft *et al.*, 2019). Deployment of effective therapeutic interventions for alleviation of MRSA infection in the clinic is particularly challenging, as the pathogen is known to display widespread resistance against many therapeutic antibiotics (Lee *et al.*, 2018; Craft *et al.*, 2019; Mlynarczyk-Bonikowska *et al.*, 2022).

Virulence factors present in pathogenic bacteria are increasingly being considered as viable therapeutic targets since they are significantly involved in pathogenesis, tissue injury and in resistance towards conventional treatment regimens (Ford *et al.*, 2021; Dickey *et al.*, 2017; El-Aleam *et al.*, 2021). MNase enzyme secreted by *S. aureus* is a virulence factor, which has a profound role in establishing infections, biofilm regulation, biofilm growth on implants and in the release of nucleotides from DNA, which can subsequently cause apoptosis and eliminate macrophages (Herzog *et al.*, 2019; Kiedrowski *et al.*, 2011; Moormeier *et al.*, 2014; Forson *et al.*, 2022). Moreover, MNase can digest the DNA scaffold of the neutrophil extracellular trap (NET) and thereby thwart pathogen sequestration and killing by NETs and neutrophils (Guerra *et al.*, 2017; de Vor *et al.*, 2020; Berends *et al.*, 2010; Thammavongsa *et al.*, 2013; Bhattacharya *et al.*, 2020). Based on its relevant role in promoting infection and evading the host innate immune response, MNase enzyme emerges as a viable anti-MRSA therapeutic target.

Although there are several reports on synthetic DNase inhibitors (Smelcerovic *et al.*, 2020; Gajic *et al.*, 2022) studies that describe the characterization of synthetic staphylococcal nuclease inhibitors are relatively limited (Sahareen *et al.*, 2018). This offers a window of opportunity to design new synthetic staphylococcal nuclease inhibitors and appraise their potential in anti-MRSA therapy. While designing the inhibitor, lipophilicity is considered one of the major design rational (Kolarevic *et al*, 2014).

By considering the aforementioned tenet, the current study evaluates the potential of rationally designed napthalimide-based synthetic ligands (C1-C3) as MNase inhibitor and unveils the mode of MNase inhibition rendered by the most potent ligand C1.

5.2. Materials and Methods

5.2.1. Growth media and chemicals

Calf thymus DNA (CT-DNA) was obtained from Sisco Research Laboratories Pvt. Ltd., India. Micrococcal nuclease (MNase), Dulbecco's Modifies Eagle Medium (DMEM), Trypsin-EDTA, human serum albumin (HSA), dialysis bag (12,000 MWCO) was procured from Sigma-Aldrich (USA). Brain Heart Infusion (BHI) broth, Toluidine blue-DNA agar were obtained from HiMedia, Mumbai, India. Dimethyl sulfoxide (DMSO) was obtained from Merck. Picogreen dye was procured from Invitrogen.

5.2.2 Bacterial strain and growth conditions

S. aureus MRSA 100 strain used in the present investigation was grown in BHI broth at 37 °C and 180 rpm for 12 h as described in an earlier study (Dey *et al*, 2018).

5.2.3. Synthetic ligands

The general structure of the napthalimide-based ligands (C1-C3) is shown in Figure 5.1. Synthesis and characterization of the ligands has been reported in earlier studies (De and Das, 2022; De and Das, 2021). A 5.0 mM stock solution of each ligand was prepared in DMSO and the working concentration of the ligands for each experiment was prepared from the stocks.

5.2.4. Potential of ligands as MNase inhibitor

In order to ascertain the MNase inhibition activity of the napthalimide-based ligands, a fluorescence-based nuclease assay was performed. CT-DNA (1.0 µg mL^{-1}) was incubated with picogreen dye (0.1 pg mL^{-1}) for 30 min in the dark. In separate sets, MNase solution (2.0 units) was incubated with varying concentrations of the ligands C1-C3 (0.25 µM, 0.5 µM, 1.0 µM, 5.0 µM and 10 µM each) for 30 min at 37 °C and 180 rpm. Following the specified incubation period, MNase-ligand complex was added to the CT-DNA-picogreen dye complex. The fluorescence emission spectra of the samples were then measured at an excitation and emission wavelength of 485 nm and 528 nm, respectively, at 30 sec time intervals till 600 sec. In a separate set of experiments, CT-DNA-picogreen dye complex samples (having 0.5 µg mL^{-1} and 1.0 µg mL^{-1} CT-DNA) were incubated separately with C1 (0.5 µM and 1.0 µM) for 30 min.

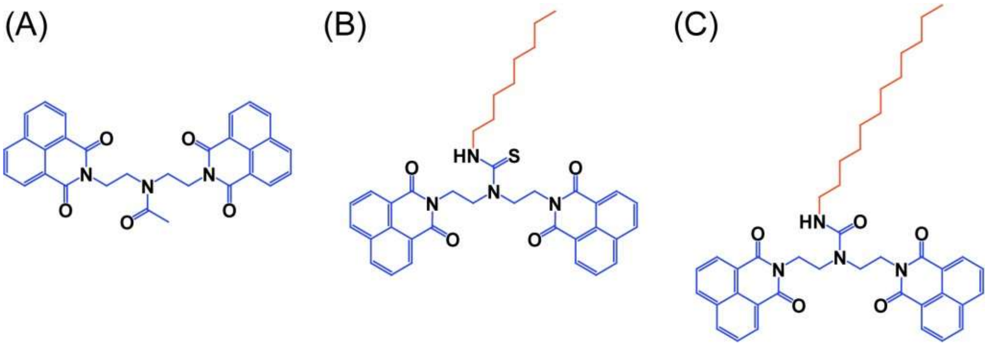

Figure 5.1. General structure of napthalimide-based synthetic ligands used in the current study. (A) C1, (B) C2, and (C) C3.

Subsequently, MNase solution (2.0 units) was added to these samples and their was measured over a period of 600 sec as mentioned previously. In a parallel experiment, the fluorescence emission intensity measured at 528 nm for MNase added to CT-DNA-picogreen dye complex in the absence of the ligands was considered as control (100 % MNase activity). In another set of experiment, MNase (1.4 µM prepared in Tris-$CaCl_2$ buffer) was incubated with 5.0 µM C1 for 30 min at room temperature. Subsequently, the MNase-C1 complex was subjected to dialysis (12,000 MWCO) against deionized water overnight and MNase activity of the dialyzed sample was also estimated by the fluorescence-based assay described earlier. For all the tested samples, nuclease activity was expressed relative to the control sample. All the experiments were performed in multiple sets. The effect of C1 on MNase kinetics was also determined. A schematic representation of the salient steps in the picogreen-based fluorescence assay for estimation of MNase activity is shown in Figure 5.2.

5.2.5. Effect of C1 on MNase kinetics

Varying concentrations of CT-DNA (350 nM -3500 nM in Tris-$CaCl_2$ buffer) were incubated with picogreen dye (0.1 pg mL^{-1}) for 30 min at 37 ºC and 180 rpm in separate sets. In another set, MNase solution (2.0 U in Tris-$CaCl_2$ buffer) and varying concentrations of picogreen-labelled CT-DNA (350 nM -3500 nM in Tris-$CaCl_2$ buffer) were incubated at 37 °C and 180 rpm in separate sets. In another set, MNase solution (2.0 U in Tris-$CaCl_2$ buffer) was initially incubated with varying concentrations of C1 (0.25 µM - 5.0 µM in Tris-$CaCl_2$ buffer) at 37 °C and 180 rpm for 30 min and then added to the CT-DNA-picogreen dye complex samples. The fluorescence emission intensity of all the samples at 528 nm were recorded at 30 sec

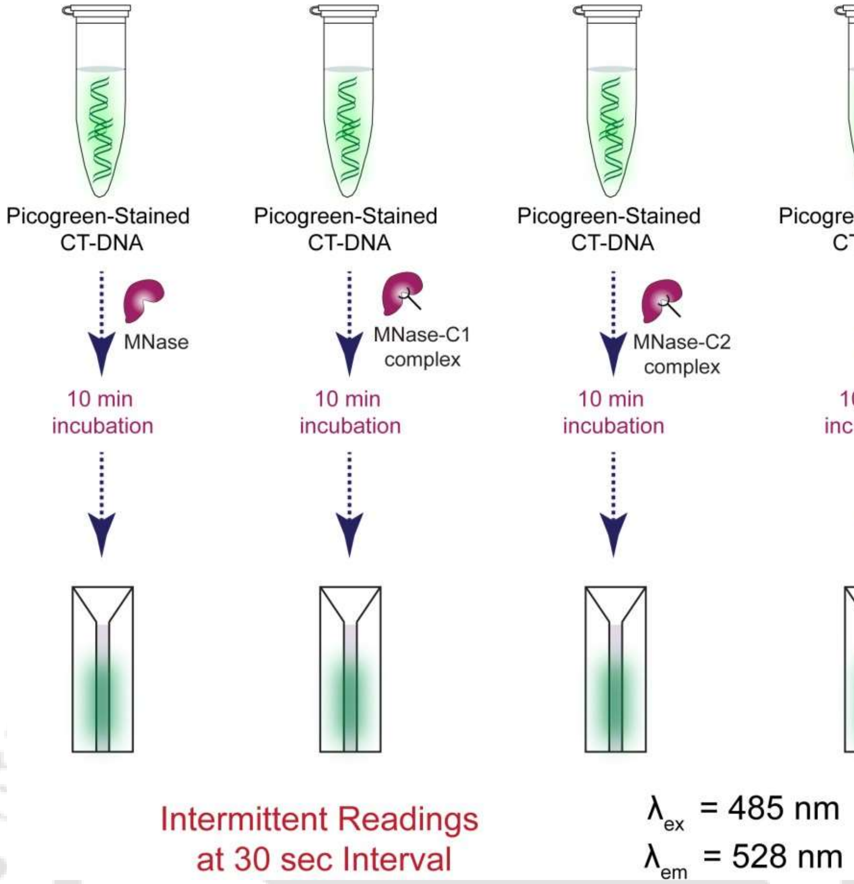

Figure 5.2. Schematic representation of the key steps in the picogreen-based fluorescence assay for estimating MNase activity.

intervals till 600 sec at an excitation wavelength of 485 nm. In parallel sets, the fluorescence emission intensity was also recorded for MNase enzyme alone added to CT-DNA-picogreen dye complex in the absence of C1. Following the addition of MNase alone or MNase-C1 in CT-DNA-picogreen dye complex, the decrease in fluorescence emission intensity (%) at 528 nm was estimated at every time interval and the values were plotted as a function of time (at 30 sec time intervals till 600 sec). Subsequently, the value of the slope derived from these plots was again plotted as a function of CT-DNA concentration in order to obtain a velocity versus substrate concentration plot analogous to a standard Michaelis-Menton plot. Thereafter, the double-reciprocal plot (akin to Lineweaver-Burk plot) and Dixon plot were constructed to estimate the kinetic parameters such as V_{max}, K_m, K_{cat} and K_i (Nelson and Cox, 2013; Segel, 2010).

5.2.6. Interaction of C1 with MNase and DNA

The fluorescence emission spectra of MNase (0.27 µM in 50 mM Tris-HCl, pH 7.5 supplemented with 10 mM $CaCl_2$) titrated with varying concentrations of C1 (0 µM – 3.0 µM) was recorded in scan mode from 310 nm - 530 nm in a spectrofluorimeter (Fluoromax-4, Horiba). The spectra were recorded at an excitation wavelength of295 nm with a slit width of 5 nm at 298 K. All the experiments were performed in multiple independent sets and each set consisted of three replicates.

The interaction of C1 and MNase was also ascertained by circular dichroism spectroscopy. To this end, CD spectra of MNase (1.4 µM prepared in Tris-$CaCl_2$ buffer) was recorded in a spectropolarimeter (Jasco, J-815) in separate sets in presence of varying concentrations of C1 (0.5 µM, 1.0 µM, 3.0 µM, 5.0 µM). A standard quartz cuvette of 2 mm path length was used and each spectrum was acquired from an average of 6 runs at a fixed temperature of 298 K. The scan range was from 190 nm to 240 nm. The spectra were expressed in milli degree (mdeg). In a separate set, the effect of C1 (1.0 µM and 5.0 µM) on HSA protein (40 µg mL^{-1}) was also evaluated by recording the CD spectra according to the conditions outlined before. In another set of experiment, MNase (1.4 µM prepared in Tris-$CaCl_2$ buffer) was incubated with 5.0 µM C1 for 30 min at room temperature. Subsequently, the MNase-C1 complex was subjected to dialysis (12,000 MWCO) against deionized water overnight and the CD spectra of the sample was recorded as mentioned before. Interaction of C1 with MNase was further studied by molecular docking as described in the Appendix section.

The absorbance-based interaction studies with C1 and CT-DNA were performed in Tris-NaCl buffer (5.0 mM Tris, 50 mM NaCl, pH 7.2). A fixed concentration of C1 (20.0 µM) was taken in separate sets and varying concentrations of CT-DNA solution (0 µM – 4.3 µM prepared in 5.0 mM Tris, 50 mM NaCl, pH 7.2) was added to each set of C1 solution and incubated for 30 min. Following incubation, the absorption spectra of the samples were recorded in a spectrophotometer (Cary 60) in scanning mode ranging from 200 nm - 600 nm and the binding constant of C1 for CT-DNA was ascertained (Ramachandran *et al.,* 2012; Wolfe *et al.,* 1987). All the experiments were performed in three independent sets wherein every set consisted of three replicates.

5.2.7. Toluidine blue-DNA (TB-DNA) agar plate assay

Inhibition of nuclease enzyme secreted by *S. aureus* MRSA 100 strain was determined by toluidine blue-DNA (TB-DNA) agar plate assay (Sahareen *et al.,* 2018). Prior to the assay, the cell-free supernatant (CFS) was collected from an overnight grown *S. aureus* MRSA 100 culture and incubated with varying concentrations of C1. In TB-DNA agar plate, 5.0 mm wells were prepared and the following samples were added in separate wells: (1) CFS, (2) CFS pre-incubated with 3.0 µM C1, (3) CFS pre-incubated with 30 µM C1, (4) CFS pre-incubated with 150 µM C1, and (5) 150 µM C1. Following overnight incubation, the images of the zone of clearance around each well were recorded.

5.2.8. Bactericidal activity of C1

For determination of the bactericidal activity of C1, 10^6 CFU of *S. aureus* MRSA 100 was grown overnight in microtiter plate wells in 200 µL BHI media at 37 ºC and 180 rpm in presence of various concentrations of C1 (25 µM - 200 µM) in separate sets. Following incubation, the relative growth of the MRSA strain with respect to the untreated control cells was ascertained (in %) by measuring the absorbance at 600 nm in a microtiter plate reader (Infinite M200, TECAN, Switzerland). The experiments were performed in three independent sets and every set consisted of three replicates.

5.2.9. Cytotoxic potential of C1

HEK 293 cells and MG-63 cells were grown in a 25 cm^2 tissue culture flask in Dulbecco's Modified Eagle Medium (DMEM) supplemented with 10% (v/v) fetal bovine serum (FBS) at 37 °C under a humidified atmosphere of 5% CO_2 in an incubator till the cells achieved ~80% confluency. THP-1 cells were grown in RPMI-1640 with 10% (v/v) fetal bovine serum (FBS) at 37 °C under a humidified atmosphere of 5% CO_2 in an incubator till the cells reached 6 x 10^5 cells/ml. The HEK-293 cells and MG-63 cells were then seeded onto 96-well tissue culture plates at a density of 8 x 10^3 cells per well and incubated in separate sets. After 24 h of incubation, DMEM media in the HEK-293 and MG-63 seeded plate was replaced by varying concentrations of C1 (3.0 µM - 100 µM) taken in DMEM in separate sets and again incubated for a period of 24 h. THP-1 cells were seeded onto 96-well tissue culture plates at a density of 10^4 cells per well with 100 nM of PMA and incubated for 48 h for activation. Following activation, RPMI-1640 media in the plates was replaced by varying concentrations of C1 (3.0 µM – 100 µM) taken in RPMI-1640 in separate sets and again incubated for a period of 24 h. Following 24 h of incubation, the media from each well was carefully removed and fresh DMEM medium containing MTT solution (25 µg mL^{-1}) was added to the wells containing HEK-293 and MG-63 cells, and fresh RPMI-1640 medium containing MTT solution (25 µg mL^{-1}) was added to the wells containing THP-1 cells and incubated for 3 h at 37 °C under 5% CO_2. Subsequently, the supernatant was aspirated and the insoluble formazan product was solubilized in DMSO and its absorbance was measured in a microtiter plate reader (Infinite M200, TECAN, Switzerland) at 570 nm. The absorbance for the untreated cells was considered as 100% cell viability and the absorbance for the treated cells was compared to determine the cell viability (%) with respect to the solvent control. All the experiments were performed in six independent sets and every set consisted of three replicates.

5.3. Results and Discussion

5.3.1. Design rational of napthalimide-based ligands

In the current investigation, the synthetic napthalimide-based ligands (C1-C3) (Figure 5.1) were selected on the basis of their salient attributes such as lipophilicity and presence of H-bond acceptor groups, which are acknowledged as key functional descriptors in known nuclease inhibitors (Smelcerovic *et al.*, 2020; Gajic *et al.*, 2022; Sahareen *et al.*, 2018). Synthesis and characterization of these ligands have been accomplished in previous studies (De and Das, 2022; De and Das, 2021). Notwithstanding the presence of a lipophilic character, H-bond acceptor groups and molecular flexibility, the ligands vary owing to the presence of an amide, thiourea and urea group in C1, C2 and C3, respectively (Figure 5.1, Appendix Table A5.1). In comparison to C1, ligands C2 and C3 are more lipophilic due to the presence of an aliphatic chain, with C3 being most hydrophobic having a 12-carbon tail (Figure 5.1C). It may also be noted here that the presence of an additional H-bond donor group in C2 and C3 may assist in achieving a higher degree of self-assembly of these ligands in solution as compared to C1. Further, the soft nature of sulfur atom in C2 may lead to an enhanced interaction with the target molecule as compared to C3. It is envisioned that the aforementioned fundamental variations in the ligands is likely to unveil a structure-function relationship and reveal the effect of ligand lipophilicity vis-à-vis their efficacy as an MNase inhibitor as well as their propensity to interact with active site residues of MNase, which are known to be buried in the hydrophobic core of a β-sheet region of the enzyme (Cotton *et al.*, 1979). Further, the choice of a napthalimide scaffold was also validated owing to their known efficacy as an antibacterial agent (Gong *et al.*, 2016; Chen *et al.*, 2017; Jin *et al.*, 2019; Zhang *et al.*, 2022).

5.3.2. Appraisal of MNase inhibition by ligands

A fluorescence-based nuclease assay was conducted in order to perform a comparative analysis of MNase inhibition rendered by the ligands. In the absence of the ligands, CT-DNA digestion by MNase was evidenced in the rapid decrease in fluorescence emission intensity of CT-DNA- picogreen dye complex at 528 nm (Figure 5.3A, Appendix, Figure A5.1). However, in presence of varying concentrations of the ligands, the extent of the decrease in the emission intensity of DNA-bound picogreen dye was less (Figure 5.3A, Appendix, Figure A5.1), which suggested that the ligands could inhibit MNase. Herein, it was also notable that the magnitude of this decrease in emission intensity of DNA-bound picogreen dye was distinctly less for ligands C1 and C2 (Figure 5.2A, Appendix, Figure A5.1), which suggested that these ligands were more efficient as MNase inhibitors as compared to C3. An estimation of the end-point fluorescence emission intensity in the assay as well as an assessment of the rate constant from the decrease of DNA-bound picogreen dye emission intensity revealed that the activity of MNase decreased in a dose-dependent manner for all the ligands, with ligand C1 imparting the most prominent effect (Appendix, Figure A5.2, Table A5.2). On comparison, the superior potency of the ligand C1 was also captured in the dose-dependent inhibition of MNase activity rendered by this ligand (Figure 5.3B, Appendix, Table A5.3). For instance, at the highest ligand concentration of 10 µM, MNase inhibition rendered by C1, C2 and C3 was observed to be ~72%, ~47% and ~10%, respectively (Figure 5.3B). The presence of a lipophilic balance as well as H-bond donor/acceptor groups have been recognized as key attributes in nuclease inhibitors (Smelcerovic *et al.*, 2020; Gajic*et al.*, 2022; Sahareen *et al.*, 2018). To this end, hydrophobicity, and presence of H-bond acceptor groups in all three ligands (Appendix, Table A5.1) does seem to account for their general ability to inhibit MNase. However, the presence of an aliphatic carbon chain in C2 and C3 may

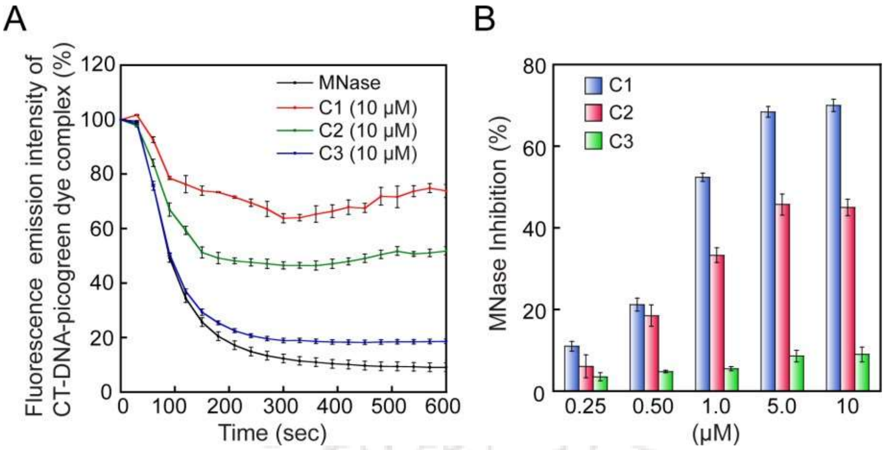

Figure 5.3. (A) Change in fluorescence emission intensity of CT-DNA-picogreen dye complex in presence of MNase and the ligands (C1-C3). (B) Dose-dependent MNase inhibition rendered by C1, C2 and C3.

promote self-assembly of these ligands in solution and thereby reduce their interaction with MNase as compared to C1. This may lead to a reduction in MNase inhibition rendered by ligands C2 and C3. Moreover, the presence of a urea group in C3 is likely to impart a H-bond donor character and trigger facile self- assembly of this ligand in solution, which may curtail its interaction with MNase, resulting in a comparatively weak inhibition of MNase activity.

5.3.3. Mechanistic studies on MNase inhibition by C1

In order to acquire a mechanistic insight on the mode of inhibition of MNase rendered by C1, experiments were conducted to ascertain the effect of C1 on the kinetics of DNA digestion by MNase. A solution-based MNase assay revealed a prominent reduction in the rate of CT-DNA cleavage upon increasing the concentration of C1 (Figure 5.4A). For instance, At the highest substrate concentration of 3500 nM CT-DNA, the velocity of MNase-catalysed CT-DNA digestion was curtailed by ~24% and ~61% in presence of 0.5 µM and 5.0 µM C1, respectively (Figure 5.4A). Based on the estimation of the velocity of MNase-catalysed CT-DNA digestion, a standard Lineweaver-Burk (L-B) plot was constructed (Figure 5.4B), which indicated that the Michaelis-Menten constant (K_m), maximum velocity of MNase-catalyzed reaction (V_{max}) and MNase turnover number (K_{cat}) was ~2857 nM, ~1.1 nM min^{-1} and ~0.04 min^{-1}, respectively. The L-B plot also indicated that increasing the concentration of C1 led to a decrease in the value of V, although K_m value for MNase remained unchanged (Figure 5.4B).

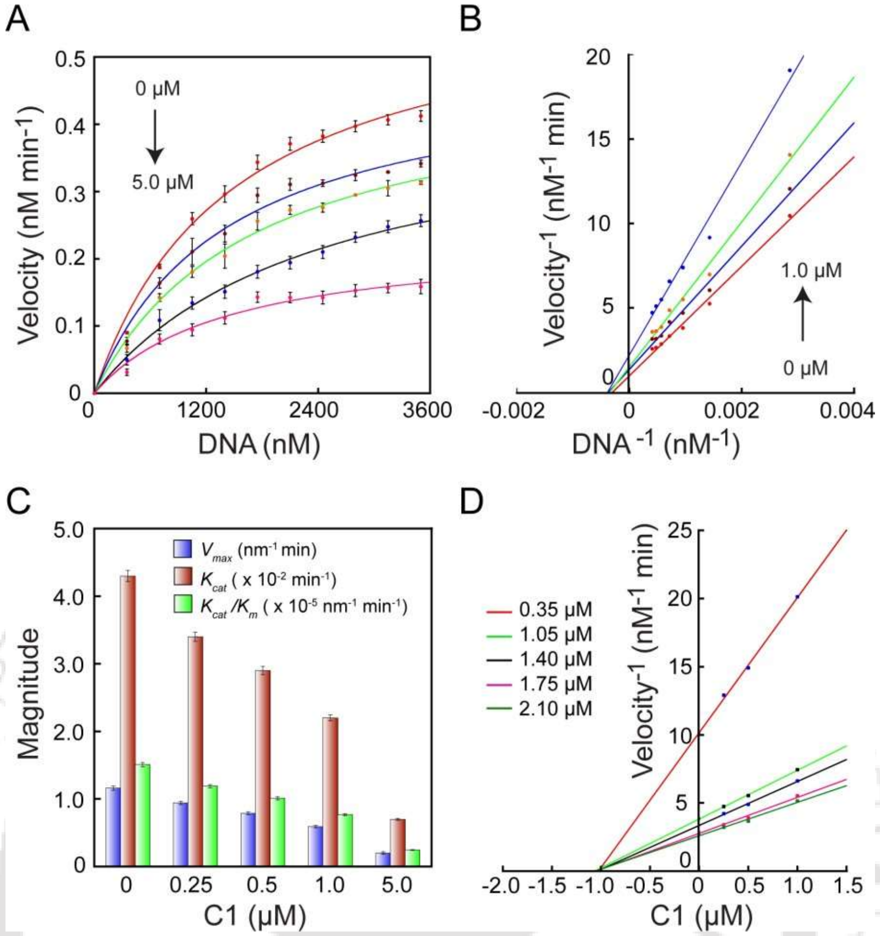

Figure 5.4. (A) Michaelis-Menten plot for MNase in presence of varying concentrations of C1. (B) Lineweaver-Burk plot to assess MNase inhibition by C1. (C) Effect of varying concentrations of C1 on the magnitude of kinetic parameters of MNase. (D) Dixon plot for MNase in the presence of varying concentrations of C1. The concentration of CT-DNA was varied from 0.35 µM to 2.10 µM in separate sets.

Table 5.1. Kinetic parameters for MNase assessed in presence of C1.

C1 (µM)	V_{max} (nM min^{-1})	K_{cat} (min^{-1})	K_{cat} / K_m (min^{-1} nM^{-1})
0	1.16	0.043	1.48×10^{-5}
0.25	0.94	0.034	1.20×10^{-5}
0.50	0.79	0.029	1.01×10^{-5}
1.0	0.59	0.022	7.62×10^{-6}
5.0	0.2	0.007	2.58×10^{-6}

This outcome clearly suggested a non-competitive mode of inhibition, wherein the ligand C1 likely binds to the MNase-CT-DNA complex and thereby hinders the rate of MNase-catalyzed reaction. Form an application point of view, the non-competitive mode of inhibition caused by C1 is indeed beneficial as it implies that even a high concentration of substrate would not be able to overcome the inhibition rendered by the ligand. In order to assess whether MNase inhibition rendered by C1 was due to the ligand interacting with DNA and thereafter modifying the substrate, additional experiments were performed. Herein, in the fluorescence-based MNase assay, the reduction of fluorescence emission intensity for preformed CT-DNA-C1 complex digested with MNase was observed to be similar to the sample wherein CT- DNA alone was digested with MNase (control) (Appendix, Figure A5.3). Further, the rate constant estimated for digestion of CT-DNA alone or CT-DNA-C1 preformed complexes were also comparable (Appendix, Table A5.4). Based on these results, it can be presumed that in solution the ligand C1 does not seem to modify the substrate DNA, which resulted in facile digestion of the CT-DNA-C1 complex by MNase. Hence, the inhibition of MNase observed in presence of C1 may be attributed to a direct effect of the ligand on the enzyme. It may also be stated here that there was also a notable reduction in V_{max} and K_{cat} of MNase in presence of an increasing concentration of C1 (Figure 5.4C, Table 5.1), which suggested that C1 could not only curtail the rate of CT-DNA digestion by MNase but also hamper the number of catalytic cycles rendered by the enzyme. Further, it was also evident that C1 could decrease the catalytic efficiency (K_{cat}/K_m) of MNase in a dose-dependent manner (Figure 5.4C, Table 5.1). Given that the K_m of MNase remained unchanged, it can perhaps be surmised that C1 likely dissuades the frequency of the binding event between MNase and its substrate. Further analysis of the kinetics data also indicated that the IC_{50} value of C1 for MNase was ~950 nM, while a Dixon plot revealed that the inhibitor constant (K_i) for C1 was ~1.0 μM (Figure 5.4D).

5.3.4. Inhibition of MRSA nuclease and bactericidal activity of C1

S. aureus secretes a thermostable nuclease, which is a key virulence factor implicated in evasion of NET-mediated host immune response and in facilitating biofilm growth (Kiedrowski *et al.*, 2011; Forson *et al.*, 2022; Berends *et al.*, 2010; Thammavongsa *et al.*, 2013, Bhattacharya *et al.*, 2020). Based on the potential of C1 as an MNase inhibitor, it was pertinent to ascertain whether C1 could also inhibit the activity of the

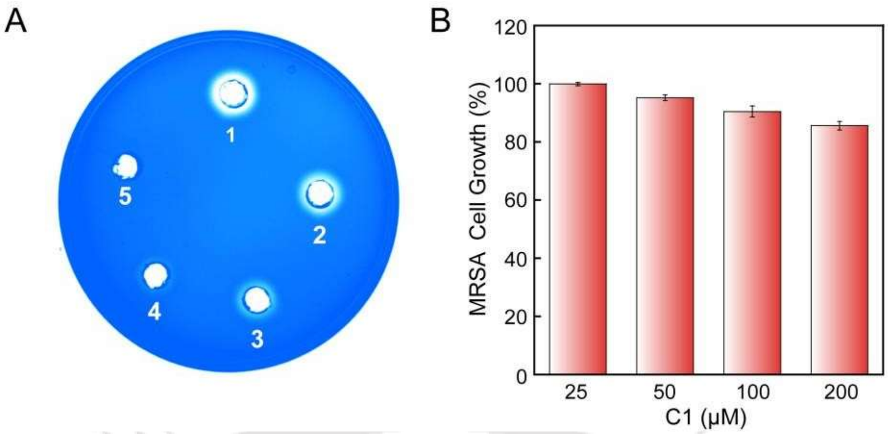

Figure 5.5. (A) Toluidine-blue DNA agar plate assay to detect inhibition of MNase present in the cell-free supernatant (CFS) of *S. aureus* MRSA 100 strain. (1) CFS alone. (2) CFS and 3.0 μM C1. (3) CFS and 30 μM C1. (4) CFS and 100 μM C1. (5) 100 μM C1. (B) Evaluation of the bactericidal activity of C1.

secreted nuclease of MRSA. To this end, a toluidine-blue DNA agar assay revealed that C1 could inhibit nuclease present in the cell-free supernatant (CFS) of the clinical MRSA strain *S. aureus* MRSA 100 in a dose-dependent manner (Figure 5.5A). This observation augers well and highlights the potential of C1 as a potential therapeutic that can be explored to target a critical virulence factor in MRSA. C1 did not display any significant bactericidal activity against *S. aureus* MRSA 100 till 200 μM (Figure 5.5B).

5.3.5. Solution-based studies on interaction of C1 with MNase and CT-DNA

In order to acquire a further insight on the interaction of ligand C1 with MNase as well as CT-DNA, spectroscopic studies were conducted. A titration spectrum revealed a reduction in the emission intensity of tryptophan fluorescence in MNase upon incubation with an increasing concentration of C1 (Figure 5.6A). Further analysis of the titration spectrum of MNase indicated that the Stern-Volmer constant and binding constant of C1 was 5.3 x 10^{13} $M^{-1}s^{-1}$ and 0.53 μM^{-1}, respectively (Figure 5.6B-5.6C). In order to estimate the binding propensity of C1 with CT-DNA, absorption spectroscopy was also pursued. Herein, a marginal hyperchromic shift was observed for the absorbance band of C1 at 260 nm (Appendix, Figure A5.4) and the intrinsic binding constant (K_{bin}) of C1 for CT-DNA was estimated to be ~3.0 nM^{-1} (Appendix, Figure A5.4).

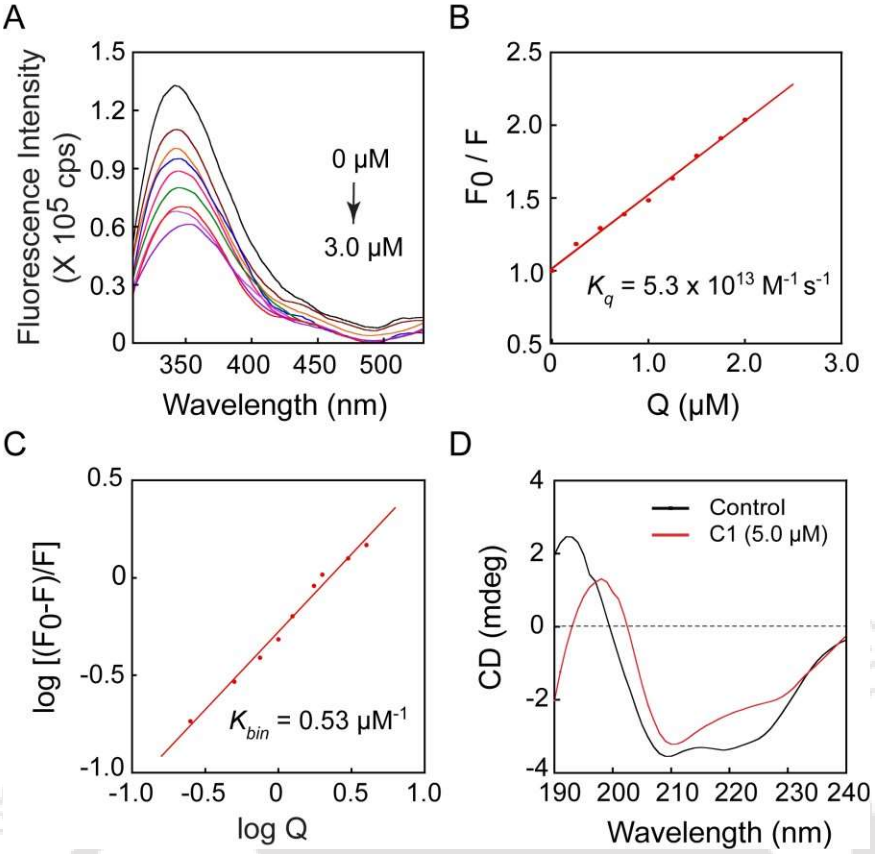

Figure 5.6. (A) Effect of C1 on tryptophan fluorescence emission spectra of MNase. (B) Stern-Volmer plot based on the fluorescence emission spectra obtained in (A). (C) Scatchard plot based on fluorescence emission spectra obtained in (A). (D) CD spectra of MNase measured in presence of 5.0 µM C1.

Table 5.2. Secondary structure analysis of MNase following interaction with C1.

Sample	**Secondary Structure Content in MNase**			
	***α* - Helix (%)**	***β* - Sheet (%)**	**Turn/Loop (%)**	**Random Coil (%)**
MNase	25	20.3	19.4	35.3
MNase + C1 (0.5 µM)	21.7	30.3	22	26
MNase + C1 (1.0 µM)	21.9	20.5	24.7	32.9
MNase + C1 (3.0 µM)	26.3	6.4	33.6	33.7
MNase + C1 (5.0 µM)	29.1	3.5	36.3	31.1

Based on the propensity of C1 to interact favorably with MNase as well as inhibit its activity, the subsequent endeavour was to ascertain whether C1 could trigger any structural perturbation in MNase upon interaction. To accomplish this objective, CD spectroscopy was pursued with MNase in the presence of varying concentrations of

C1. Interestingly, a prominent change in the peak of MNase at 209 nm and 221 nm was evident upon interaction with C1 (Figure 5.6D, Appendix, Figure A5.5). Further, a significant perturbation of the secondary structure of MNase was observed upon increasing the concentration of C1 (Table 5.2). Of note, interaction with C1 led to a remarkable change in the β-sheet content of MNase (Table 5.2). This observation highlights the merit of C1 as an inhibitor as the active site of MNase is known to be located in a β-sheet rich region of the enzyme (Cotton *et al.*, 1979). It was pertinent to determine whether C1 was selective in perturbing the secondary structure of MNase or a non-selective protein unfolder. To probe this notion, CD spectroscopy of human serum albumin (HSA) was also pursued upon interaction with C1. The concentration of C1 used in these experiments was 1.0 μM and 5.0 μM, which was sufficient to render significant inhibition of MNase activity as observed in earlier studies (Figure 5.3A). Interestingly, CD spectroscopy revealed that there was no significant change in the characteristic absorbance peaks as well as the secondary structure of HSA upon interaction with C1 (Appendix, Figure A5.6, Table A5.5). This suggested that the ligand C1 was perhaps selective in its interaction with MNase and not a generic protein unfolder, which augers well for its future therapeutic applications. Further, CD spectroscopy of the dialyzed MNase-C1 preformed complex having a high concentration of C1 (5.0 μM) revealed that the secondary structure content of the enzyme comprised of 33.5 % α-helix, 19.1 % β-sheet, 17.3 % turn/loop and 30.1 % random coil. This implied that upon removal of the ligand C1 by dialysis, MNase regained a significant proportion of its β-sheet content, which was comparable to the β-sheet content of the native enzyme (~20.3 %) (Table 5.2). The active site residues of MNase are known to be located in a β-sheet rich region (Cotton *et al.*, 1979). Given that the β-sheet content of the dialyzed sample of MNase-C1 preformed complex was comparable to the native MNase enzyme, it was thus envisaged that the dialyzed sample of MNase-C1 preformed complex will exhibit considerable MNase activity. Estimation of MNase activity in the dialyzed sample of MNase-C1 preformed complex indeed indicated retention of enzymatic activity (Appendix, Figure A5.7). Collectively, the CD-based secondary structure analysis and retention of MNase activity in the dialyzed sample of MNase-C1 preformed complex indicated that the interaction between the ligand C1 and MNase was quite selective in nature.

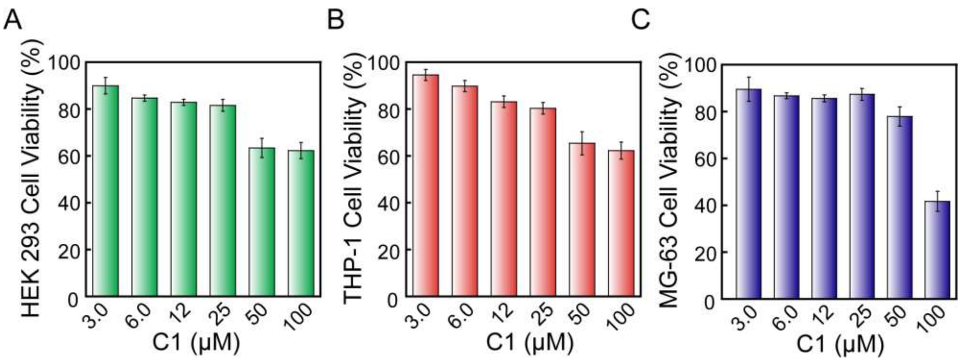

Figure 5.7. MTT assay-based evaluation of the cytotoxic effect of C1 against (A) HEK 293 cells, (B) THP-1 and (C) MG-63 cells. The data points were acquired from six independent experimental samples and considered to determine mean ± standard deviation.

Supporting evidence for interaction of ligand C1 with MNase was also acquired through molecular docking studies, which revealed that C1 could interact with specific amino acid residues of MNase by hydrophobic interactions and H-bond formation (Appendix, Figure A5.8, Table A5.6). Of note, ligand C1 displayed H-bond formation with Arg-35 (Appendix, Table A5.6), which is acknowledged as an active-site residue of MNase (Cotton *et al.*, 1979; Chaiken and Anfinsen, 1971; Sanchez *et al.*, 1973). Molecular docking studies also indicated that ligand C1 could bind with amino acid residues of bovine pancreas DNase I by hydrophobic interaction and H-bond formation (Appendix, Figure A5.9, Table A5.7). However, these residues do not belong to the active site of the enzyme as it has been shown that His 131 is the active center of DNase I (Suck *et al.*, 1984). Moreover, molecular docking studies also indicated that based on the binding energy, interaction of C1 with MNase was more favorable as compared to interaction with DNase I.

5.3.6 Cytotoxic potential of C1

In order to validate the merit of C1 as an anti-MRSA therapeutic, it was pertinent to determine its cytotoxic potential. Interestingly, C1 was non-toxic to cultured HEK 293 cells till a concentration of 25 μM(~81% cell viability) (Figure 5.7A). C1 was also found to be non-toxic to cultured THP-1 cells till a concentration of 25 μM (~80 % cell viability) (Figure 5.7B). The cytotoxic potential of C1 was also assessed against MG-63 cells, wherein it was observed that the ligand was non-toxic till a concentration of 25 μM (~80 % cell viability) (Figure 5.7C). From a therapeutic point of view, at effective MNase inhibition concentration, C1 was non-toxic to HEK 293, THP-1 and MG-63.

5.4. Significant Findings

The notable findings of the present study can be stated as follows:

1. The napthalimide-based ligands (C1-C3) could inhibit MNase in solution, wherein the most potent ligand C1 rendered a non-competitive mode of inhibition.
2. Fluorescence spectroscopy studies revealed a favorable binding of C1 with MNase while CD analysis suggested distortion of the secondary structure of MNase in presence of C1.
3. C1 could inhibit MNase present in the CFS of a clinical MRSA strain and did not significantly hinder MRSA growth till a concentration of 200 µM.
4. C1 was non-toxic to HEK 293 cells, THP-1 cells and MG-63 cells till a concentration of 25 µM, which was many folds higher than the concentration required for MNase inhibition.

By considering the aforementioned results, it was evident that C1 bears considerable prospect as an MNase inhibitor and a potential anti-MRSA therapeutic. In order to harness the therapeutic potential of C1 in anti-MRSA therapy, there is a possibility to develop a biocompatible nanocarrier which will render sustained release of the payload. In line with this objective, the subsequent chapter describes the generation of C1-loaded nanocarrier and illustrates its potential as an anti-MRSA therapeutic in *in vitro* model experiments.

Chapter 6

Therapeutic Potential of Napthalimide-based MNase Inhibitor for Mitigation of MRSA

This chapter demonstrates the potential of napthalimide-based synthetic ligand (C1) in hindering MNase-mediated CT-DNA digestion, resulting in enhanced uptake of CT-DNA entrapped MRSA cells by activated THP-1 cells. The chapter also describes the generation of C1-loaded Pluronic F-127 nano-micellar carrier (C1-PMC) for MNase inhibition and mitigation of MRSA biofilm on an orthopaedic implant.

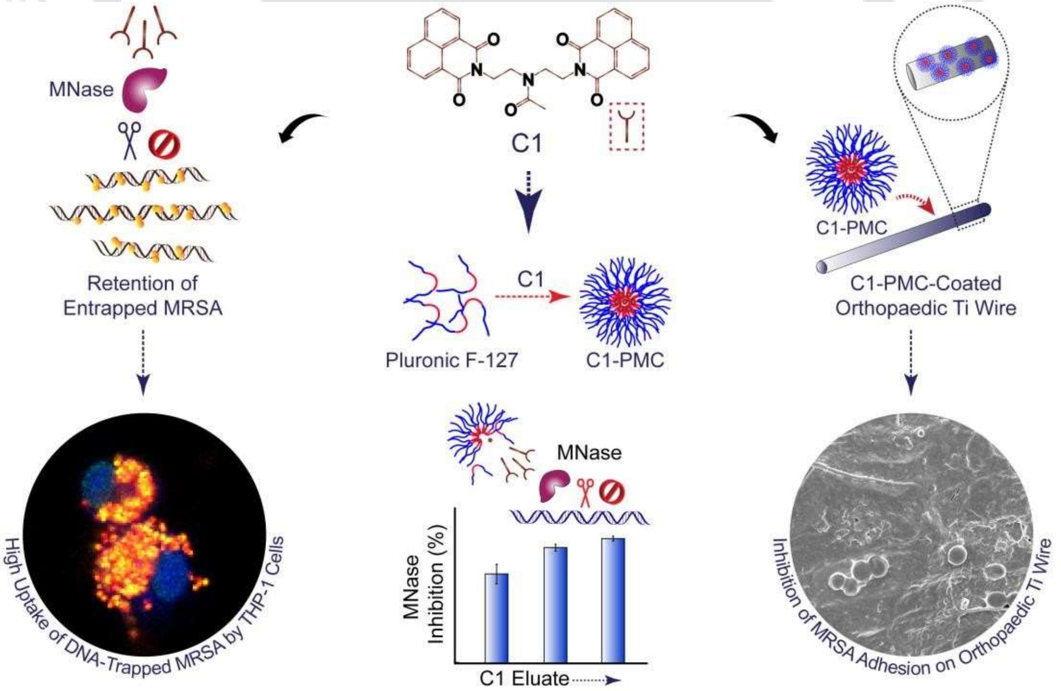

ABSTRACT

In this chapter, the therapeutic potential of napthalimide ligand (C1)-loaded Pluronic F-127 micellar carrier (C1-PMC) for MNase inhibition and mitigation of MRSA biofilm is evaluated. Initially, the uptake of CT-DNA entrapped MRSA by activated THP-1 cells was studied in presence of MNase and C1. To this end, flow cytometry- based analysis indicated that uptake of CT-DNA entrapped MRSA cells by activated THP-1 cells could be restored in a dose-dependent manner in presence of C1 compared to the low uptake levels in the case of treatment with MNase alone. Confocal microscope analysis further validated these findings, wherein the uptake of CT-DNA entrapped MRSA cells by activated THP-1 cells in presence of MNase and C1 was distinctly higher as compared to the uptake observed in case of activated THP-1 cells in presence of MNase alone. For potential therapeutic applications, C1-loaded Pluronic F-127 micellar carrier (C1-PMC) was generated and characterized. FETEM analysis indicated that the size of PMC and C1-PMC was ~35 nm and ~ 69 nm, respectively. The loading capacity of the nanocarrier was estimated as ~ 68% at the highest loading concentration of 250 µM C1. A sustained release profile of C1 was observed from C1-PMC incubated in various buffers. The magnitude of release of C1 was ~13 µM, ~31 µM and ~48 µM in simulated body fluid, citrate buffer and HEPES buffer, respectively. A concentration-dependent inhibition of MNase was observed with the eluates of C1-PMC. In a collagen adhesion assay, it was observed that C1 alone rendered a dose-dependent inhibition of MRSA adhesion onto collagen, wherein the magnitude of adhesion was ~98%, ~87% and ~53% in presence of 5.0 µM, 10 µM and 20 µM C1, respectively. Interestingly, treatment with C1-PMC (loaded with 100 µM C1) rendered a significant decrease in the extent of MRSA cell adhesion (~37%), in comparison to treatment with either PMC (~65%) or 20 µM C1 (~53%). For potential therapeutic applications of C1-PMC, a titanium (Ti) wire coated with collagen type I was selected as a model orthopaedic implant. FESEM analysis revealed copious MRSA biofilm growth on collagen-coated Ti wire, whereas a remarkable inhibition of MRSA adhesion and biofilm formation on collagen-C1-PMC-coated Ti wire was observed. Cytotoxicity assay indicated that C1-PMC (up to 100 µM) as well as the eluates from C1-PMC-coated Ti wire were non-toxic to cultured HEK-293 cells, MG-63 cells, and THP-1 cells, which suggested that the coated Ti wires were biocompatible.

2.1 Introduction

The widespread resistance of MRSA against many therapeutic antibiotics imposes a persistent healthcare burden in the clinics (Lee *et al*., 2018; Turner *et al*., 2019; Craft *et al*., 2019; Souza *et al*, 2021). MRSA is known to form invasive biofilms in soft tissues and medical implants, which is highly refractory to the action of host immune system, therapeutic arsenals and antibiotics (Craft *et al*., 2019; Arciola *et al*., 2018; Oliveira *et al*., 2018). Moreover, MRSA is armed with a host of virulence factors, of which the MNase enzyme has a key role in promoting biofilm growth on implants, elicit apoptosis and eliminate macrophages, degrade the DNA scaffold of NETs and thereby foil pathogen sequestration and killing by NETs and neutrophils (Herzog et al., 2019; Kiedrowski *et al*., 2011; Moormeier *et al*., 2014; Forson *et al*., 2022; Guerra *et al*., 2017; de Vor *et al*., 2020; Berends *et al*., 2010; Thammavongsa *et al*., 2013; Bhattacharya *et al*., 2020). Hence, therapeutics that are capable of targeting the MNase enzyme can potentially disarm the virulence of MRSA, empower the host innate immune system, curtail implant-associated infections and thereby reduce the healthcare burden levied by MRSA.

Mitigation of implant infection by MRSA is exacerbated by the deposition of host macromolecules like collagen onto the implant surface. MRSA cells can readily adhere onto collagen and establish invasive biofilm-based infections owing to the presence of collagen adhesin (Cna), which is a well characterized virulence factor (Lee *et al*., 2018; Elasri *et al*., 2002; Madani *et al*., 2017). Colonization of implants by MRSA biofilm can be stalled by surface modification or by tethering antibacterials onto the implant, which can either eliminate the planktonic cells or curtail the initial adhesion events at the onset of biofilm formation (Visperas *et al*., 2022; Ghimire and Song., 2021; Dey *et al*., 2020). Hence, there is a distinct prospect to deploy synthetic therapeutic candidates that can deter MRSA cell adhesion on collagen and thereby curb the risk of implant-related infections.

In the previous investigation outlined in Chapter 5, the synthetic napthalimide-based ligand C1 was characterized as a potent MNase inhibitor. Hence, in the current study, the potential of C1 as an anti-MRSA therapeutic was further evaluated through *in vitro* model experiments, which mimic NET-mediated entrapment and uptake of MRSA by macrophage-like cells. The study illustrates the potency of C1 in hindering MRSA cell adhesion onto collagen and describes the generation of a biocompatible

Pluronic-F127 (PF-127)-based micellar nanocarrier for encapsulation and sustained release of C1. The feasibility of deploying the nanocarrier as an anti-adhesion therapeutic to prevent MRSA adhesion onto a model orthopaedic implant is also assessed in the present study.

6.2. Materials and Methods

6.2.1. Growth media and chemicals

Calf thymus DNA (CT-DNA) was obtained from Sisco Research Laboratories Pvt. Ltd., India. Micrococcal nuclease (MNase), 5 (and 6)-carboxyfluorescein diacetate succinimidyl ester (cFDA-SE), 4′, 6-diamidino-2-phenylindole (DAPI), 5-carboxy-tetramethylrhodamine N-succinimidyl ester (TAMRA-SE), phorbol 12-myristate-13-acetate (PMA), Dulbecco's Modifies Eagle Medium (DMEM), Trypsin-EDTA, Pluronic F127, titanium wire (0.25 mm diameter), collagen type I, dialysis bag (2000 MWCO) and 0.45 µm disposable syringe filter were procured from Sigma-Aldrich (USA). Brain Heart Infusion (BHI) broth, Toluidine blue-DNA agar and RPMI-1640 medium were obtained from HiMedia, Mumbai, India. Dimethyl sulfoxide (DMSO) was obtained from Merck. CellTracker blue CMAC dye and picogreen dye were procured from Invitrogen.

6.2.2 Bacterial strain and growth conditions

S. aureus MRSA 100 strain used in the current study was propagated in BHI broth at 37 ºC and 180 rpm for 12 h as described previously (Dey *et al*, 2018).

6.2.3 Synthetic ligands

Synthesis and characterization of the napthalimide-based ligand (C1) has been reported in earlier studies (De and Das, 2022). A 5.0 mM stock solution of each ligand was prepared in DMSO and the working concentration of the ligands for each experiment was prepared from the stocks.

6.2.4. Assessment of MRSA entrapment in CT-DNA

The effect of C1 on the entrapment of MRSA cells in CT-DNA was ascertained by solution-based fluorescence studies, plating and fluorescence microscopic analysis. The protocols followed in these experiments were similar to the methods described earlier in section 4.2.10. of Chapter 4.

6.2.5. Estimation of the uptake of MRSA by PMA-activated THP-1 cells

Propagation and activation of THP-1 cells was accomplished by following the protocol outlined in section 4.2.11. of Chapter 4. The experiments performed to ascertain uptake of DNA-entrapped MRSA cells by activated THP-1 cells comprised of flow cytometry, plating and confocal microscope analysis. The protocol followed for these experiments were similar to those described earlier in section 4.2.12. - 4.2.14. of Chapter 4.

6.2.6. C1 loaded PF-127 Micellar Carrier (C1-PMC)

PF-127 micellar carrier (PMC) was synthesized by following a previously described method (Zhang *et al*, 2018). Briefly, 20 mg PF-127 was dissolved in 1.0 ml DMSO and stirred thoroughly for 24 h at 37 °C. Subsequently, the solution was filtered using a 0.45 µm filter and the filtrate was dialyzed using a 2000 MW cut-off dialysis bag against deionized water for 48 h and lyophilized. For the preparation of C1-loaded PF-127 micellar carrier (C1-PMC), 20 mg PF-127 was added in separate sets to 1.0 ml DMSO and stirred vigorously for 3 h. To these separate sets of solutions, varying concentrations of C1 solution (from a stock solution prepared in DMSO) was added dropwise to adjust the total volume to 2.0 ml. In these separate sets, the loading concentration of C1 was adjusted from 50-250 µM. The C1-PMC complex solutions were stirred for 24 h at 37 °C. Subsequently, the solutions were filtered using a 0.45 µM filter and the filtrate was dialyzed using a 2000 MW cut-off dialysis bag against deionized water for 48 h and lyophilized. A schematic representation of the essential steps followed in the generation of C1-PMC is depicted in Figure 6.1.

The lyophilized samples (PMC and C1-PMC) were finally resuspended in 1.0 mL sterile MilliQ water prior to characterization. The magnitude of loading of the ligand in C1-PMC was also estimated. Initially, a UV-visible absorbance spectra of varying concentrations of C1(1.0 µM - 35 µM) was recorded at 374 nm (the absorbance maxima of C1) in a spectrophotometer (Cary 60). The absorbance values obtained at 374 nm for varying concentrations of C1 were used to generate a calibration plot. For estimation of loading of C1, the absorbance of C1-PMC was recorded at 374 nm and the concentration of C1 encapsulated in PMC was estimated

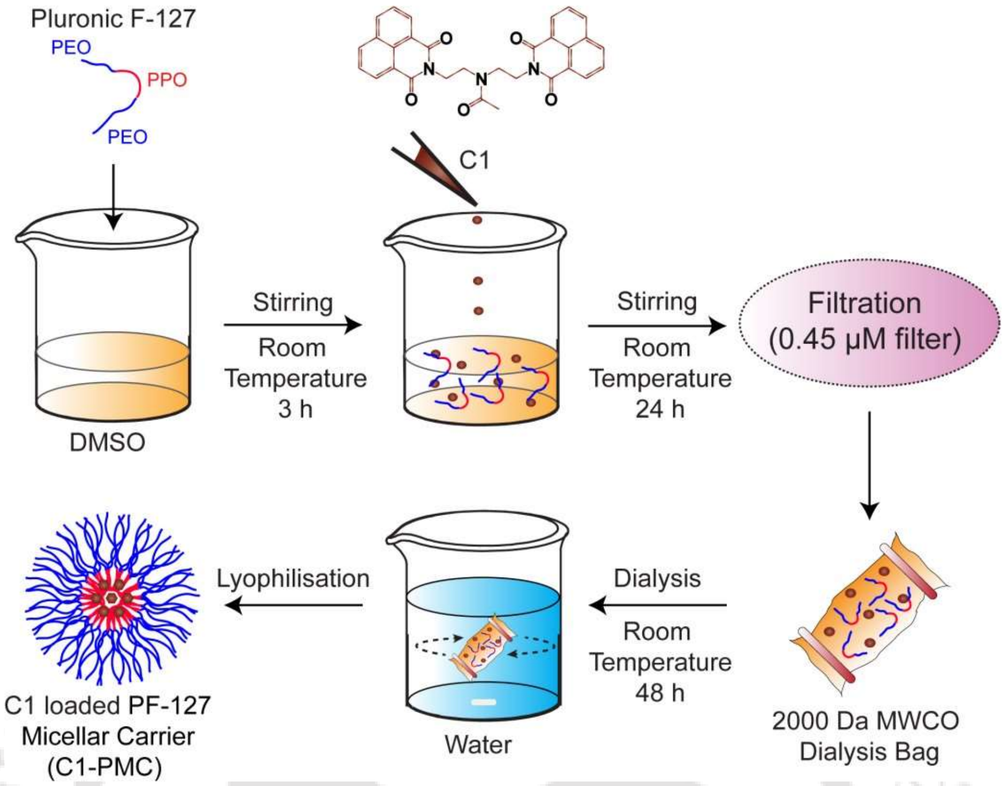

Figure 6.1. Schematic representation of the protocol used for preparation of C1-loaded Pluronic F-127 micellar carrier (C1-PMC).

from the previously generated calibration plot for C1. The encapsulation efficiency (%) of the ligand in C1-PMC was estimated by using an expression as described in a previous study (Dey *et al.*, 2018).

6.2.7. Characterization of PMC and C1-PMC

A 10 µL aliquot each of PMC and C1-PMC (loading concentration of 100 µM C1) was separately drop-casted onto aluminium foil. The samples were then dried overnight in a laminar hood and visualized in a field emission scanning electron microscope (Zeiss Sigma, USA). For FETEM analysis, both the samples were separately drop-casted onto a carbon-coated copper grid. The sample was dried overnight in a laminar hood and analyzed by FETEM (Model 2100F, JEOL) operating at 200 kV. For estimation of particle size in solution, PMC and C1-PMC (loading concentration of 100 µM C1) were resuspended in sterile MilliQ water and 0.2 ml aliquot of the sample was further diluted in sterile MilliQ water (10 × dilution) and subjected to DLS analysis (Zetasizer, Malvern, UK). The DLS experiments were performed in three independent sets and every set consisted of three replicates. The absorbance spectra of C1 (27 µM), PMC and C1-PMC (loaded with 33 µM C1) were measured in a spectrophotometer (Cary 60) in scanning mode from 200 nm to 800 nm. Absorbance measurements were recorded from three independent experimental samples. FTIR spectra of PMC and C1-PMC (PMC loaded with 100 µM C1) were recorded at 4.0 cm^{-1} resolution in an infrared spectrometer (Spectrum One, Perkin-Elmer). For each sample, eight scans were performed in the wavenumber ranging from 4000 cm^{-1} to 500 cm^{-1}.

6.2.8. In vitro release kinetics of C1 from C1-PMC

In these experiments, C1-PMC (loaded with 100 µM C1) was added in separate sets to 1.0 mL each of 10 mM HEPES buffer (pH 7.4), simulated body fluid (SBF, pH 7.4) and 10 mM citrate buffer (pH 3.0). The composition of SBF was as described in an earlier study (Marques *et al.*, 2011). Herein, the concentration of C1 loaded in C1-PMC was referred to as $C1_L$. The samples were then dialyzed using a 2000 MWCO dialysis bag against respective buffers for different time periods (6 h, 12 h, 24 h and 48 h). Following dialysis, samples from the dialysis bag were transferred into a fresh microcentrifuge tube, and the UV-visible absorbance of the solutions were measured in a spectrophotometer. The absorbance value of C1 obtained at 374 nm at various time periods in these solutions was compared with a previously generated calibration plot for C1 and the concentration of released C1 ($C1_R$) was estimated. The cumulative release of C1 (%) was estimated by determining the difference between the concentration of $C1_L$ and $C1_R$. All the experiments were performed in three independent sets and every set consisted of three replicates. A schematic representation of the protocol followed to ascertain the in vitro release kinetics from C1-PMC is shown in Figure 6.2.

6.2.9. MNase inhibition by C1-PMC eluate

C1-PMC (loaded with 129 µM C1) was incubated in 1.0 mL Tris-$CaCl_2$ buffer (buffer used in MNase assay) at 37 °C for 60 h to facilitate elution of C1 into the buffer solution. After 60 h, the concentration of C1 released as an eluate in Tris-$CaCl_2$ buffer was estimated from a previously generated absorbance-based calibration plot for C1 and varying dilutions of the eluate solution was prepared (corresponding to 5.0 µM, 10 µM and 20 µM C1) and added to MNase solution (2.0 U each) in separate sets and incubated for 30 min. Following incubation, the respective C1 eluate-MNase complex

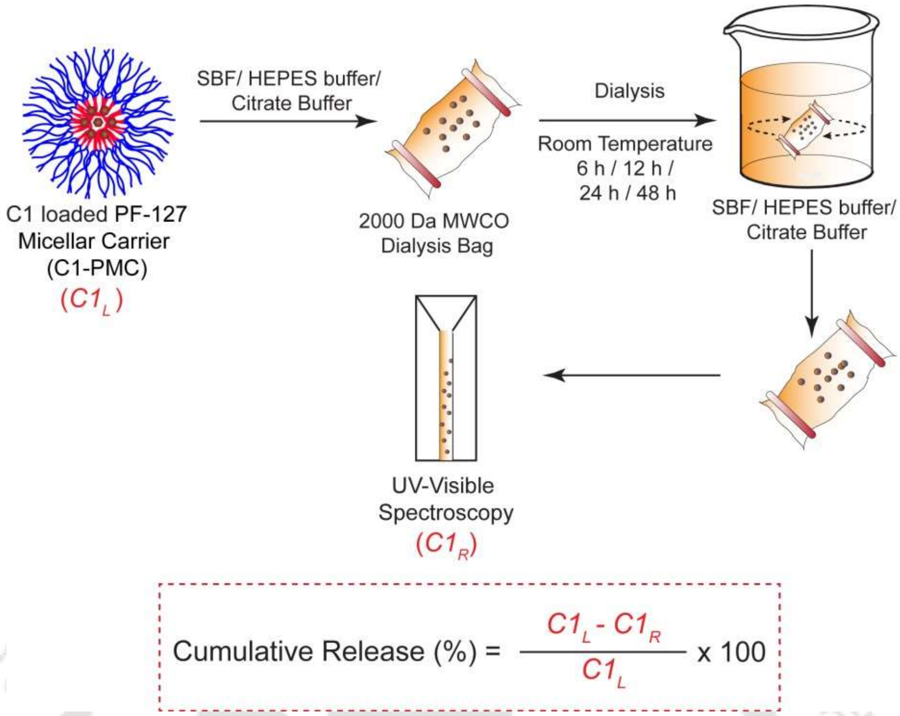

Figure 6.2. Schematic representation of the assay to estimate the release of C1 from C1-PMC incubated in simulated body fluid (SBF), HEPES buffer and citrate buffer.

solutions were added to the CT-DNA-picogreen dye complex and at regular intervals the fluorescence emission intensity of the solution was measured at 528 nm upon excitation at 485 nm. Based on the relative MNase activity, the magnitude of MNase inhibition (%) in the presence of the eluates was also estimated as mentioned before. All the experiments were performed in multiple sets.

6.2.10. Effect of C1-PMC on adhesion of MRSA onto collagen

A collagen adhesion assay was performed by essentially following a previously described method (Mukherjee and Ramesh, 2015). *S. aureus* MRSA 100 cells were grown overnight in BHI medium and labelled by cFDA-SE by following a standard method (Thiyagarajan *et al*., 2014). Prior to the adhesion assay, a 96-well tissue culture plate was coated with collagen solution (final concentration of 500 µg mL^{-1}) overnight at 4 °C. Following coating, washing and blocking of the wells was accomplished (Mukherjee and Ramesh, 2015). The fluorescence emission intensity of a 100 µL aliquot of cFDA-SE labelled *S. aureus* MRSA 100 cells (10^8 CFU mL^{-1}) was measured in a spectrofluorometer at 518 nm by exciting the solution at 488 nm. The measured fluorescence emission intensity was considered as total fluorescence (F_T). Subsequently, 100 µL of cFDA-SE labelled cells (10^8 CFU mL^{-1}) were added to the

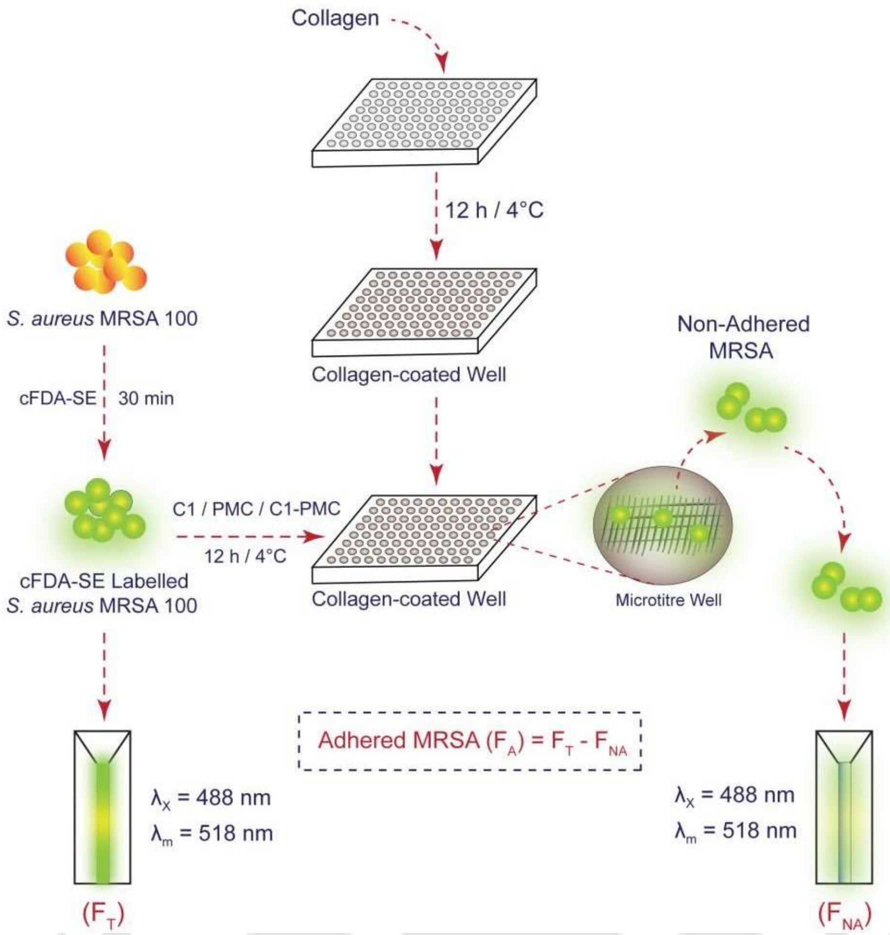

Figure 6.3. Schematic representation of the assay to evaluate MRSA adhesion onto collagen.

collagen-coated wells alone as well as collagen-coated wells with other treatment regimens (PMC, C1-PMC loaded with 5.0 µM C1, 10 µM C1, 20 µM C1 and 100 µM C1) and incubated for 12 h at 4 °C. Following incubation, the solution from the wells containing the non-adhered MRSA cells were gently aspirated and their fluorescence emission intensity was measured at 518 nm by exciting the solution at 488 nm and considered as fluorescence emission for non-adhered cells (F_{NA}). Adhesion of MRSA cells onto collagen (F_A) was measured by estimating the difference between total fluorescence (F_T) and fluorescence intensity for non-adhered cells (F_{NA}). A schematic representation of the protocol followed for ascertaining MRSA adhesion onto collagen is depicted in Figure 6.3.

6.2.11. Bactericidal activity of C1-PMC

For determination of the bactericidal activity of C1, 10^6 CFU of *S. aureus* MRSA 100 was grown overnight in microtiter plate wells in 200 µL BHI media at 37 ºC and

180 rpm in presence of various concentrations of C1-PMC (loaded with 6.3 µM-100 µM C1) in separate sets. Following incubation, the relative growth of the MRSA strain with respect to the untreated control cells was ascertained (in %) by measuring the absorbance at 600 nm in a microtiter plate reader (Infinite M200, TECAN, Switzerland). The experiments were performed in three independent sets and every set consisted of three replicates.

6.2.12. Effect of C1-PMC on adhesion of MRSA onto collagen-coated titanium wire

Titanium wire (Ti wire) was cut into several pieces of 1.5 cm in length. Initially, cleaning and sterilization of Ti wire was accomplished by a standard method (Mullick *et al*., 2022). Subsequently, the wires were coated in separate sets by incubating in 6-well tissue culture plate containing either collagen solution (1.0 mg mL^{-1} in sterile tissue culture grade water) or collagen solution (1.0 mg mL^{-1}) incorporated with either PMC or C1-PMC (loaded with 100 µM of C1) or C1 (20 µM) at 37 °C in static condition overnight. Following incubation, the solutions were removed and the plate was kept in a laminar hood overnight for drying of the Ti wire samples. The bare titanium wire (TW) and coated titanium wires were characterized by FESEM-EDX and FTIR analysis (Mullick *et al*., 2022).

In the adhesion assay, the coated Ti-wires were incubated with 10^8 CFU mL^{-1} *S. aureus* MRSA 100 cells (taken in sterile PBS) in separate sets in 6-well tissue culture plate. Collagen-coated Ti wire incubated with 10^8 CFU mL^{-1} *S. aureus* MRSA 100 alone was considered as control. The plates were incubated for 12 h at 37 °C. Following incubation, the solutions were carefully removed and the Ti wires were kept for drying in a laminar hood and visualized by FESEM.

6.2.13. Cytotoxicity studies with C1-PMC and C1-PMC eluate

Propagation and seeding of HEK 293 cells, THP-1 cells and MG-63 cells were accomplished as described in section 5.2.9. of Chapter 5. Following seeding and incubation for 24 h, DMEM media in the HEK-293 and MG-63 seeded plate was replaced by varying concentrations of C1-PMC (loaded with 3.0 µM - 100 µM of C1) taken in DMEM in separate sets and again incubated for a period of 24 h. In case of THP-1 cells, following seeding and activation by PMA for 48 h, RPMI-1640 media in the plates was replaced by varying concentrations of C1-PMC (loaded with 3.0 µM – 100 µM of C1) taken in RPMI-1640 in separate sets and again incubated for a period of 24 h. Following incubation, the media from each well was carefully removed and fresh DMEM medium containing MTT solution (25 µg mL^{-1}) was added to the wells containing HEK-293 and MG-63 cells, and fresh RPMI-1640 medium containing MTT solution (25 µg mL^{-1}) was added to the wells containing THP-1 cells and incubated for 3 h at 37 °C under 5% CO_2. Subsequently, the supernatant was aspirated and the insoluble formazan product was solubilized in DMSO and its absorbance was measured in a microtiter plate reader (Infinite M200, TECAN, Switzerland) at 570 nm. The absorbance for the untreated cells was considered as 100% cell viability and the absorbance for the treated cells was compared to determine the cell viability (%) with respect to the solvent control. All the experiments were performed in six independent sets and every set consisted of three replicates.

To assess the cytotoxic potential of the C1-PMC coated titanium wire, 1.5 cm of titanium wire was coated in separate sets with collagen and PMC, collagen and C1-PMC (PMC loaded with 100 µM of C1), collagen and C1 (20 µM) by essentially following the method described previously. The coated wires were then incubated for 12 h in separate tubes containing sterile DMEM medium or RPMI-1640 media at 37 °C at 180 rpm. The eluates from DMEM medium were then added to HEK 293 cells and MG-63 cells and the eluate from RPMI media was added to THP-1 cells and a standard MTT assay was performed to check the viability of the cells in the presence of the eluates as mentioned previously.

6.3 Results and Discussion

6.3.1 Effect of C1 on MRSA entrapment in DNA

It is established that staphylococcal nuclease is significantly implicated in the digestion of the extracellular DNA scaffold, which results in disintegration of NETs and thus enables the pathogen to elude DNA-mediated entrapment and annihilation by NETs and associated neutrophils (Herzog *et al.*, 2019; Berends *et al.*, 2010; Thammavongsa *et al.*, 2013). Based on the significant level of MNase inhibition rendered by C1, it was conceived that the ligand is likely to avert DNA digestion by nuclease enzyme and thereby promote efficient entrapment of staphylococci in DNA. To validate this tenet, model experiments were performed with fluorescently labelled CT-DNA and MRSA cells and the quantum of MRSA entrapment in DNA was ascertained in presence of spiked MNase and C1. A remarkable reduction in the relative fluorescence emission intensity of picogreen-labelled CT-DNA was observed upon digestion of CT-DNA by MNase either in the absence or presence of MRSA cells (Appendix, Figure A6.1A). Hence, it was apparent that MRSA cells did not hinder CT-DNA digestion by MNase. It was also observed that the relative fluorescence emission intensity measured for CT-DNA was ~69% and ~65% in presence of MNase-C1 complex alone and MNase-C1 complex in presence of MRSA cells (Appendix, Figure A6.1A). This further suggested that the potency of C1 as an MNase inhibitor was not significantly hampered in presence of MRSA cells. Additional plating experiments also indicated that the relative entrapment of viable MRSA cells in DNA in presence of MNase-C1 complex (~69%) was significantly higher than that observed upon treatment with MNase alone (~36%) (Appendix, Figure A6.1B). This observation substantiated the notion that the nuclease inhibitor C1 could reduce MNase-mediated digestion of the DNA scaffold and thereby enable heightened entrapment of MRSA cells.

In order to acquire additional evidence, fluorescence microscope-based experiments were conducted. To this end, a significant number of agglomerated cFDA-labelled MRSA cells trapped in DAPI-stained CT-DNA was observed for the control sample (MRSA cells incubated with CT-DNA alone) (Figure 6.4A, 6.4B, panel i, Appendix, Figure A6.1C, panels i-iii). However, upon treatment with MNase, very low levels of scattered cFDA-labelled MRSA cells entangled in a scarce mesh of DAPI- stained CT-DNA was observed (Figure 6.4A, Figure 6.4B, panel ii, Appendix, Figure A6.1C, panels iv-vi). Further, for this sample, the ratio of the mean pixel intensity of green fluorescence to blue fluorescence (G/B fluorescence) acquired from representative images was low relative to the control sample (~34%) (Appendix, Figure A6.2), which indicated that digestion of CT-DNA by MNase led to disintegration of the DNA trap and sequestration of only a few MRSA cells. Interestingly, in presence of the MNase inhibitor C1, a cluster of cFDA-labelled MRSA cells entrapped in a prominent mesh of DAPI-stained DNA was again visible, akin to the control sample (Figure 6.4A, Figure 6.4B, panel iii, Appendix, Figure A6.1C, panels vii-ix). Herein, the G/B fluorescence emission intensity was ~81% relative to the control sample (Appendix, Figure A6.2), which demonstrated the ability of C1 to effectively inhibit MNase and enhance DNA-mediated entrapment of MRSA.

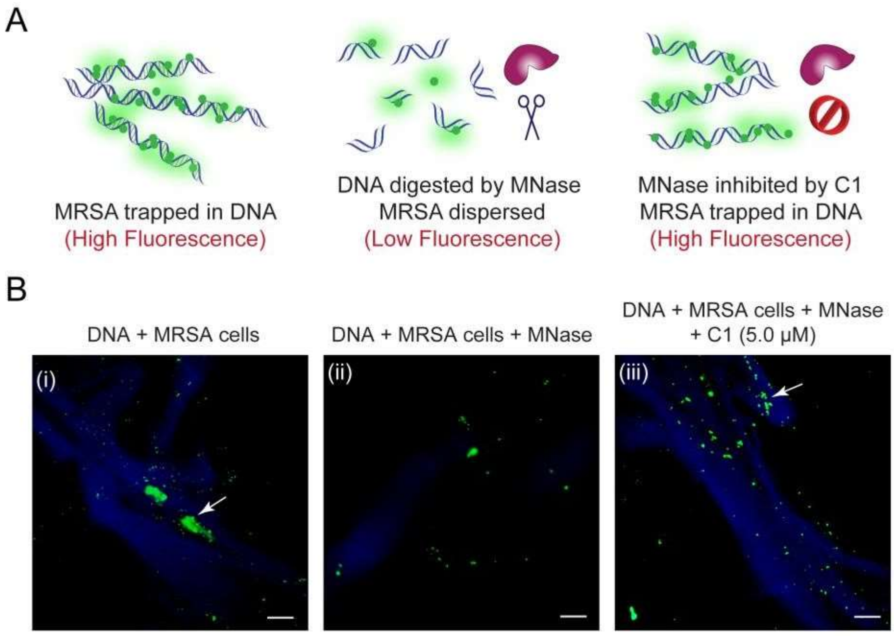

Figure 6.4. (A) Cartoon illustrating entrapment of MRSA into CT-DNA in the presence of various treatment regimens. (B) Fluorescence microscope-based detection of MRSA entrapped in CT-DNA in presence of various treatment regimens. MRSA cells and CT-DNA were labelled with cFDA-SE and DAPI, respectively. Scale bar for the images is 50 µm.

6.3.2. Uptake of DNA-entrapped MRSA by activated THP-1 cells

It is acknowledged that effective entrapment of staphylococci in the DNA scaffold is a key prerequisite for subsequent elimination by NETs and the host innate immune system (von Kockritz-Blickwede and Winste, 2022). Hence, on the basis of the leads observed in the DNA entrapment experiments, it was envisaged that deployment the synthetic MNase inhibitor C1 would ensure MRSA entrapment in DNA scaffold and subsequently enable high levels of pathogen uptake by host immune cells such as macrophage. In order to validate this notion, model experiments were performed with activated THP-1 cells (human monocyte cells) as these cells can be induced *in vitro* to differentiate into macrophage-like cells and they have been extensively used in studies probing macrophage biology and host-pathogen interactions (Chanput *et al*., 2014; Srisuwan *et al*., 2014; Starr *et al*., 2018). In the current investigation, activation of THP-1 cells into macrophage-like cells was ensured by growing the cells in presence of phorbol 12-myristate-13-acetate (PMA) for 48 h and acquisition of macrophage-like attributes in THP-1 cells was confirmed by flow cytometry and microscopic analysis as described in a previous study (Bhattacharyya and Ghosh., 2020). It may be mentioned here that PMA is known to induce differentiation in THP-1 cells and generate cells, which are akin to human monocyte-derived macrophage (Chanput *et al.*, 2014; Meijer *et al.*, 2015).

Subsequently, experiments were conducted to validate the role of C1 in facilitating higher uptake of DNA-trapped MRSA by activated THP-1 cells. To this end, flow cytometry analysis indicated a reduction in the proportion of activated THP-1 cells displaying high forward scatter (FSC) and high side scatter (SSC) signal in presence of MRSA entrapped in MNase-digested CT- DNA (~16%) in comparison to samples wherein activated THP-1 cells were incubated with MRSA entrapped in CT-DNA (~20%) alone in the absence of MNase (Figure 6.5A-6.5B, top right quadrant). Based on earlier studies, which have shown that *S. aureus*-derived products can prime neutrophils, (Guerra *et al.*, 2017; Kessel *et al.*, 2014; Askarian *et al.*, 2018), it can perhaps be surmised that in the absence of MNase, the preserved integrity of CT-DNA ensures higher levels of MRSA entrapment in the DNA scaffold, which in turn assists in priming and turnover of higher numbers of macrophage-like THP-1 cells, when compared to the sample where CT-DNA is digested with MNase. Interestingly, the potential of C1 in enabling higher uptake of DNA-entrapped MRSA by activated THP-1 cells was readily captured in the experiment as the proportion of macrophage-like THP-1 cells measured upon incubation with MRSA entrapped in CT-DNA-MNase-C1 complex (~24% and ~20% in presence of 5.0 µM and 10 µM C1, respectively) was analogous that observed upon incubation with MRSA entrapped in CT-DNA (~20%) in the absence of MNase (Figure 6.5A, 6.5C-6.8D, top right quadrant). Collectively, these results implied that the MNase inhibitor C1 primarily ensured the integrity of CT-DNA and thus facilitated contact of THP-1 cells with a higher number of DNA-entrapped MRSA cells, which resulted in effective priming and turnover of higher numbers of differentiated macrophage-like THP-1 cells. It may also be stated here that upon incubation with CT-DNA-C1 complex, the proportion of THP-1 cells was (~22%) was again comparable to that observed in case of incubation with MRSA entrapped in CT-DNA alone (~20%) (Figure 6.5A, Figure 6.5E, top right quadrant), which substantiated the notion that the impact of the ligand C1 itself on the turnover of higher numbers of macrophage-like THP-1 cells was not overriding. The essential findings from the aforementioned experiments are interesting, which warrant investigations in future to acquire additional insights on the molecular events, which trigger the turnover of a higher number of macrophage-like cells.

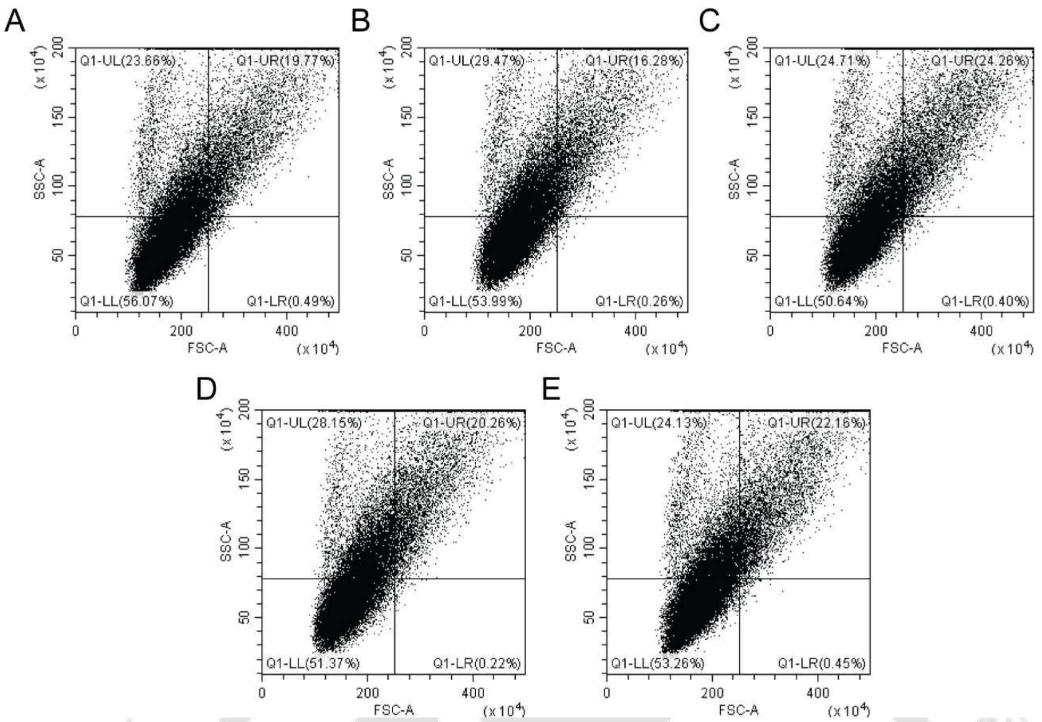

Figure 6.5. Flow cytometry-based analysis of quadrant plots for assessment of the uptake of MRSA cells by PMA-activated THP-1 cells. Activated THP-1 cells were incubated with (A) CT-DNA and TAMRA-labelled MRSA. (B) CT-DNA, MNase and TAMRA-labelled MRSA. (C) CT-DNA, MNase, TAMRA-labelled MRSA and C1 (5.0 µM). (D) CT-DNA, MNase, TAMRA-labelled MRSA and C2 (10 µM). (E) CT-DNA, TAMRA-labelled MRSA cells and C1 (10 µM).

In order to quantify the effect of C1 on uptake of DNA-trapped MRSA by macrophage-like cells, TAMRA-labelled MRSA cells were used in flow cytometry and their uptake by activated THP-1 cells was quantified by flow cytometry-based estimation of the relative median fluorescence intensity (RMFI) of TAMRA for the cell population gated in the upper right quadrant. In case of incubation of MRSA with MNase-digested CT-DNA, the estimated RMFI for gated THP-1 cells was dramatically reduced to ~56% as compared to incubation with MRSA entrapped in intact CT-DNA (RMFI of 100%) (Figure 6.6A, panel S1-S2, Figure 6.6B). Evidently, the low levels of MRSA entrapped in MNase-digested CT-DNA accounted for reduced levels of MRSA uptake by activated THP-1 cells. It was indeed noteworthy that in case of MRSA cells entrapped in CT-DNA-MNase-C1 complex, the magnitude of MRSA uptake by activated THP-1 cells was reinforced with an RMFI of ~71% and ~84% in presence of 5.0 µM and 10 µM C1, respectively (Figure 6.6A, panel S3-S4, Figure 6.6B). By virtue of MNase inhibition, ligand C1 could deter MRSA cell dispersal and render higher

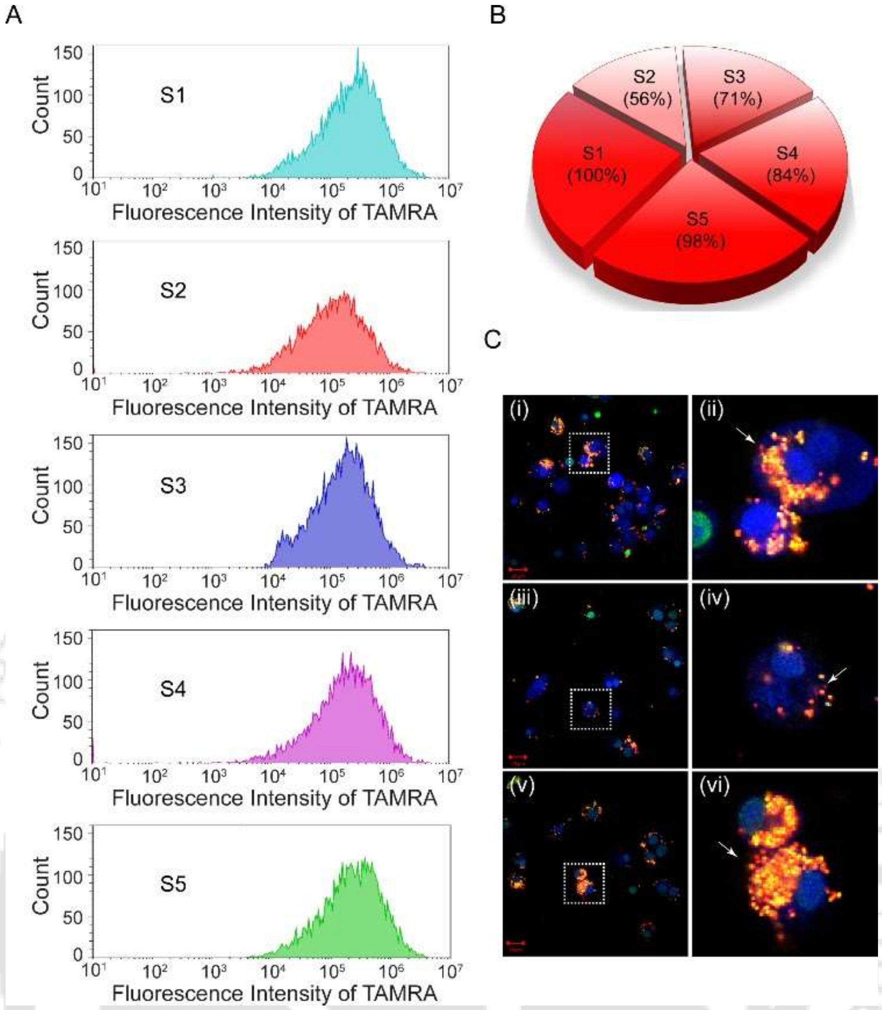

Figure 6.6. (A) Flow cytometry-based estimation of relative uptake of TAMRA-labelled MRSA cells by activated THP-1 cells in presence of various treatment regimens. TAMRA labelled MRSA was incubated with (S1) CT-DNA, (S2) MNase-digested CT-DNA, (S3) CT-DNA-MNase-C1 complex (5.0 µm C1), (S4) CT-DNA-MNase-C1 complex (10 µm C1), (S5) CT-DNA-C1 complex (10 µm C1), (B) Relative median fluorescence intensity (RMFI) of TAMRA for samples analyzed in (A). (C) Confocal microscope analysis for uptake of TAMRA-labelled MRSA cells by activated THP-1 cells incubated with (i-ii) CT-DNA and TAMRA-labelled MRSA, (iii-iv) CT-DNA, MNase and TAMRA-labelled MRSA, (v-vi) CT-DNA, MNase, TAMRA-labelled MRSA and C1 (10 µM). Panels ii, iv and vi represent the magnified region of the images shown in white dashed boxes in panels i, iii and v, respectively. White arrow in panels ii, iv and vi indicate TAMRA-labelled MRSA cells associated with CMAC-labelled THP-1 cells.

levels of pathogen entrapment in intact CT-DNA scaffold, which in turn, assisted in reinstating the efficacy of activated THP-1 cells in engulfing higher numbers of MRSA cells. Upon incubation with CT-DNA-C1 complex, uptake of MRSA cells by activated THP-1 cells (RMFI ~98%) was akin to incubation with MRSA entrapped in CT-DNA alone (RMFI of 100%) (Figure 6.6A, panel S5, Figure 6.6B), indicating that the

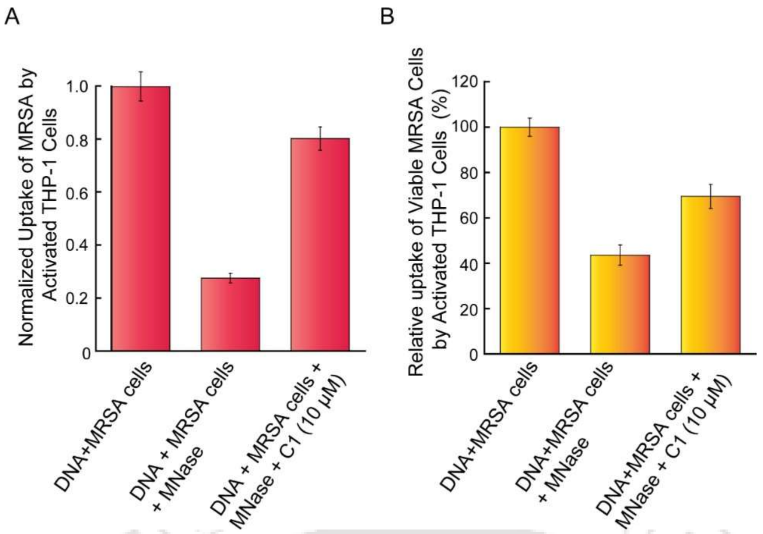

Figure 6.7. Relative uptake of MRSA cells by activated THP-1 cells in presence of various treatment regimens estimated by (A) Normalized fluorescence intensity measurement (ratio of TAMRA-labelled MRSA and CMAC-labelled THP-1 cells) and (B) Enumeration of viable cells by plating method.

presence of ligand C1 per se did not significantly impact the efficacy of uptake of DNA-trapped MRSA by activated THP-1 cells.

A multi-channel confocal microscopic analysis was also pursued to visualize the effect of C1 on the uptake of DNA-entrapped MRSA by activated THP-1 cells. In order to capture the image, CT-DNA, MRSA cells and activated THP-1 cells were stained with picogreen, TAMRA and CMAC blue, respectively in these experiments. Akin to earlier observations, the number of CT-DNA-entrapped MRSA cells taken up by PMA-activated THP-1 cells were high in the absence of MNase (Figure 6.6C, panels i-ii, Appendix Figure A6.3, panels i-v). However, the number of MRSA cells associated with activated THP-1 cells was dramatically reduced in case of CT-DNA digested with MNase (Figure 6.6C, panels iii-iv, Appendix, Figure A6.3, panels vi-x). Further, high levels of uptake of DNA-entrapped MRSA by activated THP-1 cells was again attained when MNase-mediated digestion of CT-DNA was inhibited by C1 (Figure 6.6C, panels v-vi, Appendix, Figure A6.3, panels xi-xv), which confirmed that inhibition of MNase by C1 could ensure the integrity of the CT-DNA trap and prevented MRSA dispersion, resulting in high levels of uptake of DNA-entrapped MRSA cells by THP-1 cells. Measurement of the ratio of the pixel intensity observed for red fluorescence (index of MRSA cells) and blue fluorescence (index of PMA-activated THP-1 cells) signals in confocal microscope analysis also indicated a recovery and attainment of a significantly higher uptake of CT-DNA-entrapped MRSA cells in presence of C1 as against the uptake observed in case of MRSA cells incubated with MNase-digested CT-DNA (Figure 6.7A). Further validation of these results was captured in the plating experiments, which revealed a substantially higher level of uptake of MRSA cells entrapped in either CT-DNA alone or in CT-DNA digested with MNase-C1 complex by THP-1 cells in comparison to the uptake observed in case of MNase-digested CT-DNA (Figure 6.7B). In essence, the results emerging from flow cytometry analysis, confocal microscopy and plating were concordant and provided strong evidence that the ligand C1 could be leveraged as an MNase inhibitor to ensure effective sequestration of MRSA cells by an intact DNA trap, which in turn restored the ability of macrophage-like cells to engulf higher levels of the trapped MRSA cells.

6.3.3. C1-loaded Pluronic F-127 Micellar Nanocarrier (C1-PMC)

In order to harness the potential of C1 as an MNase inhibitor in therapeutic interventions against MRSA, generation of a non-toxic and robust delivery system for sustained release of the ligand is critical. In this context, deployment of a colloidal nanocarrier based on the amphiphilic triblock copolymer Pluronic-F127 (PF-127) is particularly appealing. PF-127 is a non-toxic and FDA approved polymer, that can readily self-assemble in aqueous solution to form biocompatible nano-scale micelles that can encapsulate and render long circulation time and sustained delivery of lipophilic drugs (PJ *et al.*, 2022; Pitto-Barry and Barry, 2014; Basak and Bandyopadhyay, 2013; Zhang *et al.*, 2018). Based on these beneficial attributes associated with PF-127, the endeavour in the current study was to generate a C1-loaded PF-127 micellar nanocarrier (C1-PMC). The critical micellar concentration (CMC) of PF-127 has been reported to be ~0.56 mM at room temperature (Ghosh *et al.*, 2014). In order to facilitate micelle formation in solution, the concentration of PF-127 used for preparing the micellar carrier was substantially above the reported CMC value. Nano- scale micelles of PF-127 (PMC) as well as C1-loaded PMC (C1-PMC) were generated and characterized. FESEM analysis indicated that the size of PMC and C1-PMC was ~38 nm and ~69 nm, respectively (Appendix, Figure A6.4A, Figure 6.8A). FETEM analysis indicated that PMC and C1-PMC were spherical to oblong in shape (Appendix, Figure A6.4B, Figure 6.8B). DLS analysis revealed that the hydrodynamic diameter of PMC and C1-PMC was ~296 nm and ~400 nm, respectively (Appendix, Figure A6.5). The larger hydrodynamic diameter of C1-PMC indicated copious loading of ligand C1 in the hydrophobic core of the nanocarrier.

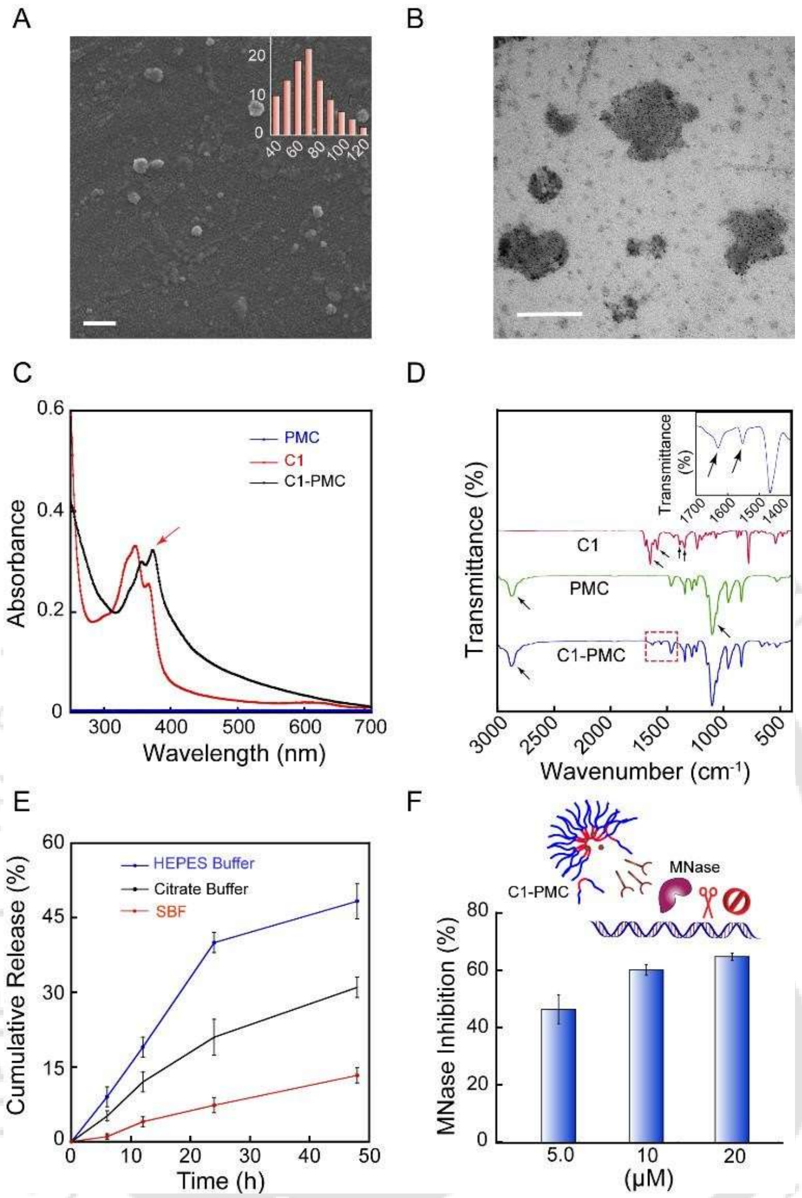

Figure 6.8. (A) FESEM image of C1-loaded PF-127 micellar carrier (C1-PMC). Inset indicates particle size distribution of C1-PMC determined by using ImageJ software.
(B) FETEM image of C1-PMC. Scale bar for the images in (A) and (B) is 200 nm and 100 nm, respectively. (C) UV-visible spectra of C1, PMC and C1-PMC. (D) FTIR spectra of C1, PMC and C1-PMC. Arrows indicate the characteristic stretching frequency for the samples. Inset represents the amplified region of the spectra for C1-PMC shown in red dashed box. Arrow in inset indicates the characteristic stretching frequency for Amide-I in C1-PMC. (E) Cumulative release of C1 from C1-PMC incubated in simulated body fluid (SBF), HEPES buffer and citrate buffer. (F) Inhibition of MNase by C1 eluates (corresponding to 5.0, 10 and 20 µM C1) obtained from C1-PMC.

Loading of C1 into PMC was ascertained from a calibration plot generated for C1 (Appendix, Figure A6.6). It was observed that loading of C1 in C1-PMC was dose-dependent wherein a highest loading of 171 µM was observed with 68% encapsulation efficiency (Table 6.1). Loading of C1 in PMC was further validated by UV-visible

Table 6.1. Estimation of the amount of encapsulated C1 in C1-PMC and encapsulation efficiency of C1.

Loading Concentration of C1 (μM)	Encapsulated C1 in C1-PMC (μM)	Encapsulation Efficiency (%)
50	11.34 ± 0.50	23
75	48.21 ± 4.01	64
100	66.09 ± 3.20	66
125	88.30 ± 2.14	71
150	99.84 ± 0.98	67
200	128.66 ± 5.37	64
250	170.54 ± 2.14	68

spectroscopy and FTIR analysis. UV- visible spectroscopy of C1-PMC indicated the presence of a characteristic peak of C1 at374 nm (Figure 6.8C). FTIR analysis of C1 indicated the presence of salient stretching frequencies at 1651 and 1587 cm^{-1} for Amide-I and at 1389 and 1343 cm^{-1} for Amide-II (Figure 6.8D). The stretching frequencies for C-C at 1097 cm^{-1} and terminal OH at2880 cm^{-1} was also evident for PMC (Figure 6.8D). Formation of C1-PMC was indeed validated by FTIR analysis, which indicated the presence of the characteristic stretching frequencies for C-C at 1097 cm^{-1}, terminal OH at 2880 cm^{-1} (Figure 6.8D) and for Amide-I at 1630 and 1552 cm^{-1} (Figure 6.8D, inset).

Prior to testing the potential of C1-PMC as an anti-MRSA therapeutic, it was critical to ascertain the extent of payload release from the micellar nanocarrier in a physiological buffer system. In this regard, a sustained release profile of C1 was observed from C1-PMC (loaded with 100 μM C1) incubated in various buffers. Following 48 h, the magnitude of release of C1 was ~13 μM, ~31 μM and ~48 μM in simulated body fluid, citrate buffer and HEPES buffer, respectively (Figure 6.8E). The quantum of C1 release in the buffers bears significance as they were several folds higher than the inhibitory concentration of C1 for MNase (IC_{50} = ~0.95 μM). In order to leverage C1-PMC as an MNase inhibitor, it is paramount that the released payload retains its ability to inhibit MNase. From a solution-based study, a concentration-dependent inhibition of MNase activity was observed with the eluates of C1-PMC (Appendix, Figure A6.7A), wherein the rate constant for MNase-mediated DNA digestion was estimated to be 0.37 and 0.24 s^{-1}, while the magnitude of MNase inhibition was ~46% and ~65% in the presence of 5.0 μM and 20 μM C1 as eluate, respectively (Appendix, Table A6.1, Figure 6.8F). It may also be mentioned here that PMC alone failed to impede MNase-mediated digestion of DNA (Appendix, Figure A6.7B), which indicated that the micellar carrier per se did not interfere with the assay. Collectively, the results clearly suggested that the potency of C1 as an MNase inhibitor was largely conserved even after encapsulation and release from PMC.

6.3.4 Mitigation of MRSA adhesion onto collagen by C1-PMC

It is acknowledged that the inherent propensity of *S. aureus* to adhere onto the extracellular matrix protein collagen plays a critical role in pathogenesis and in establishing invasive infections in collagen-rich tissues such as bone, cartilage, and skin (Kouidhi *et al*., 2010; Foster *et al*., 2014). To this end, the staphylococcal collagen adhesin (Cna) is a well characterized virulence factor, which is implicated in MRSA infection, biofilm formation and tissue colonization (Lee *et al*., 2018; Elasri *et al*., 2002; Madani *et al*., 2017). Given the profound role of collagen adhesion in MRSA infection, it is envisaged that a synthetic ligand that can curtail MRSA adhesion onto collagen would bear considerable therapeutic potential in the mitigation of tissue and device-related MRSA biofilm infections. Previous literature seems to suggest that a triblock copolymer such as PF127 can deter adhesion of staphylococci on a biomaterial (Treter *et al*., 2014). Further, amphiphilic ligands with reasonable hydrophobicity have also been shown to hinder adhesion of MRSA onto collagen (Dey *et al*., 2020). Based on the essential observations in these studies, it was thus envisaged that the PF127-based micellar nanocarrier C1-PMC loaded with the hydrophobic ligand C1 is likely to exhibit heightened anti-adhesive attributes. To test this premise, a fluorescence-based collagen adhesion assay for MRSA was performed in microtiter plates. Herein, C1 alone rendered a dose-dependent inhibition of MRSA adhesion onto collagen, wherein the magnitude of adhesion was ~98%, ~87% and ~53% in presenceof 5.0 µM, 10 µM and 20 µM C1, respectively (Figure 6.9A). Interestingly, treatment with C1-PMC (loaded with 100 µM C1) for 12 h rendered a significant decrease in the extent of MRSA cell adhesion (~37%), in comparison to treatment with either PMC (~65%) or 20 µM C1 (~53%) (Figure 6.9A, Appendix Table A6.2). This decrease in MRSA adhesion in presence of C1-PMC as against PMC or C1 was also evident in fluorescence microscope-based imaging (Figure 6.9B). It may be mentioned here that in

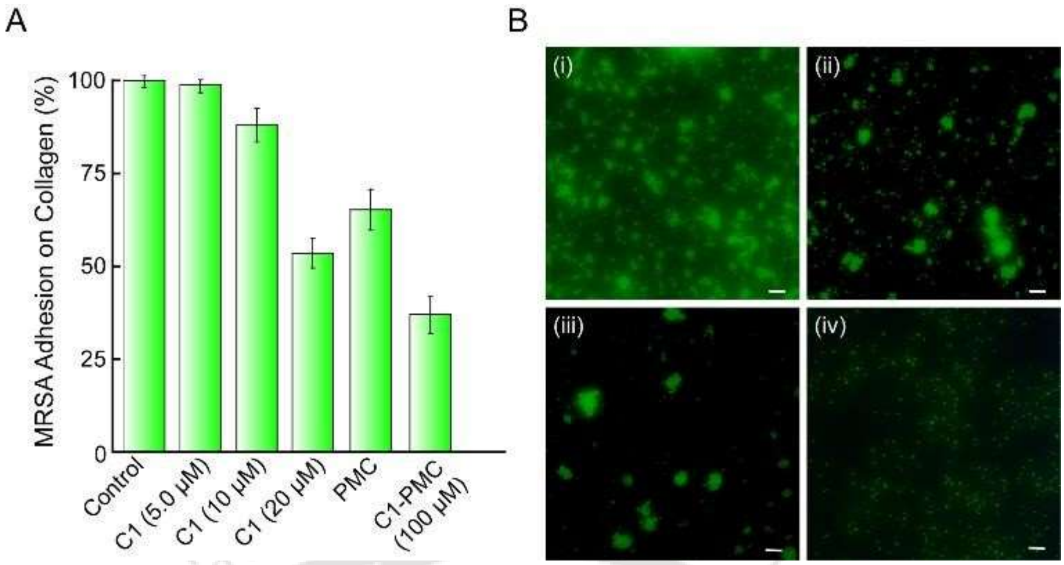

Figure 6.9. (A) Adhesion of *S. aureus* MRSA 100 cells onto collagen in presence of various treatment regimen. (B) Fluorescence microscope analysis to visualize adhesion of MRSA cells onto collagen in presence of various treatment regimen. (i) Control. (ii) PMC, (iii) C1 (20 µM) and (iv) C1-PMC (loaded with 100 µM C1). Scale bar for the images is 50 µm.

The adhesion assay, it is anticipated that the magnitude of release of C1 from C1-PMC (loaded with 100 µM C1) will be ~20 µM after 12 h, on the basis of the results observed earlier in the release kinetics studies (Figure 6.8E). Hence, the higher extent of inhibition of MRSA cell adhesion observed with C1-PMC (~37%), as compared to treatment with either PMC (~65%) or 20 µM C1 (~53%) highlights the benefit of generating a dual warhead nanocarrier wherein the anti-adhesive potential of the carrier as well as the payload could be harnessed in tandem to achieve an enhanced effect. The bactericidal activity of C1-PMC against *S. aureus* MRSA 100 strain was also determined. To this end, C1-PMC was non-bactericidal till a loading concentration of 100 µM (Appendix, Figure A6.8). Based on these results, C1-PMC can thus be considered as a non-biocidal anti-adhesive therapeutic agent, which augers well as it reduces the likelihood of resistance development.

6.3.5 Inhibition of MRSA adhesion onto orthopaedic implant by C1-PMC

Therapeutic intervention against MRSA is challenging as the pathogen is known to form resilient biofilms in tissues as well as in medical implants (Lee *et al.*, 2018; Turner *et al.*, 2019; Craft *et al.*, 2019; Arciola *et al.*, 2018; Oliveira *et al.*, 2018). Extensive colonization by MRSA can eventually result in implant failure in the clinics. Hence, there is a growing need of potential drug candidates that can mitigate the risk of

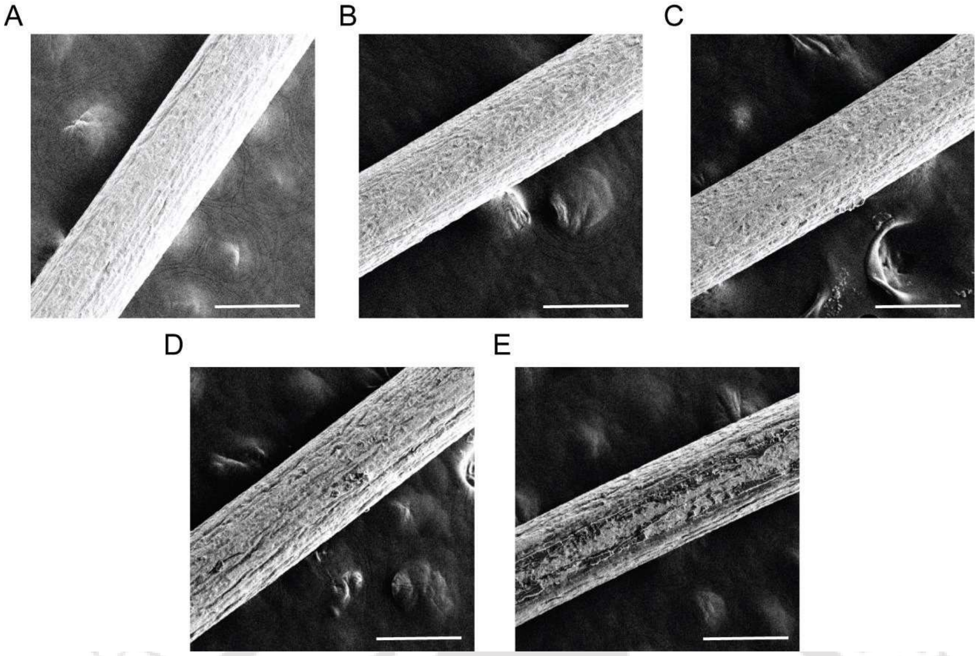

Figure 6.10. FESEM image of titanium wire (Ti wire) coated with different samples. (A) Bare Ti wire, (B) Ti wire coated with collagen, (C) Ti wire coated with collagen and C1 (20 µM), (D) Ti wire coated with collagen and PMC, (E) Ti wire coated with collagen and C1-PMC (loaded with 100 µM of C1). Scale bar for the images is 250 µm.

implant-related MRSA infections. Conceivably, MRSA invasion can perhaps be stymied by a surface modification, passive coating, or active tethering of an antibacterial onto medical implants, which can either annihilate planktonic cells or perturb the initial cell adhesion event during biofilm formation on the implant (Visperas *et al.*, 2022; Ghimire and Song, 2021; Dey *et al.*, 2020; Hetrick and Schoenfisch, 2006; Arciola *et al.*, 2012). However, a fundamental problem in implant infection is the deposition of host macromolecules like collagen onto the surface of the device, which provides a matrix for MRSA cell adhesion and biofilm formation and thus advances the infection process. Based on the high efficacy of the micellar nanocarrier C1-PMC in reducing MRSA adhesion onto collagen, it was worthwhile to ascertain its potential in reducing MRSA adhesion and biofilm formation on a medical implant. To validate this tenet, model experiments were performed with Titanium (Ti) wire, which is an extensively used orthopaedic implant. In these experiments, the Ti wire was initially coated with collagen, C1 (20 µM), PMC and C1-PMC (loaded with 100 µM C1). In FESEM analysis, the bare Ti wire exhibited a rough surface, whereas a thick notched surface was observed in case of Ti wire with various coatings (Figure 6.10). For all the coated Ti wire samples, a distinct increase in the weight % of C, O

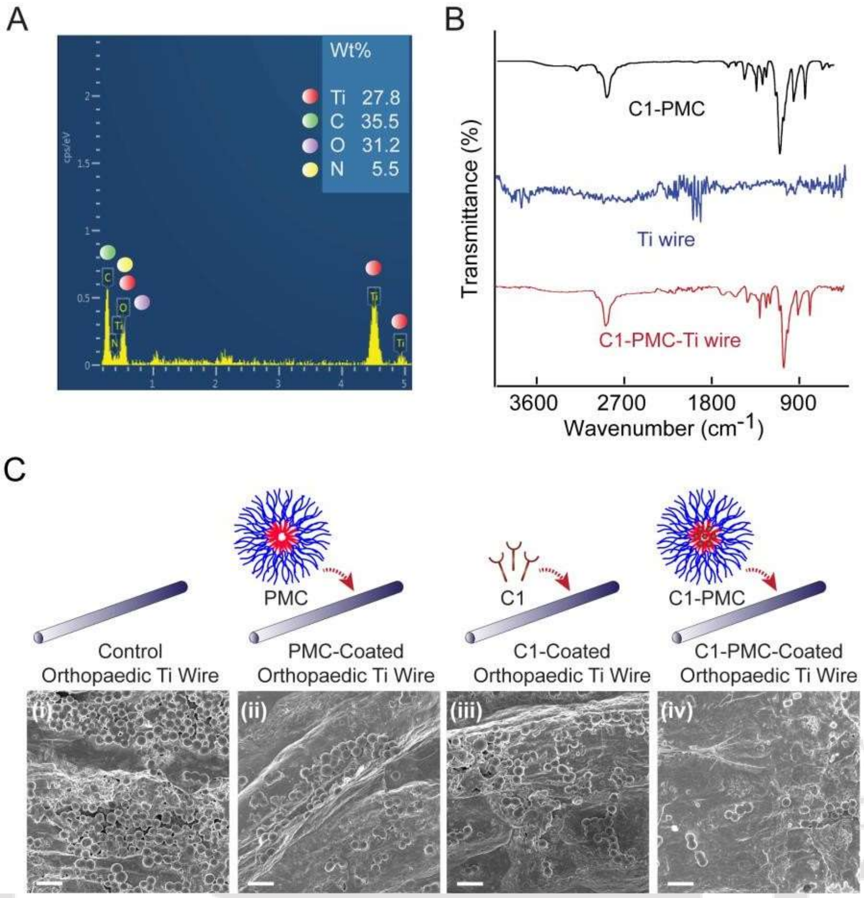

Figure 6.11. (A) Energy Dispersive X-ray (EDX) analysis of collagen and C1-PMC-coated titanium wire (C1-PMC-Ti wire). (B) FTIR spectra of C1-PMC, bare titanium wire (Ti wire) and collagen and C1-PMC-coated titanium wire (C1-PMC-Ti wire). (C) FESEM image analysis to visualize adhesion of MRSA cells onto Ti-wire coated with various samples. (i) Control (Ti wire coated with collagen), (ii) Ti wire coated with collagen and PMC, (iii) Ti wire coated with collagen and C1 (20 µM) and (iv) Ti wire coated with collagen and C1-PMC (loaded with 100 µM of C1). Scale bar for the images is 2.0 µm.

and N was noted in FESEM-EDX analysis as compared to bare Ti wire (Appendix, Figure A6.9, Figure 6.11A), which suggested the presence of collagen, PMC and C1 on the surface of Ti wire. In addition, FTIR analysis also indicated the presence of the signature stretching frequencies of PMC and C1 in C1-PMC-coated Ti wire (Figure 6.11B). The potential of C1-PMC-incorporated collagen-coated Ti wire in preventing MRSA cell adhesion and biofilm formation was ascertained by FESEM analysis. In case of collagen-coated Ti wire, a dense growth of MRSA biofilm exhibiting the quintessential cell-cell adhesion could be observed on the surface (Figure 6.11C, panel i). In comparison, the number of adhered MRSA cells were diminished in case of both PMC and C1-coated Ti wire (Figure 6.11C, panels ii-iii). Interestingly, C1-PMC

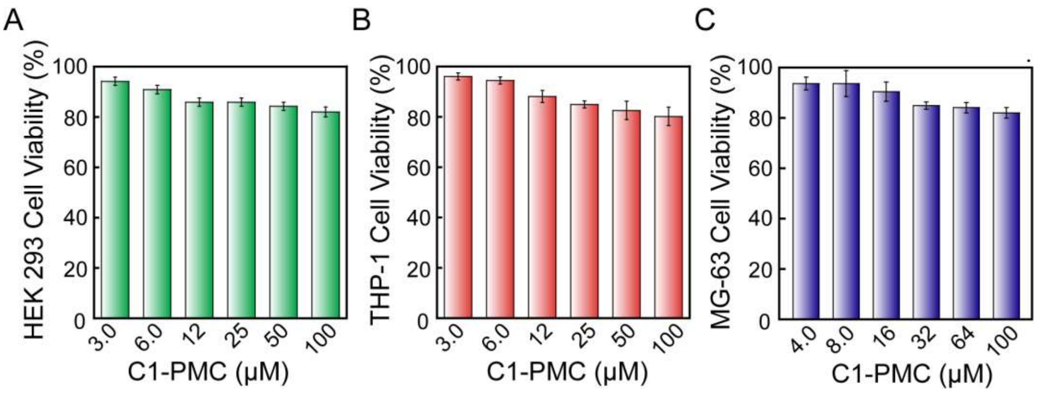

Figure 6.12. MTT assay-based evaluation of the cytotoxic effect of C1 loaded PF-127 micellar carrier (C1-PMC) against (A) HEK 293 cells, (B) THP-1 and (C) MG-63 cells.

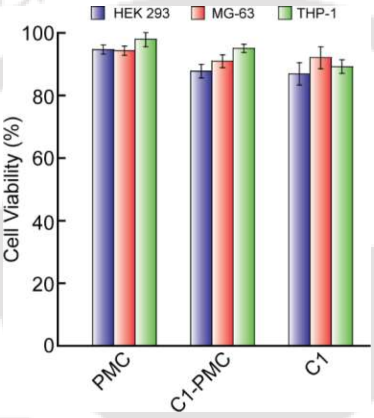

Figure 6.13. MTT assay-based determination of the cytotoxic effect of eluate from Ti-wire coated with various treatment regiments against HEK 293 cells, MG-63 and THP-1 cells. Data points acquired from six independent experimental samples were considered to determine mean ± standard deviation.

coating on Ti wire led to a dramatic decrease in the magnitude of MRSA adhesion onto Ti wire (Figure 6.11C, panels iv), which suggested that akin to the earlier observation in collagen adhesion assay (Figure 6.9), the anti-adhesion activity of both PMC as well as C1 could be leveraged in tandem to thwart MRSA adhesion and biofilm formation on the coated Ti wire. This also indicated that the payload micellar nanocarrier C1-PMC present on the surface of the Ti implant could readily disassemble and release the dual warheads PF-127 and the encapsulated C1 in adequate amounts and thereby prevent adhesion of MRSA on the implant surface. Overall, the results emerging from the current investigation compares well with previous studies, which describe functionalization of Ti-based implants for minimizing the risk of pathogen colonization (Ao *et al*., 2019; Hu *et al*., 2012).

In order to test the therapeutic utility of C1-PMC as an anti-adhesive arsenal on an orthopaedic implant, it was pertinent to assess its toxic potential. C1-PMC was observed to be non-toxic to all the tested cell lines at the highest loading concentrations of 50 µM and 100 µM C1 (Figure 6.12). This augers well from a therapeutic point of view as it clearly indicated that the micellar nanocarrier rendered a slow release and thereby reduced the local concentration of C1, which resulted in curtailing the toxicity associated with high concentration of the ligand. It may also be mentioned here that the eluates from C1-PMC-coated Ti wire were also non-toxic to cultured HEK-293 cells, THP-1 cells and MG-63 cells (cell viability of ~80%), which suggested that the coated Ti wires were biocompatible (Figure 6.13). Based on these results, it was apparent that the developed C1-loaded micellar nanocarrier holds considerable potential as a surface active therapeutic to deter MRSA-mediated infection of an orthopaedic implant.

6.4 Significant Findings

The salient findings of the present study can be stated as follows:

1. Fluorescence-based experiments and plating revealed that the entrapment of MRSA in CT-DNA could be restored in presence of C1 as compared to treatment with MNase alone.
2. Flow cytometry and confocal microscope analysis indicated uptake of CT-DNA entrapped MRSA cells by activated THP-1 cells could be restored in presence of C1 in contrast to the low levels of uptake in case of treatment with MNase alone.
3. A Pluronic F-127 based nanomicellar carrier was developed for loading of C1. The payload nanocarrier (C1-PMC) with an average particle size ~69 nm exhibited a highest loading of ~171 µM at a loading concentration of 250 µM C1, with an encapsulation efficiency of ~ 68%.
4. The magnitude of release of C1 from C1-PMC was ~13 µM, ~31 µM and ~48 µM in simulated body fluid, citrate buffer and HEPES buffer, respectively.
5. The eluate from C1-PMC rendered MNase inhibition and was nontoxic to HEK 293 cells, MG-63 cells and THP-1 cells till 100 µM C1-PMC (loaded with 100 µM C1).

6. C1 alone rendered a dose-dependent inhibition of MRSA adhesion onto collagen. Treatment with C1-PMC (loaded with 100 µM C1) rendered a significant decrease in the extent of MRSA cell adhesion (~37%), in comparison to treatment with either PMC (~65%) or 20 µM C1 (~53%).
7. Inhibition of MRSA adhesion on collagen-coated Ti wire was observed upon treatment with C1-PMC. C1-PMC coated Ti wire was biocompatible as the eluates from the coated wire was nontoxic to HEK 293 cells, MG-63 cells and THP-1 cells.

Based on the leads emerging from the present study, the nano-micellar arsenal developed in the current study emerges as a potent anti-MRSA therapeutic and in future it would be worthwhile to test its efficacy for prevention of MRSA biofilm infection in an *in vivo* model.

In the following section, the essential findings emerging from the thesis work is summarized and the future perspective is highlighted.

SUMMARY AND FUTURE PERSPECTIVE

SUMMARY AND FUTURE PERSPECTIVE

Mitigation of MRSA infections in the clinic is challenging as the number of therapeutic antibiotics targeting clinical strains of MRSA are restricted. As new clinical strains of MRSA resistant to multiple therapeutic antibiotics keep emerging, there is an impending need to develop alternate and effective therapeutic approaches in order to counter life-threatening MRSA infections. The current study is an endeavor to address this important and contemporary issue and highlights the prospect of deploying small synthetic ligands and target the staphylococcal nuclease enzyme or MNase, which is a key virulence factor present in the pathogen. The important leads and the future prospect of the study is articulated in the following section:

1. The present study describes the prospect of an anthraquinone-based ligand (C1), which could effectively inhibit MNase as well as render considerable distortion to the β-sheet content present in MNase. Mechanistic studies indicated that C1 rendered a non-competitive inhibition and decreased both the turnover number as well as catalytic efficiency of MNase. Interestingly, C1 was non-toxic to HEK 293 cells till a concentration of 12.5 µM, which was significantly higher than the concentration required for MNase inhibition. This result implies that the ligand bears a high therapeutic index and it highlights the prospect of the ligand as an anti-MRSA therapeutic.

2. A potentially therapeutic C1-loaded HSA nanocarrier (C1-HNC) was developed, which rendered a sustained and protease-triggered release of the payload in presence of the cell-free extract of a clinical MRSA strain. The nanocarrier could retain the activity of C1 as the eluates from C1-HNC could significantly inhibit MNase-catalyzed DNA cleavage. Based on the biocompatibility of C1-HNC, it would be worthwhile in future to conduct *in vivo* experiments in order to ascertain the potential of the developed payload nanocarrier in anti-MRSA therapy.

3. The *in vitro* model experiments highlighted an exciting prospect for the benzimidazole-based ligand C2 as it could significantly inhibit MNase, preserve

the integrity of the DNA scaffold and promote higher sequestration of MRSA by DNA, which in turn, enhanced the uptake of the DNA-entrapped-pathogen by activated macrophage-like cells. Hence, the ligand could reinforce the potency of the pathogen entrapment machinery and bolster the immune cells to effectively engulf MRSA. Interestingly, the ligand C2 was essentially non-toxic to cultured HEK 293 cells and activated THP-1 cells and displayed a high therapeutic index. In future, it would be interesting to further consolidate the potential of the ligand C2 by selecting *in vivo* infection models.

4. In continuation of the efforts to identify and characterize synthetic MNase inhibitors, model *in vitro* experiments demonstrated that the napthalimide-based ligand C1 could inhibit MNase and foster MRSA entrapment in DNA, which in turn enhanced pathogen uptake by activated macrophage-like cells. The results emerging from the study thus presents a guiding design principle for generating therapeutics that can curb virulence, and restore the efficacy of host innate immune response for mitigation of MRSA infections.

5. Interestingly, the napthalimide-based ligand C1 was multifunctional as it could also inhibit MRSA adhesion onto collagen. A pluronic F-127 nano-micellar carrier loaded with C1 was developed, wherein the anti-adhesion activity of both the carrier as well as the payload was harnessed in tandem, resulting in significant inhibition of MRSA adhesion onto collagen. The biocompatible C1-loaded nano-micellar arsenal could effectively prevent MRSA biofilm formation on orthopaedic Ti wire. Based on the leads, it would be worthwhile in future to test efficacy of the nano-micellar arsenal as an implant-associated anti-adhesive coating for prevention of MRSA biofilm infection in an *in vivo* model.

The present study contributes to the continuous endeavor of the research community and presents potentially therapeutic synthetic MNase inhibitors that can not only curb the virulence of MRSA but also empower the host innate immune response for effective mitigation of infections caused by the pathogen. A cartoon indicating the salient findings of the present investigation is indicated in **Scheme 1**.

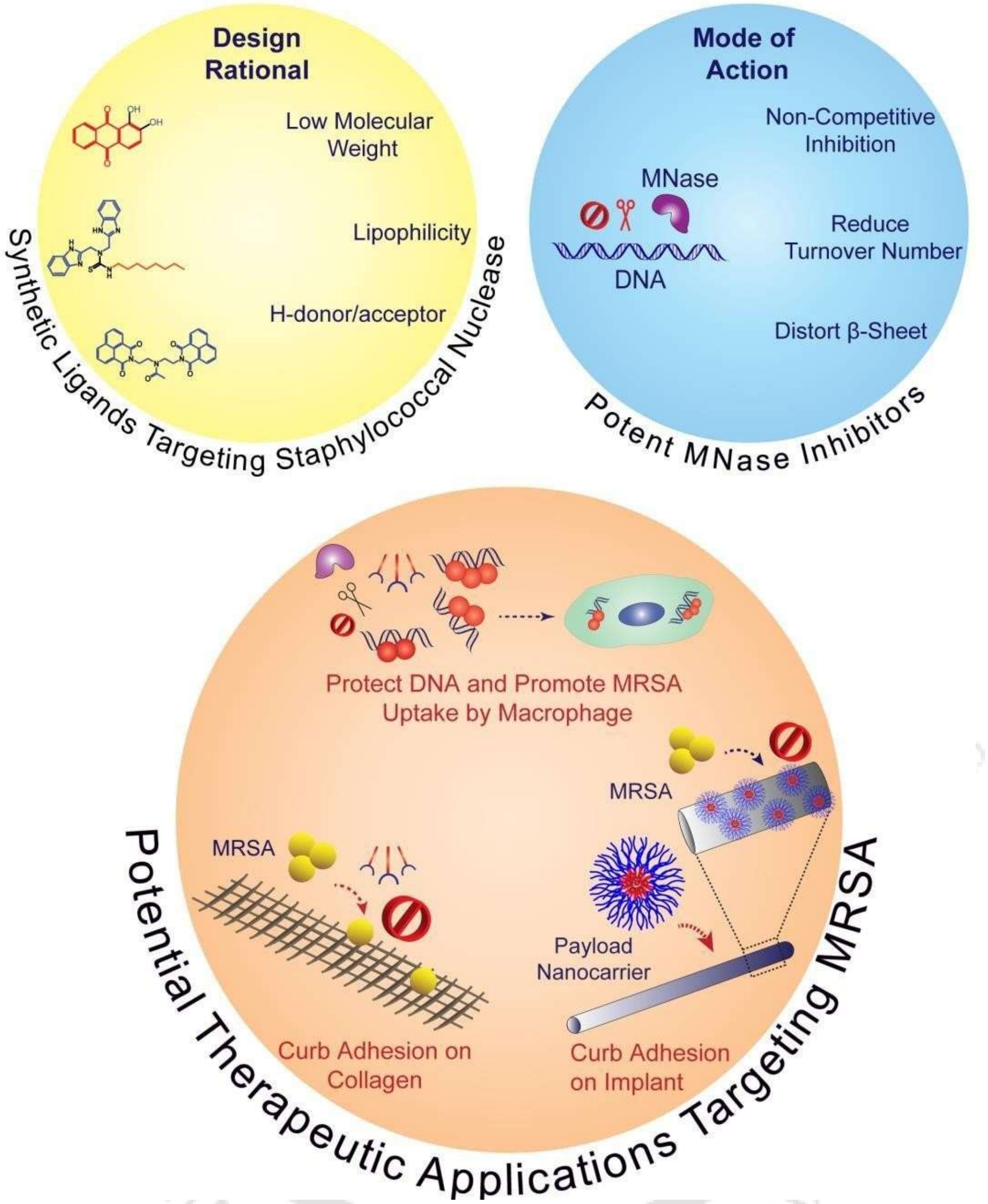

Scheme 1. Schematic representation of the significant findings of the present investigation.

BIBLIOGRAPHY

1. Adams, C.E. and Dancer, S.J. Dynamic transmission of Staphylococcus aureus in the intensive care unit. *International Journal of Environmental Research and Public Health*, **2020**, *17*, p.2109.

2. Ahmad-Mansour, N.; Loubet, P.; Pouget, C.; Dunyach-Remy, C.; Sotto, A.; Lavigne, J. P.; Molle, V. *Staphylococcus aureus* toxins: An update on their pathogenic properties and potential treatments. *Toxins* **2021**, *13*, 677.

3. Alder, K.D.; Lee, I.; Munger, A.M.; Kwon, H.K.; Morris, M.T.; Cahill, S.V.; Back, J.; Kristin, E.Y.; Lee, F.Y. Intracellular *Staphylococcus aureus* in bone and joint infections: a mechanism of disease recurrence, inflammation, and bone and cartilage destruction. *Bone* **2020**, *141*, 1-17.

4. Algammal, A.M.; Hetta, H.F.; Elkelish, A.; Alkhalifah, D.H.H.; Hozzein, W.N.; Batiha, G.E.S.; El Nahhas, N. and Mabrok, M.A. Methicillin-Resistant *Staphylococcus aureus* (MRSA): one health perspective approach to the bacterium epidemiology, virulence factors, antibiotic-resistance, and zoonotic impact. *Infection and Drug Resistance*, **2020**, 3255-3265.

5. Ao, H.; Yang, S.; Fan, Q.; Zhang, Q.; Zong, J.; Guo, S.; Zhang, X.; Tang, T. Improved antibacterial properties of collagen I/hyaluronic acid/quaternized chitosan multilayer modified titanium coatings with both contact-killing and release-killing functions. *Journal of Materials Chemistry B* **2019**, *7*, 1951-1961.

6. Archer, N. K.; Mazaitis M. J.; Costerton J. W.; Leid J. G.; Powers M. E.; Shirtliff M. E. *Staphylococcus aureus* biofilms Properties, regulation and roles in human disease. *Virulence* **2011**, *2*, 445.

7. Arciola, C.R.; Campoccia, D.; Montanaro, L. Implant infections: adhesion, biofilm formation and immune evasion. *Nature Reviews Microbiology* **2018**, *16*, 397-409.

8. Arciola, C.R.; Campoccia, D.; Speziale, P.; Montanaro, L.; Costerton, J.W. Biofilm formation in *Staphylococcus* implant infections. A review of molecular mechanisms and implications for biofilm-resistant materials. *Biomaterials* **2012**, *33*, 5967-5982.

9. Askarian, F.; Wagner, T.; Johannessen, M.; Nizet, V. *Staphylococcus aureus* modulation of innate immune responses through Toll-like (TLR), (NOD)-like (NLR) and C-type lectin (CLR) receptors. *FEMS Microbiology Review* **2018**, *42*, 656-671.

10. Bajaj, M.; Pandey, S. K.; Nain, T.; Brar, S. K.; Singh, P.; Singh, S.; Wangoo, N.; Sharma, R. K. Stabilized cationic dipeptide capped gold/silver nanohybrids: towards enhanced antibacterial and antifungal efficacy. *Colloids and Surfaces B Biointerfaces* **2017**, *158*, 397-407.

11. Balasubramanian, D.; Harper, L.; Shopsin, B. and Torres, V.J. *Staphylococcus aureus* pathogenesis in diverse host environments. *Pathogens and disease*, **2017**, *75*, ftx005.

12. Basak, R.; Bandyopadhyay R. Encapsulation of hydrophobic drugs in Pluronic F127 micelles: effects of drug hydrophobicity, solution temperature, and pH. *Langmuir*, **2013,** 29, 4350-4356.

13. Bennett, M.R.; Thomsen, I.P. Epidemiological and clinical evidence for the role of toxins in S. aureus human disease. *Toxins*, **2020**, *12*, 408.

14. Berends, E.T.; Horswill, A.R.; Haste, N.M.; Monestier, M.; Nizet, V.; von Kockritz-Blickwede, M. Nuclease expression by *Staphylococcus aureus* facilitates escape from neutrophil extracellular traps. *Journal of Innate Immunity* **2010**, *2*, 576-586.

15. Bhattacharya, M.; Berends, E.T.; Chan, R.; Schwab, E.; Roy, S.; Sen, C.K.; Torres, V. J.; Wozniak, D.J. *Staphylococcus aureus* biofilms release leukocidins to elicit extracellular trap formation and evade neutrophil-mediated killing. *Proceedings of the National Academy of Science* **2018**, *115*, 7416-7421.

16. Bhattacharya, M.; Berends, E.T.; Zheng, X.; Hill, P.J.; Chan, R.; Torres, V.J. and Wozniak, D.J. Leukocidins and the nuclease Nuc prevent neutrophil-mediated killing of *Staphylococcus aureus* biofilms. *Infection and Immunity* **2020**, *88*, e00372-20.

17. Bhattacharyya, S.; Ghosh, S.S. Transmembrane TNFα-expressed macrophage membrane-coated chitosan nanoparticles as cancer therapeutics. *ACS Omega* **2020**, *5*, 1572-1580.

18. Borah, N.; Nayak, B.; Gogoi, A.; Das, G. A benzimidazole-based non-symmetrical tripodal receptor for the ratiometric fluorescence sensing of fluoride ions and solid state recognition of sulfate ions. *New Journal of Chemistry*. **2019**, *43*, 16497-16505.

19. Boussion, K.; Zappella, N.; Grall, N.; Ribeiro-Parenti, L.; Papin, G. and Montravers, P. Epidemiology, clinical relevance and prognosis of staphylococci in hospital-acquired postoperative intra-abdominal infections: an observational study in intensive care unit. *Scientific Reports* **2021**, *11*, 5884.

20. Brinkmann, V.; Reichard, U.; Goosmann, C.; Fauler, B.; Uhlemann, Y.; Weiss, D.S.; Weinrauch, Y.; Zychlinsky, A. Neutrophil extracellular traps kill bacteria. *Science* **2004**, *303*, 1532-1535.

21. Brown, M. H.; Skurray, R. A. Staphylococcal multidrug efflux pump protein QacA. *Journal of Molecular Microbiology and Biotechnology* **2001**, *3*, 163-170.

22. Cassat J.E.; Hammer, N.D.; Campbell, J.P.; Benson, M.A.; Perrien, D.S.; Mrak, L.N.; Smeltzer, M.S.; Torres, V. J.; Skaar, E. P. A secreted bacterial protease tailors the *Staphylococcus aureus* virulence repertoire to modulate bone remodeling during osteomyelitis. *Cell Host Microbe* **2013**, *13*, 759-772.

23. CDC. Antibiotic Resistance Threats in the United States, 2019. Atlanta, GA: U.S. Department of Health and Human Services, CDC; 2019. www.cdc.gov/DrugResistance/Biggest-Threats.html DOI:

24. Chaiken, I.M.; Anfinsen, C.B. A solid phase synthetic study of the active site region of Staphylococcal Nuclease-T'. *Journal of Biological Chemistry* **1971**, *246*, 2285-2290.

25. Chambers, H. F.; Deleo, F. R.; Waves of resistance: *Staphylococcus aureus* in the Antibiotic Era. *Nature Reviews. Microbiology* **2010,** *7*, 629–641.

26. Chanput, W.; Mes, J.J.; Wichers, H.J.; THP-1 cell line: an *in vitro* cell model for immune modulation approach. *International. Immunopharmacology* **2014**, *23*, 37-45.

27. Chen, Y. Y.; Gopala, L.; Bheemanaboina, R. R. Y.; Liu, H. B.; Cheng, Y.; Geng, R. X.; Zhou, C. H. Novel naphthalimide aminothiazoles as potential multitargeting antimicrobial agents. *ACS Medicinal Chemistry Letters* **2017**, *8*, 1331-1335.

28. Cheung, G.Y.; Bae, J.S. and Otto, M. Pathogenicity and virulence of *Staphylococcus aureus*. *Virulence*, **2021**, *12*, 547-569.

29. Choi, S. J.; Sperinde, J. J.; Szoka Jr F. C. Identification of a deoxyribonuclease I inhibitor from a phage-peptide library. *Molecules and Cells* **2005**, *19*, 54-59.

30. Costa, S. S.; Viveiros, M.; Rosato, A. E.; Melo-Cristino, J.; Couto, I. Impact of efflux in the development of multidrug resistance phenotypes in *Staphylococcus aureus*. *BMC Microbiology* **2015**, *15*, 232.

31. Cotton, F.A.; Hazen Jr, E. E.; Legg, M. J. Staphylococcal nuclease: Proposed mechanism of action based on structure of enzyme—thymidine 3′, 5′-bisphosphate—calcium ion complex at 1.5-Å resolution. *Proceedings of the National Academy of Sciences* **1979**, *76*, 2551-2555.

32. Craft, K.M.; Nguyen, J. M.; Berg, L. J.; Townsend, S.D. Methicillin-resistant *Staphylococcus aureus* (MRSA): antibiotic-resistance and the biofilm phenotype. *MedChemComm* **2019**, *10*, 1231-1241.

33. Danesh, L. A.; Nejad, Z. S.; Sarmadian, H.; Fooladvand, S.; van Belkum, A.; Ghaznavi-Rad, E. Elimination of *Staphylococcus aureus* nasal carriage in intensive care patients lowers infection rates. *European Journal of Clinical Microbiology & Infectious Diseases* **2020**, *39*, 333-338.

34. Danhier, F.; Ansorena, E.; Silva, J. M.; Coco, R.; Le Breton, A.; Preat, V. PLGA-based nanoparticles: an overview of biomedical applications. *Journal of Control Release* **2012**, *161*, 505-522.

35. Davis A.; Moore I. B.; Parker D. S.; Taniuchi H. Nuclease B: A Possible Precursor of Nuclease A, an Extracellular Nuclease of *Staphylococcus aureus*. *The Journal of Biological Chemistry* **1977**, *252*, 6544.

36. De la Fuente-Nunez, C.; Reffuveille, F.; Fernandez, L.; Hancock, R. E. Bacterial biofilm development as a multicellular adaptation: antibiotic resistance and new therapeutic strategies. *Current Opinion in Microbiology* **2013**, *16*, 580-589.

37. de Vor, L.; Rooijakkers, S. H. M.; van Strijp, J. A. G. Staphylococci evade the innate immune response by disarming neutrophils and forming biofilms. *FEBS Letters* **2020**, *594*, 2556-2569.

38. De, S. and Das, G. Exploring the Aggregation and Light-Harvesting Aptitude of Naphthalimide-Based Amphiphile and Non-amphiphile AIEgen. *Langmuir*, **2022**, *38*, 6158-6163.

39. De, S.; Das, G. Self-assembly and desulfurization mediated Turn-ON mercury sensing in aqueous media by tripodal synthetic amphiphile chemosensors. *Dyes and Pigments*, **2021**, *195*, 109659.

40. Dey, P.; Mukherjee, S.; Das, G.; Ramesh, A. Micellar chemotherapeutic platform based on a bifunctional salicaldehyde amphiphile delivers a “combo-effect” for heightened killing of MRSA. *Journal of Materials Chemistry B* **2018**, *6*, 2116-2125.

41. Dey, P.; Puppala, E.R.; Naidu, V.G.M.; Das, G.; Ramesh, A. Multifunctional synthetic amphiphile for niche therapeutic applications: mitigation of MRSA biofilms and potential in wound healing. *ACS Applied Bio Materials* **2020**, *3*, 8830-8840.

42. Dickey, S. W.; Cheung G. Y.C.; Otto, M. Different drugs for bad bugs: antivirulence strategies in the age of antibiotic resistance. *Nature Reviews Drug Discovery* **2017,** *16*, 457-471.

43. El-Aleam, A.; Rehab H.; George, R. F.; Georgey, H. H.; Abdel-Rahman, H. M. Bacterial virulence factors: a target for heterocyclic compounds to combat bacterial resistance. *RSC Advances* **2021**, *11*, 36459-36482.

44. Elasri, Mohamed O.; J. R. Thomas.; R. A. Skinner.; J. S. Blevins., K. E. Beenken.; C. L. Nelson.; M. S. Smelter. *Staphylococcus aureus* collagen adhesin contributes to the pathogenesis of osteomyelitis. Bone **2002,** *30*, 275-280.

45. Elzoghby, A. O.; Samy, W. M.; Elgindy, N. A. Albumin-based nanoparticles as potential controlled release drug delivery systems. *Journal of Control. Release* **2012**, *157*, 168-182.

46. Emami, A. S. J.; Tuszynski, J. A.; Lavasanifar, A. The uniqueness of albumin as a carrier in nanodrug delivery. *Molecular Pharmaceutics* **2021**, *18*, 1862-1894.

47. Emami, S.; Esmaili, Z.; Dehghan, G.; Bahmani, M.; Hashemi, S.M.; Mirzaei, H.; Shokrzadeh, M.; Moradi, S.E. Acetophenone benzoylhydrazones as antioxidant agents: synthesis, in vitro evaluation and structure-activity relationship studies. *Food Chemistry* **2018**, *268*, 292-299.

48. Fair, R. J., Tor, Y. Antibiotics and bacterial resistance in the 21st century. *Perspectives in Medicinal Chemistry* **2014,** 25–64.

49. Floyd, J. L.; Smith, K. P.; Kumar, S. H.; Floyd, J. T.; Varela, M. F. LmrS is a multidrug efflux pump of the major facilitator superfamily from *Staphylococcus aureus*. *Antimicrob. Agents Chemother.* **2010**, *54*, 5406-5412.

50. Ford, C. A.; Hurford, I. M.; Cassat, J. E. Antivirulence strategies for the treatment of *Staphylococcus aureus* infections: a mini review. *Frontiers in Microbiology* **2021**, *11*, 632706.

51. Forson, A.M.; Rosman, C.W.; Van Kooten, T.G.; van der Mei, H.C.; Sjollema, J. Micrococcal nuclease stimulates *Staphylococcus* aureus biofilm formation in a murine implant infection model. *Frontiers in Cellular and Infection Microbiology* **2022**, *11*, 799845.

52. Foster, T.J.; Geoghegan, J.A.; Ganesh, V.K.; Hook, M. Adhesion, invasion and evasion: the many functions of the surface proteins of *Staphylococcus aureus*. *Nature Reviews Microbiology* **2014**, *12*, 49-62.

53. Friesen J, Neuber R, Fuhrmann J, Kietzmann H, Wenzel T, Schaumburg F, Müller M, Ignatius R. Panton-Valentine leukocidin-positive Staphylococcus aureus in skin and soft tissue infections from primary care patients. *Clinical Microbiology and Infection* **2020,** 26, 1416.e1-1416.e4.

54. Gajic, M.; Knez, D.; Sosic, I.; Mravljak, J.; Meden, A.; Kosak, U.; Leitzbach, L.; George, S.; Hofmann, B.; Zivkovic, A.; Steinhilber, D. Repurposing of 8-hydroxyquinoline-based butyrylcholinesterase and cathepsin b ligands as potent nonpeptidic deoxyribonuclease I inhibitors. *ChemMedChem* **2022**, *17*, 202100694.

55. Gajic, M.; Knez, D.; Sosic, I.; Mravljak, J.; Meden, A.; Kosak, U.; Leitzbach, L.; George, S.; Hofmann, B.; Zivkovic, A.; Steinhilber, D. Repurposing of 8-hydroxyquinoline-based butyrylcholinesterase and cathepsin b ligands as potent nonpeptidic deoxyribonuclease I inhibitors. *ChemMedChem* **2022**, *17*, 202100694

56. Ghimire, A.; Song, J. Anti-periprosthetic infection strategies: from implant surface topographical engineering to smart drug-releasing coatings. *ACS Applied Materials & Interfaces*, **2021,** *13*, 20921-20937.

57. Ghosh, S.; Kuchlyan, J.; Banik, D.; Kundu, N.; Roy, A.; Banerjee, C.; Sarkar, N. Organic additive, 5-methylsalicylic acid induces spontaneous structural transformation of aqueous pluronic triblock copolymer solution: a spectroscopic investigation of interaction of curcumin with pluronic micellar and vesicular aggregates. *The Journal of Physical Chemistry B* **2014**, *118*, 11437-11448.

58. Gong, H. H.; Baathulaa, K.; Lv, J. S.; Cai, G. X.; Zhou, C. H. Synthesis and biological evaluation of Schiff base-linked imidazolyl naphthalimides as novel potential anti-MRSA agents. *MedChemComm* **2016**, *7*, 924-931.

59. Gonzalez J. G.; Hernandez F. J. Nuclease activity: an exploitable biomarker in bacterial infections. *Expert Review of Molecular Diagnostics* 2022, 22, 265-294.

60. Gordon, R.J.; Lowy, F.D. Pathogenesis of methicillin-resistant *Staphylococcus aureus* infection. *Clinical Infectious Diseases* **2008**, *46*, 350.

61. Goswami, S.; Thiyagarajan, D.; Das, G.; Ramesh, A. Biocompatible nanocarrier fortified with a dipyridinium-based amphiphile for eradication of biofilm. *ACS Applied Materials & Interfaces* **2014**, *6*, 16384-16394.

62. Guerra F.E.; Borgogna, T. R.; Patel, D. M.; Sward, E. W.; Voyich, J. M. Epic immune battles of History: neutrophils vs. *Staphylococcus aureus*. *Frontiers in Cellular and Infection Microbio*logy **2017**, *7*, 286.

63. Guex, N.; Peitsch, M. C. SWISS-MODEL and the Swiss-PdbViewer: an environment for comparative protein modeling. *Electrophoresis* **1997**, *18*, 2714-2723.

64. Gunther, F.; Wabnitz, G.H.; Stroh, P.; Prior, B.; Obst, U.; Samstag, Y.; Wagner, C.; Hansch, G.M. Host defence against *Staphylococcus aureus* biofilms infection: phagocytosis of biofilms by polymorphonuclear neutrophils (PMN). *Molecular Immunology* **2009**, *46*, 1805-1813.

65. Guo, Y.; Song, G.; Sun, M.; Wang, J. and Wang, Y. Prevalence and therapies of antibiotic-resistance in *Staphylococcus aureus*. *Frontiers in cellular and infection microbiology*, **2020**, *10*, 107.

66. Hall, C. W.; Mah, T. F. Molecular mechanisms of biofilm-based antibiotic resistance and tolerance in pathogenic bacteria. *FEMS Microbiology Rev*iew **2017**, *41*, 276-301.

67. Hasanien, Y.A.; Nassrallah, A.A.; Zaki, A.G.; Abdelaziz, G. Optimization, purification, and structure elucidation of anthraquinone pigment derivative from *Talaromyces purpureogenus* as a novel promising antioxidant, anticancer, and kidney radio-imaging agent. *Journal of Biotechnology* **2022**, *356*, 30-41.

68. Heins J. N.; Suriano R.; Taniuchi H.; Anfinsen C. B. Characterization of a Nuclease Produced by *Staphylococcus aureus*. *Journal of Biological Chemistry* 1967, *242*, 1016.

69. Herzog, S.; Dach, F.; De Buhr, N.; Niemann, S.; Schlagowski, J.; Chaves-Moreno, D.; Neumann, C.; Goretzko, J.; Schwierzeck, V.; Mellmann, A.; Dubbers, A. High nuclease activity of long persisting *Staphylococcus aureus* isolates within the airways of cystic fibrosis patients protects against NET-mediated killing. *Frontiers in Immunology* **2019**, *10*, 2552.

70. Hetrick, E.M.; Schoenfisch, M.H. Reducing implant-related infections: active release strategies. *Chemical Society Reviews* **2006**, *35*, 780-789.

71. Hu, H.; Zhang, W.; Qiao, Y. Q.; Jiang, X. Y.; Liu, X.; Ding, C. Antibacterial activity and increased bone marrow stem cell functions of Zn-incorporated TiO2 coatings on titanium. *Acta Biomaterialia* **2012**, *8*, 904-915.

72. Huemer, M.; Mairpady Shambat, S.; Brugger, S.D. and Zinkernagel, A.S. Antibiotic resistance and persistence—Implications for human health and treatment perspectives. *EMBO Reports*, **2020**, *21*, e51034.

73. Ilic, B. S.; Kolarevic, A.; Kocic, G.; Smelcerovic, V. Ascorbic acid as DNase I inhibitor in prevention of male infertility. *Biochemical and Biophysical Research Communications* **2018**, *498*, 1073-1077.

74. Jang, S. Multidrug efflux pumps in *Staphylococcus aureus* and their clinical implications. *Journal of Microbiology* **2016**, *54*, 1-8.

75. Jin, C., Alenazy, R., Wang, Y., Mowla, R., Qin, Y., Tan, J.Q.E., Modi, N.D., Gu, X., Polyak, S.W., Venter, H. and Ma, S. Design, synthesis and evaluation of a series of 5-methoxy-2, 3-naphthalimide derivatives as AcrB inhibitors for the reversal of bacterial resistance. *Bioorganic & Medicinal Chemistry Letters*, **2019**, *29*, 882-889.

76. Josse, J.; Laurent, F. and Diot, A. Staphylococcal adhesion and host cell invasion: fibronectin-binding and other mechanisms. *Frontiers in microbiology*, **2017**, *8*, 2433.

77. Kaatz, G.W.; Thyagarajan, R.V.; Seo, S.M. Effect of promoter region mutations and MgrA overexpression on transcription of norA, which encodes a *Staphylococcus aureus* multidrug efflux transporter. *Antimicrobial Agents and Chemotherapy* **2005**, *49*, 161-169.

78. Karami, E.; Behdani, M.; Kazemi-Lomedasht, F. Albumin nanoparticles as nanocarriers for drug delivery: Focusing on antibody and nanobody delivery and albumin-based drugs. *Journal of Drug Delivery Science and Technology* **2020**, *55*, 101471

79. Kemegne, G.A.; Mkounga, P.; Essia Ngang, J.J.; Sado Kamdem, S.L.; Nkengfack, A.E. Antimicrobial structure activity relationship of five anthraquinones of emodine type isolated from *Vismia laurentii*. *BMC Microbiology* **2017**, *17*, 1-8.

80. Kessel, K. P. M. v.; Bestebroer, J.; van Strijp, J.A. Neutrophil-mediated phagocytosis of *Staphylococcus aureus*. *Frontiers in Immunology* **2014**, *5*, 467.

81. Kiedrowski, M.R.; Kavanaugh, J.S.; Malone, C.L.; Mootz, J.M.; Voyich, J.M.; Smeltzer, M.S.; Bayles, K.W.; Horswill, A.R. Nuclease modulates biofilm formation in community-associated methicillin-resistant *Staphylococcus aureus*. *PloS One* **2011**, *6*, e26714.

82. Kolarevic, A.; Ilic, B.S.; Anastassova, N.; Mavrova, A.T.; Yancheva, D.; Kocic, G. and Smelcerovic, A. Benzimidazoles as novel deoxyribonuclease I inhibitors. *Journal of Cellular Biochemistry* **2018**, *119*, 8937-8948.

83. Kolarevic, A.; Ilic, B.S.; Kocic, G.; Dzambaski, Z.; Smelcerovic, A.; Bondzic, B.P. Synthesis and DNase I inhibitory properties of some 4-thiazolidinone derivatives. *Journal of Cellular Biochemistry* **2019**, *120*, 264-274.

84. Kolarevic, A.; Yancheva, D.; Kocic, G.; Smelcerovic, A. Deoxyribonuclease inhibitors. *European Journal of Medicinal Chemistry* **2014**, *88*, 101-111.

85. Kong, C.; Neoh, H.M. and Nathan, S. Targeting *Staphylococcus aureus* toxins: a potential form of anti-virulence therapy. **2016** *Toxins*, *8*, 72.

86. Kouidhi, B.; Zmantar, T.; Hentati, H.; Bakhrouf, A. Cell surface hydrophobicity, biofilm formation, adhesives properties and molecular detection of adhesins genes in *Staphylococcus aureus* associated to dental caries. *Microbial Pathogenesis* **2010**, *49*, 14-22.

87. Krauss, J.L.; Roper, P.M.; Ballard, A.; Shih, C.C.; Fitzpatrick, J.A.; Cassat, J.E.; Ng, P.Y.; Pavlos, N.J. and Veis, D.J. Staphylococcus aureus infects osteoclasts and replicates intracellularly. *MBio*, **2019**, *10*, e02447-19.

88. Kwiecinski, J.M.; Horswill, A.R. *Staphylococcus aureus* bloodstream infections: pathogenesis and regulatory mechanisms. *Current Opinion in Microbiology* **2020**, *53*, 51-60.

89. Langer, K.; Anhorn, M.G.; Steinhauser, I.; Dreis, S.; Celebi, D.; Schrickel, N.; Faust, S.; Vogel, V. Human serum albumin (HSA) nanoparticles: reproducibility of preparation process and kinetics of enzymatic degradation. *International Journal of Pharmaceutics* **2008**, *347*, 109-117.

90. Lee, A. S.; Lencastre, H. D.; Garau, Javier.; Kluytmans, J.; Malhotra-kumar, S.; Peschel, A.; Harbarth, S. Methicillin-resistant *Staphylococcus aureus*. *Nature Reviews Disease Primer*s **2018**, *4*, 18033.

91. Lee, J.H.; Kim, Y.G.; Yong Ryu, S.; Lee, J. Calcium-chelating alizarin and other anthraquinones inhibit biofilm formation and the hemolytic activity of *Staphylococcus aureus*. *Scientific Reports* **2016**, *6*, 19267.

92. Lewies, A.; Wentzel, J. F.; Jordaan, A.; Bezuidenhout, C.; Du Plessis, L. H. Interactions of the antimicrobial peptide nisin Z with conventional antibiotics and the use of nanostructured lipid carriers to enhance antimicrobial activity. *International Journal of Pharmaceutics* **2017**, *526*, 244-253.

93. Li, X. Z.; Nikaido, H. Efflux-mediated drug resistance in bacteria: an update. *Drugs* **2009**, *69*, 1555-1623.

94. Liesenborghs, L.; Meyers, S.; Vanassche, T.; Verhamme, P. Coagulation: At the heart of infective endocarditis. *Journal of Thrombosis and Haemostasis*, **2020**, *18*, 995-1008.

95. Lu, Y.; Cai, W.J.; Ren, Z. and Han, P. The Role of Staphylococcal Biofilm on the Surface of Implants in Orthopedic Infection. *Microorganisms* **2022**, *10*, 1909.

96. Madani, A.; Garakani, K.; Mofrad, M. R. Molecular mechanics of *Staphylococcus aureus* adhesin, CNA, and the inhibition of bacterial adhesion by stretching collagen. *PloS one*, **2017,** 12, e0179601.

97. Malasala, S.; Ahmad, M.N.; Akunuri, R.; Shukla, M.; Kaul, G.; Dasgupta, A.; Madhavi, Y.V.; Chopra, S.; Nanduri, S. Synthesis and evaluation of new quinazoline-benzimidazole hybrids as potent anti-microbial agents against multidrug resistant *Staphylococcus aureus* and *Mycobacterium tuberculosis*. *European Journal of Medicinal Chemistry* **2021**, *212*, 112996.

98. Markovic, Z.; Jeremic, S.; Markovic, J.D.; Pirkovic, M.S.; Amic, D. Influence of structural characteristics of substituents on the antioxidant activity of some anthraquinone derivatives. *Computational and Theoretical Chemistry* **2016**, *1077*, 25-31.

99. Marques, M. R. C.; Loebenberg, R.; Almukainzi, M. Simulated biological fluids with possible application in dissolution testing. *Dissolution Technologies* **2011**, 15-28.

100. Masters, E.A.; Ricciardi, B.F.; Bentley, K.L.D.M.; Moriarty, T.F.; Schwarz, E.M. and Muthukrishnan, G. Skeletal infections: microbial pathogenesis, immunity and clinical management. *Nature Reviews Microbiology* **2022**, *20*, 385-400.

101. Meijer, K.; Weening, D.; de Vries, M.P.; Priebe, M.G.; Vonk, R.J.; Roelofsen, H. Quantitative proteomics analyses of activation states of human THP-1 macrophages. *Journal of Proteomics* **2015**, *128*, 164-172.

102. Mlynarczyk-Bonikowska, B.; Kowalewski, C.; Krolak-Ulinska, A.; Marusza, W. Molecular Mechanisms of Drug Resistance in *Staphylococcus aureus*. *International Journal of Molecular Sciences* **2022**, *23*, 8088.

103. Mo, Y.; Low, I.; Tambyah, S.K. and Tambyah, P.A. The socio-economic impact of multidrug-resistant nosocomial infections: a qualitative study. *Journal of Hospital Infection* **2019**, *102*, 454-460.

104. Moormeier, D.E.; Bose, J.L.; Horswill, A.R.; Bayles, K.W. Temporal and stochastic control of *Staphylococcus aureus* biofilm development. *MBio* **2014**, *5*, e01341-14.

105. Mukherjee, S.; Ramesh, A. Bacteriocin-producing strains of Lactobacillus plantarum inhibit adhesion of *Staphylococcus aureus* to extracellular matrix: quantitative insight and implications in antibacterial therapy. *Journal of Medical Microbiology*, **2015**, *64,* 1514-1526.

106. Mullick, P.; Das, G.; Aiyagari, R. 2-Dodecylmalonic acid-mediated synthesis of mineralized hydroxyapatite amicable for bone cell growth on orthopaedic implant. *Journal of Colloid and Interface Science*, **2022**, *608*, 2298-2309.

107. Nelson D. L.; Cox M. M. Lehninger Principles of Biochemistry, 6th Edition, W. H. Freeman, **2013**.

108. Nikaido, H. Multidrug resistance in bacteria. *Annual Review of Biochemistry* **2009**, *78*, 119–146.

109. Oliveira, W.F.; Silva, P.M.S.; Silva, R.C.S.; Silva, G.M.M.; Machado, G.; Coelho, L.C.B.B.; Correia, M.T.S. *Staphylococcus aureus* and *Staphylococcus epidermidis* infections on implants. *Journal of Hospital Infection* **2018**, *98*, 111-117.

110. Otto, M. Staphylococcal Biofilm, *Current Topics in Microbiology and Immunol*ogy **2008**, *322*, 207-228

111. Otto, M. *Staphylococcus aureus* toxins. *Current Opinion in Microbiology* **2014**, 17, 32-37.

112. Papayannopoulos, V. Neutrophil extracellular traps in immunity and disease. *Nature Reviews Immunology* **2018**, *18*, 134-147.

113. Patra, J.K.; Das, G.; Fraceto, L.F.; Campos, E.V.R.; Rodriguez-Torres, M.D.P.; Acosta-Torres, L.S.; Diaz-Torres, L.A.; Grillo, R.; Swamy, M.K.; Sharma, S.; Habtemariam, S. Nano based drug delivery systems: recent developments and future prospects. *Journal of Nanobiotechnology* **2018**, *16*, 1-33.

114. Petchiappan, A.; Chatterji, D. Antibiotic resistance: current perspectives. *ACS Omega* **2017**, *2*, 7400-7409.

115. Peterson, E.; Kaur, P. Antibiotic resistance mechanisms in bacteria: relationships between resistance determinants of antibiotic producers, environmental bacteria, and clinical pathogens. *Frontiers in Microbiology* **2018**, *9*, 2928.

116. Pietrocola, G.; Nobile, G.; Rindi, S.; Speziale, P. *Staphylococcus aureus* manipulates innate immunity through own and host-expressed proteases. *Frontiers in Cellular and Infection Microbiology* **2017**, *7*, 166.

117. Pitto-Barry, A.; Barry, N.P. Pluronic block-copolymers in medicine: from chemical and biological versatility to rationalisation and clinical advances. *Polymer Chemistry* **2014**, *5*, 3291-3297.

118. PJ, R. J.; Oluwafemi. O. S.; Thomas. S.; Adebola Omowunmi Oyedeji A. O. Recent advances in drug delivery nanocarriers incorporated in temperature-sensitive Pluronic F-127–A critical review. *Journal of Drug Delivery Science and Technology* **2022**, *72*, 103390.

119. Pongbangli, N.; Oniem, N.; Chaiwarith, R.; Nantsupawat, T.; Phrommintikul, A. and Wongcharoen, W. Prevalence of *Staphylococcus aureus* nasal carriage and surgical site infection rate among patients undergoing elective cardiac surgery. *International Journal of Infectious Diseases* **2021**, *106*, 409-414.

120. Ramachandran, E.; Raja, D. S.; Mike, J. L.; Wagner, T. R.; Zeller, M.; Natarajan, K. Evaluation on the role of terminal N-substitution in 6-methoxy-2-oxo-1, 2-dihydroquinoline-3-carbaldehyde thiosemicarbazones on the biological properties of new water-soluble nickel (II) complexes. *RSC Advances* **2012**, *2*, 8515-8525.

121. Rammler, D.H.; Bagdasarian, A.; Morris, F. Inhibition of micrococcal nuclease with 5'-deoxythymidine-5'-phosphonic acid containing oligomers. *Biochemistry* **1972**, *11*, 9-12.

122. Rizzetto, G.; Molinelli, E.; Radi, G.; Cirioni, O.; Brescini, L.; Giacometti, A.; Offidani, A. and Simonetti, O. MRSA and Skin Infections in Psoriatic Patients: Therapeutic Options and New Perspectives. *Antibiotics* **2022**, *11*, 1504.

123. Roque-Borda, C.A.; Da Silva, P.B.; Rodrigues, M.C.; Di Filippo, L.D.; Duarte, J.L.; Chorilli, M.; Vicente, E.F.; Garrido, S.S.; Pavan, F.R. Pharmaceutical nanotechnology: antimicrobial peptides as potential new drugs against WHO list of critical, high, and medium priority bacteria. *European Journal of Medicinal Chemistry* **2022**, *241*, 114640.

124. Rossi, F.; Diaz, L.; Wollam, A.; Panesso, D.; Zhou, Y.; Rincon, S.; Narechania, A.; Xing, G.; Di Gioia, T. S. R.; Doi, A.; Tran, T.; Reyes, J.; Munita, J. M.; Carvajal, L. P.; Hernandez-Roldan, A; Brandao, D.; van der Heijden, I. M.; Murray, B. E.; Planet, P. J.; Weinstock, G. M.; Arias, C. A. Transferable vancomycin resistance in a community-associated MRSA lineage. *The New England. Journal of Medicine* **2014**, *370*, 1524-1531.

125. Sahareen, T.; Dey, P.; Mukherjee, S.; Das, G.; Ramesh, A. Potential of pyridine amphiphiles as staphylococcal nuclease inhibitor. *ChemBioChem* **2018**, *19*, 1400-1408.

126. Sanchez, G.R.; Chaiken, I.M.; Anfinsen, C.B. Structure-function relationships at the active site of nuclease-T. *Journal of Biological Chemistry* **1973**, *248*, 3653-3659.

127. Scherr, T. D.; Heim, C. E.; Morrison, J. M.; Kielian, T. Hiding in plain sight: interplay between staphylococcal biofilms and host immunity. *Frontiers in Immunology* **2014**, *5*, 37.

128. Schilcher, K.; Andreoni, F.; Uchiyama, S.; Ogawa, T.; Schuepbach, R.A.; Zinkernagel, A.S. Increased neutrophil extracellular trap-mediated *Staphylococcus aureus* clearance through inhibition of nuclease activity by clindamycin and immunoglobulin. *The Journal of Infectious Diseases* **2014**, *210*, 473-482.

129. Segel I. H. Biochemical Calculations, 2nd Edition, Wiley, **2010**.

130. Sharma P.; Garg N.; Sharma A.; Capalash N.; Singh R. Nucleases of bacterial pathogens as virulence factors, therapeutic targets and diagnostic markers. *International Journal of Medical Microbiology* 2019, *309*, 151354.

131. Shimanovich, U.; Bernardes, G. J. L.; Knowles, T. P. J.; Cavaco-Paulo, A. Protein micro- and nano-capsules for biomedical applications. *Chemical Society Reviews* **2014** *43*, 1361-1371.

132. Smelcerovic, A.; Zivkovic, A.; Ilic, B.S.; Kolarevic, A.; Hofmann, B.; Steinhilber, D.; Stark, H. 4-(4-Chlorophenyl) thiazol-2-amines as pioneers of potential neurodegenerative therapeutics with anti-inflammatory properties based on dual DNase I and 5-LO inhibition. *Bioorganic Chemistry* **2020**, *95*, 103528.

133. Soe, Y.M.; Bedoui, S.; Stinear, T.P. and Hachani, A. Intracellular *Staphylococcus aureus* and host cell death pathways. *Cellular Microbiology* **2021**, *23*, e13317.

134. Song, D.; Ma, S. Recent development of benzimidazole-containing antibacterial agents. *ChemMedChem* **2016**, *11*, 646-659.

135. Souza, J.G.S.; Bertolini, M.M.; Costa, R.C.; Nagay, B.E.; Dongari-Bagtzoglou, A. and Barao, V.A.R. Targeting implant-associated infections: titanium surface loaded with antimicrobial. *IScience*, **2021**, *24*, 102008.

136. Speziale, P. and Pietrocola, G. *Staphylococcus aureus* induces neutrophil extracellular traps (NETs) and neutralizes their bactericidal potential. *Computational and Structural Biotechnology Journal*, **2021**, *19*, 3451-3457.

137. Srisuwan, S.; Tongtawe, P.; Srimanote, P.; Voravuthikunchai, S.P. Rhodomyrtone modulates innate immune responses of THP-1 monocytes to assist in clearing methicillin-resistant *Staphylococcus aureus*. *PloS One* **2014**, *9*, e110321.

138. Starr, T.; Bauler, T.J.; Malik-Kale, P.; Steele-Mortimer, O. The phorbol 12-myristate-13-acetate differentiation protocol is critical to the interaction of

THP-1 macrophages with *Salmonella typhimurium*. *PloS One* **2018**, *13*, e0193601.

139. Stoodley, P; Ehrlich, G.D.; Sedghizadehc, P.P.; Hall-Stoodley, L; Baratze, M. E.; Altmane, D.T.; Sotereanose, N.G.; Costertone, J.W.; DeMeoe, P. Orthopaedic biofilm infections, *Current Orthopaedic Practice* **2011**, *22*, 558–563.

140. Suck D.; Oefner C.; Kabschl W. Three-dimensional structure of bovine pancreatic DNase I at 2.5 Å resolution. *The EMBO Journal* **1984**, *3*, 2423-2430.

141. Swider, E.; Koshkina, O.; Tel, J.; Cruz, L. J.; de Vries, I. J. M.; Srinivas, M. Customizing poly(lactic-co-glycolic acid) particles for biomedical applications. *Acta Biomaterialia* **2018**, *73*, 38-51.

142. Tacconelli, E.; Carrara, E.; Savoldi, A.; Harbarth, S.; Mendelson, M.; Monnet, D.L.; Pulcini, C.; Kahlmeter, G.; Kluytmans, J.; Carmeli, Y.; Ouellette, M. Discovery, research, and development of new antibiotics: the WHO priority list of antibiotic-resistant bacteria and tuberculosis. *The Lancet Infectious Diseases* **2018**, *18*, 318-327.

143. Tam, K.; Torres, V.J. *Staphylococcus aureus* secreted toxins and extracellular enzymes. *Microbiology spectrum*, **2019**, *7*, 7-2.

144. Taniuchi H.; Anfinsen C. B.; Sodja A. The Amino Acid Sequence of an Extracellular Nuclease of *Staphylococcus aureus*. *Journal of Biological Chemistry* 1967, *242*, 4752.

145. Tarhini, M.; Pizzoccaro, A.; Benlyamani, I.; Rebaud, C.; Greige-Gerges, H.; Fessi, H.; Elaissari, A.; Bentaher, A. Human serum albumin nanoparticles as nanovector carriers for proteins: application to the antibacterial proteins “neutrophil elastase” and “secretory leukocyte protease inhibitor”. *International Journal of Pharmaceutics* **2020**, *579*, 119150

146. Tenland, E.; Pochert, A.; Krishnan, N.; Umashankar Rao, K.; Kalsum, S.; Braun, K.; Glegola-Madejska, I.; Lerm, M.; Robertson, B. D.; Linden, M.; Godaly, G. Effective delivery of the anti-mycobacterial peptide NZX in mesoporous silica nanoparticles. *PLoS ONE* **2019**, *14*, e0212858.

147. Thammavongsa, V.; Missiakas, D.M.; Schneewind, O. *Staphylococcus aureus* degrades neutrophil extracellular traps to promote immune cell death. *Science* **2013**, *342*, 863-866.

148. Thiyagarajan, D.; Das, G.; Ramesh, A. Amphiphilic cargo-loaded nanocarrier enhances antibiotic uptake and perturbs efflux: effective synergy for mitigation of methicillin-resistant *Staphylococcus aureus*. *ChemMedChem* **2017**, *12*, 1125-1132.

149. Thiyagarajan, D.; Das, G.; Ramesh, A. Extracellular DNA-targeting nanomaterial for effective elimination of biofilm. *ChemNanoMat* **2016**, *2*, 879-887.

150. Thiyagarajan, D.; Goswami, S.; Kar, C.; Das, G.; Ramesh, A. A prospective antibacterial for drug-resistant pathogens: a dual warhead amphiphile designed to track interactions and kill pathogenic bacteria by membrane damage and cellular DNA cleavage. *Chemical Communications* **2015**, *50*, 7434-7436.

151. Thomer, L.; Schneewind, O. and Missiakas, D. Pathogenesis of *Staphylococcus aureus* bloodstream infections. *Annual Review of Pathology: Mechanisms of Disease* **2016**, *11*, 343-364.

152. Tong, S.Y.; Davis, J.S.; Eichenberger, E.; Holland, T.L.; Fowler Jr, V.G. *Staphylococcus aureus* infections: epidemiology, pathophysiology, clinical manifestations, and management. *Clinical Microbiology Reviews* **2015**, *28*, 603-661.

153. Toprak, E.; Veres, A.; Michel, J. B.; Chait, R.; Hartl, D. L.; Kishony, R. Evolutionary paths to antibiotic resistance under dynamically sustained drug selection. *Nature Genetics* **2012**, *44*, 101-105.

154. Treter, J.; Bonatto, F.; Krug, C.; Soares, G.V.; Baumvol, I.J.R.; Macedo, A.J. Washing-resistant surfactant coated surface is able to inhibit pathogenic bacteria adhesion. *Applied Surface Science* **2014**, *303*, 147-154.

155. Truong-Bolduc, Q.C.; Hooper, D. C. Phosphorylation of MgrA and its effect on expression of the NorA and NorB efflux pumps of *Staphylococcus aureus*. *Journal of Bacteriology* **2010**, *192*, 2525-2534.

156. Tuon, F.F.; Suss, P.H.; Telles, J.P.; Dantas, L.R.; Borges, N.H. and Ribeiro, V.S.T. Antimicrobial Treatment of *Staphylococcus aureus* Biofilms. *Antibiotics* **2023**, *12*, 87.

157. Turner, N, A., Sharma-Kuinkel, B. K.; Maskarinec, S. A.; Eichenberger, E. M.; Shah, P. P.; Carugati, M.; Holland, T. L.; Fowler Jr., V, G. Methicillin-resistant *Staphylococcus aureus*: an overview of basic and clinical research. *Nature Reviews Microbiology* **2019**, *17*, 203-218.

158. Ulbrich, K.; Hekmatara, T.; Herbert, E.; Kreuter, J. Transferrin- and transferrin-receptor-antibody-modified nanoparticles enable drug delivery across the blood–brain barrier (BBB). *European Journal of Pharmaceutics and Biopharmaceutics* **2009**, *71*, 251-256.

159. van Kessel, K. P. M.; Bestebroer, J.; van Strijp, J. A. G. Neutrophil-mediated phagocytosis of *Staphylococcus aureus*. *Frontiers in Immun*ology **2014**, *5*, 467.

160. Varela, M.F.; Stephen, J.; Lekshmi, M.; Ojha, M.; Wenzel, N.; Sanford, L.M.; Hernandez, A.J.; Parvathi, A. and Kumar, S.H. Bacterial resistance to antimicrobial agents. *Antibiotics*, **2021**, *10*, 593.

161. Visansirikul, S.; Kolodziej, S.A. and Demchenko, A.V. *Staphylococcus aureus* capsular polysaccharides: a structural and synthetic perspective. *Organic & Biomolecular Chemistry*, **2020**, *18*, 783-798.

162. Visperas, A.; Santana, D.; Klika, A. K.; Higuera-Rueda, C.A.; Piuzzi, N.S. Current treatments for biofilm-associated periprosthetic joint infection and new potential strategies. *Journal of Orthopaedic Research* **2022**, *40*, 1477-1491.

163. von Kockritz-Blickwede, M.; Winstel, V. Molecular prerequisites for neutrophil extracellular trap formation and evasion mechanisms of *Staphylococcus aureus*. *Frontiers in Immunology* **2022**, *13*, 836278.

164. Wang, Y.; Zhao, N.; Jian, Y.; Liu, Y.; Zhao, L.; He, L.; Liu, Q. and Li, M. The pro-inflammatory effect of Staphylokinase contributes to community-associated *Staphylococcus aureus* pneumonia. *Communications Biology*, **2022**, *5*, 618.

165. Weigel, L. M.; Clewell, D. B.; Gill, S. R.; Clark, N. C.; McDougal, L. K.; Flannagan, S. E.; Kolonay, J. F.; Shetty, J.; Killgore, G. E.; Tenover, F. C. Genetic analysis of a high-level vancomycin-resistant isolate of *Staphylococcus aureus*. *Science* **2003**, *302*, 1569-1571.

166. Weinstein, Robert A.; Rabih O. Darouiche. Device-associated infections: a macroproblem that starts with microadherence. *Clinical infectious diseases*, **2001**, *33*, 1567-1572.

167. Whitfield, C.; Wear, S.S. and Sande, C. Assembly of bacterial capsular polysaccharides and exopolysaccharides. *Annual Review of Microbiology*, **2020**, *74*, 521-543.

168. Wojcik-Bojek, U.; Rozalska, B.; Sadowska, B. *Staphylococcus aureus* — A Known Opponent against Host Defense Mechanisms and Vaccine Development — Do We Still Have a Chance to Win ? *International Journal of Molecular Sciences*, **2022**, *23*, 948.

169. Wolfe, A.; Shimer Jr, G. H.; Meehan, T. Polycyclic aromatic hydrocarbons physically intercalate into duplex regions of denatured DNA. *Biochemistry* **1987**, *26*, 6392-6396.

170. World Health Organization (WHO). Antimicrobial resistance: Global report on surveillance (2014). Available from: http://www.who.int/drugresistance/documents/surveillancereport/en/

171. Wright, G. D. Molecular mechanisms of antibiotic resistance. *Chemical Communications* **2011,** *47*, 4055-4061.

172. Wu, H.; Jia, C.; Wang, X.; Shen, J.; Tan, J.; Wei, Z.; Wang, S.; Sun, D.; Xie, Z. and Luo, F. The impact of methicillin resistance on clinical outcome among patients with *Staphylococcus aureus* osteomyelitis: a retrospective cohort study of 482 cases. *Scientific Reports* **2023**, *13*, 7990.

173. Yamakami, K.; Tsumori, H.; Sakurai, Y.; Shimizu, Y.; Nagatoshi, K.; Sonomoto, K. Sustainable inhibition efficacy of liposome-encapsulated nisin on insoluble glucan-biofilm synthesis by *Streptococcus mutans*. *Pharmaceutical Bio*logy **2013**, *51*, 267-270.

174. Yeh, Y.C.; Huang, T.H.; Yang, S.C.; Chen, C.C.; Fang, J.Y. Nano-based drug delivery or targeting to eradicate bacteria for infection mitigation: a review of recent advances. *Frontiers in Chemistry* **2020**, *8*, 286.

175. Yi, X.; Lian, X.; Dong, J.; Wan, Z.; Xia, C.; Song, X.; Fu. Y.; Gong, T.; Zhang, Z. Co-delivery of pirarubicin and paclitaxel by human serum albumin nanoparticles to enhance antitumor effect and reduce systemic toxicity in breast cancers. *Molecular Pharmaceutics* **2015**, *12*, 4085-4098.

176. Yoshikawa, F. S. Y.; de Lima, F. J.; Sato, M. N.; Ramos, Y. A. L.; Aoki, V.; Orfali, R. L. Exploring the role of *Staphylococcus aureus* toxins in atopic dermatitis. *Toxins*, **2019**, *11*, 321.

177. Yu, J.; Jiang, F.; Zhang, F.; Hamushan, M.; Du, J.; Mao, Y.; Wang, Q.; Han, P.; Tang, J.; Shen, H. Thermonucleases contribute to *Staphylococcus aureus* biofilm formation in implant-associated infections–a redundant and complementary story. *Frontiers in Microbiology* **2021**, *12*, 687888.

178. Zha, G.F.; Preetham, H.D.; Rangappa, S.; Kumar, K.S.S.; Girish, Y.R.; Rakesh, K.P.; Ashrafizadeh, M.; Zarrabi, A.; Rangappa, K.S. Benzimidazole analogues as efficient arsenals in war against methicillin-resistance *Staphylococcus aureus* (MRSA) and its SAR studies. *Bioorganic Chemistry* **2021**, *115*, 105175.

179. Zhang, C.; Zhang, J.; Qin, Y.; Song, H.; Huang, P.; Wang, W.; Wang, C.; Li, C.; Wang, Y.; Kong, D. Co-delivery of doxorubicin and pheophorbide A by pluronic F127 micelles for chemo-photodynamic combination therapy of melanoma. *Journal of Materials Chemistry B* **2018**, *6*, 3305-3314.

180. Zhang, P. L.; Gopala, L.; Zhang, S. L.; Cai, G. X.; Zhou, C. H. An unanticipated discovery towards novel naphthalimide corbelled aminothiazoximes as potential anti-MRSA agents and allosteric modulators for PBP2a. *European Journal of Medicinal Chemistry* **2022**, *229*, 114050.

181. Zhang, X.; Hu, X. and Rao, X. Apoptosis induced by Staphylococcus aureus t oxins. *Microbiological research*, **2017**, *205*, 19-24.

APPENDIX

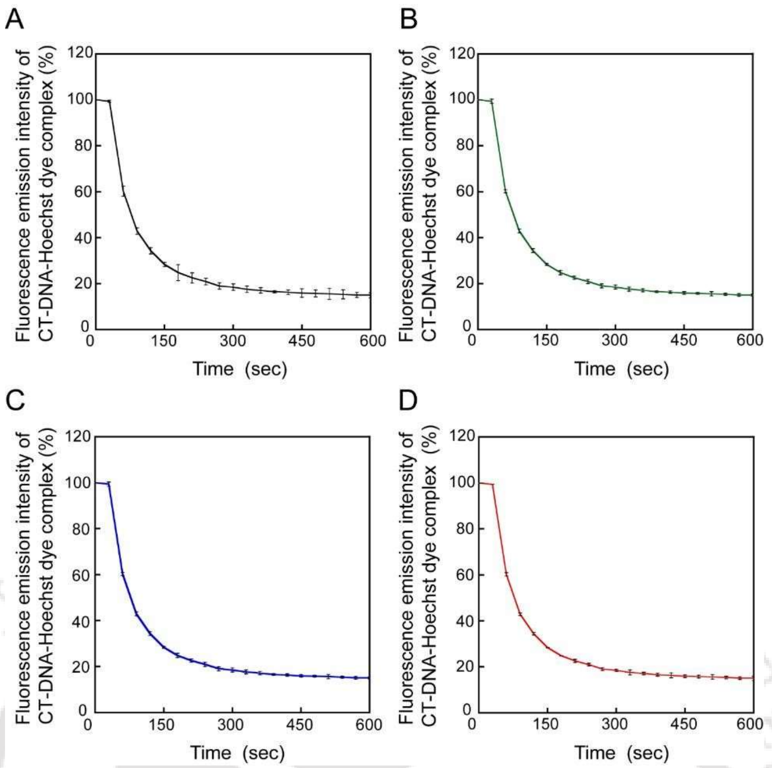

Figure A2.1. (A) Change in fluorescence emission intensity of CT-DNA Hoechst dye complex in presence of (A) MNase and (B-D) MNase in presence of C6. The concentration of C6 in the experiments were (B) 100 nM, (C) 600 nM and (D) 5.0 µM.

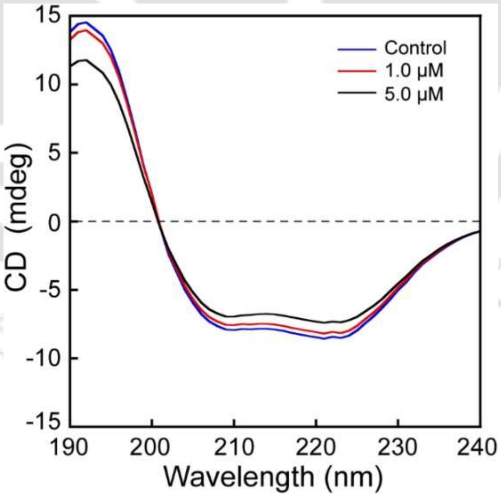

Figure A2.2. CD spectra of human serum albumin (HSA) measured in presence of an increasing concentration of C1.

Table A2.1. Statistical analysis for MNase inhibition rendered by ligands C1-C5.

Sl. No	Comparison Group	Significant Difference in MNase Inhibition*
1.	C1 (100 nM) versus C2 (100 nM)	Yes
2.	C1 (100 nM) versus C3 (100 nM)	Yes
3.	C1 (100 nM) versus C4 (100 nM)	Yes
4.	C1 (100 nM) versus C5 (100 nM)	Yes
5.	C1 (600 nM) versus C2 (600 nM)	Yes
6.	C1 (600 nM) versus C3 (600 nM)	Yes
7.	C1 (600 nM) versus C4 (600 nM)	Yes
8.	C1 (600 nM) versus C5 (600 nM)	Yes
9.	C1 (5.0 µM) versus C2 (5.0 µM)	No
10.	C1 (5.0 µM) versus C3 (5.0 µM)	Yes
11.	C1 (5.0 µM) versus C4 (5.0 µM)	Yes
12.	C1 (5.0 µM) versus C5 (5.0 µM)	Yes

* Significant difference implies *p* value < 0.001 based on analysis of variance (ANOVA) followed by all pairwise multiple comparisons (Holm-Sidak method) of relative MNase inhibition.

Table A2.2. Secondary structure analysis of HSA following interaction with C1.

Sample	Secondary Structure Content in HSA			
	α - Helix (%)	β - Sheet (%)	Turn/Loop (%)	Random Coil (%)
HSA	35.5	31.5	3.8	29.2
HSA + C1 (1.0 µM)	36.1	30.4	4.3	29.2
HSA + C1 (5.0 µM)	36.2	23.6	8.6	31.6

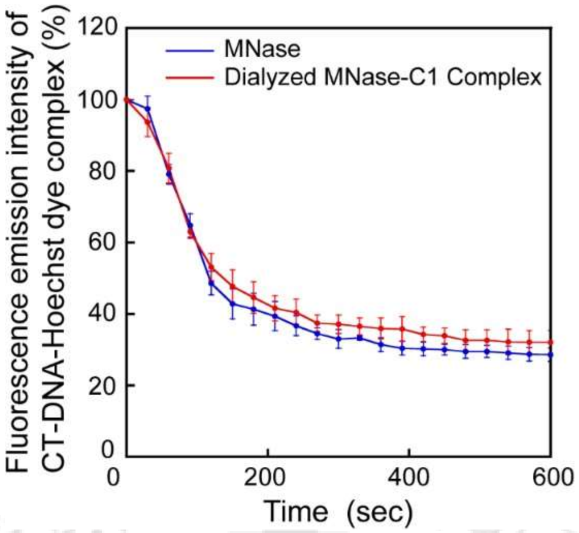

Figure A2.3. Change in fluorescence emission intensity of CT-DNA Hoechst dye complex inpresence of MNase and dialyzed sample of MNase-C1 complex.

Molecular Docking Studies

The crystal structure of DNase I (PDB ID 3DNI) and MNase (PDB ID 1EY0) was retrieved from PDB [http://www.rcsb.org/pdb/home/home.do]. Energy minimization of MNase and DNase I structure was done using Swiss Pdb Viewer 4.10 (Guex and Peitsch, 1997) and saved in .pdb format. Further, the structure was subjected to addition of hydrogens, addition of Kollman united atom charges and non-polar hydrogens. The ligand C1 was drawn using ChemDraw Ultra 8.0 and energy minimization of the molecule was performed using Chem3D Ultra 8.0 and savedin .pdb format. Docking of C1 with MNase and DNase I was accomplished by using AutoDock 4.2.5.1 version (http://autodock.scripps.edu/). For MNase, the grid was set at X = 40, Y= 30.803,Z= -4; dimensions (Å) at X= 52.000, Y= 42.000, Z= 38.000; spacing 0.375 Å. For DNase I, the grid was set at X=-42.811, Y=27.865, Z=13.246; dimensions (Å) at X=34.000, Y=38.000, Z=40.000; spacing 0.375 Å. By applying Lamarckian genetic algorithm, docking was performed between the target nucleases and C1 ligand in Autodock 4.2.5.1 version with 25 GA runs in separate sets. The generated .pdb file was analyzed using Protein-Ligand Interaction Profiler (PLIP) and the docked conformations were visualized using PyMOL version 1.7.4.5 from Schrodinger (www.pymol.org).

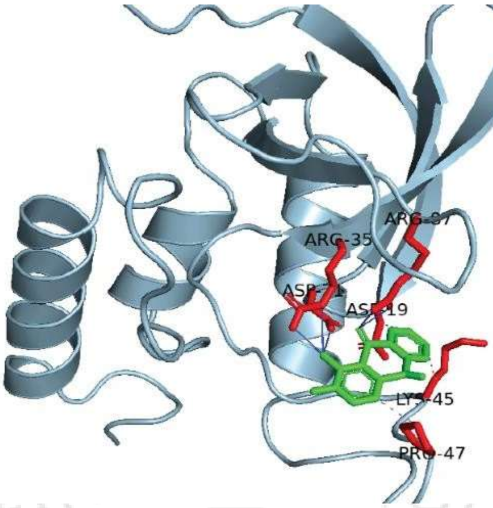

Figure A2.4. Docked structure of C1 with MNase.

Table A2.3. Binding interactions and binding energy for C1 with the amino acid residues of MNase determined in molecular docking studies.

Molecule	**Nature of Interaction**		**Binding energy (kcal/mol)**
	Hydrophobic Interaction	**Hydrogen Bonds**	
C1-MNase Complex	ASP (19) LYS (45) PRO (47)	(1) 21 ASP, Donor Angle-161.08, Distance H-A 2.15 Å, D-A 3.11 Å (2) 35 ARG, Donor Angle-120.96, Distance H-A 2.71 Å, D-A 3.33 Å (3) 35 ARG, Donor Angle-138.19, Distance H-A 1.76 Å, D-A 2.59 Å (4) 87 ARG, Donor Angle-141.55, Distance H-A 1.76 Å, D-A 2.62 Å (5) 87 ARG, Donor Angle-117.25, Distance H-A 3.04 Å, D-A 3.6 Å	-5.23

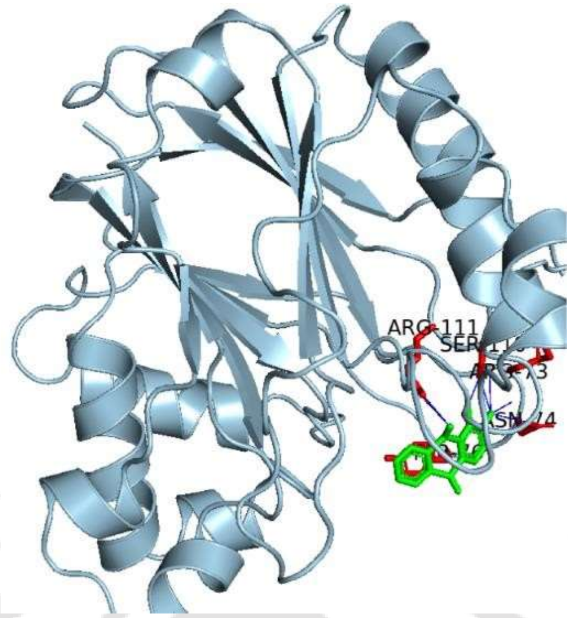

Figure A2.5. Docked structure of C1 with DNase I.

Table A2.4. Binding interactions and binding energy for C1 with the amino acid residues of DNase I determined in molecular docking studies.

Molecule	Nature of Interaction		Binding energy [kcal/mol]
	Hydrophobic Interaction	Hydrogen Bonds	
C1-DNase I	TYR (76)	(1) 73 ARG, Donor Angle-123.28, Distance H-A 3.32 Å, D-A 3.95 Å (2) 74 ASN, Donor Angle-138.94, Distance H-A 2.07 Å, D-A 2.89 Å (3) 110 SER, Donor Angle-177.83, Distance H-A 1.68 Å, D-A 2.68 Å (4) 111 ARG, Donor Angle-136.80, Distance H-A 2.74 Å, D-A 3.53 Å	-5.6

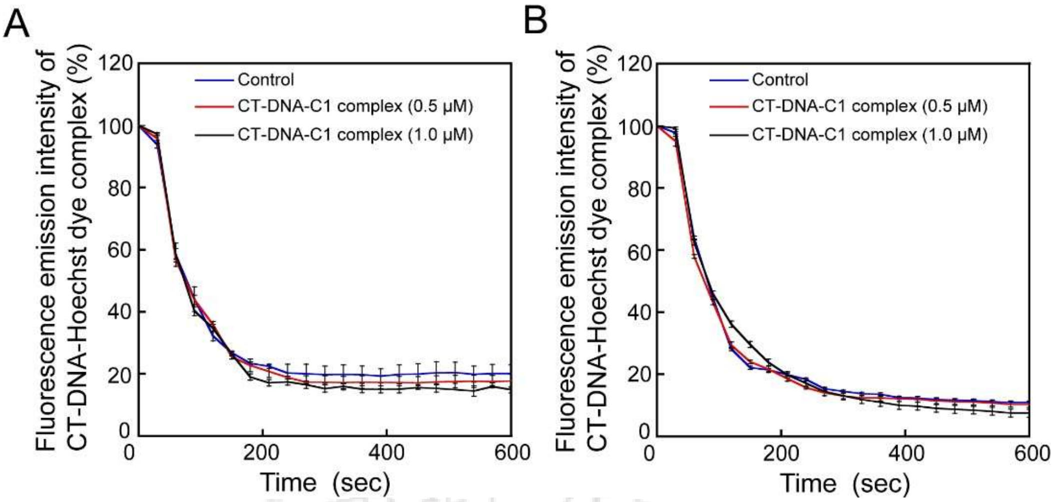

Figure A2.6. Change in fluorescence emission intensity for CT-DNA Hoechst dye-C1 preformed complex samples digested with MNase. The concentration of C1 in the preformed complex was 0.5 µM and 1.0 µM. The concentration of CT-DNA used in the experiments were (A) 0.5 µg mL^{-1} and (B) 1.0 µg mL^{-1}.

Table A2.5. Rate constant for CT-DNA Hoechst dye-C1 preformed complex samples digested with MNase.

Concentration of CT-DNA in preformed complex with C1 (µg mL^{-1})	Rate constant (s^{-1})		
	Control	Concentration of C1 in CT-DNA-C1 preformed complex	
		0.5 µM	1.0 µM
0.5	0.53	0.54	0.55
1.0	0.69	0.65	0.63

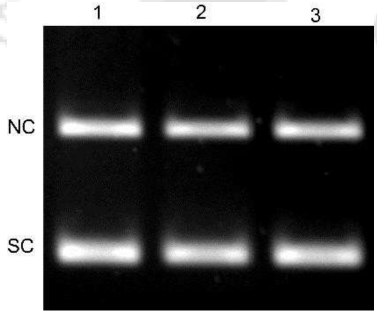

Figure A2.7. Agarose gel electrophoresis of (1) Undigested pUC18 plasmid DNA, (2-3) pUC18 plasmid DNA treated with 1.0 µM C1 and 30 mM EDTA, respectively. NC: Nicked circular DNA; SC: Supercoiled DNA.

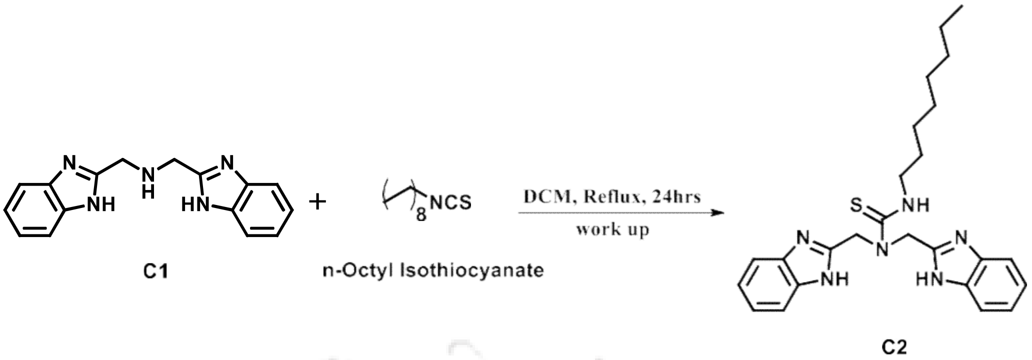

Figure A4.1. Schematic representation of the reaction for synthesis of C2.

Synthesis and characterization of ligand C2

N-octyl isocyanate (372 µL, 2 mmol) was refluxed and stirred with previously reported ligand Bis(2-benzimidazylmethyl) amine (C1) (Borah *et al.*, 2019) (554 mg, 2.0 mmol)in dry DCM for 24 h maintaining a molar ratio of 1:1. Evaporation of the brown colored solution and work up with CHCl3/H2O yields C2, 1,1-bis((1H-benzo[d]imidazol-2-yl)methyl)-3-octylthiourea. The compound was finally dried in vacuum over silica gel. The product C2 was obtained as a brown colored solid, which was characterized without further purification. The schematic for the synthesis of C2 is indicated in Figure A4.1.

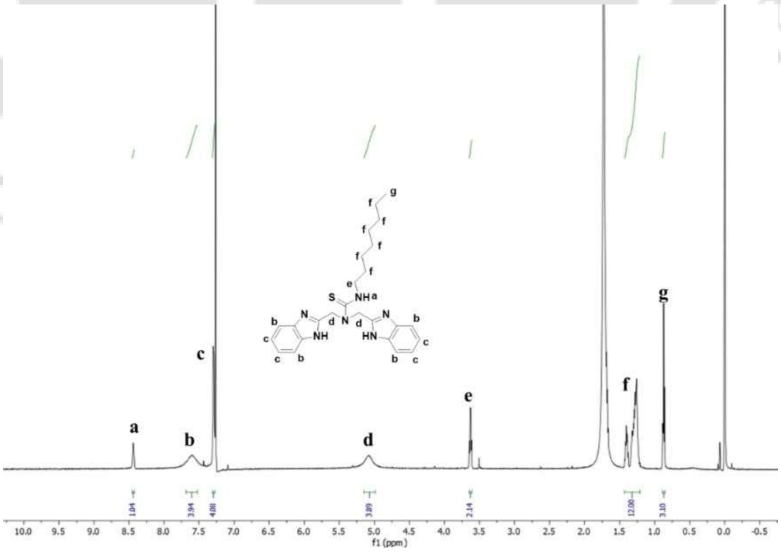

Figure A4.2. ^{1}H NMR of C2 in DMSO-d$_6$ at room temperature.

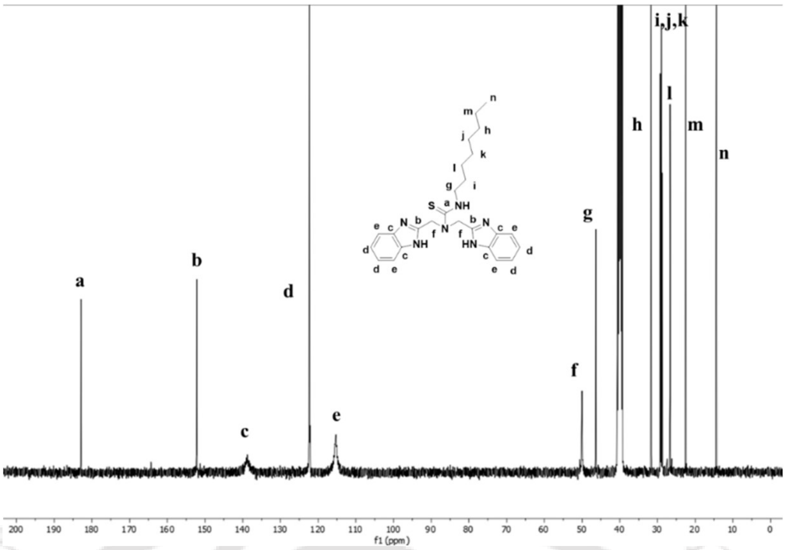

Figure A4.3. ^{13}C NMR of C2 in DMSO-d$_6$ at room temperature.

C2: ^{1}H NMR (600 MHz, CDCl$_3$) δ 8.44 (s, 1H), 7.60 (m, 4H), δ 7.29 (m, 4H)5.08 (s, 4H), 3.63 (t, J = 4.8 Hz, 2H), 1.46 – 1.20 (m, 12H), 0.87 (t, J = 6.9 Hz, 3H).
^{13}C NMR (100 MHz, DMSO) δ 182.89, 152.19, 138.77, 122.32, 115.33, 50.04, 46.37, 31.70, 29.27, 29.00, 28.74, 26.68, 22.53, 14.40.

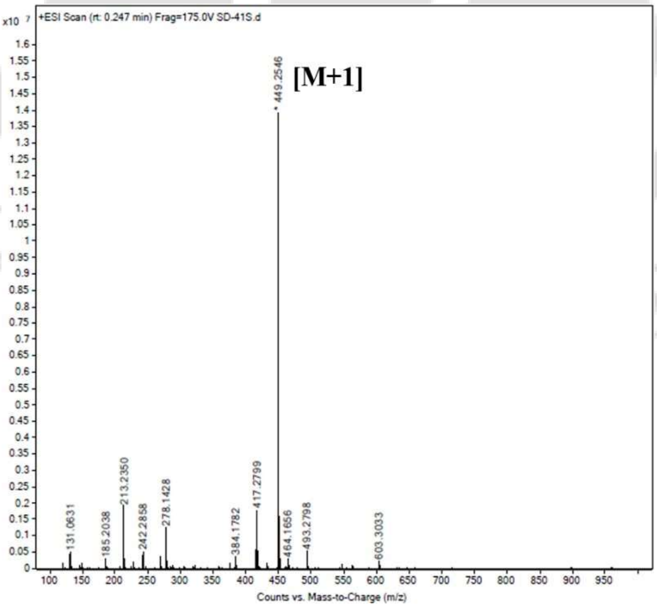

Figure A4.4. MALDI-MS spectra of C2 in dichloromethane in positive ionization mode.

ESI-MS (positive mode, m/z): calculated for $C_{25}H_{32}N_6S$: 448.24. Found: 449.25[M + H]$^+$

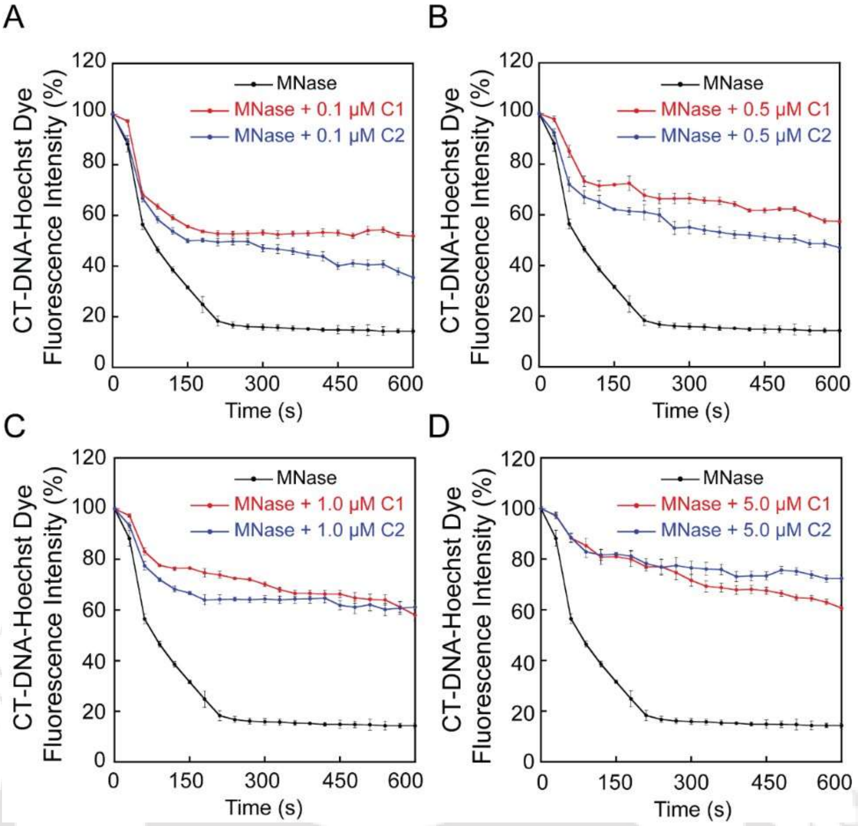

Figure A4.5. Change in fluorescence emission of CT-DNA Hoechst dye complex in presence of MNase and varying concentrations of ligands C1 and C2.

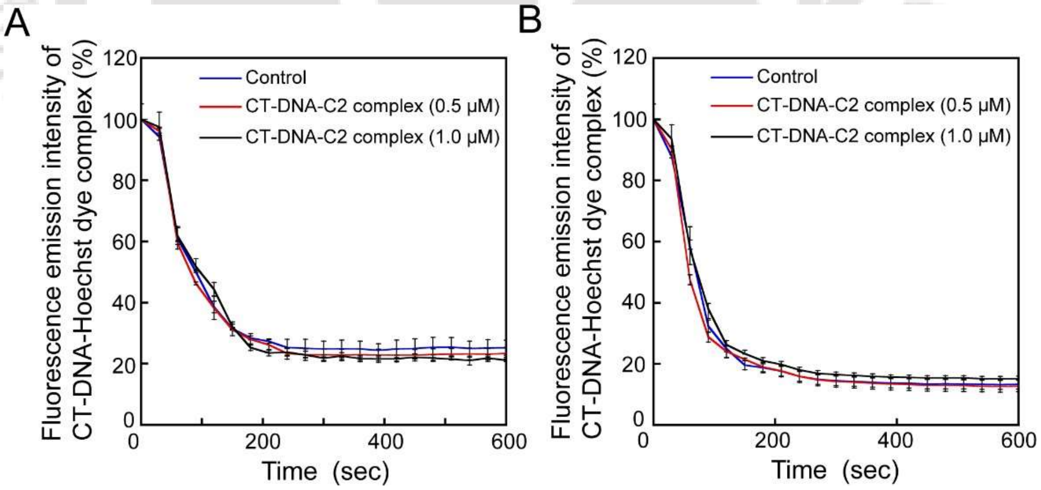

Figure A4.6. Change in fluorescence emission intensity for CT-DNA Hoechst dye-C2 preformed complex samples digested with MNase. The concentration of C2 in the preformed complex was 0.5 µM and 1.0 µM. The concentration of CT-DNA used in the experiments were (A) 0.5 µg mL^{-1} (B) 1.0 µg mL^{-1}.

Table A4.1. Statistical analysis for MNase inhibition rendered by ligands C1 and C2.

Sl. No	**Comparison Group**	**Significant Difference in MNase Inhibition***
1.	C1 (0.25 µM) versus C2 (0.25 µM)	Yes
2.	C1 (0.5 µM) versus C2 (0.5 µM)	Yes
3.	C1 (1.0 µM) versus C2 (1.0 µM)	No
4.	C1 (5.0 µM) versus C2 (5.0 µM)	Yes
5.	C1 (10 µM) versus C2 (10 µM)	Yes

* Significant difference implies *p* value < 0.001 based on analysis of variance (ANOVA) followed by all pairwise multiple comparison (Holm-Sidak method) of relative MNase inhibition.

Table A4.2. Rate constant for CT-DNA Hoechst dye-C2 preformed complex samples digested with MNase.

Concentration of CT-DNA in preformed complex with C2 (µg mL^{-1})	**Rate constant (s^{-1})**		
	Control	**Concentration of C2 in CT-DNA-C2 preformed complex**	
		0.5 µM	**1.0 µM**
0.5	0.59	0.57	0.60
1.0	0.62	0.67	0.66

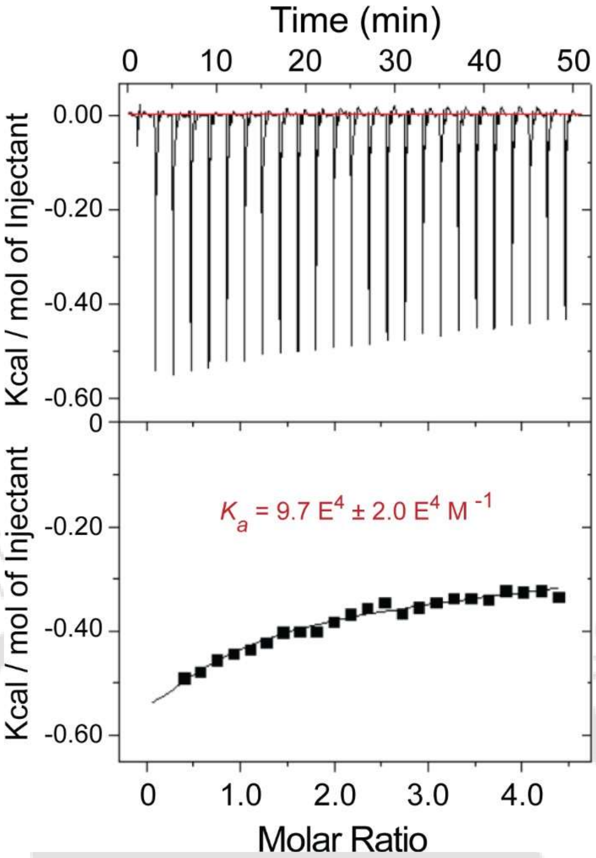

Figure A4.7. ITC analysis to ascertain the binding isotherm of C2 and MNase.

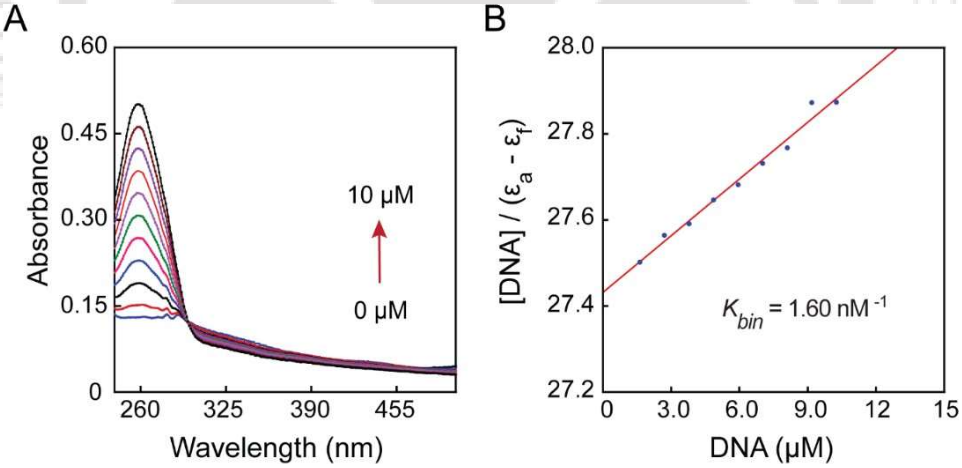

Figure 4.8. (A) UV-visible absorbance spectra of C2 in presence of CT-DNA. (B) Binding isotherm of C2 in presence of an increasing concentration of CT-DNA.

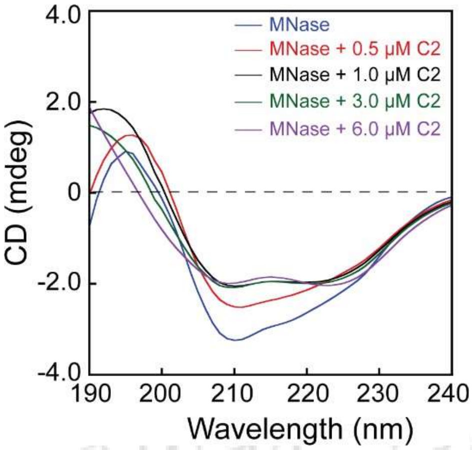

Figure A4.9. CD spectra of MNase measured in presence of varying concentrations of C2.

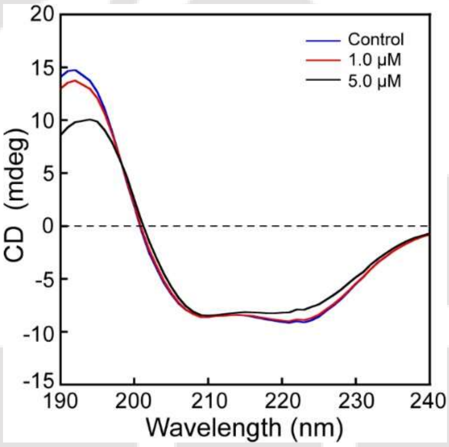

Figure A4.10. CD spectra of human serum albumin (HSA) measured in presence of an increasing concentration of C2.

Table A4.3. Secondary structure analysis of HSA following interaction with C2.

Sample	Secondary Structure Content in HSA			
	α - Helix [%]	β - Sheet [%]	Turn/Loop [%]	Random Coil [%]
HSA	34.9	28.2	6.6	30.3
HSA + C2 (1.0 μM)	34.5	26.3	9.2	30
HSA + C2 (5.0 μM)	30.2	28	14	27.8

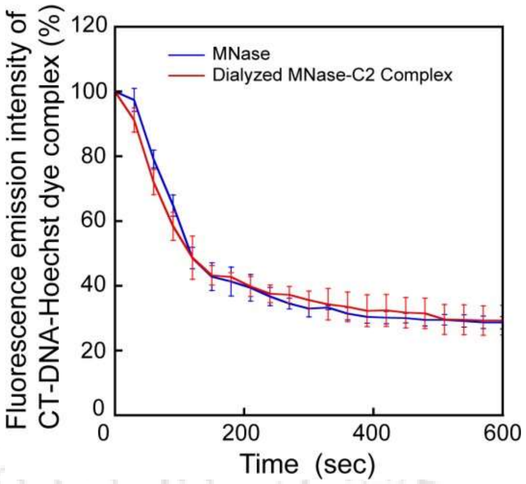

Figure A4.11. Change in fluorescence emission intensity of CT-DNA Hoechst dye complex in presence of MNase and dialyzed sample of MNase-C2 complex.

Molecular Docking

The crystal structure of DNase I (PDB ID 3DNI) and MNase (PDB ID 1EY0) were retrieved from PDB [http://www.rcsb.org/pdb/home/home.do]. Energy minimization of MNase structure was done using Swiss Pdb Viewer 4.10 and saved in .pdb format. Further, the structure was subjected to addition of hydrogens, addition of Kollman united atom charges and non-polar hydrogens. The ligand C2 was drawn using ChemDraw Ultra 8.0 and energy minimization of the molecule was performed using Chem3D Ultra 8.0 and saved in .pdb format. Docking of C2 with DNase I and MNase was accomplished byusing AutoDock 4.2.5.1 version [http://autodock.scripps.edu/]. For DNase I, the grid was set at X=-42.811, Y=27.865, Z=13.246; dimensions (Å) at X=34.000, Y=38.000, Z=40.000; spacing 0.375 Å. For MNase, the grid was set at X = 40, Y= 30.803, Z= -4; dimensions (Å) at X= 52.000, Y= 42.000, Z= 38.000; spacing 0.375 Å. By applying Lamarckian genetic algorithm, docking was performed between the target nuclease and C2 ligand in Autodock 4.0 with 25 GA runs in separate sets. The generated .pdb file wasanalyzed using Protein-Ligand Interaction Profiler (PLIP) and the docked conformations were visualized using PyMOL.

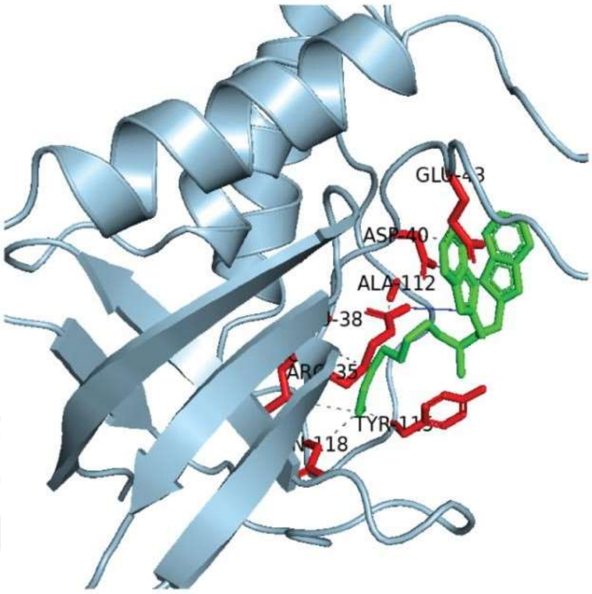

Figure A4.12. Docked structure of C2 with MNase.

Table A4.4. Binding interactions and binding energy of ligand C2 with the amino acid residuesof MNase.

Molecule	Nature of Interaction *		Binding Energy (kcal/mol)
	Hydrophobic Interaction	Hydrogen Bonds	
C2-MNase complex	LEU (37, 38) ASP (40) GLU (43) ALA (112) TYR (115) ASN (118)	1) 35 ARG, Donor Angle- 140.66, Distance H-A 2.30 Å, D-A 3.14 Å. 2) 40 ASP, Donor Angle- 140.63, Distance H-A 2.29 Å, D-A 3.15 Å	-5.28

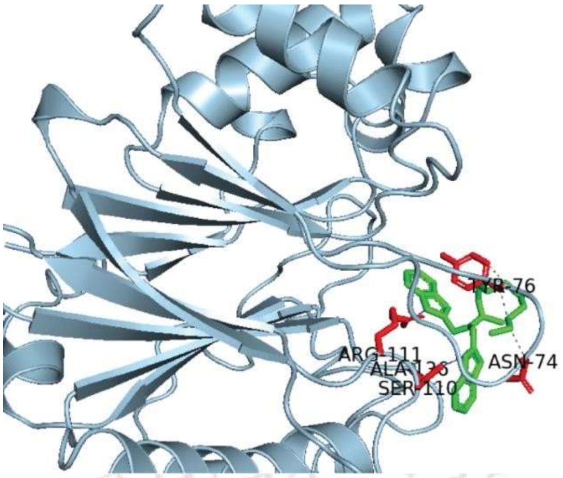

FigureA4.13. Docked structure of C2 with DNase I.

Table A4.5. Binding interactions and binding energy for C2 with the amino acid residues of DNase I determined in molecular docking studies.

Molecule	**Nature of Interaction**		**Binding energy (kcal/mol)**
	Hydrophobic Interaction	**Hydrogen Bonds**	
C2-DNaseI Complex	ASN (74) TYR (76) ALA (136)	(1) 110 SER, Donor Angle-144.77, Distance H-A 2.99 Å, D-A 3.88 Å (2) 111 ARG, Donor Angle-137.93, Distance H-A 2.97 Å, D-A 3.77 Å	-3.72

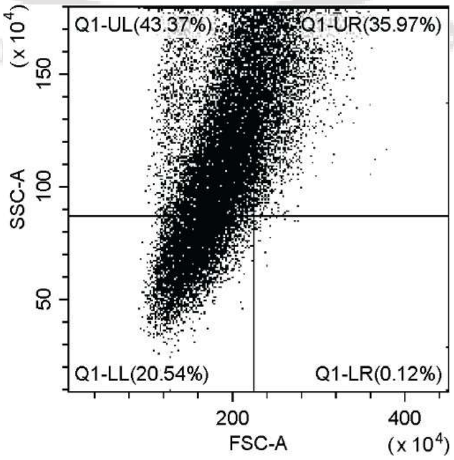

Figure A4.14. Flow cytometry-based quadrant plot for activated THP-1 cells incubated with CT-DNA and TAMRA-labelled MRSA cells (10^8 CFU) and C2 (15 µM).

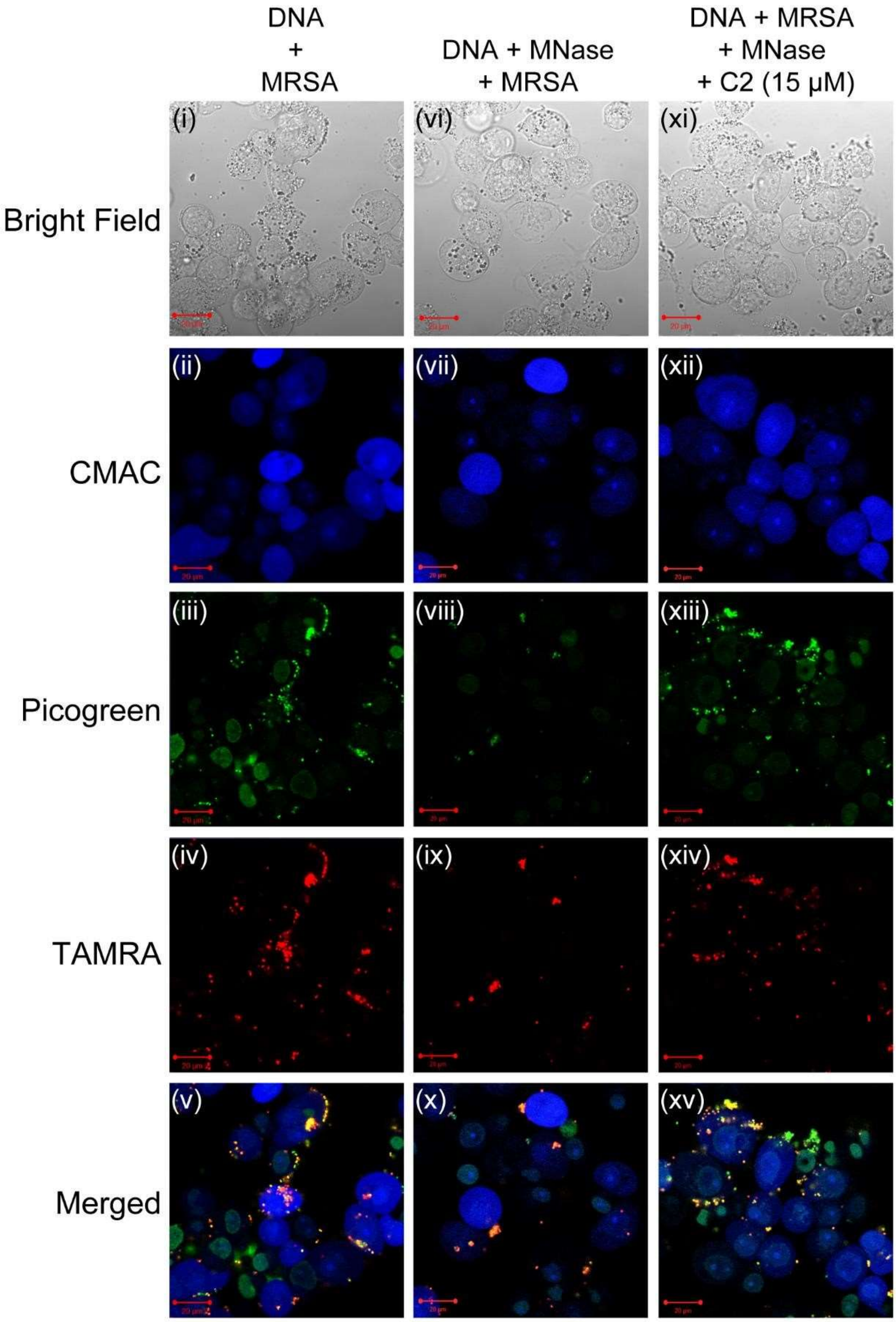

Figure A4.15. Confocal microscope-based imaging for ascertaining the uptake of TAMRA-labelled MRSA cells by activated THP-1 cells in presence of various treatment regimens.

Table A5.1. Salient attributes of napthalimide-based ligands determined by using Molinspirationtool (www.molinspiration.com)

Ligand	cLogP	nON	nOHNH
C1	5.1	8	0
C2	7.8	8	1
C3	10.8	9	1

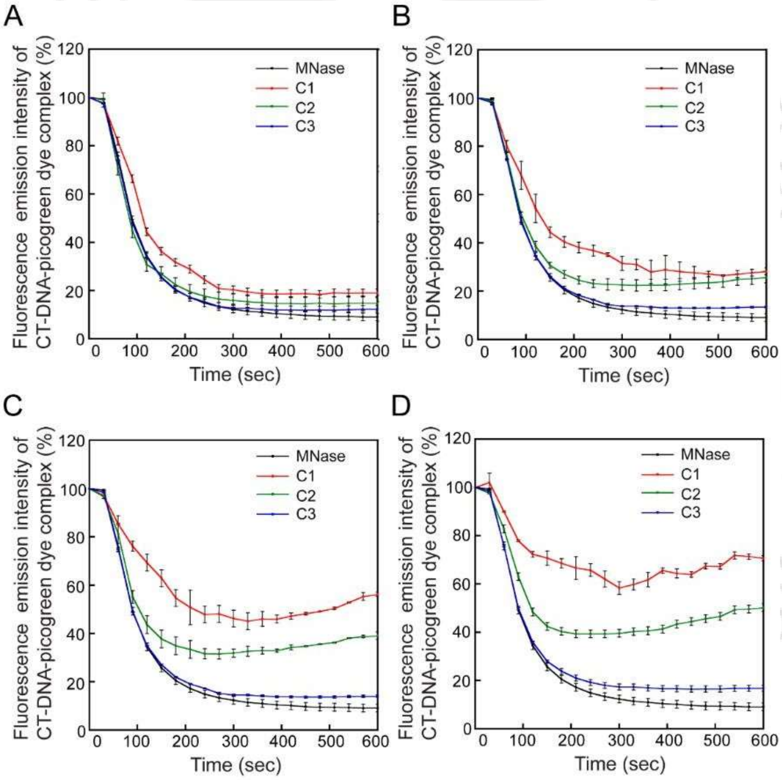

Figure A5.1. Change in fluorescence emission of CT-DNA-picogreen dye complex in presence of MNase and ligands C1-C3. The concentration of the ligands used in the experiment were(A) 0.25 µM, (B) 0.50 µM, (C) 1.0 µM and (D) 5.0 µM.

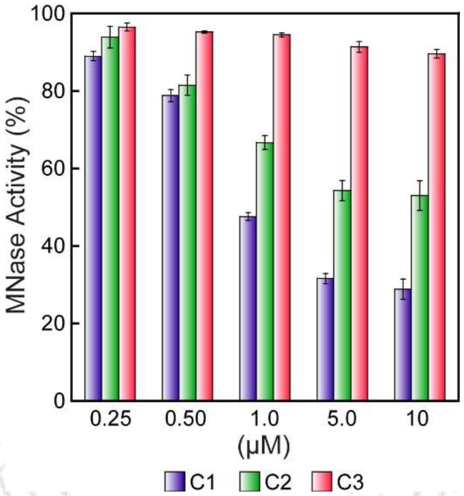

Figure A5.2. Dose-dependent reduction of MNase activity rendered by ligands C1-C3.

Table A5.2. Rate constant for decrease in fluorescence emission intensity of CT-DNA-bound picogreen dye in presence of varying concentrations of C1, C2 and C3.

Ligand Concentration (µM)	**Rate Constant (s^{-1})**		
	C1	**C2**	**C3**
0	0.70	0.70	0.70
0.25	0.61	0.65	0.70
0.50	0.53	0.60	0.68
1.0	0.24	0.41	0.66
5.0	0.16	0.37	0.64
10	0.14	0.28	0.61

Table A5.3. Statistical analysis for MNase inhibition rendered by ligands C1-C3.

Sl. No	Comparison Group	Significant Difference in MNase Inhibition*
1.	C1 (0.25 μM) versus C2 (0.25 μM)	No
2.	C1 (0.25 μM) versus C3 (0.25 μM)	Yes
3.	C1 (0.5 μM) versus C2 (0.5 μM)	No
4.	C1 (0.5 μM) versus C3 (0.5 μM)	Yes
5.	C1 (1.0 μM) versus C2 (1.0 μM)	Yes
6.	C1 (1.0 μM) versus C3 (1.0 μM)	Yes
7.	C1 (5.0 μM) versus C2 (5.0 μM)	Yes
8.	C1 (5.0 μM) versus C3 (5.0 μM)	Yes
9.	C1 (10 μM) versus C2 (10 μM)	Yes
10.	C1 (10 μM) versus C3 (10 μM)	Yes

* Significant difference implies *p* value < 0.001 based on analysis of variance (ANOVA) followed by all pairwise multiple comparison (Holm-Sidak method) of relative MNase inhibition.

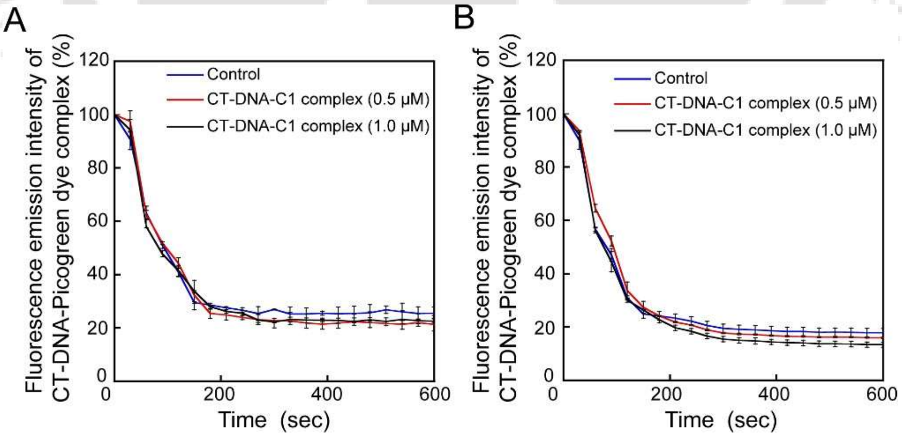

Figure A5.3. Change in fluorescence emission intensity of CT-DNA picogreen dye complex with varying concentration of C1 in presence of MNase. The concentration of CT-DNA used in the experiments were (A) 0.5 μg mL^{-1} and (B) 1.0 μg mL^{-1}.

Table A5.4. Rate constant for decrease in fluorescence emission intensity of CT-DNA picogreen dye complex with varying concentration of C1 in presence of MNase.

Concentration of CT-DNA in preformed complex with C1 (µg mL^{-1})	Rate constant (s^{-1})		
	Control	Concentration of C1 in CT-DNA-C1 preformed complex	
		0.5 µM	1.0 µM
0.5	0.51	0.54	0.55
1.0	0.63	0.65	0.64

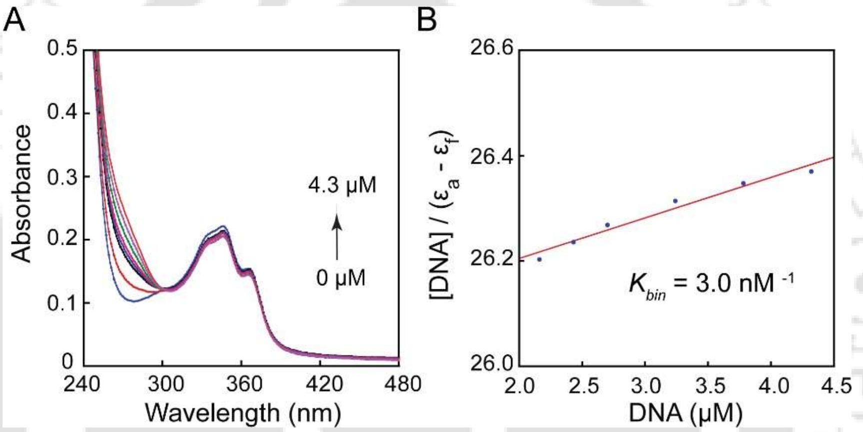

Figure A5.4. (A) UV-visible absorbance spectra of C1 in presence of CT-DNA. (B) Binding isotherm of C1 in presence of an increasing concentration of CT-DNA.

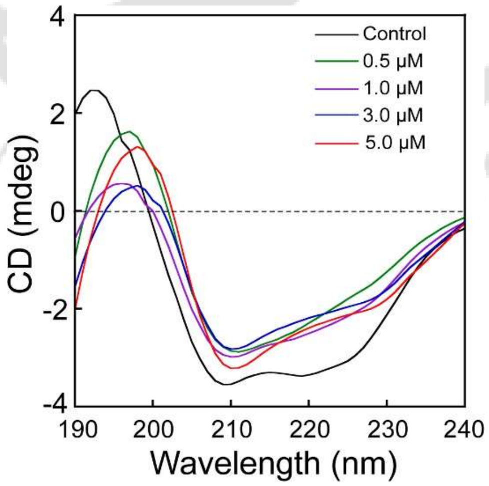

Figure A5.5. CD spectra of MNase measured in presence of an increasing concentration of C1.

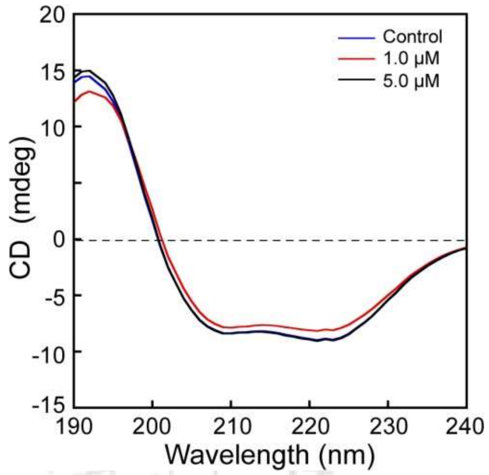

Figure A5.6. CD spectra of human serum albumin (HSA) measured in presence of an increasing concentration of C1.

Table A5.5. Secondary structure analysis of human serum albumin (HSA) following interaction with C1.

Sample	**Secondary Structure Content in HSA**			
	α - Helix (%)	**β - Sheet (%)**	**Turn/Loop (%)**	**Random Coil (%)**
HSA	35.5	26.2	7	31.2
HSA + C1 (1.0 µM)	37.1	24.9	9.6	28.4
HSA + C1 (5.0 µM)	35.7	28.2	5.7	30.4

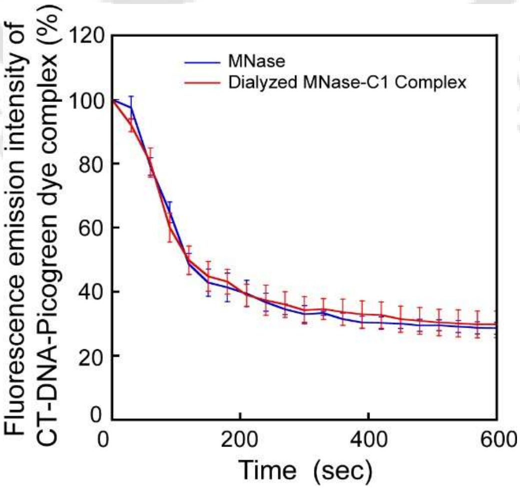

Figure A5.7. Change in fluorescence emission intensity of CT-DNA picogreen dye complex in presence of MNase and dialyzed sample of MNase-C1 complex.

Molecular Docking Studies

The crystal structure of DNase I (PDB ID 3DNI) and MNase (PDB ID 1EY0) were retrieved from PDB [http://www.rcsb.org/pdb/home/home.do]. Energy minimization of MNase structure was done using Swiss Pdb Viewer 4.10 and saved in .pdb format. Further, the structure was subjected to addition of hydrogens, addition of Kollman united atom charges and non-polar hydrogens. The ligand C1 was drawn using ChemDraw Ultra 8.0 and energy minimization of the molecule was performed using Chem3D Ultra 8.0 and saved in .pdb format. Docking of C2 with MNase was accomplished by using AutoDock 4.2.5.1 version [http://autodock.scripps.edu/]. For MNase, the grid was set atX = 40, Y= 30.803, Z= -4; dimensions (Å) at X= 52.000, Y= 42.000, Z= 38.000; spacing 0.375 Å. For DNase I, the grid was set at X=-42.811, Y=27.865, Z=13.246; dimensions (Å) at X=34.000, Y=38.000, Z=40.000; spacing 0.375 Å. By applying Lamarckian genetic algorithm, docking was performed between the target nuclease and C1 ligand inAutodock 4.0 with 25 GA runs in separate sets. The generated .pdb file was analyzed using Protein-Ligand Interaction Profiler (PLIP) and the docked conformations were visualized using PyMOL.

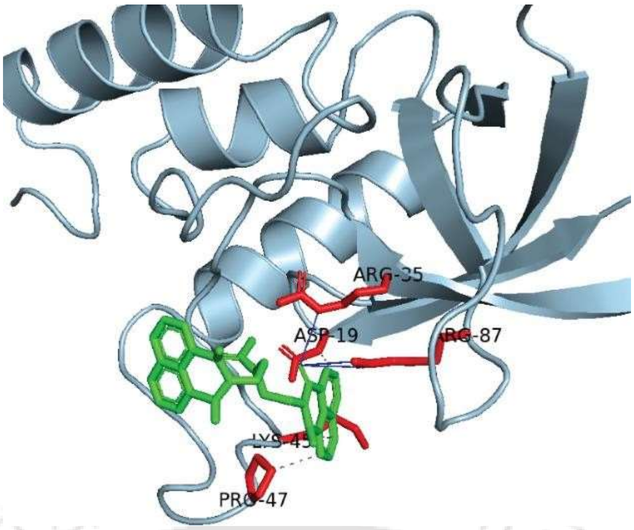

Figure A5.8. Docked structure of C1 with MNase.

Table A5.6. Binding interactions and binding energy for C1 with the amino acid residues of MNase were determined by molecular docking studies.

Molecule	**Nature of Interaction**		**Binding energy (kcal/mol)**
	Hydrophobic Interaction	**Hydrogen Bonds**	
C1-MNase Complex	ASP (19) LYS (45) PRO (47)	(1) 35 ARG, Donor Angle-134.99, Distance H-A 2.78 Å, D-A 3.55 Å (2) 87 ARG, Donor Angle-169.69, Distance H-A 2.48 Å, D-A 3.47 Å (3) 87 ARG, Donor Angle-139.97, Distance H-A 3.22 Å, D-A 4.04 Å.	-7.1

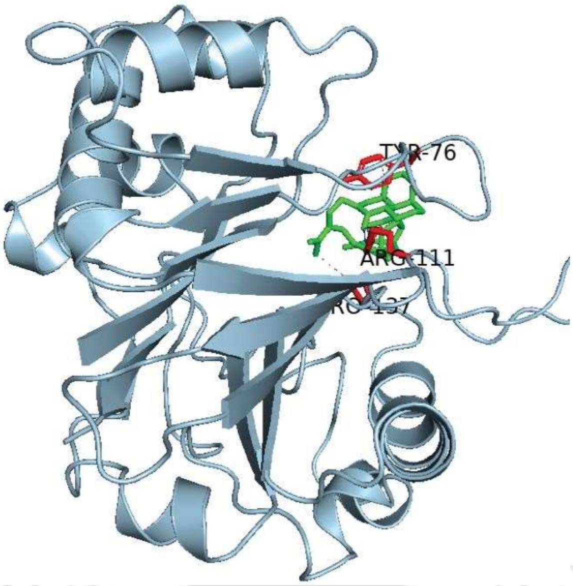

Figure A5.9. Docked structure of C1 with DNase I.

Table A5.7. Binding interactions and binding energy for C1 with the amino acid residues of DNase I determined in molecular docking studies.

Molecule	**Nature of Interaction**		**Binding energy [kcal/mol]**
	Hydrophobic Interaction	**Hydrogen Bonds**	
C1-DNase I Complex	TYR (76) PRO (137)	(1) 111 ARG, Donor Angle-140.65, Distance H-A 3.01 Å, D-A 3.84 Å (2) 111 ARG, Donor Angle-143.80, Distance H-A 2.86 Å, D-A 3.71 Å	-5.63

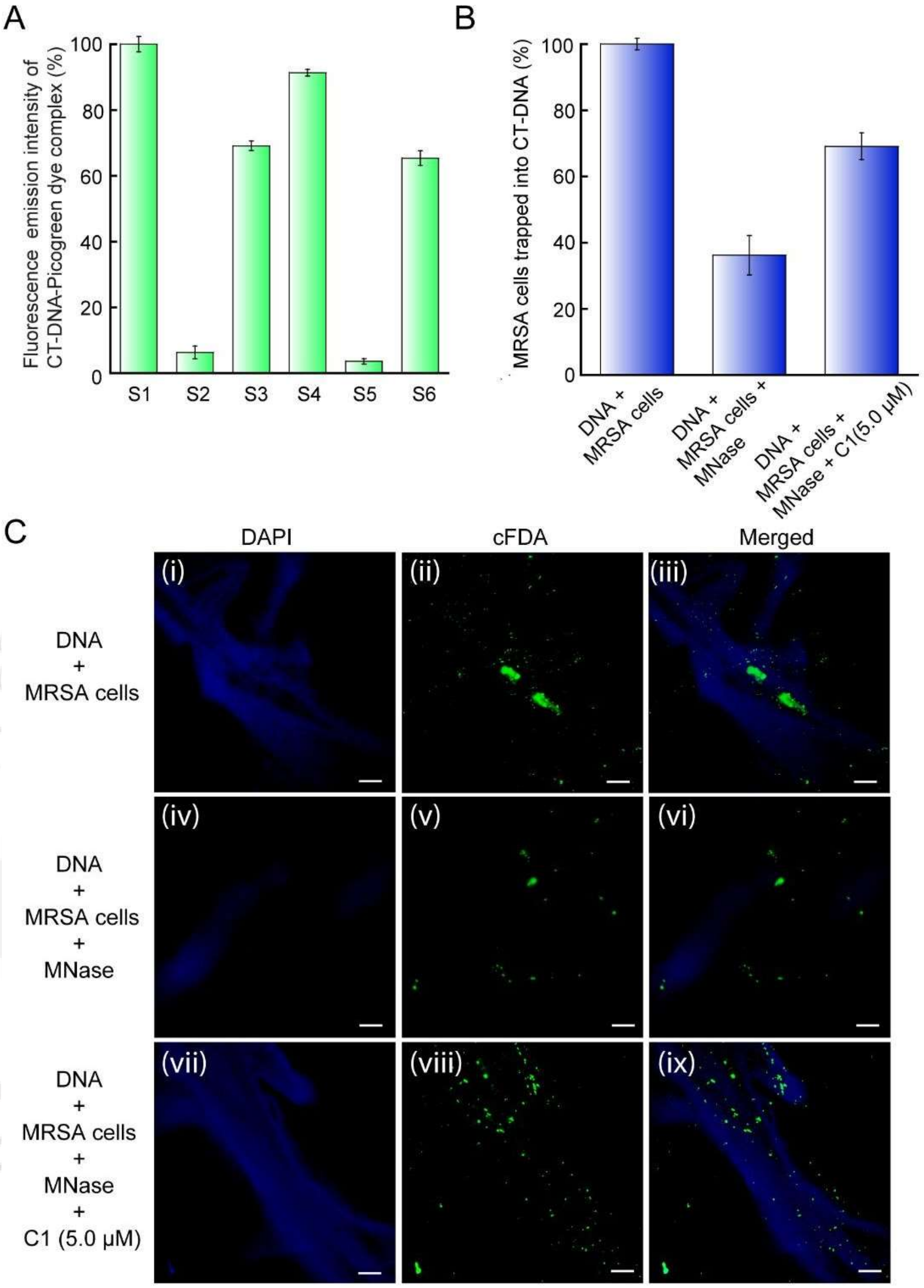

Figure A6.1. (A) Fluorescence emission of CT-DNA-picogreen complex in presence of different treatment regimens. (S1) CT-DNA. CT-DNA incubated with (S2) MNase, (S3) MNase and C1 (5.0 µM), (S4) MRSA cells, (S5) MNase and MRSA cells, (S6) MNase and C1 (5.0 µM) and MRSA cells. (B) Relative proportion of MRSA cells trapped in CT-DNA in presence of varioustreatment regimens ascertained by plating. (C) Fluorescence microscope-based detection of MRSA entrapped in CT-DNA in presence of various treatment regimens. MRSA cells and CT- DNA were labelled with cFDA-SE and DAPI, respectively. Scale bar for the images is 50 µm.

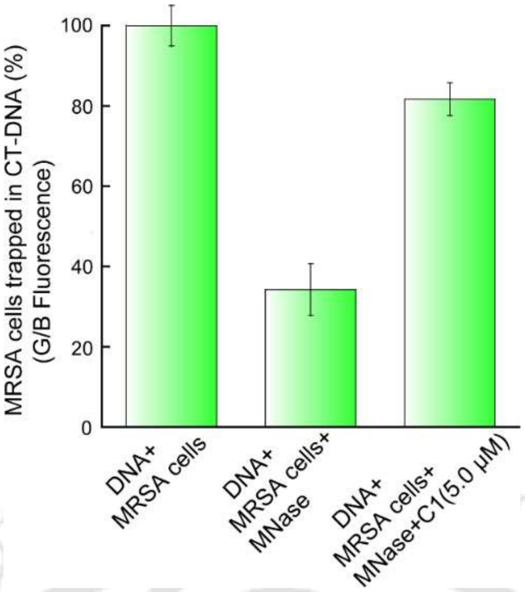

Figure A6.2. Estimation of the entrapment of MRSA cells in CT-DNA (expressed as percentage)by measuring mean relative green/blue (G/B) emission pixel intensity in fluorescence microscope-based imaging studies.

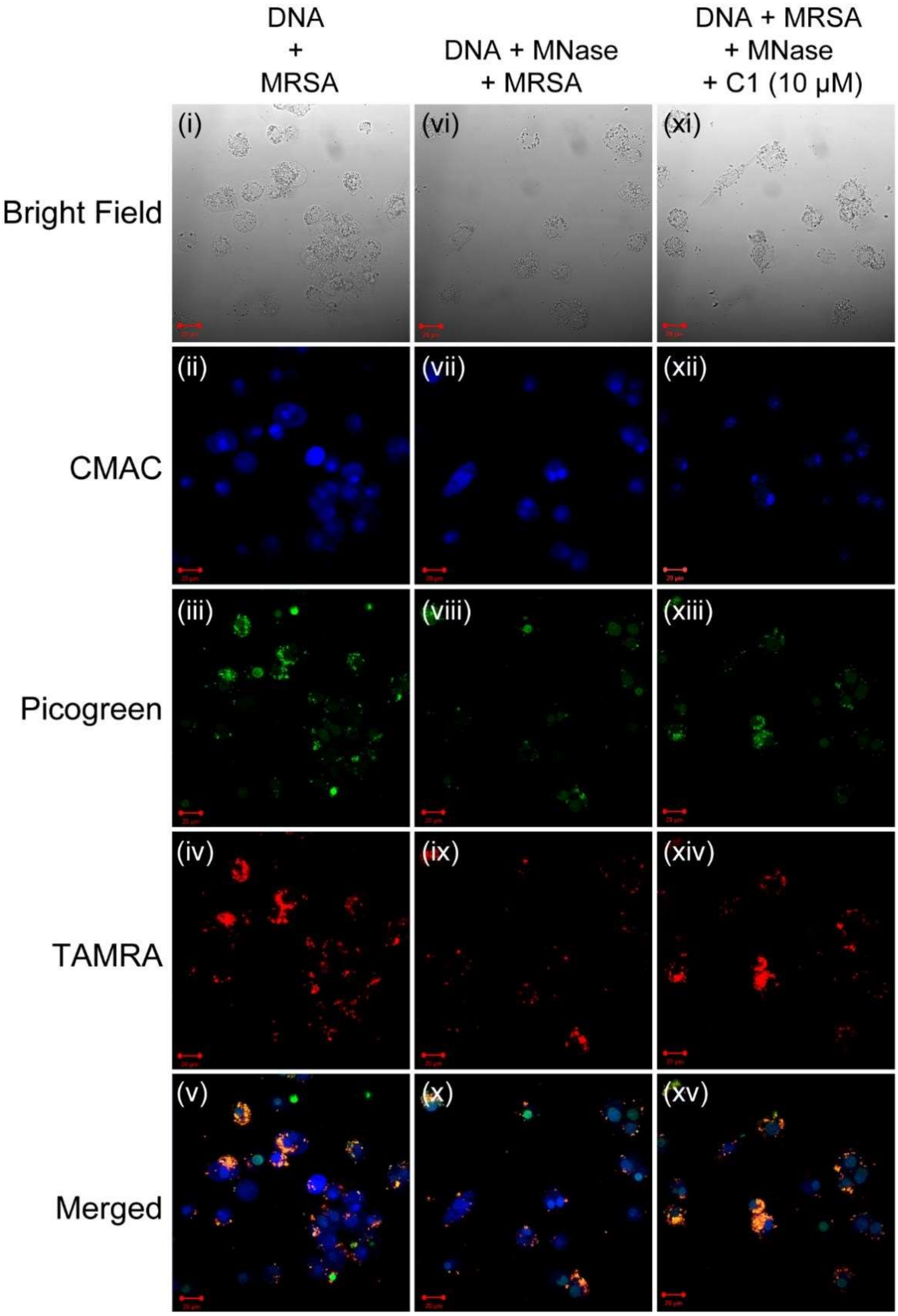

Figure A6.3. Confocal microscope-based imaging to ascertain the uptake of TAMRA-labelledMRSA cells by activated THP-1 cells in presence of various treatment regimens.

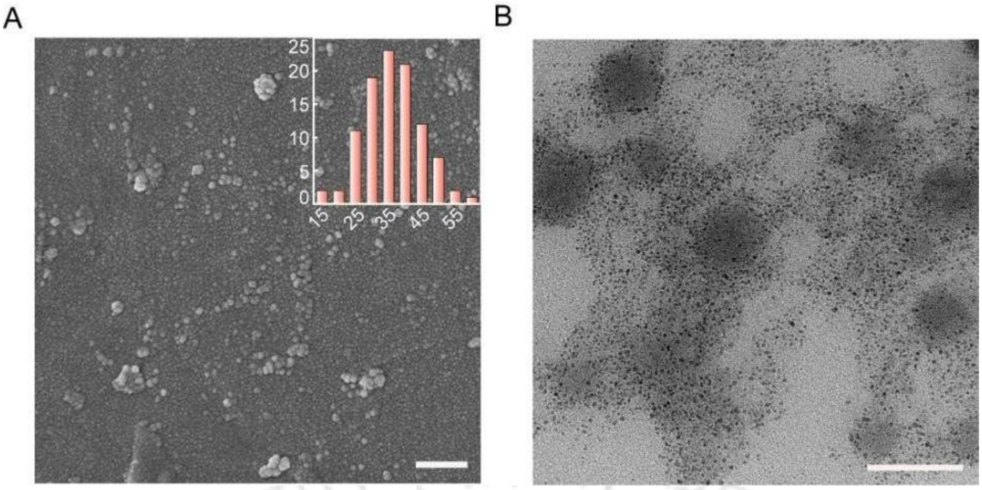

Figure A6.4. (A) FESEM image of PF-127 nanocarrier (PMC). Inset indicates particle size distribution of PMC determined by using ImageJ software. (B) FETEM image of PMC. The scale bar for the images in (A) and (B) is 200 nm and 100 nm, respectively.

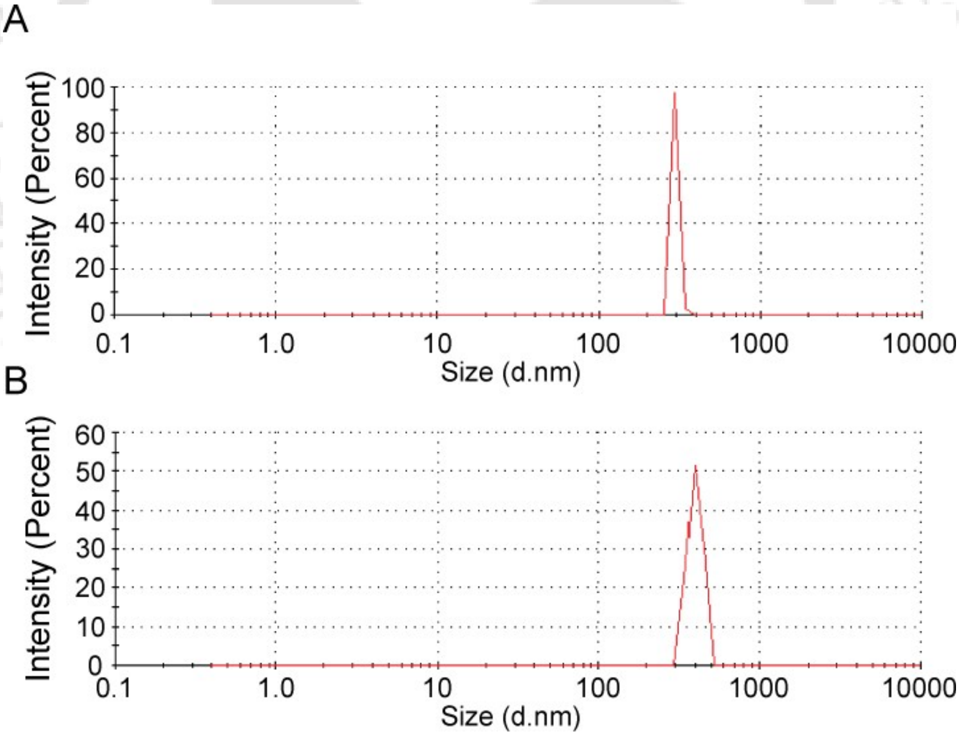

Figure A6.5. DLS-based size distribution plot for (A) PMC and (B) C1-PMC.

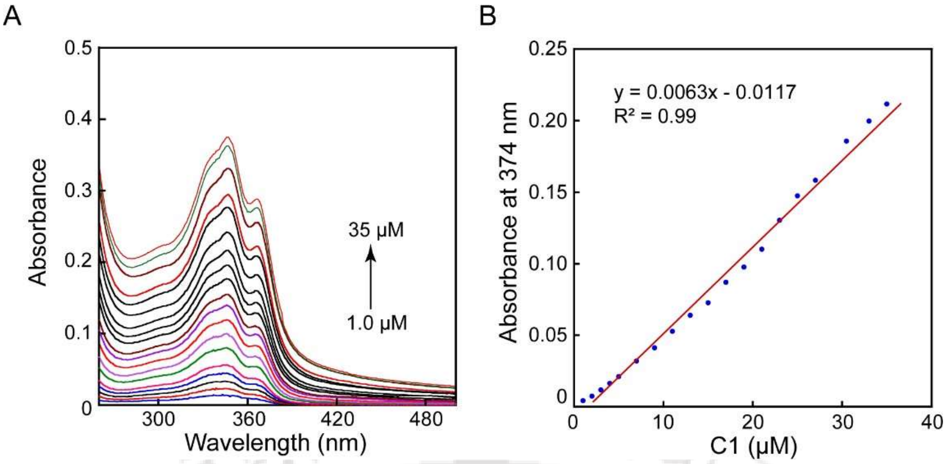

Figure 6.6. (A) Absorbance spectra of varying concentration of C1. (B) Calibration plot for C1 generated from the absorbance spectra shown in (A).

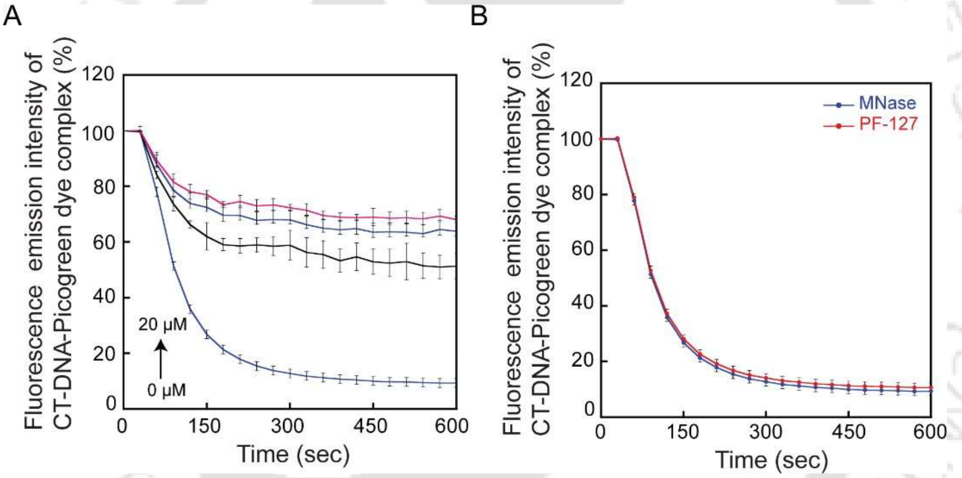

Figure A6.7. Change in fluorescence emission intensity of CT-DNA-picogreen dye complex in presence of (A) MNase and varying concentrations of C1 eluates obtained from C1-PMC and (B) MNase and PMC.

Table A6.1. Rate constant for decrease in fluorescence emission intensity of CT-DNA- bound picogreen dye in presence of varying concentrations of C1 eluates obtained from C1-PMC.

C1 (μM)	Rate Constant(s^{-1})
0	0.73
5.0	0.37
10	0.29
20	0.24

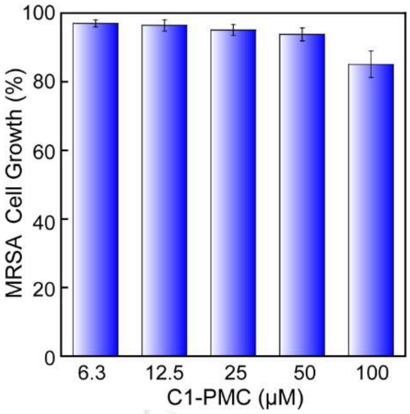

Figure A6.8. Bactericidal activity of C1-PMC (loaded with 100 μM C1) against *S. aureus* MRSA 100 strain.

Table A6.2. Statistical analysis for ascertaining the effect of various treatment regimens on adhesion of *S. aureus* MRSA 100 strain onto collagen.

Sl. No	Comparison of Treatment Groups	Significant Difference in Collagen Adhesion*
1.	Control (untreated) versus C1-PMC (loaded with100 μM C1)	Yes
2.	C1 (5.0 μM) versus C1-PMC (loaded with100 μM C1)	Yes
3.	C1 (10 μM) versus C1-PMC (loaded with100 μM C1)	Yes
4.	Control (untreated) versus C1 (20 μM)	Yes
5.	C1 (5.0 μM) versus C1 (20 μM)	Yes
6.	Control (untreated) versus PMC	Yes
7.	C1 (10 μM) versus C1 (20 μM)	Yes
8.	C1 (5.0 μM) versus PMC	Yes
9.	PMC versus C1-PMC (loaded with100 μM C1)	Yes
10.	C1 (10 μM) versus PMC	Yes
11.	C1 (20 μM) versus C1-PMC (loaded with100 μM C1)	Yes
12.	Control (untreated) versus C1 (10 μM)	Yes
13.	PMC versus C1 (20 μM)	Yes
14.	C1 (5.0 μM) versus C1 (10 μM)	Yes
15.	Control (untreated) versus C1 (5.0 μM)	No

* Significant difference implies p value < 0.001 based on analysis of variance (ANOVA) followed by all pairwise multiple comparison (Holm-Sidak method) of adhesion of *S. aureus* MRSA 100 strain onto collagen in presence of various treatment regimens.

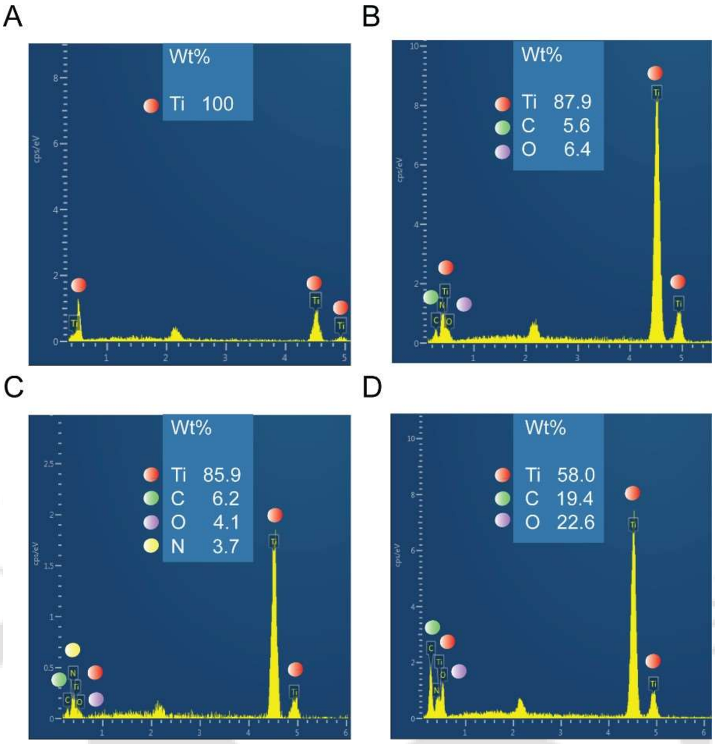

Figure A6.9. Energy dispersive X-ray (EDX) analysis of (A) Bare titanium wire, (B) Collagen-coated titanium wire, (C) Collagen and C1-coated titanium wire and (D) Collagen and PMC- coated titanium wire.

LIST OF PUBLICATIONS

List of Publications

Publications from Ph.D. Thesis Work:

(A) Journal Publications:

1. **Konwar, B.;** Mullick, P.; Das, G.; Ramesh, A. Anthraquinone-based ligand as MNase inhibitor: insights from inhibition studies and generation of a payload nanocarrier for potential anti-MRSA therapy. *ChemMedChem* **2023** *18*, e202200711.
2. **Konwar, B.;** De, S.; Das, G.; Ramesh, A. Inhibition of staphylococcal nuclease by benzimidazole-based ligand: implications in DNA-mediated entrapment and uptake of MRSA by macrophage-like cells. *Bioorganic Chemistry* **2023 Manuscript Number: BIOORG-D-23-02382 (Under Review)**.
3. **Konwar, B.;** De, S.; Das, G.; Ramesh, A. Napthalimide-based nuclease inhibitor: A multifunctional therapeutic material to bolster MRSA uptake by macrophage-like cells and mitigate pathogen adhesion on orthopaedic implant. *International Journal of Biological Macromolecules* **2023 Manuscript Number: IJBIOMAC-D-23-17413 (Under Review)**.

(B) Conference Presentations:

1. **Konwar, B.,** Das, G., Ramesh, A. Potential of low molecular weight synthetic ligands as nuclease inhibitors. Presented in 87th Annual Conference of Society of Biological Chemists (India), 25-27 November 2018, Manipal.
2. **Konwar, B.,** Dey, S., Das, G., Ramesh, A. Potential of benzimidazole-based ligands as staphylococcal nuclease inhibitor. Presented in 91st Annual Conference of Society of Biological Chemists (India), 8-11 December 2022, Kolkata.

Publications from Other Research Projects:

1. Das, A., Roy, B., **Konwar, B.,** Ramesh, A., Das, G. Trapped cyclic dimeric oxyanion assembly by a urea functionalized receptor: potent application in linear discriminant analysis and as antibacterial agents. *Crystal Growth & Design* **2022**, *22*, 1778-1791.